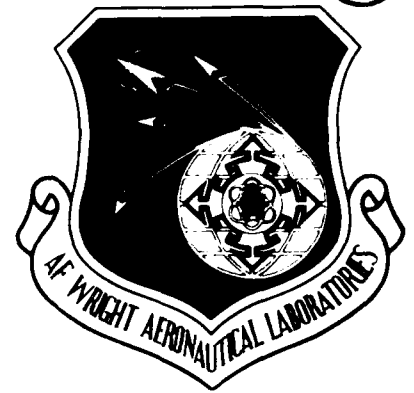AFWAL-TR-88-3084

LIQUID-VAPOR FLOW REGIME TRANSITIONS
FOR SPACECRAFT HEAT TRANSFER LOOPS

Thomas W. Lovell

AETA Corporation
Jeremiah Hart House / The Hill
Portsmouth, New Hampshire 03801

December 1988

Final Report for Period May 1986 - July 1988

Approved for Public Release; Distribution is Unlimited

FLIGHT DYNAMICS LABORATORY
WRIGHT RESEARCH AND DEVELOPMENT CENTER
AIR FORCE SYSTEMS COMMAND
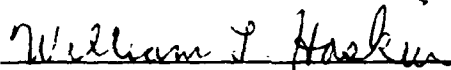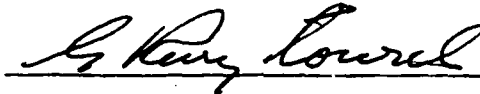WRIGHT-PATTERSON AIR FORCE BASE, OHIO 45433-6553

NOTICE

When Government drawings, specifications, or other data are used for any purpose other than in connection with a definitely related Government procurement operation, the United States Government thereby incurs no responsibility nor any obligation whatsoever; and the fact that the government may have formulated, furnished, or in any way supplied the said drawings, specifications, or other data, is not to be regarded by implication or otherwise as in any manner licensing the holder or any other person or corporation, or conveying any rights or permission to manufacture use, or sell any patented invention that may in any way be related thereto.

This report has been reviewed by the Office of Public Affairs (ASD/PA) and is releasable to the National Technical Information Service (NTIS). At NTIS, it will be available to the general public, including foreign nations.

This technical report has been reviewed and is approved for publication.

WILLIAM L. HASKIN
Project Engineer

GEORGE KURYLOWICH, Ph.D.
Technical Manager

FOR THE COMMANDER

RICHARD E. COLCLOUGH, Jr., Chief
Vehicle Subsystems Division
Flight Dynamics Laboratory

If your address has changed, if you wish to be removed from our mailing list, or if the addressee is no longer employed by your organization please notify WRDC/FIVE, W-PAFB, OH 45433-6523   to help us maintain a current mailing list .

Copies of this report should not be returned unless is required by security considerations, contractual obligations, or notice on a specific document.

REPORT DOCUMENTATION PAGE

Form Approved
OMB No. 0704-0188

1a. REPORT SECURITY CLASSIFICATION	1b. RESTRICTIVE MARKINGS
UNCLASSIFIED	

2a. SECURITY CLASSIFICATION AUTHORITY	3. DISTRIBUTION/AVAILABILITY OF REPORT
	Approved for public release;
2b. DECLASSIFICATION/DOWNGRADING SCHEDULE	distribution is unlimited.

4. PERFORMING ORGANIZATION REPORT NUMBER(S)	5. MONITORING ORGANIZATION REPORT NUMBER(S)
	AFWAL-TR-88-3084

6a. NAME OF PERFORMING ORGANIZATION	6b. OFFICE SYMBOL (If applicable)	7a. NAME OF MONITORING ORGANIZATION
AETA Corporation		Flight Dynamics Laboratory (WRDC/FIVE) Wright Research and Development Center

6c. ADDRESS (City, State, and ZIP Code)	7b. ADDRESS (City, State, and ZIP Code)
Jeremiah Hart House, The Hill Portsmouth, NH 03801 (603) 431-2205	Wright-Patterson Air Force Base, Ohio 45433-6523

8a. NAME OF FUNDING/SPONSORING ORGANIZATION	8b. OFFICE SYMBOL (If applicable)	9. PROCUREMENT INSTRUMENT IDENTIFICATION NUMBER
		F33615-86-C-3415

8c. ADDRESS (City, State, and ZIP Code)	10. SOURCE OF FUNDING NUMBERS			
	PROGRAM ELEMENT NO.	PROJECT NO.	TASK NO.	WORK UNIT ACCESSION NO.
	65502F	3005	30	42

11. TITLE (Include Security Classification)

LIQUID-VAPOR FLOW REGIME TRANSITIONS FOR SPACECRAFT HEAT-TRANSFER LOOPS

12. PERSONAL AUTHOR(S)
Thomas W. Lovell

13a. TYPE OF REPORT	13b. TIME COVERED	14. DATE OF REPORT (Year, Month, Day)	15. PAGE COUNT
Final	FROM May 86 TO July 88	December 1988	267

16. SUPPLEMENTARY NOTATION

This is a Small Business Innovation Research (SBIR) Phase II report.

17. COSATI CODES			18. SUBJECT TERMS (Continue on reverse if necessary and identify by block number)
FIELD	GROUP	SUB-GROUP	Two-Phase Fluid Flow, Flow Transitions,
20	04		Microgravity Fluid Flow.
20	13		

19. ABSTRACT (Continue on reverse if necessary and identify by block number)

The major objective of this contract was to develop prediction criteria for microgravity vapor-liquid flow regime transitions. Extensive simulation experiments were conducted using equal density, immiscible liquids. Criteria were established for bubble to slug, slug to annular, and bubble to annular flow regime transitions. These criteria were based on minimum pressure drop considerations and a new analytical model for slug flow.

Tentative pressure drop and heat transfer coefficient equations are recommended for flow conditions in two-phase vapor-liquid spacecraft-based heating or cooling loops.

20. DISTRIBUTION/AVAILABILITY OF ABSTRACT	21. ABSTRACT SECURITY CLASSIFICATION
☒ UNCLASSIFIED/UNLIMITED ☐ SAME AS RPT. ☐ DTIC USERS	Unclassified

22a. NAME OF RESPONSIBLE INDIVIDUAL	22b. TELEPHONE (Include Area Code)	22c. OFFICE SYMBOL
Mr William L. Haskin	513-255-6078	WRDC/FIVEA

DD Form 1473, JUN 86 — Previous editions are obsolete.

TABLE OF CONTENTS

APPENDICES

DTIC COPY INSPECTED 1

Accesion For		
NTIS CRA&I	☑	
DTIC TAB	☐	
Unannounced	☐	
Justification		
By		
Distribution /		
Availability Codes		
Dist	Avail and / or Special	
A-1		

LIST OF FIGURES

NOMENCLATURE

Units are given in MKS system for clarity, although any consistent system of units will work with equations in this report, unless otherwise noted.

Symbol		Description	Units
A	–	cross sectional area of pipe	[m^2]
A_f	–	cross sectional area of pipe occupied by liquid	[m^2]
A_g	–	cross sectional area of pipe occupied by vapor	[m^2]
c_1	–	slip velocity ratio in slug flow	–
c_i	–	interfacial friction factor	–
c_w	–	wall friction factor	–
c_{pf}	–	specific heat of liquid	[J/kg-K]
D	–	diameter of pipe	[m]
d_o	–	diameter of vapor core in annular flow	[m]
E	–	enhancement factor	–
F	–	enhancement factor	–
G	–	total mass flux	[kg/s-m^2]
g	–	acceleration due to gravity	[m/s^2]
g_o	–	acceleration due to standard earth gravity	[m/s^2]
h	–	heat transfer coefficient	[W/m^2K]
h_f	–	heat transfer coefficient of liquid film	[W/m^2K]
h_{pool}	–	pool boiling heat transfer coefficient	[W/m^2K]
h_c	–	convective heat transfer coefficient	[W/m^2K]
h_{NCB}	–	nucleate boiling heat transfer coefficient	[W/m^2K]
h_{TP}	–	two-phase heat transfer coefficient	[W/m^2K]
h_{fg}	–	latent heat of vaporization	[J/kg]

j	–	total volumetric flux	[m/s]
j_f	–	liquid volumetric flux (or superficial velocity)	[m/s]
j_g	–	vapor volumetric flux (or superficial velocity)	[m/s]
j_i	–	component volumetric flux (i.e., liquid or vapor)	[m/s]
j_1	–	volumetric flux (or superficial velocity) of the <u>more viscous</u> fluid of a liquid pair.	[m/s]
j_2	–	volumetric flux (or superficial velocity) of the <u>less viscous</u> fluid of a liquid pair.	[m/s]
k_f	–	turbulent coefficient for liquid friction factor or thermal conductivity of liquid	– [W/mK]
k_g	–	turbulent coefficient for vapor friction factor	–
L	–	length of pipe	[m]
L_s	–	total length of slugs in pipe	[m]
L_t	–	total length of Taylor bubbles in pipe	[m]
L_s^*	–	unit slug length $(0 \leq L_s^* \leq 1)$	–
L_t^*	–	unit Taylor bubble length $(0 \leq L_t^* \leq 1)$	–
M	–	molar mass	–
Nu	–	Nusselt number	–
P	–	perimeter	[m]
ΔP	–	pressure drop	[N/m^2]
P_r	–	reduced pressure	–
Pr	–	Prandtl number	–
ΔP_f	–	pressure drop of liquid	[N/m^2]
ΔP_g	–	pressure drop of vapor	[N/m^2]
Q_1	–	total volumetric flow of the more viscous fluid	[m^3/s]
Q_2	–	total volumetric flow of the less viscous fluid	[m^3/s]
Q_f	–	total liquid volumetric flow	[m^3/s]
Q_g	–	total gas or vapor volumetric flow	[m^3/s]

q"	–	heat flux	[W/m^2]
R	–	radius of pipe (= constant = D/2)	[m]
r	–	radius (variable)	[m]
R_o	–	radius of vapor core in annular flow	[m]
Re	–	Reynold's Number	–
Re_f	–	liquid Reynold's Number	–
Re_g	–	vapor Reynold's Number	–
S	–	suppression factor	–
S'	–	suppression factor	–
v	–	velocity	[m/s]
v_f	–	velocity of liquid	[m/s]
$\tilde{v}_{ft}$	–	velocity of liquid film along a Taylor bubble	[m/s]
v_g	–	velocity of gas or vapor	[m/s]
v_i	–	velocity of interface	[m/s]
x	–	mass (vapor) quality	–
X_{tt}	–	two-phase Martinelli parameter	–

Greek Letters

α	–	void fraction	–
δ	–	film thickness	[m]
ρ	–	density	
ρ_f	–	density of liquid	[kg/m^3]
ρ_g	–	density of gas or vapor	[kg/m^3]
μ	–	viscosity	
μ_f	–	viscosity of liquid	[N-s/m^2]
μ_g	–	viscosity of gas or vapor	[N-s/m^2]

σ	-	surface tension	[N/m]
τ	-	shear stress	[N/m^2]
τ_i	-	shear stress at interface	[N/m^2]
τ_w	-	shear stress at pipe wall	[N/m^2]

Subscripts

a	-	refers to annular flow
f	-	refers to liquid
g	-	refers to gas or vapor
h	-	refers to homogeneous (bubble) flow
i	-	refers to interface, or rarely, to component
m	-	refers to an average, or "mean" condition
s	-	refers to conditions inside liquid slugs or to slug flow in general
t	-	refers to conditions inside Taylor bubbles
w	-	refers to pipe wall

Note: The subscripts "1" and "2" are used for the more viscous and less viscous fluid respectively of an immiscible liquid-liquid flow. The subscript "2" labels the liquid which, by virtue of its lower viscosity, is assumed to simulate vapor.

The subscripts "f" and "g" refer to the two phases of true liquid-vapor flows.

Superscripts

m	-	liquid turbulent velocity profile exponent	-
n	-	vapor turbulent velocity profile exponent	-
x	-	exponent for turbulent liquid friction factor	-
y	-	exponent for turbulent vapor friction factor	-
~	-	average value	-

PREFACE

The following report and analysis were made possible only by the combined work of several people:

V.K. Mathur, S.B. Karri Reddy, and Jeff O'Hearn at the University of New Hampshire Chemical Engineering Department designed and ran the liquid-liquid flow regime experiments. They have documented their work and data in Appendix A, the Data Report. Karri [1988] wrote a Ph.D. thesis on the experimental work. There have been, in addition, several recent papers in the AIChE Journal written by Mathur, Karri, and/or O'Hearn which further report this work.

John Dzenitis of Dartmouth College had the original idea that flow regime transitions may be determined by considerations of minimized pressure gradient. In his thesis (Dzenitis [1988]), he applied the concept to successfully predict the bubble-slug transition of equi-density liquid-liquid flow regimes and microgravity vapor-liquid flows. His concept is applied here. A number of his observations and explanations have influenced this report. In addition, Appendix B is taken directly from his thesis, as indicated.

Horst Richter, also of Dartmouth College, had the idea in 1984 that equal density liquids might simulate low velocity microgravity vapor-liquid flows. He has since then continuously and significantly aided both Dzenitis and the author with analytical insight, guidance, and encouragement. Richter's ideas have influenced the implementation of the minimization of pressure gradient prinicple and the formulation of the new slug flow model. His technical and editorial help in re-reading and re-writing this report was substantial. In addition, he wrote most of the literature review and, in writing Section 7, did all the work in boiling and condensing heat transfer.

1. INTRODUCTION

"I had less difficulty in the discovery of the motion of heavenly bodies, in spite of their astonishing distances, than in the investigations of the movement of flowing water before our very eyes"

<div align="right">Galileo Galilei
1564-1642</div>

Motivation to Study Microgravity Flow Regimes

The study of microgravity vapor-liquid flow regimes is motivated by the benefits of heat transfer systems which use phase change. Phase change releases or absorbs, essentially at constant temperature, latent heat of vaporization -- a quantity two to three orders of magnitude that of sensible heat. Thus, thermal systems based on vapor-liquid phase change are compact, lightweight, require little pumping power, and can operate at virtually constant temperatures.

Such advantages have, for decades, spurred the study of vapor-liquid flow in earthbound systems. However, the same size, weight, power and temperature advantages are far more important in space applications. There, each kilogram, each watt, each cubic meter, costs dearly.

However, equipment used in space flight must be especially reliable and must perform as expected. To design, but not over-design, thermal equipment requires accurate knowledge of pressure drop, heat transfer, and such potentially destructive phenomena as water hammer. Each of these are strongly dependent on flow regime. Therefore, the ability to predict, for example, bubble flow, slug flow or annular flow, becomes quite important. The capability of predicting flow regimes should substantially increase the ability to predict, and therefore design for, heat transfer and pressure drop, and to protect against potentially damaging phenomena.

Present Experiments and Analysis

Extensive experiments were performed with equal density, immiscible liquids to simulate microgravity buoyancy conditions. The experimentally observed flow regimes and pressure drops were used to help develop a microgravity flow regime analysis.

The analysis is built on the assertion that fluids adjust to the flow regime which produces the least resistance, measured as pressure gradient. The major transitions predicted are those between bubble, slug, and annular flow. The analytically predicted flow regime transitions vary with tube diameter and

fluid viscosities. Surface tension is not included in the analysis but can be, when the effect of surface tension on interfacial shear is quantified. The analytical model and its predictions match the liquid-liquid pressure drop and flow regime data quite well.

To extend the analysis to true microgravity vapor-liquid flows, a more detailed model for slug flow than any found in the literature was developed. This slug flow model also uses the minimization of pressure drop principle to determine average slug geometry, and the related velocities. The model predicts a region of churn flow and a region of hysteresis along the slug-annular boundary.

The resulting analytical predictions of vapor-liquid flow regime are in good agreement with the limited quantity of microgravity air-water flow regime data found in the literature. However, more true microgravity vapor-liquid pressure drop and flow regime data are needed to verify the proposed method for predicting flow regimes.

2. ORGANIZATION AND CONTENTS OF REPORT

The research program documented here had one major purpose: to discover prediction criteria for microgravity flow regime transitions.[1] A number of subsidiary activities were performed in pursuit of this goal. These activities, and certain details of the major research activities, are discussed in the appendices. For example, experimental results are discussed in the report body, but details of the experiments themselves are covered in Appendix A, the Data Report. The major outcome of the research -- the analytical flow regime models developed -- are covered in the report body.

2.1. Report Body

The body of this report is structured in eight major sections:

Section 1, the Introduction (preceding page), summarizes both the motivation for this study and its results.

Section 2, the present section, describes the organization of the report. The contents of each section, especially the appendices, are summarized here.

Section 3 is a brief literature review. Microgravity data from several experimenters are included. Some of these data have been generated since this contract began.

Section 4 briefly discusses the water-oil (equi-density liquids) simulation experiments and presents plots of the data. The relatively short discussion given the simulation experiments is not indicative of the effort involved or their value. On the contrary, these experiments were a major part of the present work. Without the insights they provided, the main object of the study -- analysis of microgravity flow regimes -- would likely be much curtailed. However, the focus of this final report is analysis of the data. Therefore, the details of the simulation experiments have been assembled into a separate Data Report (Appendix A).

Section 5 presents and discusses the criteria developed to predict flow regime transitions. The liquid-liquid analysis and comparison to data is undertaken first. A number of further subsections develop concepts, such as a newly developed model for slug flow, needed to extend the analysis to apply to microgravity

---

[1] A secondary purpose was to propose suitable pressure drop and heat transfer equations for each microgravity flow regime encountered.

vapor-liquid flow. Finally, the predictions so developed are compared with microgravity flow regime data from the literature.

Section 6 presents recommended pressure drop equations for each microgravity flow regime. These recommendations follow directly from the flow regime analysis of Section 5.

Section 7 presents recommended heat transfer correlations for microgravity. Heat transfer experiments were beyond the scope of this contract. Therefore, these heat transfer recommendations are based only on physical reasoning and the literature, not on any data generated in the present work.

Section 8 summarizes conclusions and recommendations arising from the experimental and analytical work.

2.2. Appendices

Appendix A is a Data Report detailing results of the liquid-liquid simulation experiments. It includes experimental technique, calibration of flow meters, devices used to measure fluid properties, etc.

Appendix B reports supplemental wave duct experiments done to examine interfacial shear and wave behavior in microgravity flows. The wave duct used two liquids of nearly equal density to explore wave formation, growth, and travel, in the absence of a strong gravity effect.

Originally it was intended to use the results of these supplementary experiments for the analysis of microgravity flow regimes. The wave duct experiments did have encouraging results and useful analysis. For example, the onset of waviness was shown to occur at a threshold shear. However, these were preliminary experiments. Much more data are needed to predict the interfacial shear coefficient of microgravity vapor-liquid flows with confidence. Furthermore, the prediction of flow regime transitions via the minimum pressure gradient method was developed simultaneously. It proved to be the simpler analysis to predict flow regime. For this reason the interfacial shear data and analysis are placed in the appendices. The results will be useful for future work. A quantitative expression for interfacial shear across wavy surfaces may emerge from this or similar work.

Appendix C presents data and predictions of interface wave speed observed in the wave duct. A simple equation based on surface tension and density predicts, with reasonable accuracy, wave speed as a function of amplitude and depth, in minimally buoyant conditions. The equation contains no dependency on gravity.

The exploration of wave speed was undertaken to help detect flow regime transitions. It was anticipated that a prediction of wave speed in annular flow would be part of the prediction of the microgravity annular to slug transition. However, despite the apparent success at predicting wave speed, this approach (extended to an annular geometry) has so far yielded no successful transition criteria. Again, the prediction of flow regimes by the minimization of pressure gradient proved simpler. Therefore, the wave speed analysis is placed in the appendices as useful information for future work. A flow regime transition criteria may yet emerge from a similar wave speed analysis.

Appendix D presents details and solutions of the integral annular flow analysis. These details were deemed inappropriate for the general discussion in the main report. Equations for such items as velocity profiles in each phase are presented. These annular equations are used repeatedly in the flow regime transition analysis to predict pressure drop and to describe annular flow. They are also used to describe flow in the Taylor bubble portion of the detailed slug flow model.

Appendix E shows how the expressions for liquid-liquid pressure gradient were developed. Largely analytical pressure drop equations for each flow regime are fitted to the liquid-liquid pressure drop data. The resulting semi-analytical curve fits are compared to data. In the case of bubble flow, no curve fitting was required. The recommended equation remains purely analytical. In the case of annular flow, a minor correction factor was required. The result is a nearly pure analytical expression for annular pressure drop.

3. LITERATURE REVIEW

Generally, two-phase flows of vapor (or gas) and liquid are subject to the following six basic forces:

- surface tension $\sim$ σD (N)

- viscous force of the liquid $\sim$ $\mu_f j_f D$ (N)

- viscous force of the vapor $\sim$ $\mu_g j_g D$ (N)

- inertia of the liquid $\sim$ $\rho_f j_f^2 D^2$ (N)

- inertia of the vapor $\sim$ $\rho_g j_g^2 D^2$ (N)

- buoyancy (gravity) force $\sim$ $(\rho_f - \rho_g) g D^3$ (N)

D is some characteristic length, usually related to the geometry of the flow conduit. The volumetric fluxes j_f and j_g are, equivalently, the superficial velocities of the liquid and the vapor, respectively.

In the absence of gravitational forces, only five of the basic six forces are important. Thus, without gravity, the complexity of a two-phase flow is substantially decreased. Two-phase flow behavior should be simpler in microgravity than on earth. However, strong interest in microgravity flows has existed only since the start of the space age. It has been difficult to perform inexpensive reduced-gravity experiments. The resulting small knowledge base is insufficient for reliable design of evaporation or condensation systems.

Below, the highlights of existing microgravity two-phase flow and heat transfer literature are reviewed.

3.1. Flow Regime Definitions and Plotting Conventions Used in this Report

Before discussing the literature, a brief review is offered of some basic definitions.

When vapor and liquid flow together in a pipe, various overall flow patterns may occur. Each general flow pattern type may be assigned a qualitative description called a "flow regime". Pressure drop and heat transfer have been found to be very dependent on flow regime.

6

Flow regimes which have been observed in microgravity vapor-liquid flows are primarily one of the following four basic types:

Bubble Flow : Bubbles of vapor are carried by a continuous liquid flow.

Slug Flow : Large bullet-shaped ("Taylor bubbles"), elliptical, or irregular-shaped bubbles flow within a continuous liquid. These vapor bubbles, if permitted to become spherical, would be of a diameter equal to or larger than the pipe diameter

Drop Flow : Drops of liquid are carried by a continuous vapor flow. In most circumstances, drop flow occurs in combination with annular flow, defined below.

Annular Flow : Liquid flows continuously on the inside wall of the pipe, enclosing a continuous central vapor flow.

It is common for a rapidly flowing vapor core to entrain liquid droplets to form "drop" or "mist" flow in the core. However, a continuous deposition process ensures that a portion of the liquid always flows as an annulus on the perimeter. Thus, drop flow and mist flow in vapor-liquid systems are most frequently subsets of annular flow.

There are two gravity-dominated flow regimes frequently observed on earth in horizontal vapor-liquid flows:

Stratified Flow : Liquid flows continuously as a "river" at the bottom of the pipe; vapor flows continuously above the flat liquid-vapor interface.

Wavy Flow : Same as above, except the vapor flow is of sufficient velocity to cause waves on the liquid surface.

The last two flow regimes are not observed in microgravity environments. In fact, the study of microgravity flow regimes

might be phrased as: In the absence of gravity, what flow regimes occur where stratified or wavy flow would otherwise be expected?

Flow regimes and the boundaries between them have been found to be functions of the fluid properties of both phases (such as density, viscosity, and interfacial tension), mass flow rates, void fraction, entrance geometry, and the orientation of the flow channel with respect to gravity. However, the complete functional relationship between these factors and flow regime has yet to be discovered.

Therefore, it is common practice to simply show flow regime boundaries as functions of the vapor and liquid flow rates, or quantities variously related to the flow rates. These boundaries section a plot by areas, each of which shows a particular flow regime. Such plots are called "flow regime maps". By predicting flow regimes, these maps, whether empirically or theoretically derived, help predict pressure drop, condensation, and evaporation.

Throughout this report, flow regime maps and data will be plotted on the basis of volumetric fluxes: liquid volumetric flux j_f and vapor volumetric flux j_g. These terms are also known as superficial liquid velocity and superficial vapor velocity, respectively. While referring to liquid-liquid simulations, the term j_1 will refer to the more viscous liquid, the term j_2 to the less viscous liquid. For simulations purposes, j_1 is assumed to correspond to j_f, and j_2 is assumed to correspond to j_g.

3.2. Flow Regime Maps from the Literature

3.2.1. Earth Gravity Flow Regime Maps

Two-phase phenomena and flow regimes observed on earth can be tolerably well predicted, but frequently through the use of correlations. However, these predictions and correlations are in part strong functions of gravity. Only in the last two decades has extensive research been initiated to evaluate the influence of reduced gravity on two-phase flow.

One of the first (and still popular) flow regime prediction schemes was a flow regime map proposed by Baker [1954]. It is empirically based on experimental data, using combinations of physical parameters for the plotting axes to give some generality. In another early paper, Quandt [1965] specifies only three flow regimes (separated, intermittent, and dispersed) and uses Froude number as a criterion for the transitions.

Recent efforts for normal gravity flow regimes have become more refined in regime specification and transition prediction

accuracy. Though the criteria for the transitions have some physical reasoning behind them, they are still largely empirical. One set of widely used predictions were given by Taitel and Dukler for horizontal pipes [1976]. Experimentation by Weisman et al. [1979] led them to introduce changes to Taitel-Dukler. Chisholm produced further refinements applicable to a wider range of density ratios. Taitel, Barnea, and Dukler [1980] later proposed models for vertical pipes, and Weisman and Kang [1981] for vertical and inclined pipes. There have been many other efforts applied to individual regime transitions.

3.2.2. Microgravity Flow Regime Maps

At high mass fluxes it is anticipated that gravity effects on flow regimes and heat transfer become negligible. At such fluxes, microgravity two-phase behavior should resemble that at normal gravity. Therefore, some earth gravity flow regime maps may, at high fluxes, correctly predict microgravity flow regimes.

The real basis for all flow regime predictive models is a large amount of experimental data. Unfortunately, the database for microgravity two-phase flow is still quite small. Feldmanis [1966] performed one of the early studies into microgravity conditions. Only qualitative heat transfer and pressure drop results were obtained. Keshock et al. [1973] obtained flow regime observations in their flights. Heppner et al. [1975] made quantitative flow regime observations, though their test section was rather short. More confidence is placed in recent microgravity flights by Hill et al. [1987], Dukler et al. [1987], and those quoted by Lee [1987]. The data of Dukler et al., compared to the other two sets, are particularly valuable in the wide range and density of their data points.

The increasing microgravity database has allowed preliminary development of methods to predict observed flow regime transitions. Heppner et al. [1975] made the first attempts by applying Quandt's [1965] criteria to their data, using a reduced gravity value in the Froude number expressions. Lovell [1985], Lee [1987], and Karri [1988] all took this questionable method to an extreme and applied reduced gravity terms into normal gravity predictive schemes such as Taitel-Dukler [1976], Weisman et al. [1979], Taitel et al. [1980], and Weisman-Kang [1981]. Little success was achieved in the above efforts because the criteria used in these prediction schemes are really semi-theoretical correlations based on normal gravity data. These correlations cannot be expected to be accurate for large changes in any parameters, such as varying the gravity force towards zero. Lee's major effort, however, was creating theoretical transitions; he equated what was identified as the dominant

force for each regime to the neighboring regime's dominant force. The results he obtained did not match his data particularly well.

The only major success to date in prediction of observed microgravity flow regimes is that given by Dukler et al. [1987], based on lines of constant void fraction.

3.3. Heat Transfer (Boiling and Condensation) in Low or Zero Gravity

Comprehensive overviews of boiling and condensation under free and forced convection conditions are given by Collier [1972] and Whalley [1987].

Recent studies by Abdollahian and Levy [1985] make some progress towards a better understanding of boiling heat transfer under microgravity conditions.

3.3.1. Pool boiling in reduced gravity

The most comprehensive overview of reduced gravity heat transfer was given by Siegel [1967]. A few results are highlighted here. In zero gravity, free convection is eliminated. Thus, in nucleate pool boiling, no buoyancy force removes bubbles formed at the heater surface. Reasoning that vapor would be formed continuously with no mechanism to remove it, one might intuitively predict an immediate transition to film boiling. However, Sherley [1963] reports microgravity tests with liquid hydrogen using a drop tower. It is interesting to note that first experiments indicate essentially no difference between the nucleate boiling heat flux in microgravity and normal gravity fields. Nevertheless, it can be difficult to draw valid conclusions for steady-state pool boiling from drop tower experiments, since these are of very short durations, see e.g. Cochran et al. [1970].

The microgravity critical heat flux was reduced by almost a factor of 3 in Merte and Clark's [1964] experiments. This result indicates the bubble detachment rate in microgravity is less than with buoyancy forces present.

A decrease in bubble detachment rate, or the increase in bubble size, was verified also by Siegel and Keshock [1964] in their drop tower experiments with water. The authors argue that smaller bubbles are detached and sucked into the wake of larger bubbles, increasing the turbulence in the vicinity of the heater surface.

It is agreed by several authors that the nucleate boiling heat transfer coefficient at critical heat flux changes with $g^{1/4}$. In contrast, Lyon et al. [1965] measured in an oxygen system that the peak heat flux is almost constant below 0.25g and falls off by about a factor of 10 at zero gravity.

Pool boiling consists not only of nucleate but also of transition and film boiling. The latter is probably insensitive to gravitational effects since in horizontal orientations on earth it already defies gravity.

Film boiling was studied in detail by Siegel and Keshock [1964] as well.

For heat transfer in spacecraft, a forced convection system is generally envisaged. Thus, pool boiling is only of marginal interest, namely in the case of pump failure in the cooling system. Therefore, consideration should be taken of critical heat flux to assure safe operation even under such deterrent conditions.

3.3.2. Forced convection in reduced gravity

In forced boiling convection, bubble departure occurs due to drag forces on the growing bubble. Departure may be suppressed if the liquid film on the heater surface is thin enough. These effects might be expected to be similar in either normal or reduced gravity.

In horizontal evaporator tubes on earth, stratification of the two phases can be of importance if the overall mass flux is small. Then, heat fluxes around the circumference can vary substantially. This variation in heat flux was discussed by Bar-Cohen et al. [1986], who were concerned about isothermality in horizontal boiler tubes.

However, stratification effects are not expected in microgravity. Thus, uniform heat transfer around the circumference is anticipated. In contrast to gravity-caused stratification, surface tension is expected to dominate, causing the liquid to wet the whole tube wall (barring critical heat flux) until dryout occurs.

Therefore, forced convection two-phase flow heat transfer coefficients such as those developed by Chen [1963] and more recently refined by Gungor and Winterton [1986] are believed to be valid correlations in microgravity evaporation and condensation loops. The latter authors present a comprehensive overview of data and correlations of forced convection heat transfer coefficients for two-phase systems.

3.4. Existing Microgravity Air-Water Flow Regime Data

A review and compilation of the existing microgravity flow regime data has proven useful.

Heppner, King, and Littles [1975] published air-water microgravity flow regime data obtained in a looping KC-135 aircraft. The apparatus had a flow section with 1 inch id and approximately 22 inch length. Their data is plotted in Figure 1.

Recently, Dukler et al. [1987] published microgravity air-water data, some obtained in a drop tower, some in a looping Learjet. The test section of the drop tower apparatus measured 1.5 feet (0.457 m) long and 3/8 inches (9.52 mm) in diameter. The test section of the flight apparatus had a 3.48 feet (1.06 m) straight length test section and a 1/2 inch (12.7 mm) tube diameter. Both sets of data are plotted in Figure 2.

An on-going effort at Texas A&M University, headed by Best, has also obtained air-water and nitrogen-water microgravity flow regime data in a looping KC-135 airplane in apparatus of various sizes. This data has been obtained, to date, in 0.24 inch (6 mm) diameter tubes with straight flow sections approximately 5 feet (1.52 m) long. The data is plotted in Figure 3.

All the data mentioned above, except the data from one inch tubes, are plotted in Figure 4. This compilation helps to show general flow regime boundaries but obscures the possible effects of diameter variation on flow regimes. However, the diameters are reasonably close, there is not much microgravity flow regime data available, and the liquid-liquid simulations showed only a small effect on flow regime for large changes in diameter (25.4 mm down to 8 mm). Therefore, at the present level of analysis, and with the few data poi ts available, it seems worthwhile to view all the nominal 1/4, 3/8, and 1/2 inch (6, 9.52, and 12.7 mm) air-water data together.

The average of the nominal 1/4, 3/8 and 1/2 inch (6, 9.52, and 12.7 mm) diameters is very nearly 3/8 inches (9.52 mm). Therefore, analysis will be done on the basis of 3/8 inch (9.52 mm) diameter, as if all the data were obtained in that size tube.

It is further assumed that all the data (including the one inch air-water data) were taken at a nominal 10 psia -- the cabin pressure typical of the aircraft used in the experiments. (The Texas A&M data were reported to be at this pressure.) In any event, analysis suggests a noticeable, but small, effect of vapor density on flow regime transitions.
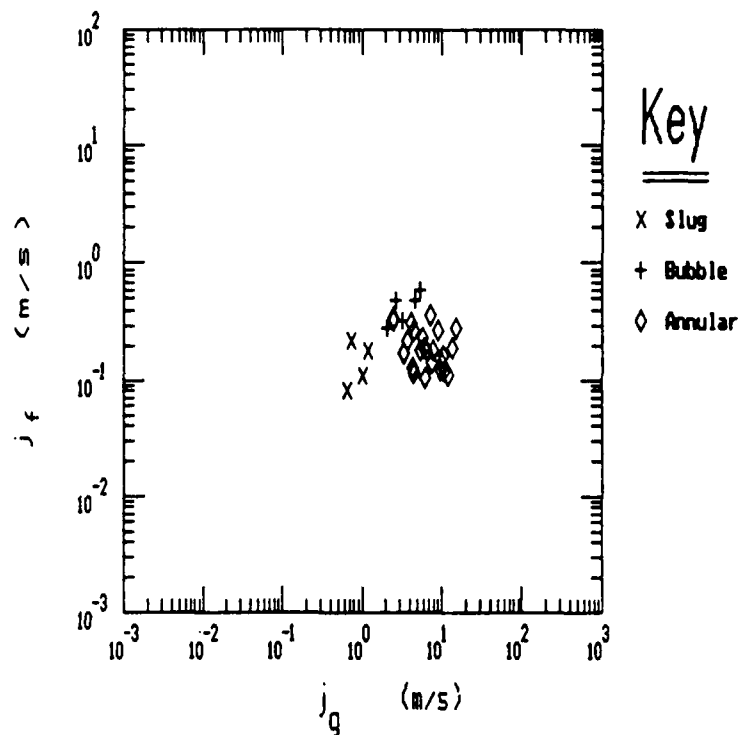
Figure 1.   Heppner, King, and Littles Microgravity Flow Regime Data

Air / Water   Diameter = 1 inch
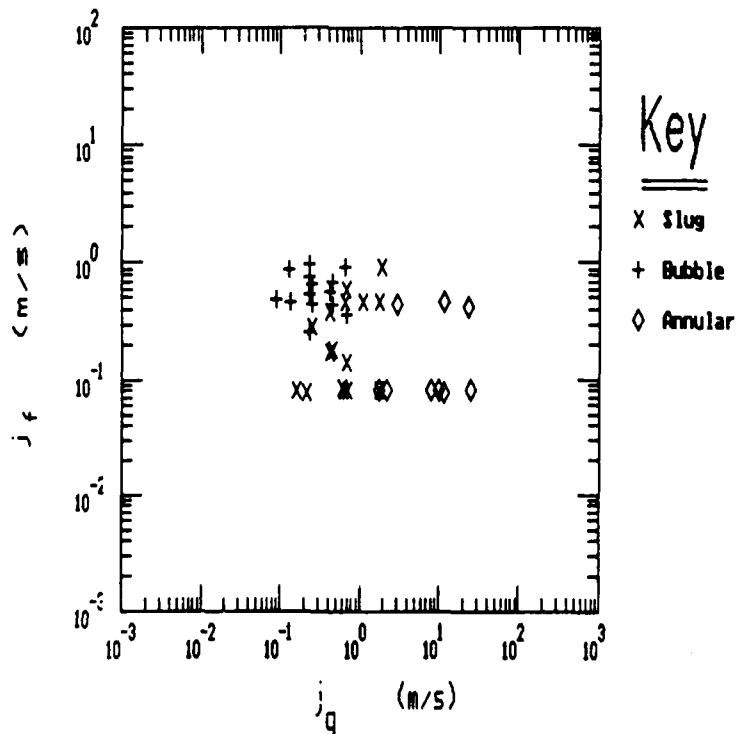
Figure 2.   NASA-Lewis / Dukler Microgravity Flow Regime Data

Air / Water   Diameter = 3/8 inch (9.52 mm) and 1/2 inch (12.7 mm)
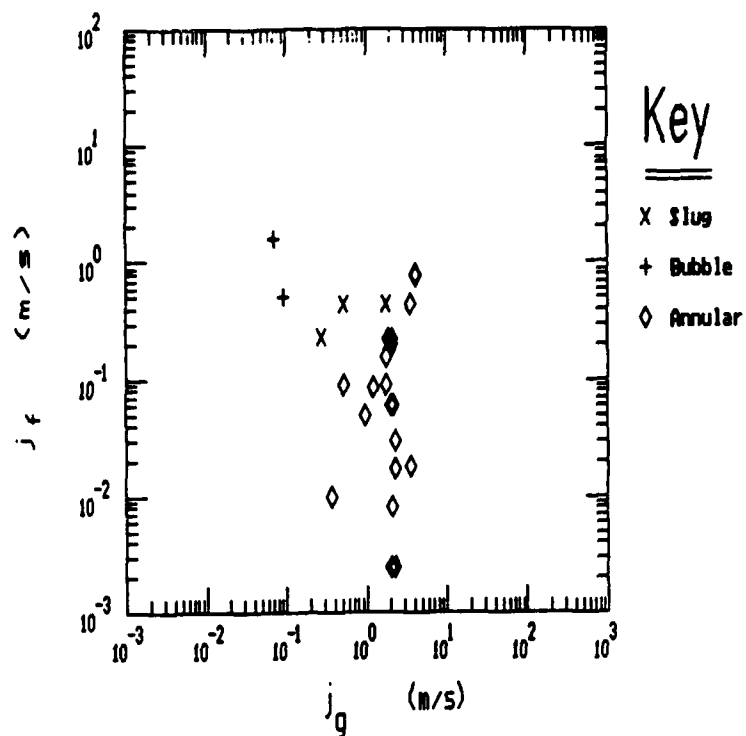
Figure 3.   NASA-Johnson / Wright Patterson / Best   Microgravity Flow Regime Data
Air (or nitrogen) / Water   Diameter = 6 mm
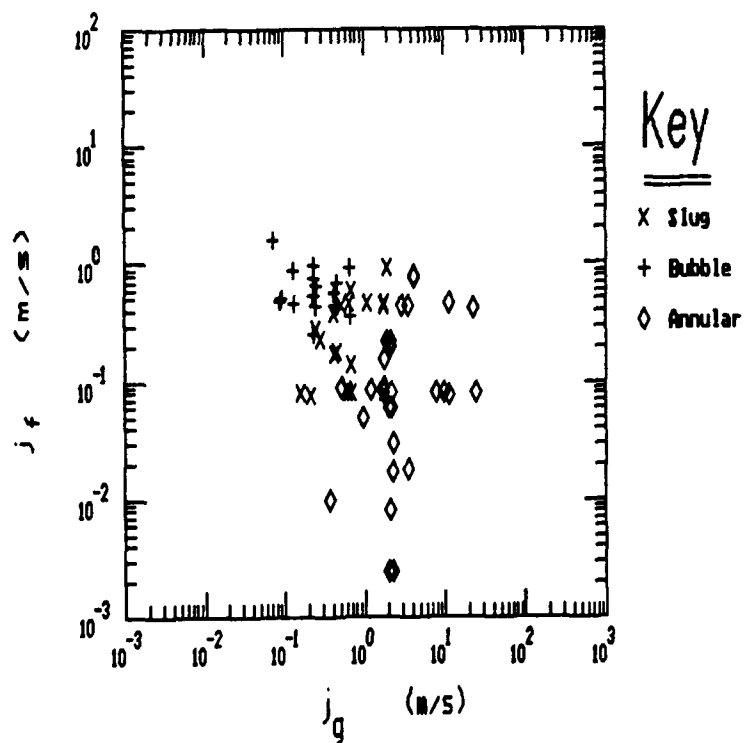
Figure 4.   Compilation of Best and Dukler Microgravity Flow Regime Data
Air (or nitrogen) / Water   Diameters = 6, 9.52, and 12.7 mm

14

From this point onward, these 1/4, 3/8, and 1/2 inch compiled data will subsequently be referred to simply as the "air-water" data. The one inch air-water data of Heppner et al. [1975] will be handled separately for two reasons. First, the diameter is significantly larger than the rest. Second, the short flow section likely prevented fully developed flow.

4. MICROGRAVITY SIMULATION EXPERIMENTS

True microgravity vapor-liquid flow regime data is obtained in drop towers, in aircraft flying parabolic trajectories, or in space vehicles. The expense of these methods is large. Except for the last one, these methods yield a relatively short time of microgravity[2]. Therefore, until recently, very little microgravity flow regime data existed. The data base of microgravity flow regimes is still small.

At high flow rates gravity becomes a secondary factor in determining even earth gravity flow regimes. Thus, at high flow rates, microgravity flow regimes will probably match or closely approach those of earth gravity.

The limited microgravity data support this assertion. Figure 1 (referred to in the previous section) shows the Heppner, King, and Littles microgravity flow regime data. Note that the bubble to annular transition is an approximately 45° line sloping upward to the right. Figure 5 plots the bubble to annular boundary of several <u>earth gravity</u> flow regime maps, one of which is for vertical flows. Note that they all qualitatively predict a bubble to annular transition that slopes generally upward and to the right. Of the four maps, Dukler's and Baker's horizontal maps best predict the high-flux bubble-annular transition of the Heppner, King, and Littles one inch tube diameter air-water microgravity data. In fact, the prediction is quite good. This suggests that at high fluxes microgravity flow regime behavior matches that of standard earth gravity high flux flows.

However, the quantitative disagreement among them of up to an order of magnitude shows that more earth gravity flow regime research effort is needed. Perhaps future work should center on obtaining consistent and accepted flow regime definitions. Nevertheless, limited microgravity data at high flow rates do agree in trend with the high flow rate region of the earth gravity flow regime maps shown in Figure 5.

4.1. Liquid-Liquid Simulation of Vapor-Liquid Microgravity Flow

The major question for microgravity flow regimes then becomes: What flow regimes occur at low flow rates in microgravity?

A method for simulating microgravity flow regimes has been developed which focuses on low flow rates. Two immiscible, equally dense liquids are pumped through a horizontal glass tube.

---

[2] Several seconds at the most for drop towers, thirty seconds at the most for parabolic looping aircraft.
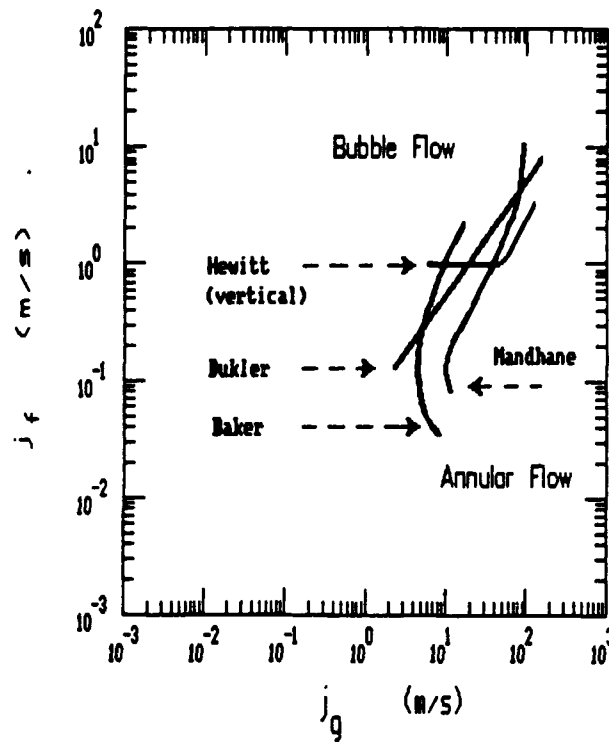
Figure 5. Four Earth Gravity Flow Regime Maps Compared
at High Flow Rates

By using immiscible liquids of equal density, the buoyancy effect, and therefore the gravity effect, is eliminated. So, unfortunately, are inertial differences eliminated.[3] However, it was originally hoped that the simulation would be valid at low flow rates. At low flows, inertial differences should be less important than other factors such as viscosity and surface tension.

The microgravity flow regimes of greatest interest are those occurring at low flow rates. Therefore, it seemed that the simulation experiments could be of value. In fact, the simulation experiments have shown results partly similar to true microgravity vapor-liquid flows. The simulations have, in fact, yielded helpful analytical insight into flow regime transitions.

An advantage of the simulation is its low cost, compared to experiments in drop towers, parabolic airplane flights, or space flights. Another advantage is that the simulation uses relatively conventional equipment. These experiments also allow a wide range of fluid and system parameters to be explored. Furthermore, detailed observations and measurements can be made over a relatively long duration time. This duration time also helps the flow become fully developed.

The microgravity simulation experiments were carried out at the University of New Hampshire by Mr. S. B. Karri Reddy and Mr. Jeff O'Hearn under the direction of Dr. V. K. Mathur of the Chemical Engineering Department. Appendix A, the Data Report, details the results, the apparatus used, the fluids and their properties, devices used to measure fluid properties, etc.

The immiscible liquids used were various oils, always matched with water. The density of each oil was adjusted to match water by dissolving in it sufficient carbon tetrachloride. Water, being less viscous than the oils used, was always assumed to simulate vapor.

A water-oil mixture often exhibits flow regimes, such as inverse annular[4], that are virtually unknown to vapor-liquid flows. In

---

[3] Several modeling problems arise when inertial differences are eliminated. First, the velocities of each phase differ significantly only if one phase maintains sole contact with the tube wall. Second, no mechanism exists for droplet deposition. Entrainment rates are therefore unrealistically high.

[4] Inverse annular flow occurs when the less viscous fluid (eg, water) flows along the wall, and the more viscous substance (eg, oil) flows in a continuous core. This is a common liquid-liquid flow regime. However, for vapor-liquid systems, it is only imaginable in situations of critical heat flux.

addition, the nearly complete absence of buoyancy AND inertial differences remove the major forces which, given sufficient flow length, usually override entrance effects. Thus, obtaining "fully developed flow" is problematic. Entrance effects can determine much of the flow regime map.

However, these experiments were not designed as an investigation of liquid-liquid flow regimes. They were specifically designed to model microgravity vapor-liquid flow. Even sparse literature data indicated early in the study that annular flow was a predominant vapor-liquid microgravity flow regime.

Therefore, annular flow was deliberately promoted. The reasoning was that if the liquid-liquid flow could be set artificially close to a known microgravity regime (i.e., annular), what flow regimes then developed might be passable simulations. It may be argued that the data has been thus deliberately biased. That is true. However, the results of the analysis show that this "biased" simulation was quite useful.

With the above reasoning, experimental technique was designed to promote annular flow. The technique is summarized as follows:

- The inside surface of the glass visualization section was coated[5] to create a hydrophobic surface. Oil, not water, then tended to wet the wall.

- The fluids were introduced into the pipe in an annular fashion: oil onto the perimeter, water into the core through a nozzle.

- Each experiment was begun by turning on the oil flow first and alone, until it filled the pipe and wet the tube wall.

Other details of the experiment, such as temperature control and property measurement, are covered in Appendix A.

Five oils (or mixtures) were obtained which equaled the density of water. Each of the five was paired with water for a set of microgravity flow regime simulations. The five oils were chosen for their varying viscosity and interfacial tension with respect to water. Table A-1 on page A-10 (Appendix A) lists the properties of each oil mixture. Except for the first fluid, both the surface tension and the viscosity ratio with respect to water are reasonably similar to that of air-water or freon vapor-liquid systems. However, there is enough variation in properties among the various fluids to observe effects of fluid properties on flow regime transitions.

---

[5] A carnauba wax with no additives was used because it resists dissolution by oil.

4.2. Liquid-Liquid Flow Regime Results

Results of the simulation experiments are presented and discussed in the three following subsections. Subsection 4.2.1 discusses the flow regimes observed. Subsection 4.2.2 discusses the effects of surface tension and liquid viscosity on flow regime transitions. Subsection 4.2.3 discusses the effect of pipe diameter on flow regime transitions.

In all following references and figures, the oil -- representing liquid -- is indicated by the subscript "1". Water -- simulating the less viscous vapor -- is indicated by the subscript "2". For the remainder of this report when the liquid simulations are being discussed, the term "vapor" or "gas", if used, will refer to the water component of the flow. The term "liquid" will refer to the oil, which is the more viscous component of the flow.

4.2.1. Liquid-liquid flow regime observations

Figures 6 through 9 show flow regime data for Fluid Systems #2 through #5.[6] These simulations were done in 1 inch diameter tubes. Figures 10 and 11 show flow regime data for Fluid System #3 (water and silicone oil) in 12.7 mm (1/2 inch) and 8.0 mm (approx 5/16 inch) pipes, respectively. The data were taken by fixing the water flow rate, then increasing the oil flow rate by fixed steps to its maximum value. These same fixed steps in oil flow were repeated each time the water flow rate was brought to a new, predetermined level. As a result, the data in the Figures nearly always falls on a grid of vertical and horizontal lines.

The flow regimes in Figures 6 through 11 were interpreted from video tapes taken by the UNH experimenters. These interpretations differ in some cases from the regimes reported in Appendix A by the UNH researchers. Note that at some data points the flow is classified as two regimes. In such cases, either two regimes were observed or the flow could not be clearly seen and two interpretations were possible. These cases are plotted with more than one symbol at the same point.

---

[6] Initial experiments with the Fluid System #1 (water simulating vapor; polypropylene glycol 2000 (PPG-2000) representing liquid) showed inverse annular flow. Therefore, subsequent experiments were modified to promote annular flow. The initial learning experiences with PPG-2000 and water were not regarded as a valid part of the simulations. The PPG-2000 data is included in Appendix A, but it is not plotted here.
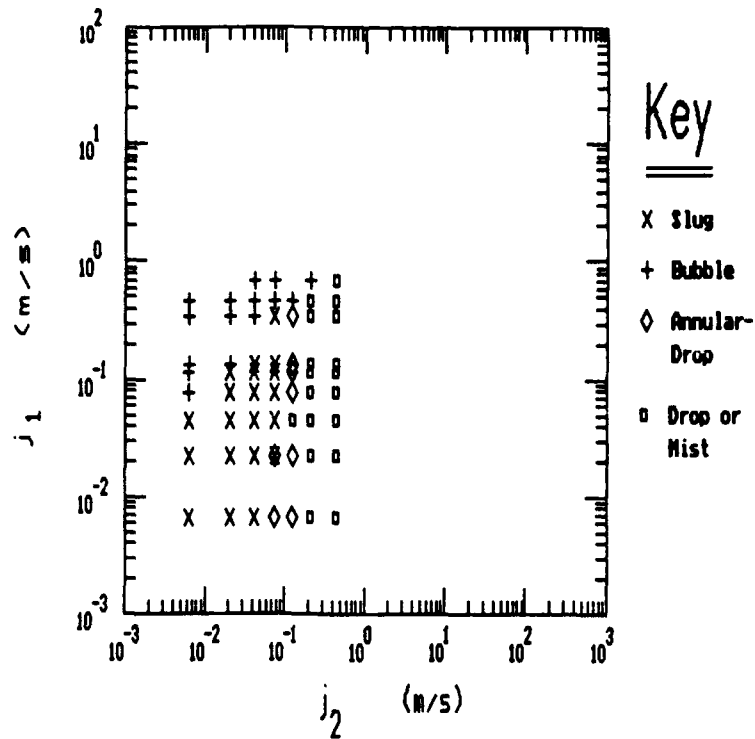
Figure 6. Mineral Oil / Water Equi-density Flow Regime Data
in One Inch Tubes   (j2 is water)
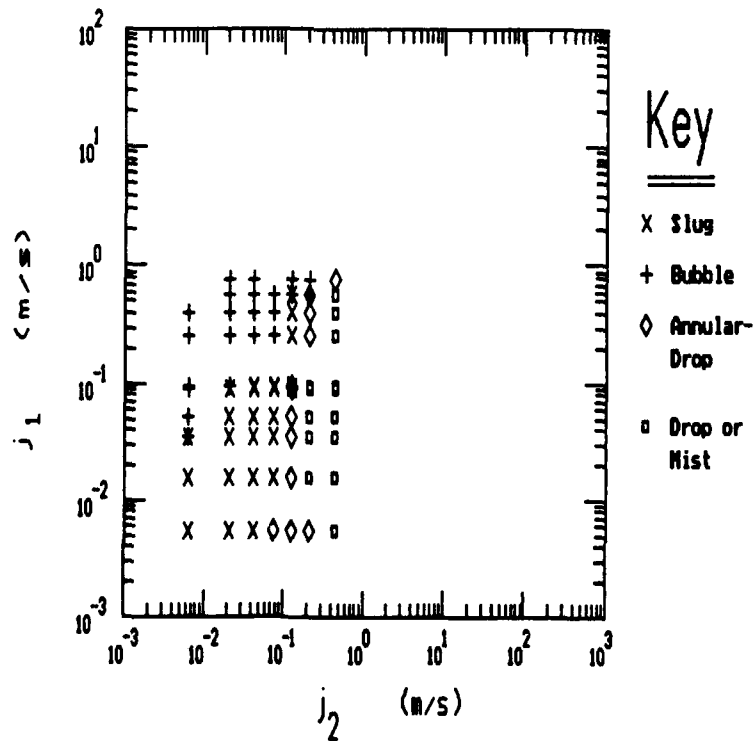
Figure 7. Silicone / Water Equi-density Flow Regime Data
in One Inch Tubes   (j2 is water)
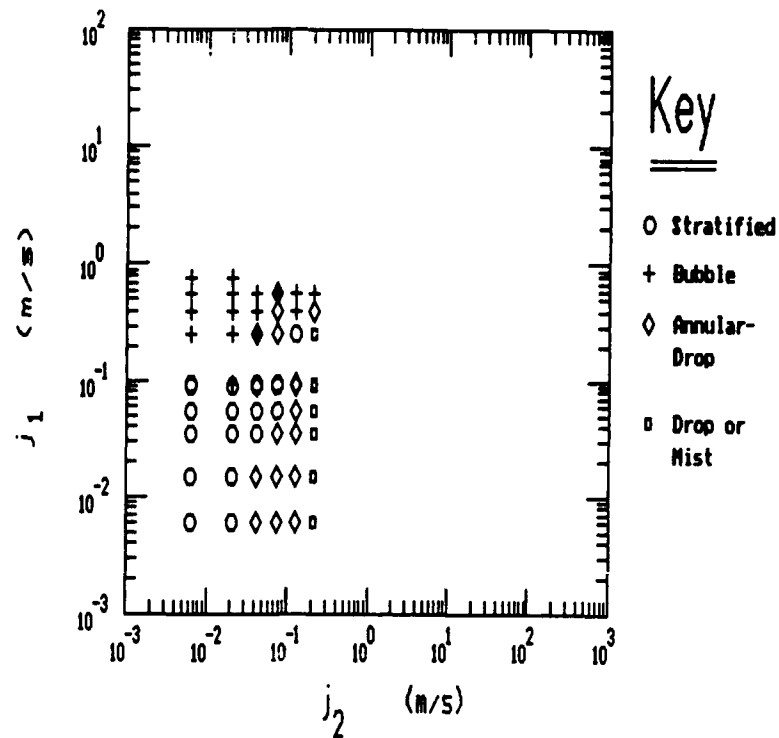
Figure 8.   Low Surface Tension Silicone / Water Equi-density
             Flow Regime Data in One Inch Tubes   (j2 is water)
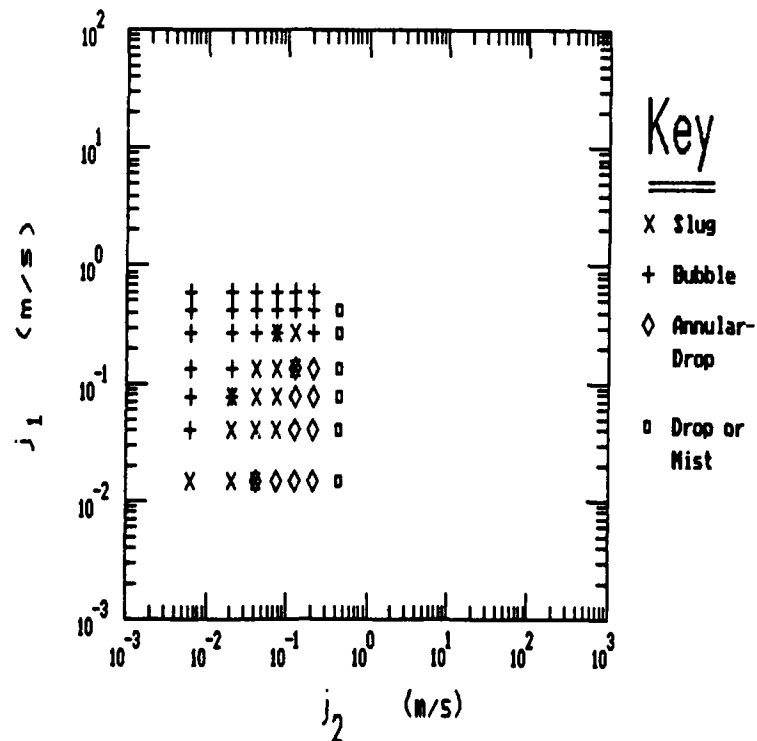
Figure 9.   Kerosene / Water Equi-density Flow Regime Data
             in One Inch Tubes   (j2 is water)
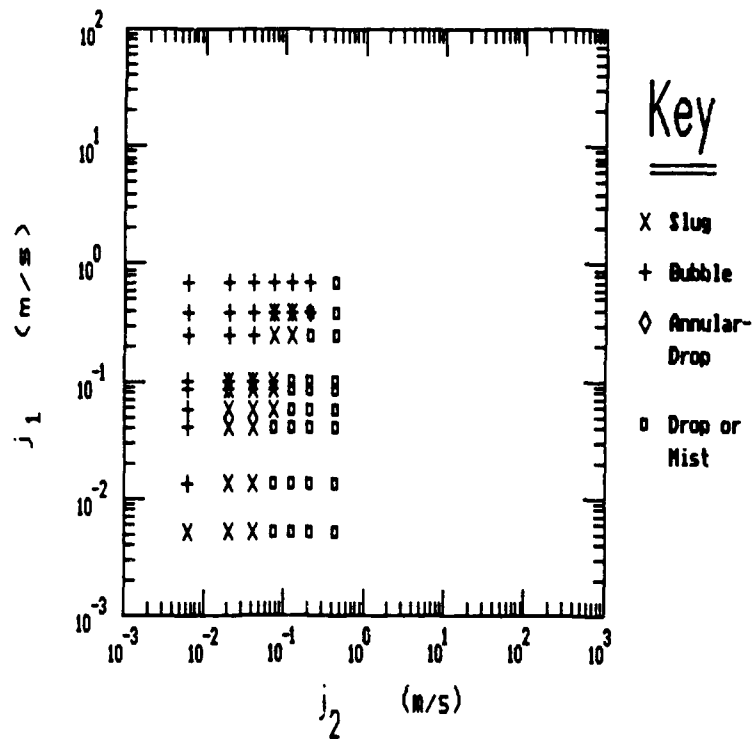
Figure 10.   Silicone / Water Equi-density Flow Regime Data
in Half-Inch Tubes.   (j2 is water)
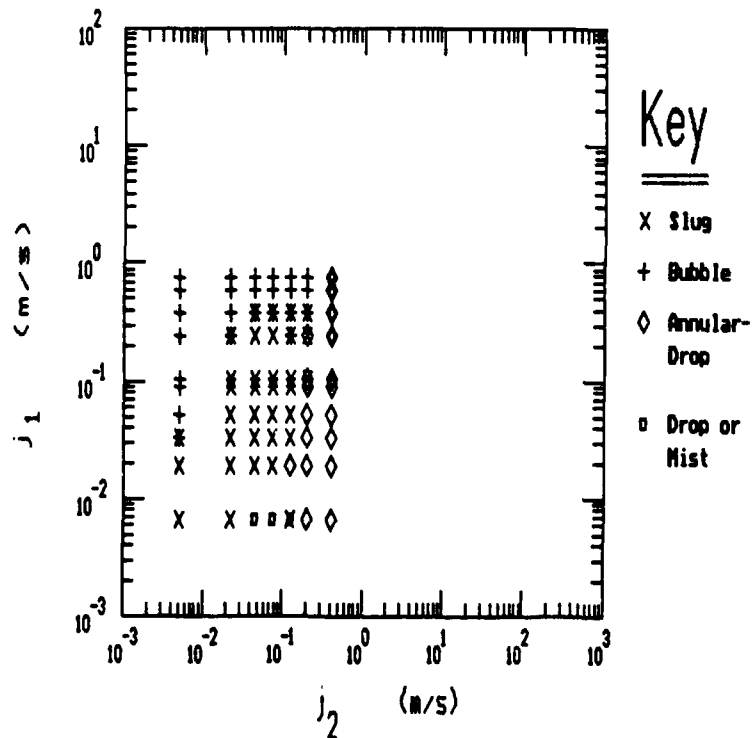
Figure 11.   Silicone / Water Equi-density Flow Regime Data
in 5/16 Inch Tubes.   (j2 is water)

Liquid-Liquid Flow Regimes -- General Observations

The dominant observed regimes were bubble, slug and drop flows. "Annular" flow was only observed with a much liquid entrainment in the core. These few cases were classified annular-drop. Only in a narrow range of flows, if at all, did the liquid along the pipe wall contribute significantly to the total liquid flow.

In most cases the liquid "annulus" was a thin stationary film. This flow regime was classed drop or mist.

The small number annular-drop cases occurred along the boundary to slug flow. Analysis of the pressure drop measurements show that this flow behaved similarly to pure annular flow. Therefore, the flow is loosely termed annular, and the boundary, the slug-annular transition.

As discussed earlier, bubble and slug flows both consist of gas bubbles in continuous liquid. The two are differentiated by the size of the gas bubble relative to the pipe diameter. Drop flow is the case of discontinuous liquid in continuous gas. In some of the liquid-liquid experiments, the drops reached a size that could be classed "inverse slug flow". In some of the low water flow simulations, a regime formed which had a small layer of liquid attached to part of the tube wall, but drop flow in most of the cross section. This regime was called drop-stratified and is lumped together with drop flow.

Fluids of equal density are accelerated to the same velocity by the pressure gradient unless the wetting effects of one fluid keep it on the tube wall. In the absence of a pronounced wetting effect, there is little chance of the viscous liquid staying on the wall at any but the lowest flow rates. At quiescent flow rates the liquid with most affinity for the tube wall will wet the perimeter. The other liquid will flow in the core. Thus, with a hydrophobic tube wall, slug flow formed as placid, low-slip Taylor bubbles. At the same flow rates without a hydrophobic wall "inverse annular flow" resulted -- (inviscid) water on the wall, viscous oil in the core.

However, it is unlikely for viscous liquid to remain on the wall at the higher flow rates typical of true annular flow. Shear forces from the other liquid will tend to wash the tube wall clean of the viscous liquid. Thus, the effects of shear at the wall and equal velocities elsewhere cause a trend away from annular flow and towards perfectly homogeneous drop flow.

Only when the viscous flow greatly exceeds the inviscid does bubble flow occur. Here, the viscous liquid thoroughly wets the tube wall even at high flow rates. However, in these experiments, that happened only when the viscous flow reached about 80 percent of the total flow. In fact, the transition

could be quite well described by a line of 20 percent void fraction. At higher voids than this (i.e., at viscous fluid fractions less than 80 percent), bubble flow did not occur.

A line of 45 percent void fraction has been tentatively proposed by Dukler [1987] as the bubble-slug transition line for vapor-liquid microgravity flows. This proposal was made on the grounds of geometrical packing of spheres. Geometrical packing arguments should not change for the liquid-liquid experiments. However, the bubble-slug transition for these liquid-liquid data occurred at 20 percent void fraction. This result suggests that the bubble-slug transition cannot be predicted on the basis of void fraction alone.

Liquid-Liquid Flow Regimes -- Specific Observations

Most of the following observations are paraphrases from Dzenitis [1988], who spent much time observing video tapes of the experiments, and analyzing the results.

Qualitatively, similar regimes and transitions are seen for Fluid Systems #2, #3, and #5. With low-to-medium liquid and gas flow rates, slug flow is observed. High liquid flow with low gas flow causes bubble flow. The converse situation yields drop flow, with perhaps a narrow region of annular flow.

Fluid System #4 (silicone and water, with an added surfactant) showed phenomena quite different than the other systems. Surprisingly, many of its low flow rate points showed stratified flow, apparently due to very small density differences. Many of these points were classed as unstable slug flow by the University of New Hampshire researchers. However, except the flow rates, little or no evidence points to slug flow. The videotapes suggest that residual buoyancy forces and wetting effects cause the components to stratify. Once stratification occurs, it remains, even when the liquid flow is increased all the way to the bubble flow boundary.

Wetting (i.e., wall-affinity) does not usually dominate flowing liquids. Likewise, buoyancy was very small in these experiments. However, for the low surface tension of Fluid System #4, the small forces of wall affinity and minimal buoyancy were large enough to control the flow regime. This result indicates that wall affinity and micro-buoyancy can determine the flow regime of low flux microgravity flows, if the surface tension is low.

In addition to this stratification inconsistency, Fluid System #4 shows other inconsistencies. These also may be the result of wetting. For example, the observed flow regimes show a consistent trend with increasing liquid j_1, as occurred in the

experimental procedure. However, there is no consistent trend across the j_2 range at constant j_1. This inconsistency suggests hysteresis or that steady-state was not reached. Hysteresis may permit multiple stable (but path-dependent) flow regimes.

Because of its major difference in flow regime type, Fluid System #4 is not included in any further analysis or discussion.

Dzenitis [1988] reported that observation of low velocity slug flow regimes in the smaller diameters clearly showed large bubbles forming as various bubble sizes overtook one another and coalesced. Cases were observed where small bubbles overtook large ones, and vice-versa. The observation suggests that either the flow had not reached steady state or that a flow regime transition was in progress.

4.2.2. Effect of surface tension and liquid viscosity on flow regime transitions

The results of Fluid System #4 indicate that for low flow rate microgravity flows, a negligible surface tension can be significant. In such cases, wall affinity and micro-buoyancy may become determining factors of flow regime. In the case of Fluid System #4, the flow regime boundary was not shifted so much as a different flow regime was formed altogether.

However, variations in non-negligible surface tension should also have an effect on the location of flow regime transitions.

Figures 6 through 9 have shown flow regimes and transitions for Fluid Systems #2, #3, and #5. These simulations were all done in 1 inch diameter tubes. Therefore, the varying fluid properties permit these results to be used to see the effect of surface tension and liquid viscosity on flow regime transitions.

A summary of the effects of liquid viscosity and surface tension is shown in Figure 12. This figure shows "best-fit" transition lines for Fluid Systems #2, #3, and #5 in 1 inch diameter tubes. The lines are subjectively drawn by Dzenitis [1988]. As he notes, they could be shifted significantly by including or excluding a data point or two. The upper-left line divides bubble flow from slug and annular flow. The lower-right line divides slug flow from annular flow. An initial observation is that the transition lines show little change among the various fluids. However, the log-log plots do minimize differences.

26
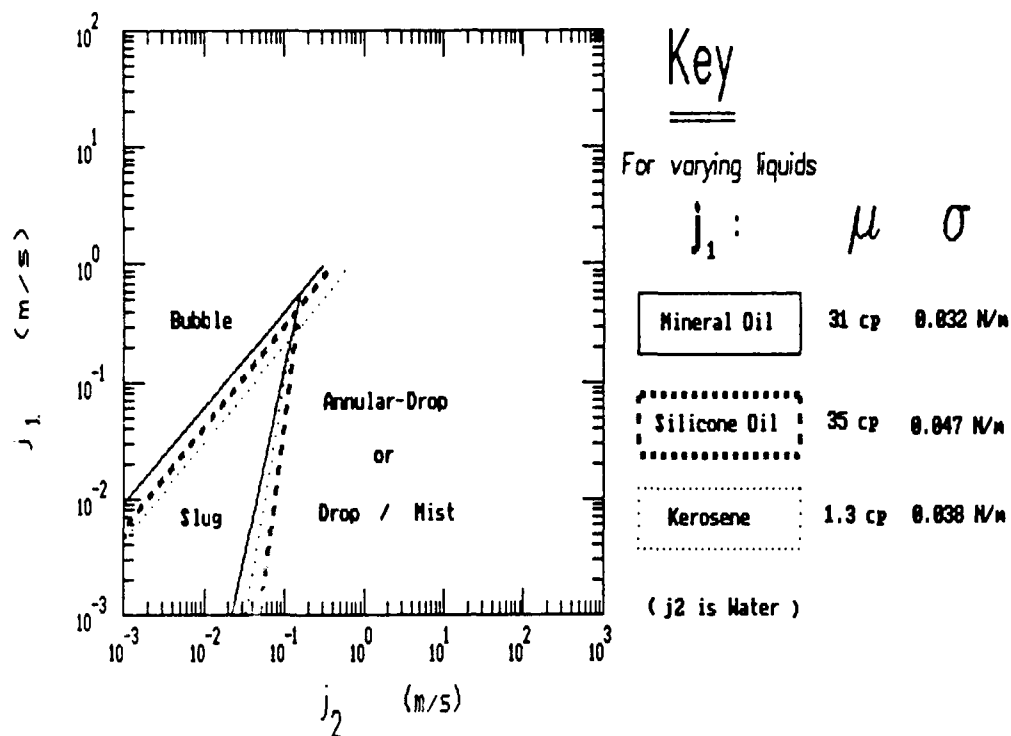
Figure 12. Effect of Fluid Properties on Observed Liquid-Liquid
Flow Regime Transitions   Diameter = 1 inch
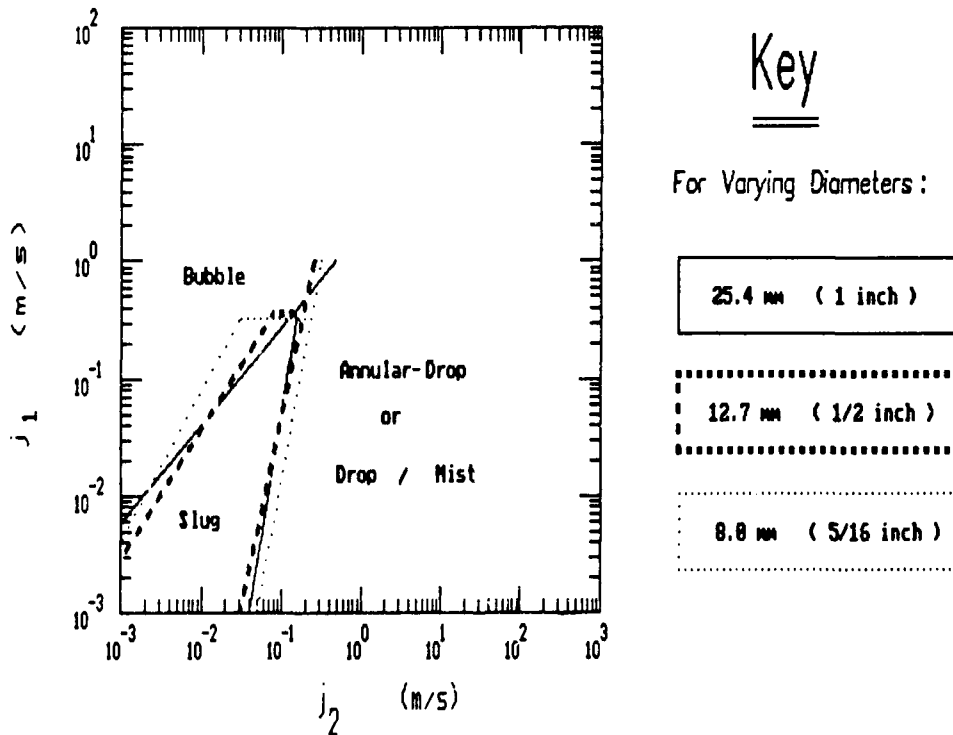
Figure 13. Effect of Diameter on Observed Liquid-Liquid
Flow Regime Transitions.   Silicone Oil (j1) and Water (j2).

27

Both paired with water, mineral oil (Fluid System #2) compared to silicone oil (fluid system #3) shows a 47 percent increase in surface tension, but a small (15 percent) increase in viscosity ratio. From this viewpoint, it appears that an increase in surface tension shifts the bubble-slug transition to the right, giving more bubble flow. The increase in surface tension also shifts the slug-annular transition to the right, giving more slug flow in this part of the flow regime map.

On the other hand, comparison of mineral oil and kerosene (Fluid System #5), both paired with water, shows a 96 percent decrease in viscosity ratio with a small (19 percent) increase in surface tension. The decrease in viscosity causes both the bubble-slug and the slug-annular transition to move to the right.

A decrease in viscosity shows the same trend as for an increase in surface tension. However, the effect of viscosity appears to be more on the bubble-slug transition; the effect of surface tension appears to be more on the slug-annular transition.

As noted in the discussion of Fluid System #4, a negligible surface tension can change the observed flow regime altogether.

4.2.3. Effect of tube diameter on flow regime transitions

Figures 10 and 11 showed flow regime data for Fluid System #3 (water and silicone oil) in 12.7 mm and 8 mm diameter pipes respectively. Figure 13, from Dzenitis [1988], summarizes these results.

Figure 13 therefore shows the effect of tube diameter on liquid-liquid flow regime transitions. As pipe diameter decreases, the region of slug flow tends to increase, especially at higher liquid flow rates. The bubble-slug transition shifts left and the slug-annular transition shifts right.

FIgure 13 also shows an interesting phenomenon. It indicates an apparent upper limit of slug flow at a constant j_1 (approximately 0.37 m/s). This limit appears to be independent of diameter or j_2. The results of the analysis presented later will briefly address this horizontal section of the bubble-slug transition line.

4.3. Comment on Reynold's Number and Momentum Flux Plots

During the course of this study, similitude analyses were attempted to learn how the liquid-liquid simulations might be properly extrapolated to real microgravity vapor-liquid flow regime behavior. Initially, plots of liquid-liquid flow regimes based on Reynold's number were compared to similar plots of microgravity vapor-liquid flow regime data. Similarly, superficial momentum fluxes (density times the square of superficial velocity) were attempted as correlating parameters. Such plots were often part of monthly progress reports.

However, this correlating scheme breaks down when used in an attempt to match the liquid-liquid bubble-slug transition to the vapor-liquid bubble slug transition. The liquid-liquid transition boundary is an order of magnitude different from the vapor-liquid boundary. Plots of momentum flux further break down because they include neither a viscosity, a diameter, nor a surface tension term. The data show that diameter, viscosity, and surface tension do have an effect on flow regime transitions.

The better analysis, presently recommended, is based on pressure drops of each flow regime (see Section 5). The flow regime predicted to occur is the one with the minimum pressure drop for any given set of conditions. Pressure drop equations for turbulent conditions in each phase can be formulated as a function of superficial momentum fluxes, void fraction, viscosities, and tube diameter. Once the underlying importance of pressure drop is discovered, it is obvious why plots of superficial momentum flux show some limited similitude success. Superficial momentum flux is simply a subset of pressure drop. Thus, momentum flux offers a limited ability to extrapolate from liquid-liquid simulations to vapor-liquid observations.

From this perspective, the causes for the breakdowns in similitude using superficial momentum flux become obvious. Predictions based on pressure drop calculations do not neglect tube diameter or viscosity, and need not neglect surface tension. Furthermore, they do not neglect the laminar to turbulent transitions of each fluid. However, simple plots of superficial momentum flux neglect all these factors.

The cause for the breakdown in predicting the bubble-slug transition by similitude of superficial momentum fluxes is that the more viscous liquid of an equi-dense liquid pair is usually in laminar flow. Its laminar pressure drop is NOT a function of superficial momentum flux, but simply of superficial velocity (i.e., volumetric flux).

On the contrary, the analysis based on a minimized pressure gradient correctly predicts both the viscosity and the diameter effect. It also takes into account laminar-turbulent

29

transitions. It does not presently contain a surface tension term. However, suggestions are made whereby a surface tension effect could be included (e.g., in the calculation of interfacial shear). It is important to note that by properly calculating pressure drop and using the minimization of pressure gradient principle, flow regime transitions can be predicted consistently for liquid-liquid flows and for vapor-liquid flows. This prediction is successful regardless of turbulent or laminar conditions.

The minimization of pressure gradient flow regime transition analysis is presented in Section 5.

4.4. Pressure Drop Data from Liquid-Liquid Simulation Experiments

Data from the liquid-liquid simulations show that flow regime transitions are associated with (sometimes relatively abrupt) changes in pressure gradient. In Figure 14 average pressure gradient (Pa/m) is plotted as a function of vapor volumetric flux j_2 (m/s). The lines of constant j_1 in Figure 14 correspond to the horizontal rows of Figure 6. At constant liquid flow j_1 and increasing "vapor" flow j_2, the generally observed succession of flow regimes is: bubble, slug, annular, drop.

Within any given regime and with liquid flow held constant, increasing vapor flow generally causes increased pressure gradient. However, at each flow regime transition there is often a significant and relatively abrupt reduction in pressure gradient. Sometimes pressure gradient, rather than dropping, simply does not rise quadratically with increasing j_2 (as would be expected if the flow remained in one regime). Instead, pressure gradient remains surprisingly flat, and the flow changes to a new regime.

The net result of these regime adjustments is sometimes an approximately constant pressure drop as vapor flow j_2 is increased, until the final regime for maximum vapor flow is reached. In the liquid simulations this final regime is drop flow. Increasing vapor flow from drop flow onward results in the expected quadratic rise in pressure gradient.

Figure 14 shows a sample of the pressure drop data from the liquid simulations and illustrates the observations of the preceding paragraph.

30
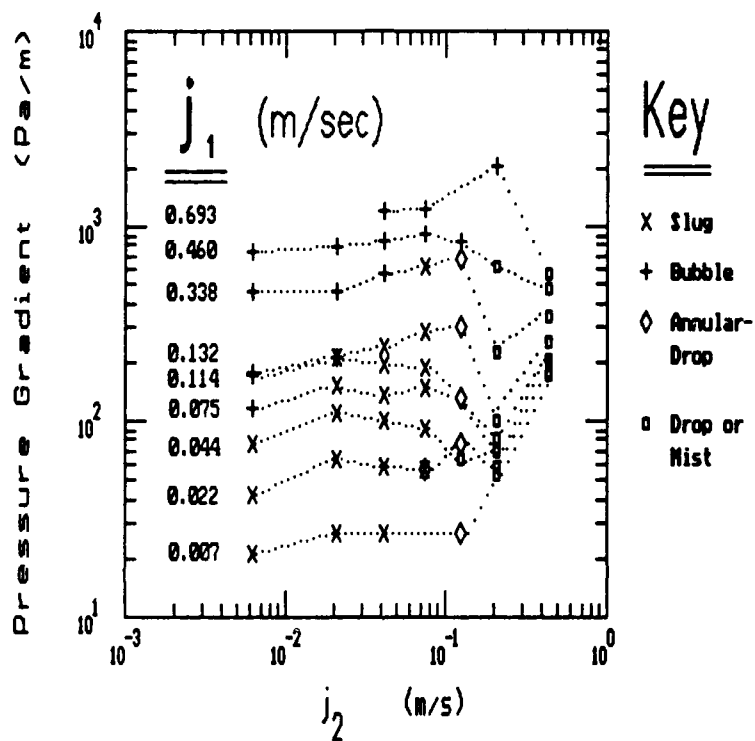
Figure 14. Measured Pressure Gradients and Liquid-Liquid Flow Regimes
Mineral Oil (j1) and Water (j2)   Diameter = 1 inch

Note that for constant j1 and increasing j2, flow regime tansitions
are often associated with a decrease in pressure gradient.

31

5. ANALYSIS

As observed in the previous section, equi-density liquid-liquid flow regime transitions are accompanied by local reductions in pressure gradient. This observation inspired Dzenitis [1988] to hypothesize a major underlying principle in all flow regime transitions. To wit, he proposed that **fluids will adopt the flow regime that minimizes flow resistance, as measured by pressure gradient.** This one principle is sufficient to predict the observed <u>liquid-liquid</u> flow regime transitions.

The physical reasoning behind this concept is quite simple. To quote Dzenitis [1988]:

> "A flow regime with some slip offers less resistance (in the form of pressure drop) than homogeneous bubble flow, where the viscous liquid is dragged along at the same velocity as the inviscid liquid (or gas). Conceptually, flow that begins in the bubble regime at low gas flow j_2 experiences grater pressure gradient resistance as j_2 increases, and at some point is able to adjust by changing flow regime to slug flow."

The same reasoning can be extended to the slug-annular transition:

> Slug flow offers some slip velocity, since the vapor bubbles travel faster than the slugs of liquid. However, the slugs of viscous liquid are still forced to travel, by continuity considerations, at a velocity equal to the total of vapor and liquid volumetric flux. Annular flow offers greater slip velocity so that vapor and liquid flow are further "de-coupled". In annular flow, liquid travels totally along the pipe wall --no slugs are forced to travel at high velocity like viscous bullets in a rifle. The vapor, with greater slip velocity, travels in the core, directly inhibited only by interfacial shear, not by the shear forces within slugs of an impeding, viscous liquid. At high vapor fluxes, interfacial shear offers less hindrance than that created by viscous forces inside liquid slugs, which would bridge the tube.

To predict all <u>microgravity</u> vapor-liquid flow regime transitions, two additional criteria were added to Dzenitis' original hypothesis. (These criteria are needed for the slug-annular and bubble-annular transition. The microgravity vapor-liquid bubble-slug transition can be predicted with minimum pressure gradient considerations alone.)

First, a minimum annular void fraction criterion was added. This criterion is similar, but not equivalent, to that proposed by

Dukler [1987]. The void fraction criterion determines whether annular flow, once favored by its low pressure gradient, can feasibly exist.

Second, a new, detailed model of slug flow was created. This new slug flow model, it is believed, describes vapor-liquid slug flow, and the transition to annular flow, better than previous models. The detailed slug flow model is itself based substantially on the principle of minimized pressure gradient to determine slug geometries. Therefore, the major underlying principle which determines flow regime is still hypothesized to be the minimization of pressure gradient.

Using this approach, analyses have been developed to predict the flow regime transitions of both the liquid-liquid simulations and those of microgravity vapor-liquid flow. There were two major flow regime transitions observed in the range of the present data:

    1) Bubble to Slug

    2) Slug to Annular

A third transition exists, but did not occur significantly in the range of the present data:

    3) Bubble to Annular

The focus of each analysis was to develop criteria to predict the first two transitions. Of the three transitions, these are the two most gravity-influenced ones. However, the results of the analysis also suggest criteria to predict the bubble to annular transition for both liquid-liquid and microgravity flows. The very limited data suggest that these criteria for the bubble-annular transition are reasonable.

5.1. Flow Regime Analysis -- Framework and Implementation

The proposed flow regime transition analysis consists of two parts:

1) A model or framework -- the hypothesized physical mechanisms and underlying principles.

2) An implementation -- the specific equations and correlations used to calculate the physical mechanisms.

As better equations and correlations become available, the same framework may yield better predictions. Therefore, it is important to keep the concepts of the framework separate from the specific implementations demonstrated here.

For example, the present implementation has not included any effect of surface tension on flow regime transitions, even though such an effect was observed in the simulations. However, there is nothing in the framework of the analysis that prohibits surface tension from being included. Specifically, surface tension should have an effect on microgravity interfacial shear and therefore on pressure drop. Furthermore, it should have an effect on maximum stable annular film thickness. However, since these effects have not been quantified, they are not included in the present implementation of the analysis. Future work may remedy such deficiencies.

5.2. Summary of Proposed Flow Regime Transition Criteria

5.2.1. Equi-density liquid-liquid flow regimes

As noted, data from the liquid-liquid simulations exhibit a local decrease in pressure gradient at all flow regime transitions. From this observation, Dzenitis [1988] proposed a flow regime transition criterion -- minimization of pressure drop. Stated simply, fluids adjust to the flow regime which produces the least resistance, measured as frictional pressure gradient.

Only flow regimes which have also been observed in microgravity are considered here. Regimes which occur only in exceptional circumstances have not been considered[7].

Dzenitis implemented this criterion only for the bubble-slug transitions of the liquid simulations and the air-water microgravity data. Therefore, to also predict the slug-annular transition of the liquid simulations, his approach has been modified and extended:

- A more analytically based model for slug flow pressure drop was substituted for the separate cylinders correlation he used.

- An analytical model of annular flow pressure gradient was added.

These two models adequately fit the liquid-liquid pressure drop data. Using them, the minimization of pressure drop criterion now predicts the slug-annular transition as well as the bubble-slug transition of the liquid-liquid simulations. The bubble-slug transition of air-water microgravity data is still equally well predicted.

---

[7] For example, inverse annular flow (liquid flows in the core, vapor on the pipe perimeter) has a theoretically very low pressure drop. However, centrifugal force (from swirls in the flow) and the wetting properties of liquid will usually keep some liquid on the pipe wall. An exception may occur during critical heat flux. Likewise, a perfectly "dry wall" drop flow creates only a small frictional pressure gradient. For the same reasons (centrifugal force and liquid wetting), it is unlikely to occur.

However, if exceptional circumstances do occur, such as critical heat flux or use of a non-wetting liquid, the same minimization of pressure gradient criteria could probably be easily extended to include the less common flow regimes which would result.

The liquid-liquid microgravity simulation data show a noticeable drop[8] in frictional pressure gradient when bubble flow changes to slug and again when slug flow changes to annular.[9] The pressure gradient, at constant liquid flow, does generally rise with increasing vapor flow. However, there are local decreases in pressure gradient which mark flow regime transition.

Using analytical models as a basis, equations are developed to match the measured liquid-liquid pressure gradient data for bubble flow, slug flow, and annular flow.

The key to the liquid-liquid analysis was to develop adequate expressions for the observed bubble, slug, and annular flow pressure gradients. The pressure gradient equations for each flow regime are found in Section 6, Pressure Drop. Comparisons of these equations to liquid-liquid data are found in Appendix E. Details of the transition model are discussed in this section devoted to analysis.

---

[8] As previously noted, sometimes this "drop" is simply a flat spot in the curve of pressure gradient data, compared to the expected quadratic rise with increasing j_2.

[9] The pressure gradient declines once again when annular flow, immediately thereafter, changes to drop flow. However this nearly immediate change to drop flow is almost certainly a character of equi-density liquid-liquid flow regimes. In an equi-density flow there is no significant mechanism for droplet deposition. Therefore, with increasing turbulence in the core, liquid-liquid annular flow is quickly converted to homogeneous drop flow. Tube walls are virtually stripped "dry" of the liquid, that is, clear of the more viscous of the two liquids.
    There is little basis to assume that this aspect of the liquid-liquid simulations mirrors a true vapor-liquid flow. Rather, a vapor-liquid flow would be expected to remain in annular flow. As the vapor rate increased, some liquid (as drops or mist) would be picked up by the core. However, a continuous deposition process, counteracting the continuous entrainment process, would keep a significant portion of the liquid flow on the tube walls, in true annular flow. A condition of critical heat flux might be an exception.
    Because this study is concerned principally with typical microgravity vapor-liquid flow regimes, the liquid-liquid transition from annular to drop flow is not pursued. However, from the pressure gradient data, it appears that the annular-drop transition could be calculated with the same general technique used to predict the other flow regime transitions. The major requirement would be for an accurate expression to match the drop flow pressure gradient data.

36

Summary of liquid-liquid flow regime transition criteria

1) The **bubble** to **slug** transition is predicted when the calculated homogeneous bubble pressure gradient rises above the calculated slug pressure gradient.

2) The **slug** to **annular** transition is predicted when the calculated slug pressure gradient begins to rise significantly above the calculated annular pressure gradient.

3) The **bubble** to **annular** transition follows from the same rationale. It is hypothesized as the extension of the bubble-slug transition line, but in the region where annular flow is simultaneously favored over slug flow. There is little simulation data of this transition either to confirm or refute this prediction. However, what little simulation data exist do support it.

5.2.2. Microgravity vapor-liquid flow regimes

The idea that flow regimes can be determined according to a minimized pressure gradient is intuitively compelling. The concept was therefore applied to microgravity vapor-liquid flows.

However, at present, the analysis of microgravity vapor-liquid flow regimes is complicated by the almost complete lack of pressure drop data correlated with flow regime. In the present case, the difficulty is compounded because the regime transition criteria are based directly on pressure gradient calculations. In the absence of microgravity pressure drop data, assumptions based on the liquid simulations and earth gravity two phase flow data have been made. These pressure gradients, based on assumptions, lead to a flow regime map which can be compared with existing microgravity flow regime data.

The **single** criterion of minimized pressure gradient **appears insufficient** to predict the observed slug-annular transition of

37

microgravity vapor-liquid flow. Therefore, the criterion was extended in several ways:

- A **minimum stable annular void fraction**[10] is proposed to determine a portion of the slug-annular transition. It is suggested that at some minimum void fraction, even when annular flow is favored by pressure gradient, a continuous vapor core cannot be maintained. Below this annular void fraction, the core will break into small bubbles (bubble flow) or elongated bubbles (slug flow). This void fraction approach is similar to Dukler's [1987] preliminary suggestion that a line of constant void fraction may determine the slug-annular transition.

- A rough-interface interfacial shear correlation from earth gravity literature is introduced into the slug and annular flow pressure gradient calculations. The correlation predicts a rapid rise in pressure drop once vapor flow becomes turbulent. However, this correlation also dominates the minimum annular void fraction line. This void fraction line in turn dominates most of the predicted slug-annular transition.

OR, instead of the rough-interface shear correlation,

- A new, detailed model for slug flow is proposed. The model uses the minimization of pressure drop criterion to predict various details of slug flow geometry. These details lead to new transition criteria.

For example, the model predicts when the elongated bubbles of slug flow will lengthen to form a continuous annular core. It also predicts the existence and location of hysteresis and a churn flow region.

The detailed slug model is quite insensitive to the choice of shear correlation. The resulting transition model does rely on a minimum void fraction criterion. However, unlike the simpler transition model, this minimum void criterion does not determine most of the slug-annular transition.

---

[10] It will be shown later that a <u>maximum annular film thickness</u> is probably more fundamental. Thus, minimum void fraction is a function of at least diameter. No analysis is offered here to predict maximum annular film thickness from first principles. Therefore, minimum annular void fraction is used to stress that part of the present flow regime boundary is in effect a line of constant void fraction. However, it is expected that in the future this line of void fraction will be determined by a maximum film thickness criterion. Interfacial tension, among other factors, will likely enter into that calculation.

Summary of microgravity vapor-liquid flow regime transition criteria

The proposed microgravity flow regime transition criteria can be qualitatively summarized as follows:

1) **Bubble flow changes to slug flow** when its pressure gradient rises above that for slug flow at the same phase flow rates.

   (This criterion is identical to the liquid-liquid case.)

2) **Slug flow changes to annular flow** when the resulting annular flow will be above a minimum stable void fraction, **AND**:

   - Slug pressure gradient rises above that for annular flow.

     For this simple criterion to work well, a rough-interface shear correlation <u>must</u> replace the smooth surface equations used for the liquid-liquid transition criteria. This correlation then dominates the minimum stable void fraction line, which largely becomes the slug-annular transition. Pressure gradients become secondary. They are calculated only to see where annular flow is favored, not where it will occur.

   OR

   - Based on a <u>detailed model for slug flow</u>, predicted slug pressure gradient rises above that of annular flow, **AND**:

     Taylor bubble length can increase (to form a continuous vapor core) without creating a transitional rise in slug flow pressure gradient. Otherwise the flow remains "stuck" in slug flow, with the pressure gradient at a local minimum above the global minimum offered by annular flow.

     If the minimum annular void fraction does not exist, but pressure gradient nevertheless drives the flow away from classic Taylor bubble slug flow, churn[11] (slug) flow results.

3) **Bubble flow changes to annular flow** when pressure gradient drives the flow towards slug flow, but slug flow cannot, by

---

[11] Churn flow is a chaotic flow. It is sometimes described as occurring near the slug to annular boundary, which is the location predicted by the present analysis. Churn flow is here considered a subset of slug flow because its pressure fluctuations are likely to be as energetic as classic slug flow.

the above criteria, exist. That is, the annular pressure gradient is favored over the slug pressure gradient, and the annular void fraction is above the minimum. In practical terms this line is the extension of the slug-annular boundary, which is presently a line of constant void fraction.

Note: But for the added minimum void fraction criterion and the detailed slug flow model, the vapor-liquid analysis is similar to the liquid-liquid analysis. However, these additions could not apply to the liquid-liquid cases because of the large amount of entrainment exhibited. Regarding a void fraction limit, entrainment dominates liquid-liquid annular flow, always keeping the annular film thin. The detailed slug flow model does not account for entrainment in the Taylor bubble, so does not apply to the liquid-liquid case.

5.3. Equations for Bubble Flow

Bubble flow is defined here as bubbles of vapor (or liquid simulating vapor) in a continuous liquid flow. The bubbles are assumed roughly spherical and smaller than the tube diameter. Throughout this analysis bubble flow is assumed homogeneous. The defining assumption of homogeneous flow is that the velocities of the two phases are equal:

$$v_f = v_g = \frac{Q_f + Q_g}{A} = j \tag{5-1}$$

This condition makes the calculation of the following identities straightforward:

$$j_f = \frac{Q_f}{A} \tag{5-2}$$

$$j_g = \frac{Q_g}{A} \tag{5-3}$$

$$j = j_f + j_g \tag{5-4}$$

$$\alpha = \alpha_h = \frac{j_g}{v_g} \tag{5-6}$$

$$\rho_m = \alpha \rho_g + (1 - \alpha) \rho_f \tag{5-7}$$

The pressure drop of bubble flow can then be calculated from single phase flow equations by properly selecting a homogeneous viscosity. A theoretical expression for homogeneous viscosity from the literature was chosen because it clearly best matched the data. No adjustments to it were necessary to fit the liquid-liquid data. Section 6 gives the equations for homogeneous viscosity and for the pressure drop of bubble flow. Appendix E shows how these equations compare to the liquid-liquid data.

5.4. Equations for Slug Flow

Slug flow is here defined as a flow of elongated bubbles alternating with slugs of pure liquid. The elongated bubbles are of a size that cannot fit spherically within the pipe diameter. They are often bullet-shaped "Taylor bubbles". Sometimes the vapor exists more as elliptical or irregular shaped long bubbles. This condition is here termed a "churn" slug flow.

Before flow regime transitions can be addressed, a basis for calculating slug flow variables must be developed.

A complete mathematical description of slug flow would be quite involved. It would include bubble and slug lengths, frequencies, film thickness, bubble speed, and liquid slug speed. It would also include pressure fluctuations, pressure loss due to "end effects" around noses and tails of elongated bubbles, and the possibility of small vapor bubbles in the liquid slugs. An analysis which can accurately predict all these variables has not, it is believed, been developed.

Fortunately, simplified models of slug flow can be developed which yield useful results. Two such models are used here. The first is called the "simplified slug model" and has been used by many other investigators. It proved sufficient for the analysis of liquid-liquid flow regimes and is covered below.

The second slug model is called the "detailed slug model" and was created to help predict vapor-liquid microgravity flow regimes. Section 5.10 is devoted to a discussion of this newly proposed model of slug flow.

5.4.1. Unit cell

Both slug flow models use a key simplifying concept. Namely, each model assumes a dimensionless "unit cell", comprised of a unit Taylor bubble and a unit slug. The unit cell represents the average geometry of the flow per unit pipe length. The cell has a dimensionless length of unity.

The sum of all Taylor bubble lengths (L_t), divided by the total flow length (L) is the unit Taylor bubble length, L_t^*. The sum of all slug lengths (L_s), divided by the total flow length (L) is the unit slug length, L_s^*. The sum of unit Taylor bubble length and unit slug length forms the unit cell and is always unity:

$$L_t^* + L_s^* = 1.0 \qquad (5\text{-}8)$$

Figure 15 diagrams the unit cell length and shows some slug flow relationships of the simple model.
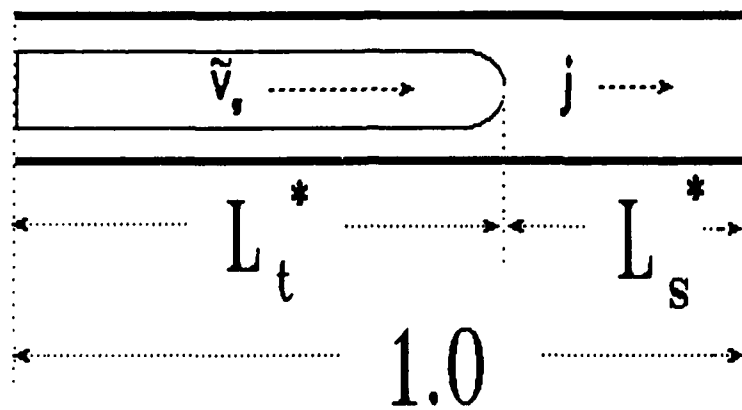
$$j = j_f + j_g$$

$$\tilde{v}_g = c_1 j$$

$$\text{typically } c_1 = 1.2$$

Figure 15.   Simple Slug Flow Model

43

A formula to calculate L_t^* is derived in the discussion of the detailed slug model in Section 5.10.1.

The assumption of a dimensionless unit cell eliminates the possibility of predicting true slug length or frequency. The assumption also eliminates the prediction of actual pressure fluctuations or pressure drop due to end effects around the Taylor bubbles.

However, the unit cell concept does describe the behavior on average of all slugs and Taylor bubbles in the pipe. The average pressure gradient can be calculated.[12]   As will be seen, other significant slug flow quantities can also be calculated.

All further mention of slug length or Taylor bubble length refers to geometries within the unit cell, as defined above.

5.4.2. Simplified slug model

The simplified slug model first assumes Taylor bubble slug flow. Two additional simplifications commonly used to help model slug flow are:

1) Assume zero velocity in the annular liquid film around the Taylor bubble.

2) Assume a constant slip velocity between the Taylor bubbles and the liquid slugs.

Once these assumptions are made, it is straightforward to use the unit cell concept to calculate pressure gradient.   It is important to note that average slug flow <u>pressure gradient</u>, **NOT** <u>pressure drop</u> is being calculated.   For example, slug pressure drop as a function of time cannot be calculated with this model. This limitation is created because the unit cell concept is an averaging technique which buries such details.

---

[12] However, pressure drop due to end effects of Taylor bubbles is not analytically calculated in this model. As a first order approximation, end effects are ignored.   Therefore, this approach will underestimate slug pressure gradient.   In fact, to fit the water-oil data, the prediction given by this method was boosted by 21 percent.

Unit Cell of the Simplified Slug Model

Figure 15, already referred to, diagrams the unit cell of the simplified slug model. In Section 5.10.1, devoted to the detailed slug model, it will be shown, by continuity, that in the most general case:

$$L_t^{\bullet} = \frac{j_g}{j - \tilde{v}_{ft}\left(1 - \alpha_t\right)} \tag{5-9}$$

where:

$\tilde{v}_{ft}$ = average film speed along Taylor bubble.

α_t = local void fraction in Taylor bubble cross section.

However, in this simplified slug model, film velocity is assumed zero. Thus $L_t^{\bullet}$ is approximated as follows:

$$L_t^{\bullet} = \frac{j_g}{j} = \alpha_h \tag{5-10}$$

Equations 5-9 and 5-10 show that the minimum possible L_t^{*} is equivalent to the homogeneous void fraction at the same flow rates. Because L_t^{*} may equal the calculated homogeneous void fraction does not mean that this is the void fraction of the existing slug flow. On the contrary, because of the slip (assumed constant in the simple model), the slug void fraction will always be lower than the homogeneous void fraction at any given phase flow rates. However, unit Taylor bubble length can never be less than what the homogeneous void fraction calculates to be.

Equation 5-10 holds true for any thickness film, so long as the film is assumed motionless when the Taylor bubble passes. Such a result is perhaps surprising. However, because the film velocity is assumed zero, it contributes nothing to the total liquid flow rate. All liquid flow is, in this simplified case, assumed to occur in the liquid slugs. Thus, a thick (but assumed motionless) film detracts from a potentially higher j_f and increases L_t^{*}. L_t^{*} will still be equal to the calculated homogeneous void fraction, which is based only on the vapor and liquid actually moving in the pipe.

When unit Taylor bubble length reaches unity, the flow is by definition annular. However, if the fiction of zero film velocity is maintained, the calculated liquid flow will be zero. Again, this "annular" flow might have any film thickness, but the homogeneous void fraction would calculate to 100 percent. (That is, the only actual flow in the pipe is vapor, since by assumption the liquid isn't flowing.) Of course, these

45

statements all reflect the inherent contradictions which surface when simplifying assumptions are taken to their limits. However, these contradictions do suggest that, near the annular transition, the simplified slug model will not accurately simulate slug flow.

Slip Velocity

The slip velocity is usually expressed as the ratio $C_1 = \tilde{v}_g/j$. By continuity, j is the average velocity of pure liquid slugs between each Taylor bubble. Wallis [1969] (p. 293 and p. 301) and other researchers have suggested $C_1 = 1.2$ for slug flows observed on earth. However, in this study, $C_1 = 1.86$ was chosen to best fit measured pressure drop from the liquid-liquid experiments. Appendix E documents this choice.

Pressure Gradient of the Simplified Slug Model

Equations to calculate frictional pressure gradient for slug flow, assuming the simplified slug model, are given in Section 6. Briefly, the pressure gradient is equal to the total pressure drop calculated over the unit cell. This pressure gradient consists primarily of the pressure drop along the length of the unit liquid slug (L_s^*). For completeness, the (usually negligible) pressure drop along the unit Taylor bubble (L_t^*) should be added. This latter term is only important at high vapor flow rates.

As noted, this method offers no calculation for pressure loss due to end effects around Taylor bubbles. Therefore, an arbitrary overall multiplier of 1.21 was used to better match predictions with liquid-liquid pressure drop measurements. To further improve the fit, the slip velocity C_1 was also adjusted to 1.86 as noted above.

The basic simplified slug model might be considered reasonably analytical. However, the adjusted pressure gradient equations derived from it must be considered semi-analytical at best.

Assumptions and Techniques of the Simplified Slug Flow Model

To summarize, the major assumptions of the simplified slug model
are:

- Assume slug flow can be modeled by elongated Taylor bubbles
  alternating with liquid slugs.

- Assume zero liquid flow in the film around Taylor bubbles.

- Assume a fixed slip velocity.

- Assume a pure liquid slug.

- Ignore pressure loss due to Taylor bubble end effects.

In addition, an averaging technique based on continuity
arguments is used to calculate average values from the complexity
that is slug flow:

- Unit slug length is the total of liquid slug lengths per
  unit pipe length; parallel calculation for Taylor bubbles.

5.5. Equations for Annular Flow

Analytical expressions for idealized annular flow were developed. These are covered in some detail in Appendix D. For the liquid-liquid data, the annular analysis has obvious shortcomings, such as neglect of entrained droplets. However, the chosen annular flow model appears adequate for the data and the problem at hand. Appendix E compares its predictions to measured pressure gradients of liquid-liquid annular flow.

The equations which govern annular flow are derived via an integral analysis of separated flow. The analysis assumes an arbitrary power law velocity profile (e.g., the $1/7^{th}$ power law velocity distribution) for each phase. Appendix D presents equations which permit the actual exponent used in the power law to vary, for example as a function of Reynold's number. However, the equations presented here are simplified somewhat by uniformly using an exponent of $1/7^{th}$ to express the turbulent velocity profiles of each phase.

In the case of annular flow with both liquid and vapor laminar, Appendix D offers fully analytical equations. These were derived via a differential shear analysis assuming Newtonian fluids. They are essentially Navier-Stokes equations of laminar, annular, two phase flow.

Equations for annular flow can be derived from a balance of pressure drop on the vapor and the liquid:

$$- \frac{dP}{dz} = \frac{2C_i \, \rho_g \left(\tilde{v}_g - v_i \right)^2}{d_o} = \frac{2C_w \, \rho_f \tilde{v}_f^2}{D} \qquad (5\text{-}11)$$

By simplifying Equation 5-11, the flow and void relationships of annular flow can be summarized as follows:

$$\frac{C_i \, \rho_g \left(\tilde{v}_g - v_i \right)^2}{d_o} = \frac{C_w \, \rho_f \tilde{v}_f^2}{D} \qquad (5\text{-}12)$$

where:

$$\tilde{v}_f = \frac{j_f}{(1 - \alpha)} \qquad (5\text{-}13)$$

$$\tilde{v}_g = \frac{j_g}{(1 - \alpha)} \qquad (5\text{-}14)$$

$$\alpha = \alpha_a = \frac{d_o^2}{D^2} \qquad (5\text{-}15)$$

(equations continue on next page)

48

(equations continue)

$$Re_f = \frac{D(1 - \alpha) \rho_f \tilde{v}_f}{\mu_f} = \frac{D \rho_f j_f}{\mu_f} \tag{5-16}$$

$$Re_g = \frac{d_o \rho_g \left(\tilde{v}_g - v_i \right)}{\mu_g} \tag{5-17}$$

for   laminar liquid: $C_w = \frac{16}{Re_f}$ (5-18)

$$v_i = 2 \tilde{v}_f \tag{5-19}$$

turbulent liquid: $C_w = \frac{0.046}{Re_f^{0.2}}$ (5-20)

$$v_i = \frac{\frac{60}{49} j_f}{\left(1 - \sqrt{\alpha} \right) \left(1 + \frac{8}{7}\sqrt{\alpha} \right)} \tag{5-21}$$

for   laminar vapor: $C_i = \frac{16}{Re_g}$ (5-22)

turbulent vapor: $C_i = \frac{0.046}{Re_g^{0.2}}$ (5-23)

Equations 5-11 through 5-23 relate volumetric flow rates to annular void fraction for all combinations of laminar and turbulent flow of each phase. The summary Equations 5-11 or 5-12 can be solved numerically. However, Appendix D shows exact solutions for j_g for any given j_f and α for the four combinations of liquid and vapor laminar and turbulent flow. These solutions help speed the numerical calculation of what is more commonly required -- a solution for void fraction given j_g and j_f. Interface velocity and pressure drop are solved in the process.

Normally, the interface velocity v_i can be assumed zero, compared to the core vapor velocity. However, with equi-density liquid-liquid flows, the validity of that assumption was not immediately obvious. The liquid-liquid flows do show more of an effect due to v_i than do the vapor-liquid flows. However, on hindsight, the effect is in most instances unimportant.

5.6. Analysis of Equi-Density Liquid-Liquid Flow Regimes

Using the minimization of pressure drop criterion with the three flow regime models -- the homogeneous bubble, the simplified slug, and the idealized annular -- the observed liquid-liquid flow regimes can be reasonably well predicted.

Figures 16 through 18 compare the predicted flow regime transitions to data for the 1 inch tube diameter liquid-liquid simulation experiments.

The system of mineral oil and water in Figure 16 is quite well predicted. So, too is the system of silicone oil and water in Figure 17.

The bubble-slug transition of the liquid-liquid systems occurs at about 20 percent homogeneous void fraction. For the 9 mm air-water microgravity data shown later, the same transition occurs (and is predicted by the same pressure gradient argument) at about 40-50 percent homogeneous void fraction.

Dukler [1987] has tentatively proposed, based on geometrical packing arguments of spherical bubbles, that the microgravity vapor-liquid bubble-slug transition is a line of 45 percent void fraction. These arguments do not change for the liquid-liquid experiments. However, the liquid-liquid data convert from bubble to slug flow at about 20 percent void, significantly before "maximum packing".

On the other hand, the minimized pressure gradient analysis successfully predicts the bubble-slug transition for both air-water and liquid-liquid systems. This result suggests that a minimized pressure gradient is a more fundamental principle than geometrical packing.

Figure 18 shows flow regime data and less well-predicted transitions for the kerosene / water system. The bubble-slug transition calculation can be started, but fails when predicted slug pressure drop exceeds predicted bubble pressure drop. The problem seems to be caused by the nearly identical viscosities of water and kerosene (kerosene is only 20-30 percent more viscous than water). In essence, the two liquids are mathematically nearly identical (same density, very similar viscosity). The approximations of the simplified slug model apparently cannot accurately reflect such subtle differences.

For the same apparent reason, the predicted slug to annular transition is quite poor in this particular case. Unlike any other transition presented in this report, the slug-annular transition of Figure 18 used a slug pressure drop correlation specially fit to kerosene and water. This device was required to get any result at all. Nevertheless, the slug-annular result is
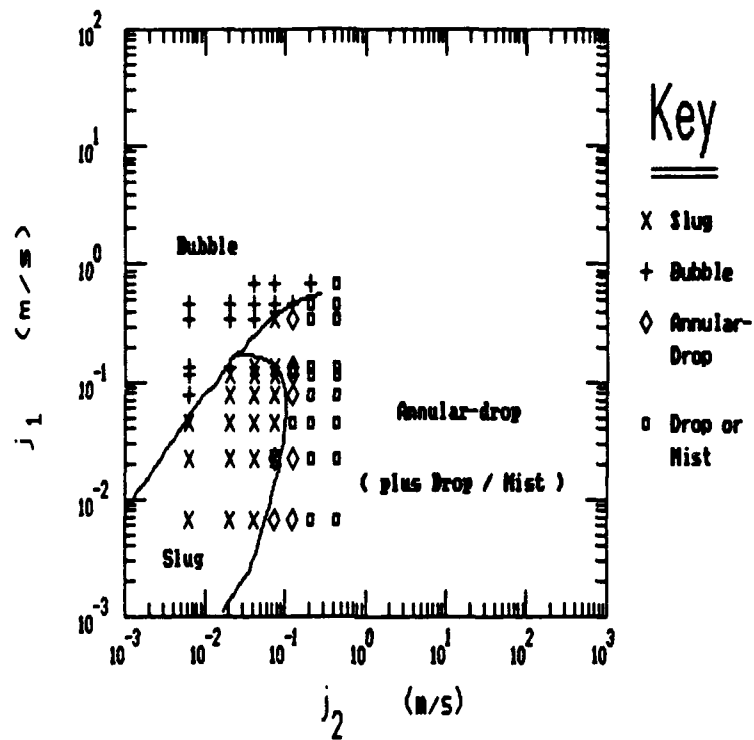
Figure 16. Predicted Mineral Oil / Water Flow Regime Transitions.
(j2 is water)   Diameter = 1 inch
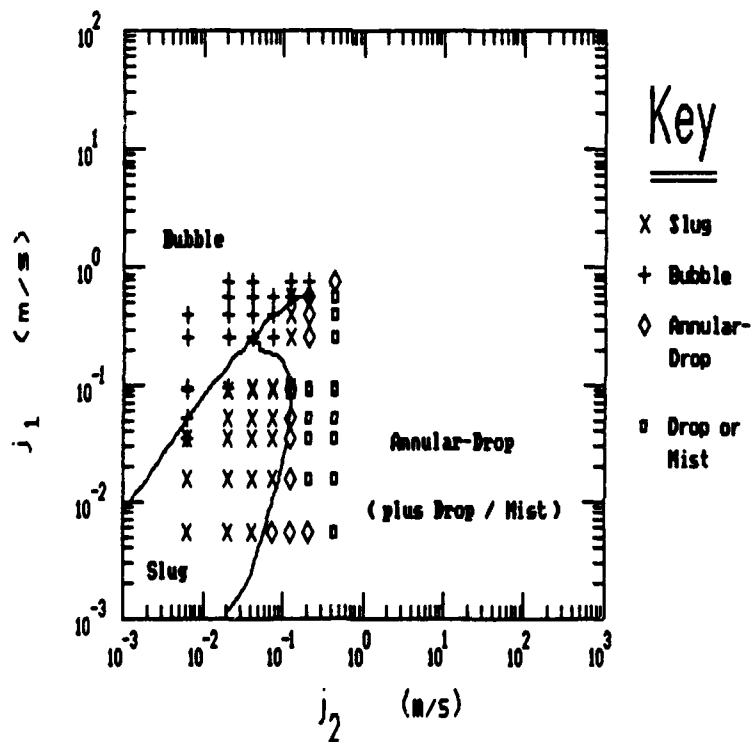
Figure 17. Predicted Silicone / Water Flow Regime Transitions.
(j2 is water)   Diameter = 1 inch
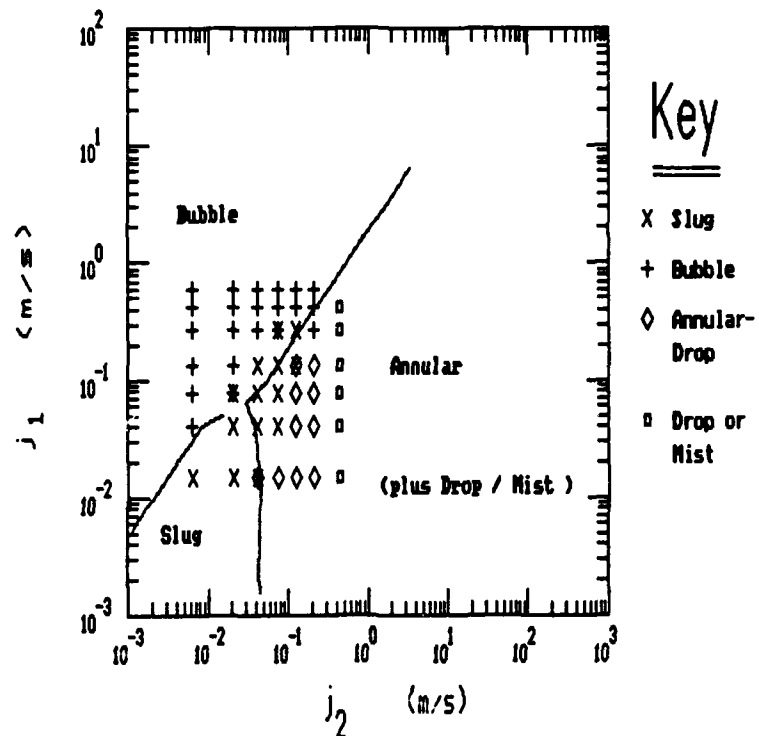
Figure 18.   Predicted Kerosene / Water Flow Regime Transitions.
(j2 is water)   Diameter = 1 inch

interesting in that it matches quite closely other fluid systems' bubble-slug transition, which generally parallels void fraction lines.

Figures 19 and 20 show flow regime data for reduced diameters, and the transition predictions. The predictions match the data and follow its trends quite well, particularly in Figure 20.

5.6.1. Effect of viscosity and tube diameter

Sections 4.2.2 and 4.2.3 showed that viscosity, surface tension, and tube diameter all have an effect on liquid-liquid flow regime transitions. The analysis so far includes no effect for surface tension. It includes an effect for tube diameter which follows the observed trends quite well. The viscosity effects predicted compare somewhat well with the data.

Figure 21 shows the effect of viscosity on predictions of liquid-liquid flow regime transitions. Predicted transitions for kerosene, silicone, and mineral oil (each paired with water) in one inch diameter tubes are shown. This comparison corresponds to an increase in viscosity of the viscous liquid from 1.3 cp to 31 cp to 35 cp, respectively. The change predicted is that with increasing viscosity, both flow regime boundaries shift outward and upward, to increase the area of slug flow. These predictions should be compared to the trends of data summarized in Figure 12. The predicted influence of viscosity on the bubble-slug boundary in Figure 21 matches that of the data summarized in Figure 12. On the other hand, the predicted influence of viscosity on the slug-annular transition does not match at first seem to match the trends summarized in Figure 12. However, in the kerosene-water data, the surface tension effect is tangled with the viscosity effect. The predicted kerosene-water slug-annular transition line in Figure 21 is difficult to calculate and is the only predictive line which fails to follow the trends of the data. The problems of predicting the behavior of these two nearly equal viscosity fluids were noted previously. The predicted viscosity effect therefore agrees at least partly with the data.

The predicted diameter effect shown in Figure 22 is quite satisfactory when compared to the data summarized in Figure 13. Figure 13 showed that decreasing diameter caused both boundaries to shift outward and upward, to increase the area of slug flow. This same effect is predicted by the theory, Figure 22.

Of particular interest in Figure 22 are the relatively horizontal sections of the predicted slug-annular transitions. Previously, it was observed that data suggested an "upper limit of liquid flux" for the occurrence of slug flow. (See Section 4.2.3.) The analysis predicts quite successfully this horizontal portion of
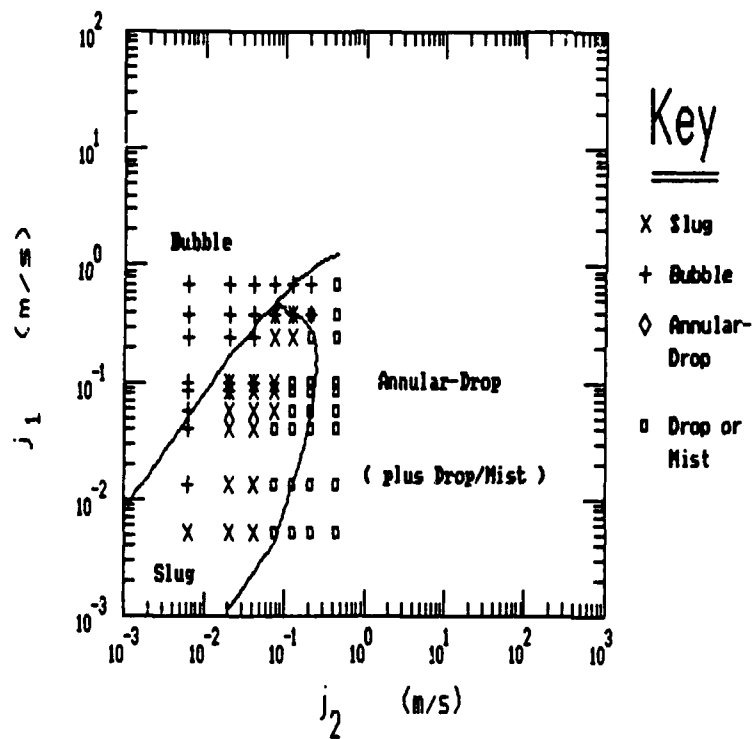
Figure 19. Predicted Silicone / Water Flow Regime Transitions
in Half-Inch Tubes.   (j2 is water)
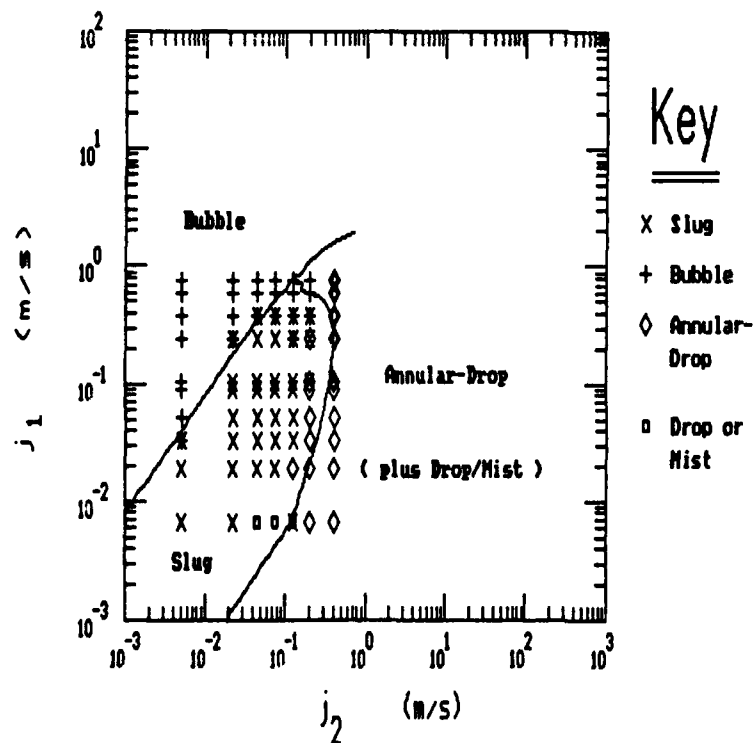
Figure 20. Predicted Silicone / Water Flow Regime Transitions
in 5/16 Inch Tubes.   (j2 is water)

54
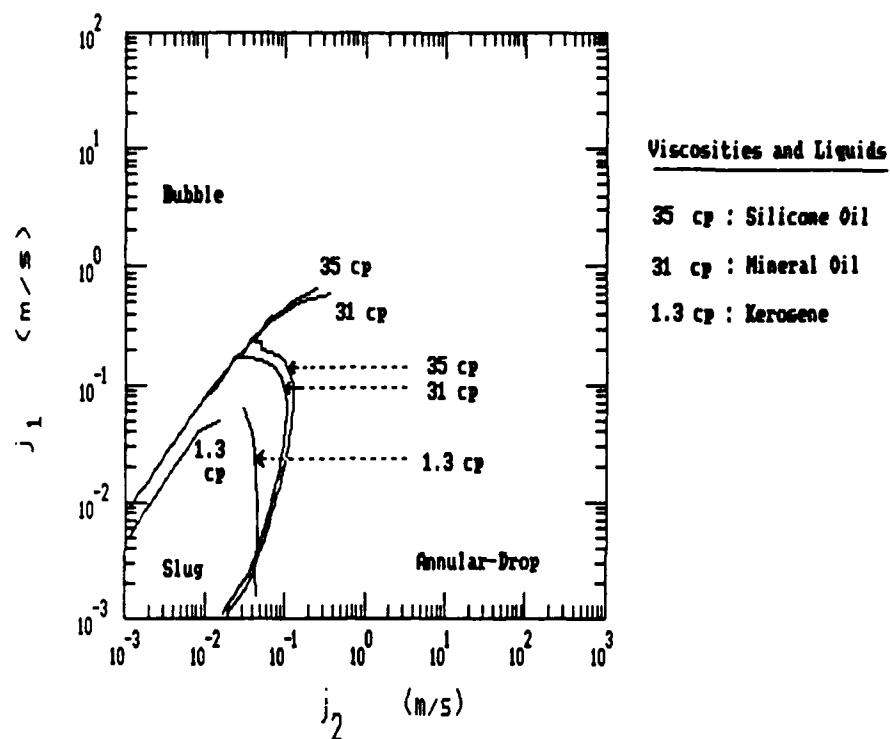
Figure 21. Predicted Effect of Viscosity on Liquid-Liquid Flow Regime
Transitions. (j2 is water)   Diameter = 1 inch
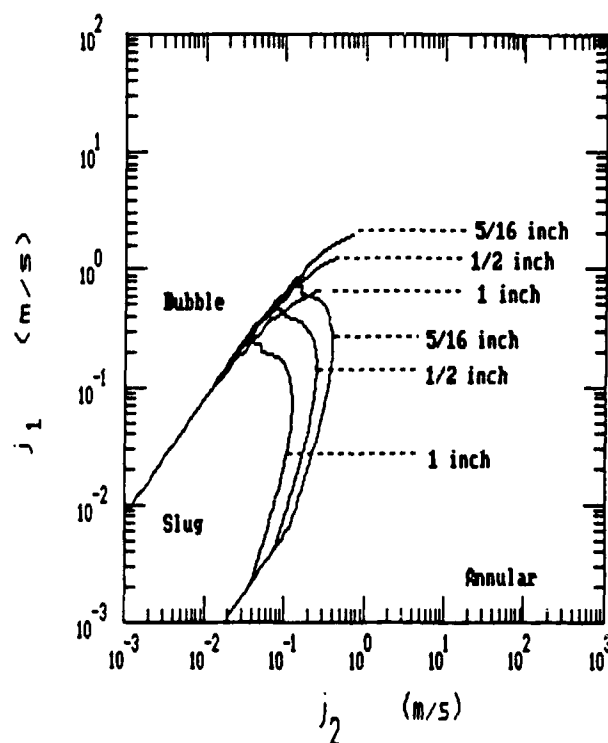
Figure 22. Predicted Effect of Tube Diameter on Liquid-Liquid Flow Regime
Transitions.   Silicone) and Water (j2).

the observed slug-annular transitions.   Yet, no single "upper
limit" is predicted, per se, by this minimization of pressure
gradient analysis.   The interplay of the laminar and turbulent
pressure gradients of bubble and slug flow, seems to create the
apparent "upper limit".

It is encouraging how well theory matches data regarding the
effect of tube diameter on flow regime transition.

The viscosity predictions are not so cleanly matched with data.
However, because of the small viscosity difference involved in
the only predictive failure (i.e., the kerosene-water slug-
annular boundary), and the manner in which surface tension is
tangled into the data, it is not presently justified to discount
the theory.

There is no predicted effect of surface tension on flow regime
transition, even though observations show that surface tension
does have an effect.   However, it is only ignored because its
effect on interfacial shear is unknown.   When this effect is
quantified, surface tension can easily be included in the
analysis.

5.6.2.   Numerical solution of the slug-annular transition

Obtaining solutions to the slug-annular flow regime transition by
the minimization of pressure gradient method is not as simple in
practice as it is in principle.   Problems arise because pressure
gradient correlations do not completely match data.   The methods
used to obtain the previous solutions are discussed and
presented below.

The method to calculate the bubble-slug transition needs no
comment.   Using the equations presented above, the point at which
bubble pressure gradient rises above slug pressure gradient at
each liquid flux jf can be directly computed.

The same general method is used to find the slug-annular flow
regime transitions.   A liquid flux j_f is chosen.   Search is then
made for the vapor flux j_g at which slug flow pressure gradient
begins to rise significantly above the calculated annular
pressure gradient.   This selected vapor flux defines the slug-
annular transition at the chosen liquid flux.

Often the slug pressure gradient calculated from the correlations
is higher than the annular pressure gradient at ALL vapor flow
rates.   However, in most of these cases, the slug pressure
gradient is, at low vapor fluxes, only slightly above the annular
gradient.   If the full pressure gradient curve is inspected by
eye, there is always evident a point at which the predicted slug

56

pressure gradient rises dramatically away from the predicted annular pressure gradient. However, a method for determining when one flow regime pressure drop departs significantly from another must be computerized.

The method used here is to first find, for any given liquid flux j_f, the vapor flux j_g where the minimum ratio of slug to annular pressure drop occurs. If this ratio is greater than 1.0, the vapor flux is selected as the slug annular transition at the given liquid flux. It will be found from this point onward, that slug pressure drop rises dramatically away from annular pressure drop as j_g, at constant liquid flux j_f, is increased.

If the minimum ratio of slug to annular pressure drop at a given j_f is less than 1.0, a numerical search is made for the point where increasing j_g causes the slug pressure drop to equal (and surpass) the annular pressure drop at constant liquid flux j_f. The vapor flux j_g at the cross-over point is taken as the slug-annular transition.

This approach is necessary to handle the various cases that arise when the two pressure drop correlations move through the various combinations of turbulent and laminar flow. This approach was used absolutely consistently to generate all slug-annular liquid-liquid predictions presented in this report. It was developed as a method to allow computerized selection of flow regime transitions based on changes in pressure gradient. These same transitions, it is believed, would be selected by the human eye, if time was available to view every pressure gradient curve across the flow regime map.

5.7. Difficulties of Liquid-Liquid Criterion Applied to Vapor-Liquid Transitions

There is presently not enough pressure drop data to suggest whether or not the principle of a minimized pressure gradient applies to microgravity. However, the principle is intuitively compelling. Therefore, the liquid-liquid flow regime model was applied without modification to microgravity air-water flow in a 9.52 mm tube.

Figure 23 shows the resulting flow regime map. For comparison, the 6-12.7 mm air-water data are plotted on the same figure.

The predicted bubble-slug transition matches the data quite well. However, the predicted slug-annular transition does not. Clearly, the slug-annular transition, as implemented for the liquid-liquid case, is inadequate for air-water microgravity flow.

Possible reasons for the failure of the liquid-liquid slug-annular transition model applied to microgravity air-water data follow:

- **The void fraction of annular flow** in the liquid-liquid experiments is unrepresentative of true vapor-liquid annular flow. Specifically, the void fraction is significantly altered by substantial entrainment in the core flow. Therefore, the thickness of the annular film is never very large or a limiting factor to liquid-liquid annular flow.

  In low-entrainment vapor-liquid annular flow, a maximum stable film thickness probably limits the occurrence of annular flow. This limit could be expressed equivalently by a minimum stable void fraction. Below this void fraction, waves on the thick annular film would bridge to create slug flow, regardless of a favorable annular pressure gradient. This approach is consistent with the suggestion by Dukler [1987] that some microgravity flow regimes are determined by void fraction.

- **The interfacial shear** in the liquid simulations is successfully modeled using a smooth interface assumption. This assumption works, probably because the liquid phase (modeled by oil) is always in laminar flow. Therefore, even when the vapor core (modeled by water) becomes turbulent, most interfacial roughness is dampened.

  However, in the air-water microgravity flows, water is turbulent throughout most of the annular region and some of the slug region. Therefore, when the vapor core in annular (or in Taylor bubble) flow becomes turbulent, significant
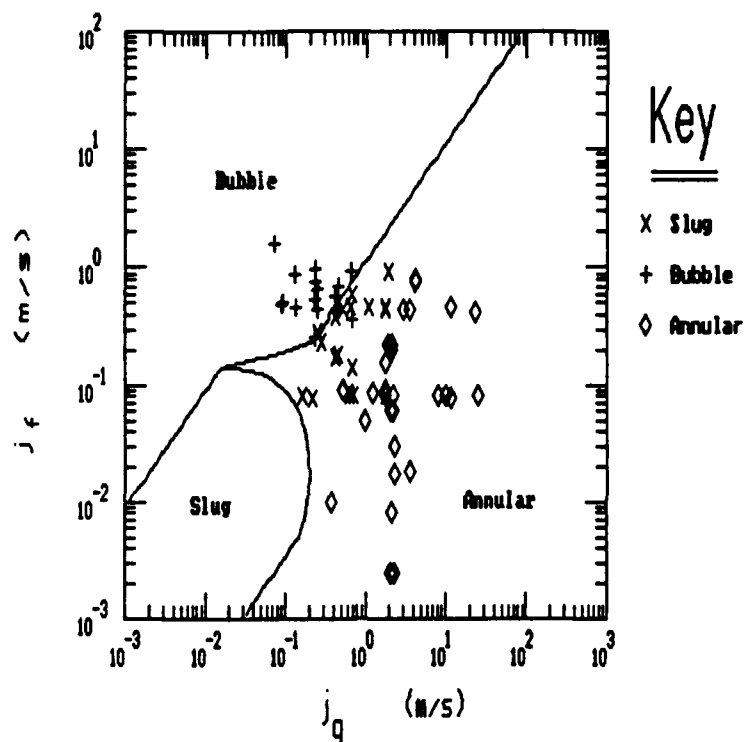
Figure 23. Predicted Microgravity Air / Water Flow Regime Transitions Using
Liquid-Liquid Model. 10 psia ; 68° F ; Diameter = 3/8 inch (9.52 mm)

Bubble-Slug Transition Succeeds, Slug-Annular Transtion Fails.

interfacial roughness is likely. Certainly, data from the literature of earth gravity annular flow support this contention (Wallis [1969], page 320).[13]

Therefore, for vapor-liquid flows near the slug-annular transition, the smooth-interface assumption may not be adequate. Pressure gradient and void fraction calculations would be incorrect. For true vapor-liquid flows, the interfacial shear calculation for slug and annular flow may need modification.

- **The simple slug model** only works well for air-water flows at the bubble-slug transition. Here, classic (relatively quiescent) Taylor bubble flow might reasonably be expected.

  However, at the slug-annular transition, the simple slug model presumes an unrealistic transition for vapor-liquid flows. The model assumes that slug flow suddenly changes from small (constant, assumed) slip velocity and zero film velocity, to the large slip and significant film velocity of annular flow.[14]

  A detailed model of slug flow is needed to express the more gradual changes in flow conditions which, realistically, are more likely.

---

[13] As often noted, there is presently no known pressure drop data correlated with microgravity flow regimes available. Without such data, it is hard to know much about the roughness of a vapor-liquid annular or slug interface. Films of a limited qui tity of microgravity flows show a rough interface at times. However, the interface is not as rough (ie, four times the film thickness) as the reference in Wallis implies.

[14] Despite these shortcomings, the simple slug model DOES work well for the slug-annular transition of the liquid-liquid flows. This success is explained by the substantial entrainment which occurs in the liquid-liquid cases. Near the slug-annular transition, liquid-liquid flows exhibit much entrainment in both Taylor bubbles and the core of annular flow. Furthermore, the annular films of both the Taylor bubble flow and the annular flow DO have nearly zero velocity. Thus, the slug-annular transition, unlike the true vapor-liquid case, is a transition from classic, low slip (and nearly zero film) velocity Taylor bubbles <u>with much entrainment</u> to nearly zero film velocity annular flow, <u>with much entrainment</u>. The simple slug model describes such flow quite well. The entrainment is accounted for in the correlating multipliers used to match the simple slug and the annular flow model pressure gradient predictions to data.

To be valid for true vapor-liquid microgravity flows, the analysis was modified to account for the issues just raised. Specifically, a minimum void fraction was added, a new interfacial shear correlation for rough films was introduced, and a new detailed model of slug flow and its pressure drop was created.

These three subjects are covered respectively in the following three sections. Following these sections, the resulting vapor-liquid flow regime transition model is compared to the air-water microgravity data.

5.8. Minimum Void Fraction in Stable Annular Flow

The previous section noted that a small void fraction (or equivalently, a thick annular film) may form a limit to vapor-liquid annular flow. This section discusses the limiting annular void fraction and film thickness suggested by the microgravity vapor-liquid data. Beyond this limit, waves on the annular film may bridge, forming slug flow. Thus, stable annular flow could not exist, even if its pressure gradient was favored over that of slug flow. (The liquid-liquid data could not exhibit this limit because void fraction was substantially modified by entrainment in both annular and slug flow.)

The next two subsections show curves of void fraction to help visualize flow regimes and their transitions. Further subsections present the minimum void fraction and maximum film thickness of annular flow indicated by the microgravity flow regime data.

5.8.1. Void fraction in bubble, slug, and annular flow

To see the role void fraction plays in limiting annular flow, it is first helpful to view lines of constant void fraction in bubble, slug, and annular flow. Please note that the following plots (Figures 24 - 27) of void fraction show what void fractions would occur only if the assumed flow regime existed at the flow rates given.

For example, homogeneous bubble flow was not observed above about 20 percent void fraction in the liquid-liquid simulations or above about 45 percent void fraction in the 9 mm. diameter vapor-liquid microgravity data. Bubble flow was, however, reported at up to almost 90 percent homogeneous void fraction in the Heppner, King, and Littles 1 inch data presented earlier. These examples show that whether or not homogeneous flow (and its void fraction) can exist depends on the conditions which determine flow regime.

Similarly, the plots show annular void fractions down to 10 percent. These plots simply mean that if annular flow did exist at the given flow rates, the void fraction would be 10 percent. It is not suggested that annular flow would actually maintain itself at the given flow rates.

Figure 24 shows lines of void fraction for homogeneous bubble flow. These are created using the assumption that vapor and liquid velocity are equal. Thus, the lines of void fraction for homogeneous bubble flow are identical to those for homogeneous drop flow. They are a function ONLY of liquid flow rate and vapor flow rate. Diameter, viscosity, surface tension, etc., have no effect whatsoever on lines of homogeneous void fraction.

62
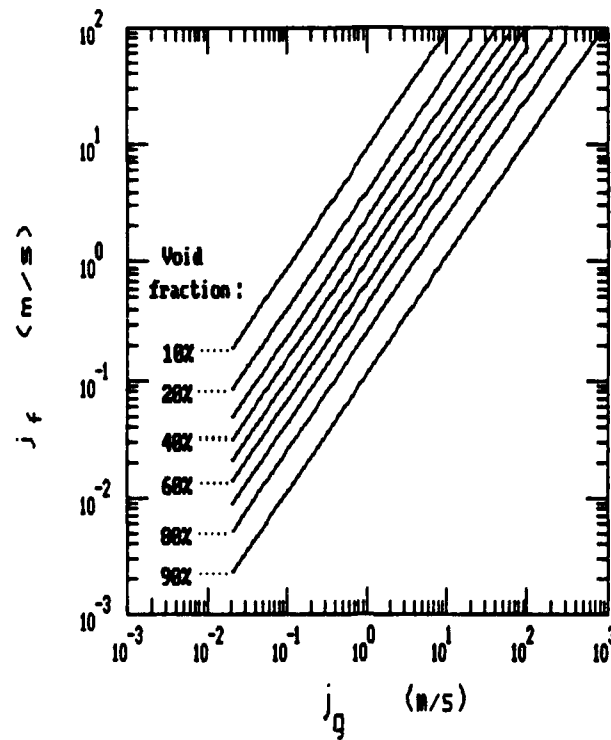
Figure 24. Homogeneous Void Fraction.
(Function only of flow rates j_f and j_g)
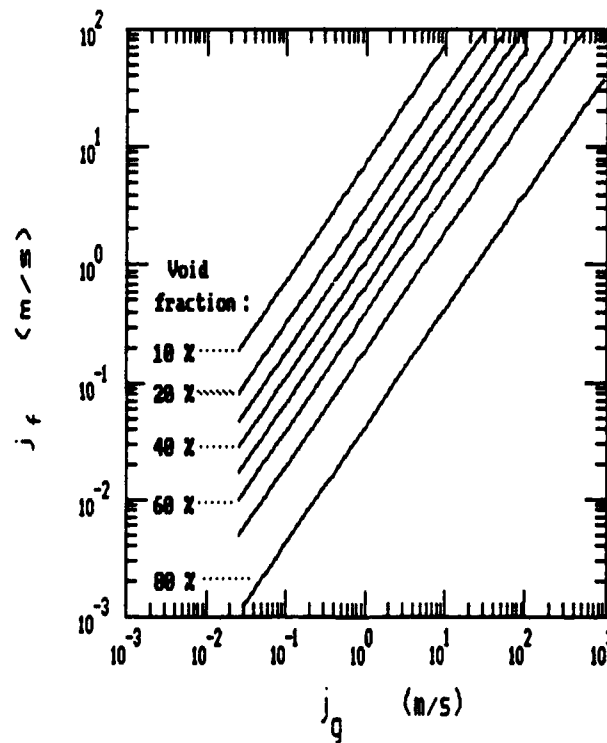
Figure 25. Simplified Slug Void Fraction. $C_1 = 1.2$
(Function only of flow rates j_f , j_g , and constant (assumed) slip velocity.)

63

Figure 25 shows lines of void fraction for the simplified slug model with C_1 = 1.2. These are a function only of vapor and liquid flow rates and the assumed slip velocity, expressed by C_1. Notice that, compared to the homogeneous void fraction lines, the slug flow lines are shifted slightly to the right. The shift is due to the slip velocity. This shift shows that slightly more vapor can flow in slug flow at any given liquid flow and void fraction than in homogeneous flow. Because of the definitions of the simple slug model, a slug void fraction greater than $1/C_1$ is not possible. At this void, the flow is by definition annular, because the overall void fraction equals the local void of the Taylor bubble -- which is always $1/C_1$. (See Section 6.2 Equation 6-15). With C_1 = 1.2, the limiting void is 83.33 percent.

Figure 26 shows lines of void fraction for idealized annular flow with a smooth interfacial shear assumption. Slope changes mark the laminar-turbulent transitions of both vapor and liquid. The annular void fraction lines are a function of viscosity, diameter, and flow rates. For fixed fluid properties, the void fraction lines will be identical at the lower left (both phases laminar) and the upper right (both phases turbulent). When diameter is varied, the location of the laminar-turbulent transitions is all that will change. Note that the annular void fraction lines are significantly shifted to the right, compared to those for slug or bubble flow. This shift is due to annular flow's relatively large slip velocity. The annular slip velocity permits much more vapor flow at any given liquid flow and void fraction than permitted by bubble or slug flow.

5.8.2. Effect of interfacial shear on annular void fraction

Figure 27 shows lines of annular void fraction using a rough interface shear correlation for turbulent vapor flow. The interfacial shear correlation is used when the vapor flow becomes turbulent. The correlation itself is taken from the literature of earth gravity flow regimes (Wallis [1969], page 320) and is presented in Section 5.9. Note the abrupt change that occurs when the vapor becomes turbulent. The increased interfacial shear sharply reduces slip velocity. Therefore, compared to the smooth-interface void fraction lines of Figure 26, the turbulent vapor portions of these lines are shifted significantly towards lower vapor flow rates.

This comparison shows that, in the region of turbulent vapor, the shape of the annular void fraction lines are determined by the interfacial shear assumed.

64
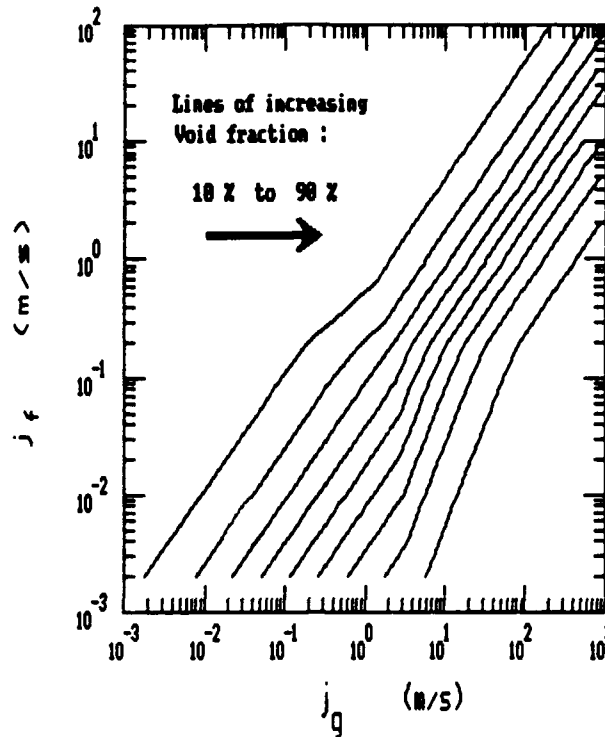
Figure 26. Annular Void Fraction -- Smooth Interface.
Air and Water ; 10 psia ; 68°F ; Diameter = 3/8 inch
Function of flow rates, fluid properties, and diameter.
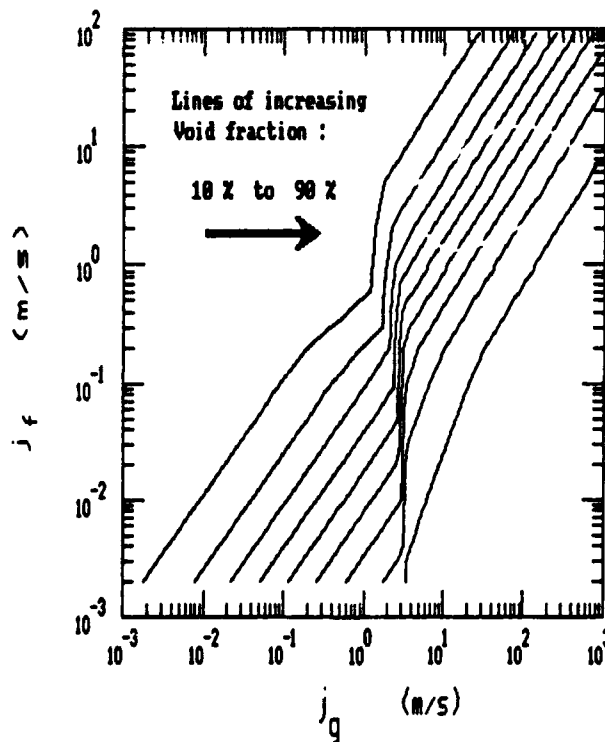
Figure 27. Annular Void Fraction -- Rough Interface.
Air and Water ; 10 psia ; 68°F ; Diameter = 3/8 inch
Function of flow rates, fluid properties, and diameter.

5.8.3. Minimum annular void fraction indicated by data

Dukler [1987] has suggested that void fraction may determine microgravity flow regimes. It is suggested here that void fraction is one criterion that helps determine the slug-annular boundary. However, other criteria, such as a minimized pressure gradient, are also asserted to play a major role. Nevertheless, it is instructive to see how well lines of constant void fraction, alone, fit the microgravity slug-annular transition.

Figure 28 shows air-water microgravity flow regime data taken in 6, 9.52, and 12.7 mm diameter tubes. The average diameter is about 9.52 mm, and on this diameter the void calculations were based. A line of 20 percent annular void fraction, based on the SMOOTH interfacial shear assumption, is plotted through the data. It does not very well describe whole the slug-annular boundary, although it may do well on the upper portions of the boundary. The line may describe the bubble-annular boundary, but data trends must be extrapolated to conclude this.

The figure shows that if the smooth interface assumption is correct, stable annular flow exists down to 20 percent void fraction. (Here, the vapor core occupies about 45 percent of the tube diameter.) The line of 20 percent void fraction will be used later as part of the detailed slug flow model.

Figure 29 shows the same air-water microgravity flow regime data. However, this time a line of 30 percent annular void fraction, based on the rough interfacial shear assumption, is plotted through the data. Notice that it quite well describes the slug-annular boundary. The line will be used later as part of the simple slug-annular flow regime transition model.

Figure 30 shows air-water microgravity flow regime data taken in 1 inch (25.4 mm) diameter tubes. A line of 60 percent annular void fraction, based on the rough interfacial shear assumption, is plotted through the data. Notice that it quite well describes the slug-annular and the bubble-annular boundary.

5.8.4. Maximum annular film thickness

The two minimum annular (rough interface) void fractions proposed above (30 percent for 9.52 mm diameter and 60 percent for 25.4 mm diameter) can be somewhat reconciled. It is suggested that a maximum annular film thickness is the key to calculating the minimum stable annular void fraction. From the standpoint of film thickness, 30 percent void fraction in 9.52 mm pipes is equivalent to 69 percent void fraction in 25.4 mm pipes. From this perspective, the two minimum annular void fractions indicated from the data are not dissimilar.

66
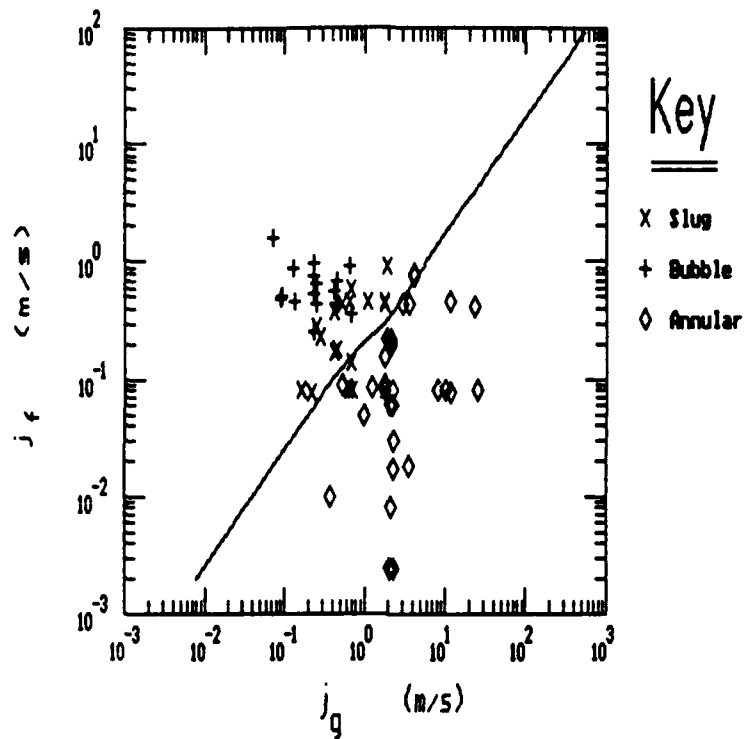
Figure 28. Twenty Percent (smooth) Annular Void Line as Slug-Annular Transition
for Air/Water Microgravity Data. (Line taken from Figure 26.)
10 psia ; 68° F ; Diameter = 3/8 inch (9.52 mm)
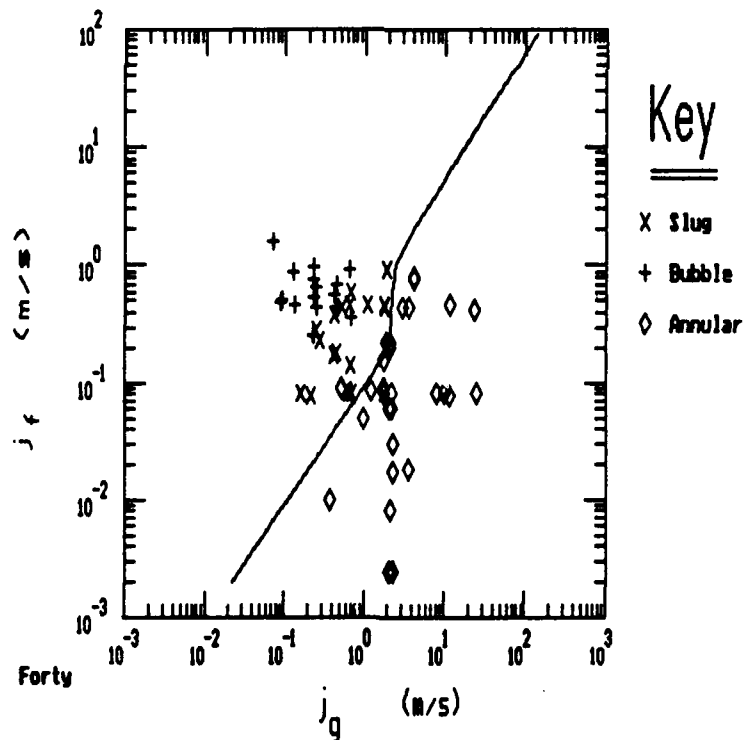
Figure 29. Thirty Percent (rough) Annular Void Line as Slug-Annular Transition
for Air/Water Microgravity Data. (Line taken from Figure 27.)
10 psia ; 68° F ; Diameter = 3/8 inch (9.52 mm)

67
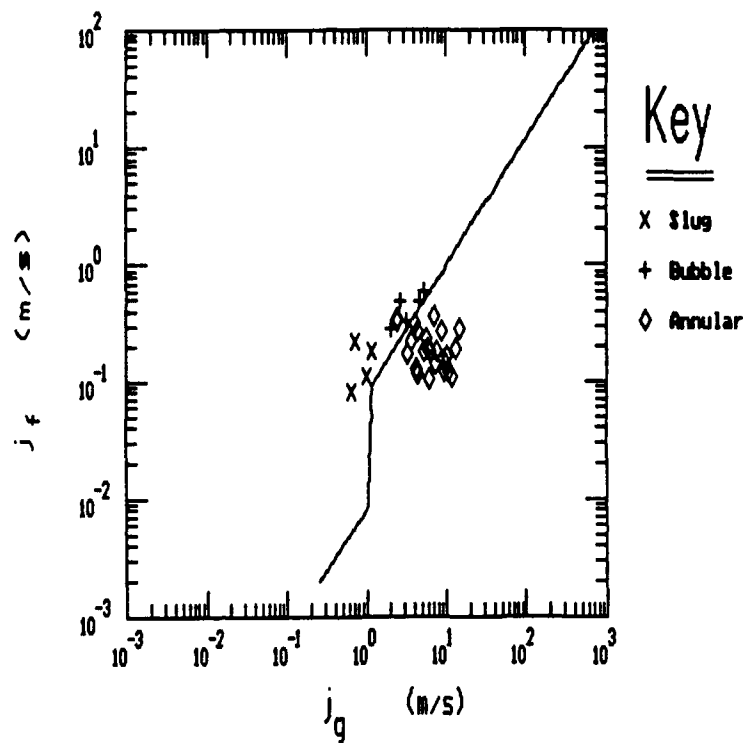
Figure 30.   Sixty Percent (rough) Annular Void Line as Regime Transition
for One Inch Air/Water Microgravity Data.

Assuming the concept of a maximum annular film thickness to be correct, a tentative maximum film thickness can be deduced from the limited flow regime data. The deduced maximum thickness is 2.15 mm in the 9.52 mm pipe and 2.86 mm in the 25.4 mm (1 inch) pipe. These film thicknesses are within 33 percent of each other. The agreement is not very good, but it is better than the apparent 100 percent discrepancy when compared on a basis of void fraction (30 percent vs 60 percent).

In any event, the 1 inch tube diameter data of Heppner et al. [1975] must be used cautiously. The apparatus used had only a 22 inch long flow section. Thus, the flow was probably not fully developed.

It will be noted in Section 5.9 that the rough film shear correlation discussed implies a surface roughness equal to four times the film thickness. This surface roughness implies a maximum void fraction of 56 percent in any diameter tube before bridging occurs. In itself, this is a crude prediction of limiting void fraction. Admittedly, this prediction doesn't accurately fit the 9.52 mm (average diameter) data, since the 30 percent void fraction which fits the data is "impossible". Neither does the shear correlation suggest that maximum film thickness is independent of tube diameter. It may be that this calculation extrapolates the correlation to films thicker than for which it was intended. Nevertheless, this particular rough film shear correlation still implies the concept of a limiting film thickness. Furthermore, the implied limit to void fraction is in the correct range to fit the 1 inch data anyway.

Effect of Interfacial Shear Assumption on Calculated Film Thickness

The minimum void is deduced from the data by assuming some interfacial shear. For example, the 9.52 mm (average diameter) data implied a minimum void of 20 percent using a smooth interface assumption. This condition would be a quiescent annular flow with a vapor core occupying 45 percent of the tube diameter. It is hard to imagine annular flow tranquil enough to exist at much lower void fractions.

However, photographs show that the microgravity annular interface is not smooth. Photographs also suggest that the interface does not have a roughness of four times the film thickness, as implied by the rough film shear correlation. Unfortunately, with a lack of time, the analysis is presently taken no further. The true interfacial shear for microgravity annular films is probably between the smooth and the "very rough" assumption. Thus, the limiting void fraction in 9.52 mm pipes is probably somewhere between 20 percent and 30 percent minimum annular void.

69

However, as noted, the associated maximum stable annular film thickness is probably more fundamental. The 9.52 mm diameter data suggests a maximum film thickness of about 2 mm; the 25.4 mm data suggest a maximum closer to 3 mm, based on the rough interface assumption. The 9.52 mm data, assuming a smooth interface, yields about 2.5 mm as the limiting thickness that occurs at twenty percent void fraction. Therefore, as a first order approximation, the maximum stable annular film thickness in air/water microgravity flows is proposed to be 2.5 mm.

The calculation of maximum film thickness is clearly tied to the interfacial shear coefficient assumed. Therefore, future analysis and experimentation need to tackle these two related issues simultaneously.

Effect of Surface Tension on Maximum Stable Film Thickness and the Slug-Annular Transition

Maximum annular film thickness is almost certainly a function of surface tension, pipe diameter, flow rates, and possibly of viscosities. Thus, a proper expression for limiting annular film thickness would likely introduce surface tension into the analysis of microgravity flow regimes.

It is interesting that data discussed in Section 4.2.2 showed that surface tension has its major impact on the slug-annular transition. The suggestion that surface tension influences the slug-annular boundary via maximum stable annular film thickness is consistent with this observation.

Unfortunately, the present implementation of the analysis expresses no quantitative dependency on surface tension. Neither has any attempt been made to predict a maximum annular film thickness from first principles.

5.9. Slug-Annular Transition Assuming Rough Interface

The smooth interface assumption, which fits the liquid-liquid pressure drop data, may not be valid for true microgravity vapor-liquid flow. The smooth interface assumption may have caused the model for the slug-annular transition to fail for vapor-liquid flow. Therefore, a new expression for interfacial shear was introduced. The expression is a correlation from the literature of earth gravity flow regimes (Wallis [1969], page 320). The correlation gives an increased interfacial shear as annular film thickness increases:

$$C_i = 0.005 \left[1 + 300 \frac{\delta}{D} \right] \tag{5-24}$$

Or, re-written as a function of void fraction:

$$C_i = 0.005 \left[1 + 150 \left(1 - \sqrt{\alpha} \right) \right] \tag{5-25}$$

As pointed out by Wallis, these equations imply a surface roughness equal to four times the film thickness. This is seen by comparing them to rough-pipe correlations of single phase flow (Wallis [1969], page 320-321).

Hewitt [1969] has presented evidence that annular flow on earth usually has surface waves equal to five times the film thickness. The foregoing shear correlation is reasonably consistent with his observations.

A surface roughness four times the annular film thickness would cause bridging when the film thickness was one-eighth of the tube diameter. As noted previously, this would mean a minimum possible void fraction of 56 percent before bridging occurs.

However, except as an approximation, this limit should probably not be taken too seriously because it is based on a correlation. Such bridging calculations may be extrapolating the correlation beyond conditions for which it was intended. The correlation could be taken to state only that interfacial shear is equivalent to a surface roughness equal to four times the film thickness. For example, the effects of entrainment or occasional large circumferential roll waves might be buried in the correlation. This would increase apparent interfacial shear without implying bridging. But this is speculation on a correlation that has not been proved or disproved for eith r thick or thin microgravity annular films.

The Rough Interface Shear Correlation May Not Apply to Microgravity

Keshock et al. [1973] noted that one distinguishing characteristic of microgravity annular flow was its smoothness. Annular flow in earth gravity, at the same flow rates, exhibited a much rougher, more irregular liquid film. Subsequent photographs of microgravity flow confirm this observation.

Therefore, Equation 5-24 or 5-25 can be used only tentatively. It probably over-predicts microgravity interfacial shear and pressure drop. Similarly, it is likely to influence too strongly predicted annular void fractions.

Photographs do show some surface roughness in microgravity annular flow. Therefore, the smooth interface assumption probably under-predicts pressure drop when the vapor flow is turbulent. Similarly, void fractions will not be properly predicted.

In the absence of microgravity interfacial shear or pressure drop data, the shear correlation above is taken as a first-order approximation. When incorporated into the annular and slug flow models of this paper, it is used only when the vapor flow becomes turbulent. The assumption is made that turbulent vapor will cause either a laminar or a turbulent liquid interface to become rough.

5.9.1. Simple slug-annular transition

Figure 31 shows the slug-annular transition predictions using the simple slug model. It is compared with the air-water microgravity flow regime data. Two criteria are shown: the pressure drop criterion and the minimum stable annular void fraction criterion. The minimum annular void fraction line has been chosen as 30 percent, as discussed.

The predicted transition is a combination of the two criteria. By the simple slug pressure gradient model alone, annular flow is favored almost everywhere slug flow has actually been observed. However, to the left of the minimum stable annular void fraction line annular flow cannot, by hypothesis, exist. Therefore slug flow occurs here, even though annular flow may be favored by pressure gradient.

Logically, the region between the pressure drop criterion and the void fraction line is a region of churn flow. That is, stable Taylor bubbles don't exist because annular flow is favored by pressure drop. However, once the flow converts to annular, it is quickly unstable because the resulting void fraction is too small. The indicated result is unstable flow with erratically
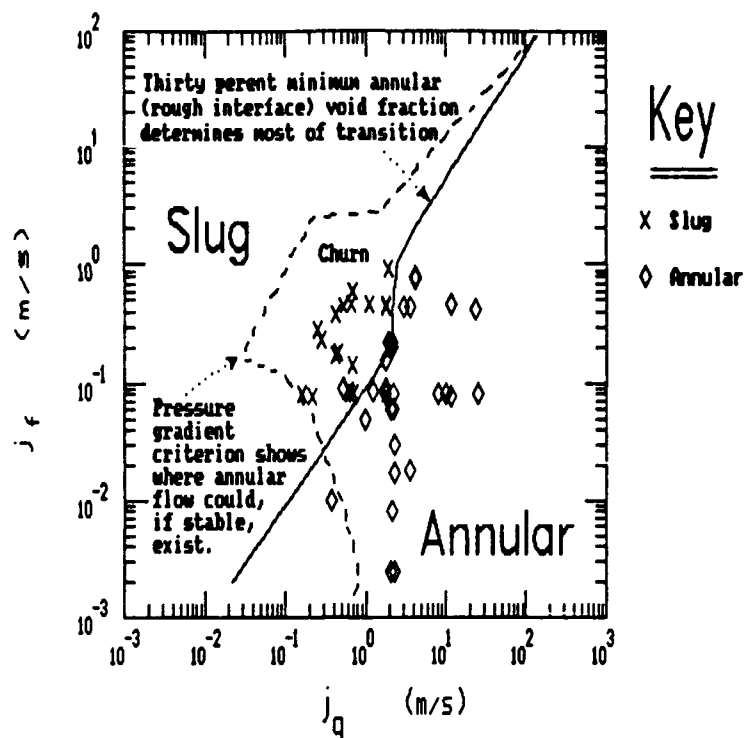
Figure 31. Predicted Microgravity Air/Water Slug-Annular Transition Using Simple Transition Model. 10 psia ; 68° F ; Diameter = 3/8 inch
(9.52 mm)
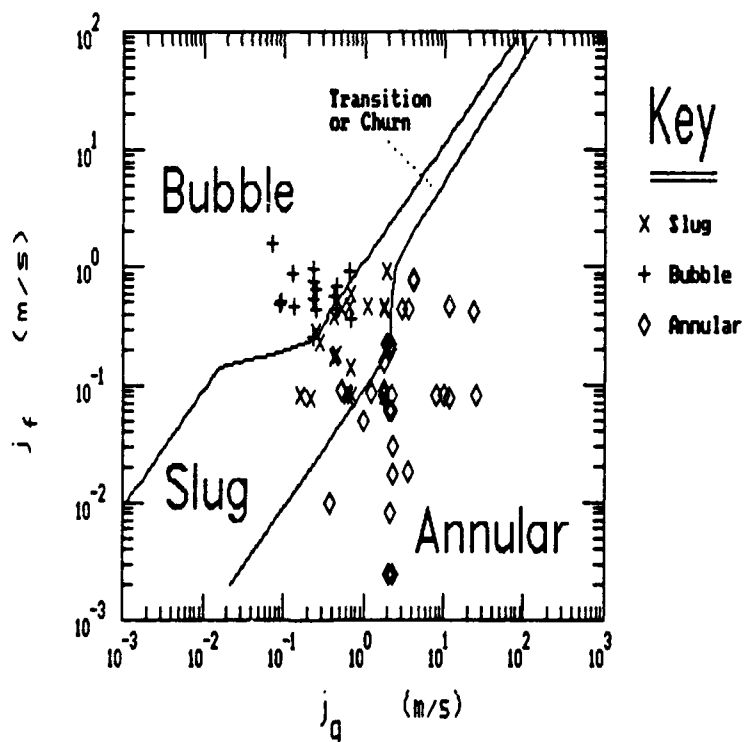
Figure 32. Predicted Microgravity Air/Water Flow Regime Transitions Using Simple Transition Model. 10 psia ; 68° F ; Diameter = 3/8 inch
(9.52 mm)

shaped long bubbles, nearly, but not quite, forming annular flow. Thus, the simple model indicates a region of churn flow that virtually covers the entire slug flow region.

Figure 31 has shown that the void fraction criterion is the determining factor for virtually the whole simple slug-annular transition. Thus, this 30 percent annular (rough-interface) void fraction line alone might be used quite well as a slug-annular transition in 9.52 mm tubes.

Whether or not it is quantitatively accurate, the turbulent shear correlation presently used for the slug-annular transition does express what seems intuitively obvious:

> Once the core of annular goes turbulent, interfacial shear is dramatically increased. Vapor turbulence almost certainly creates waves on the surface of a turbulent annular film. (A laminar vapor flow may tend to dampen waves on the annular film.) The resulting increase in interfacial shear leads to a rise in pressure gradient and causes void fraction lines to locally become quite steep. Assuming some maximum stable annular film thickness, a reasonable slug-annular transition can be calculated from the resulting line of constant void fraction.
>
> The minimization of pressure gradient principle becomes a secondary criterion. It only determines where annular flow is favored, by pressure gradient, over slug flow. However, the film thickness or void fraction criteria determine where stable annular flow actually does form.

5.9.2. Simple vapor-liquid microgravity flow regime map

Using the minimum annular void fraction line from above and the previous bubble-slug transition line, a vapor-liquid flow regime map can be created. Figure 32 shows this map, calculated for 9.52 mm (3/8 in) tubes. For comparison, the 6-12.7 mm data are also plotted.

This flow regime map reasonably well matches the data. One possible exception is the "corridor" of slug flow predicted at high volumetric fluxes. For now, this region has been labeled a "transition zone" between bubble and annular flow. A future section argues that the bubble-annular transition, in this high flux region, might better be taken as the line of minimum annular void fraction.

74
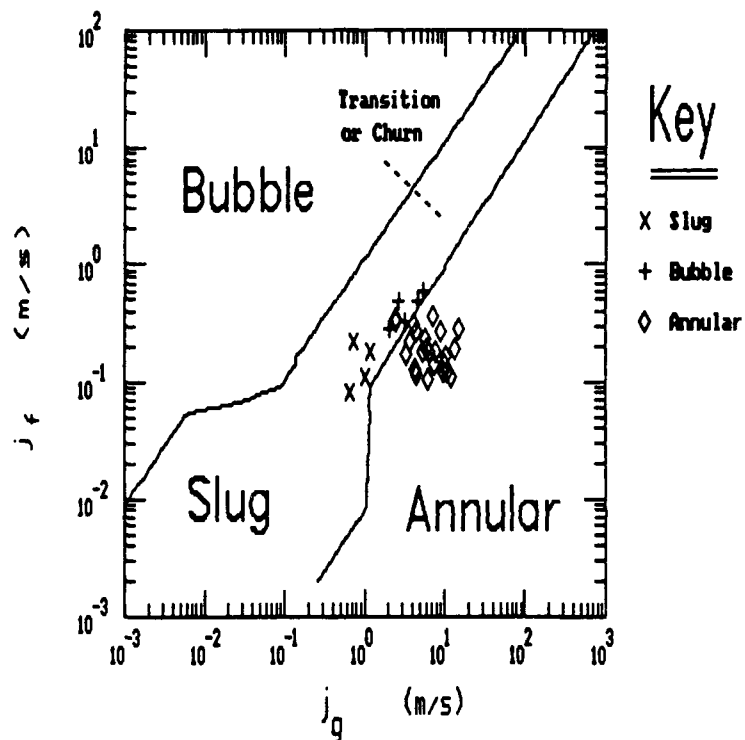
Figure 33. Predicted Microgravity Air/Water Flow Regime Transitions for
One Inch Tubes Using Simple Transition Model. 10 psia ; 68°F

75

Figure 33 shows a similar flow regime map, created for 1 inch (25.4 mm) diameter tubes. The minimum annular void fraction line, as previously chosen to fit the 1 inch data, is 60 percent. The bubble-slug transition line is calculated as always, but for 1 inch diameter. For comparison, the 1 inch microgravity data are also plotted.

The slug-annular transition matches the 1 inch tube diameter data quite well. The bubble-annular transition can be taken as the extension of the same void fraction line that forms the slug-annular transition. Or, the few bubble data points can be considered part of the "transition zone".

There is no prediction given for the transition from bubble to slug flow within the high flux region inside the transition zone. The bubble-slug transition model applies only to the low flux region of bubble and slug flow.

Unfortunately, there are no 1 inch data to prove or disprove the bubble-slug transition in the low flux region for which it was developed.

As noted previously, the 1 inch data of Heppner et al. [1975] must be used cautiously. The apparatus used was only 22 inches long in its flow section. Thus, fully developed flow may not have existed.

5.9.3. Advantages and disadvantages of the simple slug-annular transition

Advantages

The general approach for obtaining the simple slug-annular transition is uncomplicated and quite quick to calculate. It may be that no more complex an approach is necessary to predict the vapor liquid slug-annular transition of microgravity flows. The simple correlation for interfacial shear used here seems reasonable as a first order approximation. Other expressions of the same turbulent shear phenomena may yield similar, even better results.

Disadvantages

There are several difficulties with the simple flow regime map:

- As noted earlier, photographs of microgravity flow near the slug-annular transition show, qualitatively, a relatively smooth liquid film. The waviness that does appear is not

76

as rough as the turbulent interfacial shear correlation implies.

- It is disturbing that a shear correlation which is unknown and questionable in microgravity virtually determines two flow regime boundaries -- the slug-annular and the bubble-annular. First, the slug-annular transition is very dependent on the shear correlation to drive the (30 percent) annular void fraction line nearly vertical at the right point to split the slug from the annular data. Second, the bubble-annular transition is dependent on the correlation to continue the vertical rise far enough that the upper portion of the same void fraction line splits the bubble and annular data.

  A rough-interface correlation which expressed less surface roughness -- as qualitatively observed -- would drive all void fraction lines less steeply and less far. Then, any given void fraction line would not so well divide the slug and annular data. Neither would the same void line reach far enough to split the bubble and annular data.

- The simple slug model suggests churn flow almost everywhere between the bubble and annular boundaries, as explained in Section 5.9.1. However, photographs suggest an orderly Taylor bubble type of slug flow for much of the slug flow region. The churn flow implied by the simple transition model is inconsistent with this observation.

5.9.4. Interfacial research

The lack of pressure drop data correlated with microgravity vapor-liquid flow regime has forced approximations of pressure drop in this analysis. Interfacial shear was the chief quantity estimated. Section 5.8.4 has shown how the approximation of interfacial shear influences the calculation of the apparent maximum stable annular film thickness.

Section 5.8.4 also indicated that surface tension undoubtedly plays a role in maximum stable film thickness. Surface tension probably plays a very related role in determining film roughness, and therefore interfacial shear. Once either of these roles is understood, surface tension may be quantitatively introduced into the present analysis.

Because these inter-related issues are not well understood, there is a need for more detailed microgravity flow regime research. This research would preferably address pressure gradient, interfacial shear, and annular film thickness simultaneously. Without such data, the present analysis might never proceed much further.

77

Experiments with a Minimal Buoyancy Liquid-Liquid Interface

Because of the recognized need for information about microgravity vapor-liquid interfaces, further simulation experiments were undertaken. The interfacial behavior between two liquids with a small density difference was explored.

Appendix B details the results and analysis of wave duct experiments which were aimed at interfacial conditions of microgravity flows. Two liquids of nearly equal density flowed through a duct of rectangular cross section. Data on interfacial waves were taken. Analysis showed at what value of _laminar_ interfacial shear the interface first became rough. Unfortunately, the analysis has not yet proceeded to the point of predicting turbulent interfacial shear as a function of fluid flow rates and properties. However, future work of this type may lead to an improved expression for a turbulent interfacial shear coefficient.

Minimum annular void fraction is another area of analysis related to interfacial waves. It was originally hoped that the wave duct experiments would provide information about unstable waves in microgravity. Unfortunately, no unstable waves occurred. As discussed in Appendix B, this may be due to limitations of the apparatus. However, it is quite likely that the formation of unstable waves has to do with inertial differences between the two fluids. Two liquids of nearly equal density have little inertial differences perpendicular to the interface between them. Inertial differences normal to the surface that are thought to play a significant role in large or unstable wave growth. Again, surface tension would probably play a role and thus would be included as a factor to predict microgravity flow regimes. An understanding of such phenomena may lead to the ability to predict minimum annular void fraction.

Appendix C compares wave speed data from the wave duct experiments of Appendix B to a simple microgravity wave speed equation. The equation was derived (as shown in Appendix C) to predict wave speed as a function of surface tension, when gravity forces are negligible. The match of theory with data is good at all but low wave amplitudes. This work was part of an effort to explore mechanisms of the microgravity slug-annular transition. An effort was made to examine the interaction of wave speed, core vapor velocity, and bridging. For this calculation, the wave speed equation was converted to an annular geometry.

However, the pressure gradient analysis has so far proven easier and more successful. Nevertheless, the wave speed work may be of use in future detailed studies of the slug-annular transition. Therefore, the work has been documented in Appendix C.

78

5.10. Detailed Slug Flow Model

Like the simplified model, the detailed slug flow model is a model of Taylor bubble slug flow which uses the concept of a unit cell. However, the detailed model is based on a <u>continuity solution of all terms of the unit cell</u>. The local flow in and around the Taylor bubble is described by the annular model. Slip velocity is calculated, not assumed. The model predicts pressure gradient, phase and interface velocities, average geometries of classic Taylor bubble slug flow, and some of the boundaries to other flow regimes. It also predicts a region of hysteresis between slug and annular flow.

The detailed slug model also predicts the existence and location of a <u>churn flow</u> region separate from a region of Taylor bubble slug flow. However, neither the pressure gradient, the velocities, nor any average geometries of churn flow are predicted.

5.10.1.
Unit cell of the detailed slug flow model

The basis for the detailed slug model is a complete liquid continuity equation over the unit cell (diagrammed in Figure 34). Unlike the simplified model just presented, liquid flow in the film around the Taylor bubble is not disregarded:

Total Liquid Flow = Liquid Flow in Slug + Liquid Flow in Film

$$Q_f = j \frac{\pi D^2}{4} L_s^* + \tilde{V}_{ft} (1 - \alpha_t) \frac{\pi D^2}{4} L_t^* \qquad (5-26)$$

where: all items subscripted with "t" refer to local conditions in the Taylor bubble, which is treated as a local annular flow, namely:

$\tilde{V}_{ft}$ = average film speed along Taylor bubble.

α_t = local void fraction in Taylor bubble cross section.

From the liquid continuity relationship:

$$j_f = \tilde{V}_{ft}(1-\alpha_t) + j_g \frac{1-L_t^*}{L_t^*} \qquad (5-27)$$

Or, re-arranged to solve for L_t^*:

$$L_t^* = \frac{j_g}{j - \tilde{V}_{ft}(1-\alpha_t)} \qquad (5-28)$$

79
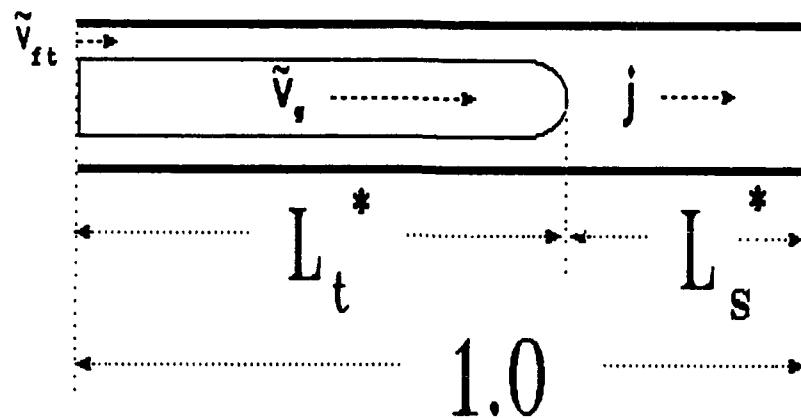
$$j = j_f + j_g$$

$$\alpha_t = \alpha \, L_t^{\,*}$$

$$j_f = \tilde{v}_{ft}\left(1 - \alpha_t\right) + j_g \frac{1 - L_t^{\,*}}{L_t^{\,*}}$$

$$L_t^{\,*} = \frac{j_g}{j - \tilde{v}_{ft}\left(1 - \alpha_t\right)}$$

Figure 34.   Detailed Slug Flow Model

80

Equation 5-28 for L_t^* was presented (without derivation) as Equation 5-9 in Section 5.4.2, covering the simplified slug model. The equation was used to show that when film velocity is assumed zero, L_t^* calculates to be j_g/j, which is equivalent to the homogeneous void fraction. However, in the general case, the film velocity v_{ft} around the Taylor bubble is non-zero. When L_t^* is be determined as discussed in the next subsection, v_{ft} can be calculated.

Combining the definition of the unit cell with Equation 5-28 (and setting $\tilde{v}_{ft}$ to zero) shows the limits of L_t^* to be:

$$\alpha_h \leq L_t^* \leq 1 \qquad (5-29)$$

Equation 5-29 shows that the minimum possible L_t^* is equal to the calculated homogeneous void fraction. The maximum possible L_t^* is 1, which is annular flow. To closely approach (and even reach) this maximum makes physical sense because the detailed slug model accounts for liquid flow in the film around the Taylor bubble. If L_t^* increases at constant j_f and j_g, the liquid film velocity increases. When L_t^* reaches 1, all liquid flows as an annular film and has velocity. At this point, the liquid film flowing around the (infinitely long) Taylor bubble is simply the liquid component of annular flow. Thus, the detailed slug flow model offers a continuous description of flow parameters throughout the whole region of Taylor bubble slug flow. This description of flow reaches all the way to (and includes) pure annular flow.

Some conditions in and around the Taylor bubble are determined from the global slug flow conditions, by continuity:

$$\alpha_t = \frac{\alpha}{L_t^*} \qquad (5-30)$$

$$\tilde{v}_{gt} = \tilde{v}_g = \frac{j_g}{\alpha} \qquad (5-31)$$

$$j_{gt} = \tilde{v}_{gt}\, \alpha_t \qquad (5-32)$$

The remaining conditions in and around the Taylor bubble are governed locally by the equations of annular flow. That is, given $\tilde{v}_{gt}$ and α_t, the interface velocity and average film velocity can be calculated, locally, as an annular flow.

The next subsection discusses a method to determine L_t^*. Once this is done, the detailed slug flow model can be uniquely solved.

81

5.10.2. Assertions used to determine unit Taylor bubble length

Alone, the equations above cannot be uniquely solved. Infinite combinations of L_t^*, $\tilde{v}_g$, and $\tilde{v}_{ft}$, meet all stated conditions (and also the annular relationships within the bubble). There is a missing condition. This condition may be provided by assertions, discussed in detail immediately afterwards, regarding L_t^*:

1) L_t^* is determined such that the pressure gradient is a local, if not the global, minimum. (If the pressure gradient is only a <u>local</u> minimum, the slug flow may exhibit hysteresis, shifting between slug flow and annular or churn flow.)

2) If no L_t^* exists which gives a local or a global pressure gradient minimum, then the flow cannot exist as classic Taylor bubble slug flow.

3) If a local minimum pressure gradient exists, it will usually be for a value of L_t^* close or virtually equal to the minimum possible L_t^*.

4) Therefore, if stable slug flow exists, then L_t^* will take on the minimum possible value (or be close to it). This minimum value is, as noted in the previous section, equivalent to the calculated homogeneous void fraction.

The third assertion in particular may not seem intuitively satisfying. However, it results from experience with numerical solutions to the detailed slug flow model. These solutions showed how slug flow pressure gradient changed at each set of flows as L_t^* was uniformly varied. Specifically, L_t^* was increased from its minimum value (α_h) to its maximum value (1.0) across much of the flow regime map. In all cases, if a local minimum pressure gradient existed, it was at or very near the minimum possible L_t^*. Qualitatively, pressure loss is usually minimized when the vapor component of slug flow is kept at its lowest possible velocity. This occurs when Taylor bubbles are as short and fat as possible, namely, when L_t^* is at its minimum.

The other assertions are based on the principle of a minimized pressure gradient. Thus, the detailed slug model is as much an extension as it is an addition to the single underlying principle hypothesized to determine flow regimes -- the minimization of pressure gradient.

Discussion of Assertions

These assertions might best be understood by using plots of slug pressure gradient versus L_t^*. To show the relationship to annular flow, it is convenient to divide the slug pressure gradient by the calculated (constant) annular pressure gradient at the same phase flow rates. Figure 35 shows the six basic relationships between L_t^* and this normalized pressure gradient that have so far, by numerical solution, been found to exist.

Notice that in the lower four curves there is a local minimum pressure gradient at or near the lowest possible L_t^*. In these four curves it is asserted that L_t^* will take on the value determined by the local pressure gradient minimum. This assertion is a logical extension of the proposed general principle that two phase flow adjusts to minimize pressure gradient.

In the upper two curves there is no local minimum. In these two curves, classic Taylor bubble slug flow will not, by hypothesis, exist. A small increase in L_t^* will reduce pressure gradient and precipitate further increase until $L_t^* = 1.0$, which is annular flow. From this point the flow may remain annular, or if unstable as annular flow (e.g., due to an untenably low void fraction), convert to bubble or churn flow.

Sometimes this reasoning predicts conditions where stable Taylor bubbles cannot exist, but where neither bubble flow nor annular flow can be expected to exist either. In these cases, bubble flow cannot exist because slug pressure drop is significantly lower. Hence, the flow would adjust away from bubble to permit a slip velocity. Similarly, annular flow cannot exist in these cases because the resulting annular void fraction would be too small to maintain a continuous vapor core. Such situations are predicted to be unstable slug flow (i.e., "churn" flow). Such a flow would not be a series of stable Taylor bubbles. Elongated elliptical or irregular shaped bubbles would be expected, mixed chaotically with smaller spherical bubbles. Pressure fluctuations similar in strength to more classic slug flow would be expected. Therefore, churn flow is here defined as a subset of the slug flow regime.

A Region of Hysteresis Predicted

Returning to the lower four curves of Figure 35, more can be deduced. In these curves the favored L_t^* is virtually equal to the calculated homogeneous void fraction, or (in the lowest curve) not far from it. In the three lower curves, the favored L_t^* will also yield the lowest possible pressure gradient. That is, the favored L_t^* occurs at a global minimum pressure drop.

Figure 35. Unit Taylor Bubble Length vs. Normalized Pressure Gradient
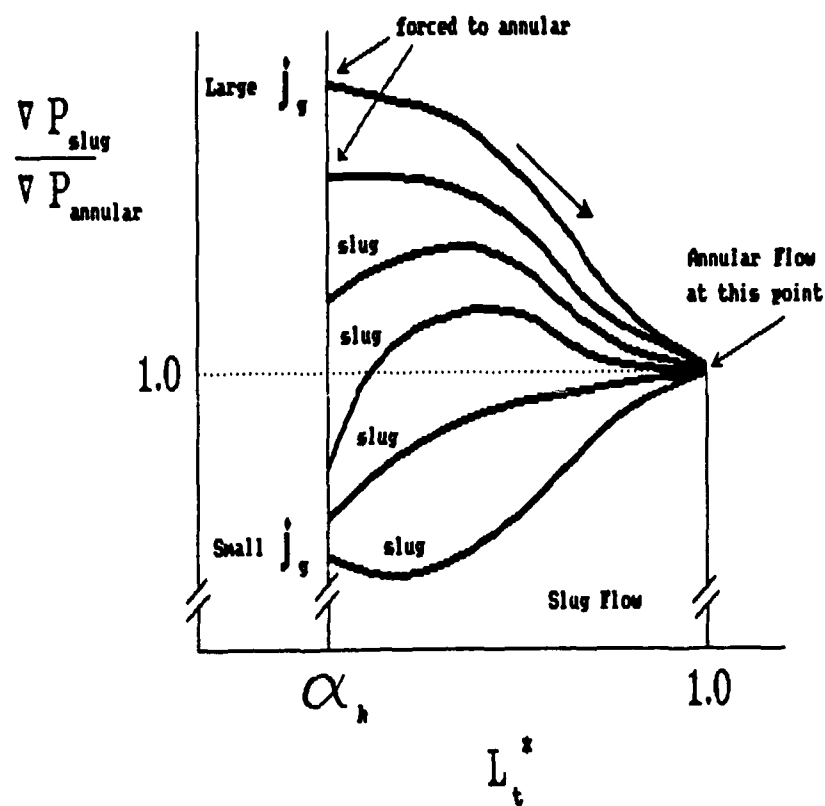
$\mathbf{j}_f$ fixed ; six typical curves of constant $\mathbf{j}_g$ shown.

α_h (homogeneous void fraction) increases with increasing $\mathbf{j}_g$;
is equal to minimum possible L_t^*.

L_t^* (unit Taylor bubble length) stabilises at local minimum
of $\dfrac{\nabla P_{slug}}{\nabla P_{annular}}$ if it exists ; otherwise, flow becomes annular.

84

Neither annular flow nor bubble flow, it will be found, offer less pressure gradient.[15]

In the <u>fourth</u> curve from the bottom in Figure 35, the favored L_t^* yields only a local pressure gradient minimum. However, it is hypothesized that the fluids remain "stuck" in slug flow. For L_t^* to increase towards annular flow requires the pressure gradient to temporarily increase through a local maximum. It is asserted that this pressure gradient rise prevents the flow from adjusting to annular flow and an ultimately lower pressure gradient.

The situation illustrated by the third and fourth curves is one which frequently occurs in the regions of slug flow near the annular or the churn boundary. These curves may help explain the tendency for slug flows to exhibit hysteresis. That is, once a slug flow forms, it sometimes persists, even when flow conditions are returned to those which had created annular flow. Such hysteresis could be caused by the situations these curves illustrate. Namely, a local **minimum** pressure gradient favors **slug flow**, but **the global minimum** pressure gradient favors **annular flow, or vice versa.** It is not hard to imagine that random pressure or flow fluctuations could "switch" the flow between these two flow regimes. Each regime would exist stably until a (possibly random) pressure or flow fluctuation caused a switch to the other stable regime.

Solution of the Detailed Slug Flow Model

By using the above assertions, L_t^* and therefore the detailed slug flow model can be solved. The Taylor bubble portion of the unit cell is treated as a local annular flow. These annular relationships are solved in conjunction with the unit cell continuity relationships, Equations 5-28 to 5-32. This permits the calculation of slug flow slip velocity, film thickness and velocity, as well as frictional pressure gradient. As discussed, the model suggests necessary criteria for the existence of stable Taylor bubbles. As also shown, it predicts a region of unstable slug, or churn, flow and indicates hysteresis near the annular boundary. The hysteresis suggests the slug-annular transition is a zone, not a sharp boundary line. Churn flow also suggests that the regime transition is a zone, not a sharp boundary.

---

[15] A perfectly "dry wall" drop flow will offer less pressure gradient, but such an occurrence in normal vapor-liquid flow is unrealistic except in conditions of critical heat flux.

5.10.3. Numerical technique to solve the slug flow model

A comment needs to be made about an assumption used for solving the general slug flow model. Figure 35, just discussed, shows a series of six curves. By examining solutions to many curves, it was discovered that only two specific points on any curve need be solved to deduce the qualitative shape of the rest of the curve. The first point solved is at the minimum possible L_t^* (i.e., the homogeneous void fraction). The second point to solve is one iteration step to the right of this minimum L_t^*. The calculated pressure gradient of these two points (above or below the annular pressure gradient) is noted. Then, it is noted whether the pressure gradient of the second point is greater or less than that for the first point. From these two observations, the general shape of the curve can be deduced, since all curves pass through 1.0 when L_t^* reaches its maximum. The general shape of the curve will match one of the six basic possibilities shown in Figure 35. This two-point solution technique greatly shortens numerical calculation times.

The remaining issue is choice of iteration step size between these first two points. If chosen too large, a local maximum may be missed. If too small, a local "maximum" may be virtually equal to the nearby minimum, such as in the second curve from the top in Figure 35. Either missing the maximum or allowing a tiny maximum to predict a barrier to the formation of annular flow would compromise the intent of the model.

The following choice of step size was adopted: the minimum L_t^* determines the first point; the second point is determined by increasing the minimum L_t^* by 0.5 percent. It is asserted that fluctuations in flow or pressure drop would cause Taylor bubbles to randomly lengthen this much. Thus, if a 0.5 percent lengthening by-passes a local pressure gradient maximum, it is considered that the maximum cannot prevent an increase in L_t^*. The assumed random increase in unit Taylor bubble length (L_t^*) can also be arbitrarily set at 1 percent or 2 percent. Part of the predicted slug-annular transition line will shift, but not much. It is, nevertheless, somewhat disturbing that the prediction is partly based on this arbitrary "coefficient of lengthening". However, at the present level of the analysis, it seems reasonable and somewhat intuitive to assume a random lengthening that is proportional to the unit Taylor bubble length. The proportion chosen is 0.5 percent.

This present choice of "coefficient of lengthening" should only be considered as part of the current implementation of the slug flow model. Future work may produce a better method to predict how L_t^* lengthens. For example, the lengthening may have to do with dynamic pressure or turbulent fluctuations at the nose of the Taylor bubble. Possibly the lengthening involves interfacial

86

shear along the Taylor bubble which causes it to be "extruded". The framework of the model should remain basically the same.

5.10.4. Maximum realistic unit Taylor bubble length in slug flow

The detailed slug flow model can be used to suggest further flow regime transition criteria. Suppose, for example, that the vapor flow rate is so large that the minimum possible L_t^* is 98 percent or more of the unit cell ($0.98 \leq L_t^* \leq 1.00$). Without any recourse to pressure gradient arguments, can a flow be called slug flow when only 2 percent of the total pipe length contains liquid bridges? If yes, then at still higher vapor flow could the regime be defined as slug when only 0.1 percent of the total pipe length has liquid bridges? When a liquid bridge carries neither a major portion of the liquid flow nor of its momentum, the regime is virtually annular. Some practical limit must exist for which liquid bridges can be ignored. In the present work it is proposed that for L_t^* above 98 percent, the flow must practically be defined as annular.

This last proposed condition uses only the results of the general slug flow continuity equation (Equation 5-28 and 5-29). No use is made of pressure gradient arguments. The reasoning is strictly one of an arbitrary limit on the minimum percentage length of liquid bridges.

In the future, a minimum bridge size might be better calculated by using a force balance. For example, turbulent vapor fluctuations or stagnation pressure at the nose of Taylor bubbles may balance against surface tension. Based on these forces, a resulting minimum stable bridge size might be calculated. This could lead to a minimum stable L_s^*, hence a limit to slug flow.

Assumptions and Techniques of the Detailed Slug Flow Model

The assumptions made for the detailed slug model are fewer than those made for the simplified slug model. To summarize, these assumptions are:

- Assume slug flow can be modeled by elongated Taylor bubbles with non-zero film velocity, alternating with liquid slugs.

  NOTE: The model does recognize a churn slug flow regime (i.e., not a Taylor bubble flow) with a predictable location. However, for churn flow, no predictable pressure drops, local velocities, etc., are calculated.

- Assume a pure liquid slug.

- Ignore pressure loss due to Taylor bubble end effects.

In addition, an averaging technique based on continuity arguments is used to calculate average values from the complexity that is slug flow:

- Unit slug length is the total of liquid slug lengths per unit pipe length; parallel calculation for Taylor bubbles.

5.11. Microgravity Flow Regime Map Using Detailed Slug Model

Using the detailed slug model, a more satisfactory vapor-liquid slug-annular transition has been calculated. This new transition overcomes the major objections to the simple slug-annular transition. (See Section 5.9.3.) Namely, the detailed slug model yields a flow regime transition that is not dependent upon a specific interfacial shear correlation. It works well with either a smooth or rough interface assumption. This is important because, with little pressure drop data available, no turbulent interfacial shear correlation has yet been proven for microgravity. The detailed model also predicts a region of churn flow which does not dominate the whole of the slug flow region.

Below, predictions from the detailed slug model are compared with flow regime data. These predictions match the data well and do not appear to be sensitive to the assumptions necessarily made.

5.11.1. Microgravity bubble-slug transition

The vapor-liquid bubble-slug transition was discussed in Section 5.7. It was calculated with the same technique used for the liquid simulations, and shown to fit the data quite well. Specifically, the principle of minimized pressure gradient was used with the homogeneous bubble model and the simple slug model. The homogeneous model for vapor-liquid bubble flow was exactly the same as that used for liquid-liquid flow. The simple slug model was used because slug flow along most of the bubble-slug boundary was assumed quiescent.

The bubble-slug transition line so calculated is used in the following flow regime maps, with no further analysis.

5.11.2. Slug-annular predictions of the detailed slug model

The detailed slug flow model was presented and discussed in Section 5.10. Figure 36 compares the detailed slug model prediction for the slug-annular transition to the microgravity air-water data. Prediction matches data quite well.
Note that there are three sections to the predicted slug-annular transition. These sections show how the slug-annular transition is successively controlled by different criteria.

The lowest part of the curve is a line of 98 percent homogeneous void fraction. This is the boundary for which the minimum L_t^* becomes so close to 1.0 that for practical purposes the flow is defined as annular.
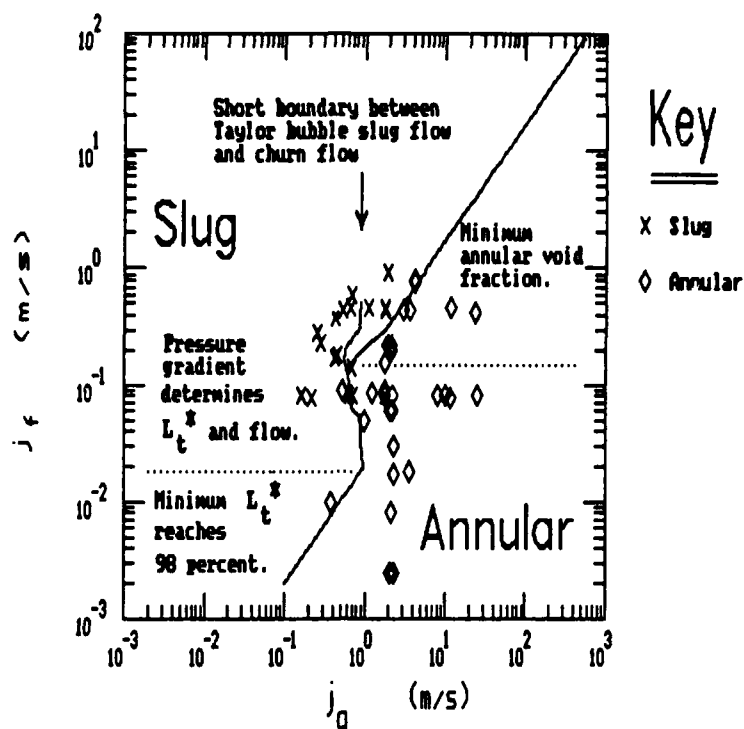
Figure 36. Detailed Slug Model with Smooth Interface -- Predictions for Microgravity Air / Water Slug-Annular Transition. 10 psia; 68° F ; Diameter = 3/8 inch (9.52 mm)
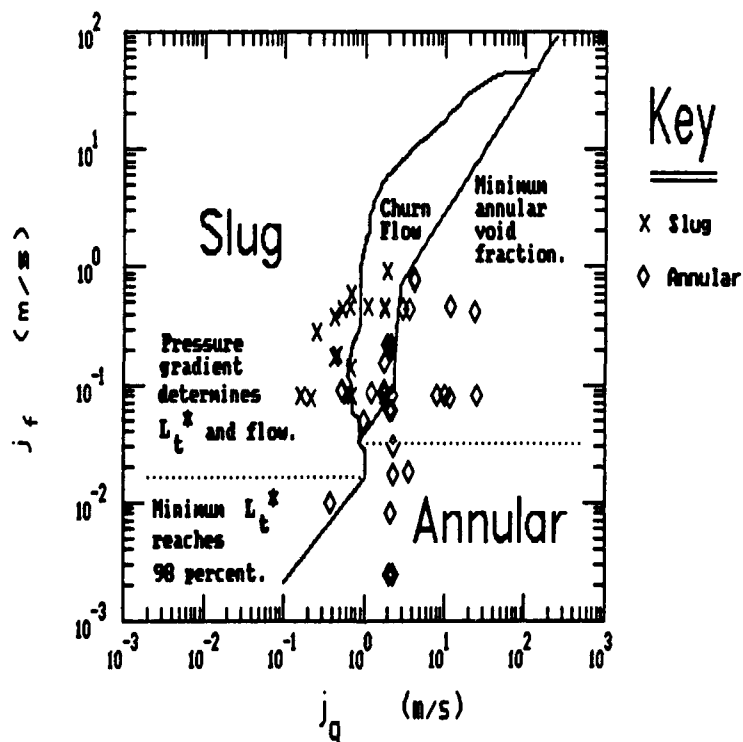
Figure 37. Detailed Slug Model with Rough Interface -- Predictions for Microgravity Air / Water Slug-Annular Transition. 10 psia ; 68° F ; Diameter = 3/8 inch (9.52 mm)

90

The middle part of the curve is the boundary where a minimized pressure gradient drives the flow to annular. To the left of this boundary, slug flow is favored by either a global or local minimum in slug pressure gradient. The short vertical extension of this same line forms the boundary between classic slug flow (i.e., long Taylor bubbles) and churn flow.

The upper part of the slug-annular transition is determined by a line of minimum annular void fraction. This particular boundary prediction was made using the smooth interface assumption. Therefore, 20 percent minimum annular void fraction used from Section 5.8.3.

When the rough interface assumption is made (Figure 37), the minimum void fraction line is the same as in Figure 31. Figure 37 shows that the rest of the detailed slug model transition line remains fundamentally the same -- but the void fraction line in this case controls most of the curve. However, the line generated by the detailed slug model shows that it is relatively insensitive to interfacial shear. (The smooth-interface line does not yet calculate well above the point reached in Figure 36. Therefore, the upper part of the two curves cannot be compared.)

Figure 37 illustrates another interesting point. The left-most transition line derives from the detailed slug flow model. Yet it basically parallels, then joins, a line of void fraction. Similarly, the bubble-slug transition of Figure 32 is derived from pressure gradient arguments, yet forms a transition boundary which parallels void fraction lines. The void fraction lines are easy to fit to the data. However, pressure gradient arguments may be more fundamental. With more research effort, it may be possible to predict all flow regime transitions more accurately on the basis of a minimized pressure gradient.

The smooth interface transition has been presently chosen because in photographs the annular film appeared more smooth than rough.

Figure 38 compares data to the flow regime map predicted using the detailed slug model for the slug-annular transition. The bubble-slug transition is the one previously discussed. This flow regime map matches the data quite well.

5.11.3. Bubble-annular transition

From the (nominal 3/8 inch pipe diameter) air-water data, it is unclear where the bubble-annular transition is located. The liquid-liquid data suggest that it is an extension of the bubble-slug transition. In the liquid-liquid simulations, the slug-annular transition line reaches up to the region of bubble flow. This arrangement forms a flow regime map with three clearly
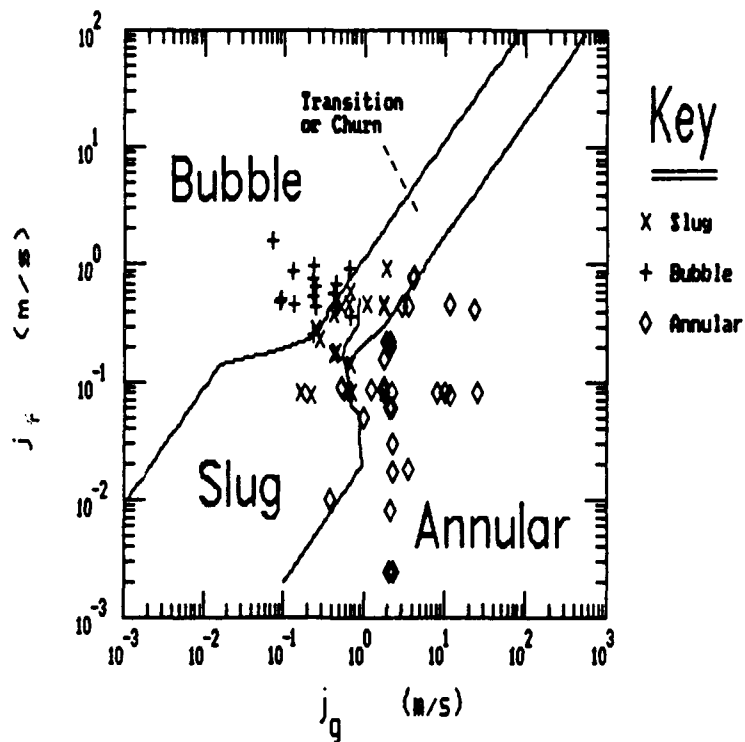
Figure 38. Predicted Microgravity Air/Water Flow Regime Transitions
Using Detailed Transition Model. 10 psia; 68° F; Diameter= 3/8 inch
(9.52 mm)

92

defined areas: bubble, slug, and annular. The analysis of liquid-liquid regime transitions duplicated these observations.

However, Figure 38 for air-water transitions, contains a narrow region titled "transition zone" between the bubble and annular regions. The predicted slug-annular line does not reach fully to the bubble region. Thus, the present implementation of the analysis, followed consistently, yields a narrow corridor between bubble and annular flow.

Qualitatively, however, it can be argued that this transition zone may be only an artifact of assumptions built into the analysis. Namely, the bubble-slug transition line is derived using the pressure gradient of Taylor bubble slug flow. However, the detailed slug model indicates a region of churn flow throughout the transition zone. Therefore, that part of the bubble-slug transition adjacent to churn flow is probably fallacious since it is not based on the (unknown, but likely higher) pressure gradient for churn flow.[16] A higher churn flow pressure gradient would move the upper part of the bubble-slug transition line to the right, perhaps to intersect with the slug-annular transition. The Taylor bubble slug flow model simply cannot be accurately extended to such high flow rates.

No criteria are presently suggested to quantitatively calculate how to shift this extension of the bubble-slug transition. Therefore, the analysis is presented as it stands, even though it contains an inconsistency in this region. Future work may develop an expression for microgravity churn flow pressure gradient which could be used in the framework proposed here. The bubble-slug transition line would then likely be shifted more to the right in the regions of high flux.

From the above argument, however, it is recommended that at high fluxes the **bubble-annular** transition line be calculated as an **extension of the slug-annular** transition. At this location on the map, the slug-annular transition is a line of constant void fraction. Therefore, the bubble-annular line is currently proposed as a line of constant void fraction. Figure 33 showed that this approach worked well for the one inch tube diameter air-water microgravity data. This is the only microgravity data presently known which includes the bubble-annular transition.

The bubble-annular transition should probably not be calculated as an extension of the bubble-slug transition line, even though

---

[16] Churn flow, with large, irregular shaped elliptical bubbles is hypothesized to have larger pressure loss due to end effects. However, with a slip velocity between pure annular and Taylor bubble slug flow, it might have an intermediate pressure drop.

this approach worked for the liquid-liquid regime transitions. The available microgravity air-water data do not support this choice. However, if corrected at high fluxes to account for the greater pressure drop of churn flow, this approach may work. It would then be totally consistent with the analysis of liquid-liquid flow regime transitions.

Engineering judgment must be used at present to connect the slug-annular transition to the bubble-slug transition. Otherwise, the recommendation is to leave an ambiguous "transition zone", as has been done here.

Whether this transition zone is actually bubble, annular, or churn flow is unknown. This high flux region of the map is beyond the data and stretches the limits of the zero entrainment assumption of the annular flow model. As noted, it also stretches the limits of the Taylor bubble slug model used to help calculate the bubble-slug transition line. Therefore, the predictions in this region must be taken as extrapolations. It is interesting that the two parallel lines agree as well as they do. However, it is not surprising that they leave an undefined "transition zone".

6. RECOMMENDED PRESSURE DROP CALCULATIONS

Analytically-based frictional pressure gradient equations, corrected to fit the liquid-liquid data, are presented here with little theoretical comment. Until microgravity pressure drop data are available, the same equations are recommended to predict vapor-liquid microgravity pressure gradients. However, without microgravity data to confirm them, it is difficult to so use these expressions with much confidence.

The theory behind these equations is covered in Section 5 (Analysis). More details of the derivation of the annular flow equations can be found in Appendix D. The method of correlating equations to data is discussed in Appendix E. Plots in Appendix E demonstrate that the equations presented here fit the liquid-liquid data quite well.

The recommended approaches, with comments, for both liquid-liquid flow regimes and microgravity vapor-liquid flow regimes follow:

1) Homogeneous pressure drop is used for bubble flow. Homogeneous viscosity is based on the analytically developed expression previously presented. These equations work very well for the laminar liquid-liquid data, although the expression for homogeneous viscosity is extrapolated to void fractions four times its theoretical 5 percent limit.[17] In the microgravity vapor-liquid case the extrapolation is a factor of eight, to 40 percent or more void fraction. This extrapolation is less likely to be successful for the turbulent vapor-liquid case, but is used nevertheless.

   However, despite these caveats, the homogeneous viscosity calculation has several advantages. First, other standard approaches were a significantly worse fit to the liquid-liquid data (see Appendix E). Second, the present choice

---

[17] With the present equi-density liquid-liquid systems there is a possible explanation why this homogeneous viscosity works, despite the theoretical void fraction limit. The 5% void fraction limit may derive from an assumption of non-interference among bubbles. An equi-density liquid-liquid flow with the continuous liquid being laminar seems to effectively prevent most interference between bubbles. Without knowing the derivation of the homogeneous viscosity equation, such thoughts are purely speculative. However, for the equi-density liquid-liquid data, the equation work_. And it works very well.

Caution is urged in assuming the equation to hold for a vapor-liquid microgravity bubble flow. Due to bubble wakes, turbulence will created in the continuous inviscid liquid. If these wakes are strong, it will not be valid to assume the bubbles move independently.

for homogeneous viscosity accounts for which fluid flows continuously and wets the tube wall. Other standard equations for homogeneous viscosity include no such effect. These equations incorrectly equate the homogeneous viscosity of drop and bubble flow at matching void fractions. Possibly they are designed more to permit mathematical continuity than to reflect physical reality. Mathematical continuity permits all flow regimes to be simplistically treated as a homogeneous flow. For this purpose, they may give a passable first order approximation of pressure drop. However, such an approach is not recommended for calculating the pressure drop of a flow known to be bubble (or conversely, drop).

2) A simplified slug model is used to predict slug flow pressure gradient. The predicted gradient is increased 21 percent to fit the liquid-liquid data. This factor can be considered to account for pressure drop due to end effects around Taylor bubbles. On the film around the Taylor bubble, the smooth interfacial assumption is used. Because it best fit the liquid-liquid data. Thus, shear along the film contributes very little to the pressure drop, except at high flow rates.

The detailed slug flow model offers in most cases very little or no improvement in pressure drop predictions[18]. Its strength is in predicting details of slug flow and the transition to annular flow. Without adequate microgravity pressure drop data, the complexity introduced by the detailed slug analysis seems unwarranted. The adjustment to account for end effects overrides subtleties of the more complex approach.

Of the methods presented here for calculating pressure drops, the one for slug flow has more assumptions than for the other two flow regimes. Without microgravity data, it is difficult to say whether the model under-predicts or over-predicts pressure drop. However, in the region of churn flow, the approach probably under-predicts pressure drop. The neat geometrical assumptions of a Taylor bubble

---

[18] This is because the simple slug model assumes L_t^* to be its minimum possible value. The detailed slug model confirms that this assumption is usually valid. C_1 also proves to be generally quite constant, between 1.0 and 2.0. Churn flow, for which there is no pressure drop calculation offered, is the only major exception. Subtle differences between the simple and the detailed slug model, such as interface velocity, have minimal impact on the calculation of pressure drop, except near the annular boundary.

slug model do not account for the turbulence and attendant pressure loss of churn flow.

3) An integral annular analysis is used to predict annular pressure drop, using a smooth interface assumption. The predicted smooth-interface pressure gradient is boosted by 17 percent to fit the liquid-liquid data.

   For microgravity flows, a smooth interface shear equation probably-under predicts pressure drop; the rough interface shear correlation sometimes used in the analysis of Section 5 probably over-predicts pressure drop. These two assertions come from qualitative assessment of photographs showing the interfacial roughness of microgravity annular flows. This problem is presently handled by assuming the same 17 percent correction factor for microgravity flows as used for the liquid-liquid flows. It will take real microgravity pressure drop data to prove whether or not this approach is valid.

Equations for bubble, slug, and annular flow are given below. The subscripts "1" and "2" are used to refer to the more viscous and the less viscous fluids, respectively. When applied to vapor-liquid flows, the "1" clearly corresponds to the liquid, "2" to the vapor.

In the following equations, these quantities are frequently used:

$$j_1 = \frac{Q_1}{A} \qquad (6\text{-}1)$$

$$j_2 = \frac{Q_2}{A} \qquad (6\text{-}2)$$

$$j = j_1 + j_2 \qquad (6\text{-}3)$$

6.1. Bubble Flow Pressure Gradient

Using the homogeneous assumption, calculating a mean density and a mean viscosity, bubble flow can be treated as a single phase flow:

$$- \frac{dP}{dz} = \frac{2 \, C_f \, \rho_m j^2}{D} \tag{6-4}$$

$$\alpha = \frac{j_2}{j} \tag{6-5}$$

$$\rho_m = \alpha \rho_2 + (1 - \alpha) \rho_1 \tag{6-6}$$

$$\mu_m = \mu_1 \left[1 + 2.5\alpha \frac{\mu_2 + 2/5 \, \mu_1}{\mu_2 + \mu_1} \right] \tag{6-7}$$

$$C_f = \frac{16}{Re} \quad \text{for laminar flow} \tag{6-8}$$

$$= \frac{0.046}{Re^{0.2}} \quad \text{for turbulent flow} \tag{6-9}$$

$$Re = \frac{\rho_m \, j \, D}{\mu_m} \tag{6-10}$$

6.2. Slug Flow Pressure Gradient

Using the unit cell concept and the simple slug model, slug flow pressure gradient can be calculated as the sum of the pressure drops in the unit slug length and the unit Taylor bubble length:

$$- \frac{dP}{dz} = F_s \left[\frac{2 \, C_w \, \rho_1 j^2 \left(1 - L_t^* \right)}{D} + \frac{2 \, C_i \, \rho_2 \tilde{v}_2^2 \, L_t^*}{d_o} \right] \qquad (6\text{-}11)$$

$$F_s = 1.21 \quad \text{from Appendix E} \qquad (6\text{-}12)$$

$$C_1 = 1.86 \quad \text{from Appendix E} \qquad (6\text{-}13)$$

$$\tilde{v}_2 = C_1 \, j \qquad (6\text{-}14)$$

$$d_o = \sqrt{\frac{1}{C_1}} \, D \qquad (6\text{-}15)$$

$$L_t^* = \frac{j_2}{j} \qquad (6\text{-}16)$$

$$Re_1 = \frac{D \, \rho_1 j}{\mu_1} \qquad (6\text{-}17)$$

$$Re_2 = \frac{d_o \, \rho_2 \, \tilde{v}_2}{\mu_2} \qquad (6\text{-}18)$$

$$\text{for} \quad \text{laminar liquid:} \quad C_w = \frac{16}{Re_1} \qquad (6\text{-}19)$$

$$\text{turbulent liquid:} \quad C_w = \frac{0.046}{Re_1^{0.2}} \qquad (6\text{-}20)$$

$$\text{for} \quad \text{laminar vapor:} \quad C_i = \frac{16}{Re_2} \qquad (6\text{-}21)$$

$$\text{turbulent vapor:} \quad C_i = \frac{0.046}{Re_2^{0.2}} \qquad (6\text{-}22)$$

The overall correction factor $F_s = 1.21$ can be considered to account for end effects around Taylor bubbles. This reasoning is applied to both the liquid simulations and microgravity vapor-liquid flows.

C_1 is the assumed constant slip ratio. In earth gravity vapor-liquid flows a good approximation is 1.2, as previously noted. However, to best match the pressure rise with vapor flow, $C_1 =$

99

1.86 was chosen (Appendix E). The higher slip ratio implies a higher Taylor bubble velocity than the usual $C_1 = 1.2$ choice.

For liquid-liquid flows, the higher implied Taylor bubble velocity is realistic for three reasons. First, the observed film thickness of oil around water Taylor bubbles was qualitatively thicker than for typical vapor-liquid flows. Less flow area means larger slip velocity. Second, the Taylor bubbles often contained many liquid drops. These increase Taylor bubble volume and thus velocity with respect to the liquid slugs. Third, the interface around the Taylor bubbles is not perfectly smooth. Mathematically boosting the slip velocity has a similar effect as increasing the unrealistically low smooth interface shear coefficient.[19]

However, the increase of C_1 to 1.86 may seem excessive and insupportable for vapor-liquid data. Droplet entrainment in Taylor bubbles is an artifact of the liquid simulations; microgravity vapor-liquid flows may or may not have thicker liquid films around Taylor bubbles. A rough liquid film during vapor turbulence, not accounted for in the smooth interface assumption, might cause the effective C_1 to increase. But would the value rise to 1.86? There is no data to answer the question. However, the question is only of importance at high vapor flow rates when the vapor contribution to pressure drop is not negligible. Therefore, the vapor-liquid flow regime predictions were run with both values of C_1. The higher value (1.86) works slightly better, but the lower value (1.2) gives adequate results, too.

For pressure gradient calculations, the 1.86 value may over-predict and therefore be more conservative. Since its influence is mostly at higher vapor fluxes, it may somewhat better predict the higher pressure losses of churn flow.

The approach detailed above is presently recommended to calculate slug flow pressure gradient. However, if microgravity data ultimately shows it to be an under-prediction, there is one correction which should be tried. A rough interface shear correlation such as Equation 5-24, could be introduced into the pressure gradient equations given above.

---

[19] An interfacial shear coefficient for a wavy interface was tried. The particular correlation used greatly over-predicted liquid-liquid slug pressure gradient at turbulent vapor flow rates.

6.3. Annular Flow Pressure Gradient

An integral annular analysis (detailed in Appendix D) was used to derive the following equations for annular pressure gradient. They are usually solved numerically.

$$-\frac{dP}{dz} = F_a \left[\frac{2C_i \, \rho_2 \left(\tilde{v}_2 - v_i \right)^2}{d_o} \right] = F_a \left[\frac{2C_w \, \rho_1 \tilde{v}_1^2}{D} \right] \qquad (6\text{-}23)$$

$\quad F_a = 1.17 \quad$ (annular correction factor from liquid-liquid experiments, see Appendix E.; may account for interfacial roughness.)

$$\tilde{v}_1 = \frac{j_1}{(1 - \alpha)} \qquad (6\text{-}24)$$

$$\tilde{v}_2 = \frac{j_2}{(1 - \alpha)} \qquad (6\text{-}25)$$

$$\alpha = \frac{d_o^2}{D^2} \qquad (6\text{-}26)$$

$$Re_1 = \frac{D \, (1 - \alpha) \, \rho_1 \tilde{v}_1}{\mu_1} = \frac{D \, \rho_1 \, j_1}{\mu_1} \qquad (6\text{-}27)$$

$$Re_2 = \frac{d_o \, \rho_2 \left(\tilde{v}_2 - v_i \right)}{\mu_2} \qquad (6\text{-}28)$$

for laminar "1": $\quad C_w = \frac{16}{Re_1} \qquad (6\text{-}29)$

$$v_i = 2 \, \tilde{v}_1 \qquad (6\text{-}30)$$

turbulent "1": $\quad C_w = \frac{0.046}{Re_1^{0.2}} \qquad (6\text{-}31)$

$$v_i = \frac{\frac{60}{49} \, j_1}{\left(1 - \sqrt{\alpha} \right) \left(1 + \frac{8}{7}\sqrt{\alpha} \right)} \qquad (6\text{-}32)$$

for laminar "2": $\quad C_i = \frac{16}{Re_2} \qquad (6\text{-}33)$

turbulent "2": $\quad C_i = \frac{0.046}{Re_2^{0.2}} \qquad (6\text{-}34)$

One numerical method for solving the equations above is, for any desired j_1 and j_2, to iterate on α until Equation 6-23 is satisfied. However, Appendix D gives exact solutions for j_2 given any j_1 and α. These solutions help speed the intermediate calculations of such iterations.

7. RECOMMENDED MICROGRAVITY HEAT TRANSFER CORRELATIONS

7.1. Pool Boiling in Reduced Gravity

As indicated in the literature review earlier, forced convection evaporation and condensation is envisioned to be the major mode of heat transfer in two-phase flow loops in spacecraft. Pool boiling will only be of importance in the case of pump failure, when the critical heat flux will be of concern.

Siegel [1967] summarized the pool boiling experiments of different authors and showed clearly the dependency on the gravity term (see Figure 39, from his work). In Figure 39, the ratio of the critical heat flux under reduced gravity conditions to the critical heat flux on earth is plotted as a function of the fraction of earth gravity.
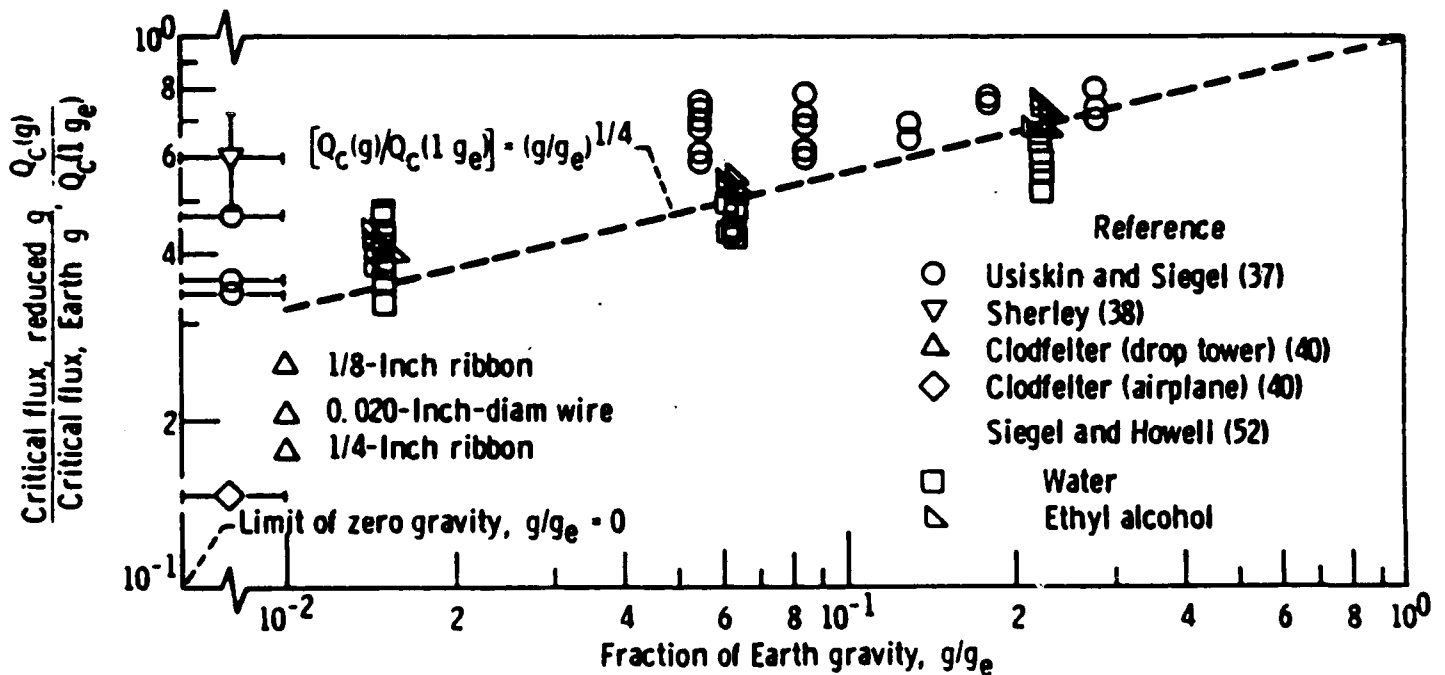
Figure 39. Effect of Gravity Reduction on the Critical Heat Flux in Pool Boiling from Siegel [1967].

7.2. Forced Convection Heat Transfer

It was mentioned earlier that forced convection heat transfer coefficients such as those developed by Chen [1963] and Gungor and Winterton [1986] should probably be valid for microgravity heat transfer if forced convection, rather than pool boiling, dominates. Chen evaluated the two-phase heat transfer coefficient h_{TP} as consisting of a sum of the nucleate boiling and the forced convection heat transfer coefficients, each modified with correction factors:

$$h_{TP} = S h_{NCB} + F h_c \qquad (7-1)$$

S is a suppression factor, which is a function of the two-phase Reynolds number:

$$Re = \frac{(1-x) GD}{\mu_f} \qquad (7-2)$$

S is less than 1, and decreases with increasing Reynolds number, indicating that nucleate boiling becomes unimportant with an increase in inertia. The relationship of S to Reynolds number is shown in Figure 40 below.
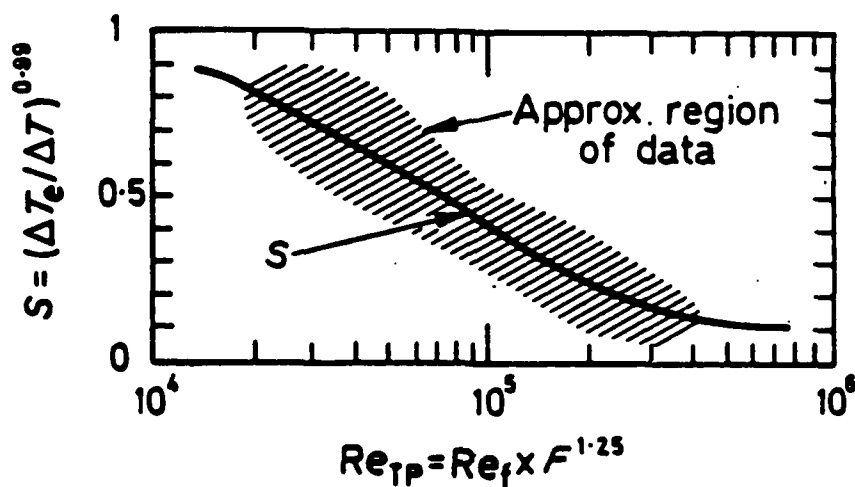
Figure 40. Suppression Factor S.

The heat transfer coefficient for nucleate boiling proposed by Chen (see Equation 7-3 below) does not contain the gravity term at all. However, as discussed in the literature review of Section 3, the gravity term is of major importance to reduced gravity nucleate boiling.

$$h_{NCB} = \frac{0.00122 \left(k_f^{0.079} c_{pf}^{0.49} \right)}{\sigma^{0.5} \mu_f^{0.29} \left(h_{fg} \rho_g \right)^{0.24}} \Delta T_{SAT}^{0.24} \Delta P_{SAT}^{0.75} \tag{7-3}$$

One could argue that this heat transfer coefficient should be multiplied by $(g/g_o)^{1/4}$ where g_o is the earth gravity constant. But this raises the question if Chen's empirical correlation scheme, based on earth gravity, can be extrapolated to microgravity conditions.

The convective term in Equation 7-1 is the so-called Dittus-Boelter equation:

$$h_c = 0.023 \ Re_f^{0.8} \ Pr_f^{0.4} \ \frac{k_f}{D} \tag{7-4}$$

The enhancement factor F, which is always greater than 1, is a function (see Figure 41) of the two-phase Martinelli parameter:

$$X_{tt} = \sqrt{\frac{\left(\frac{dP}{dz} \right)_f}{\left(\frac{dP}{dz} \right)_g}} = \left(\frac{1-x}{x} \right)^{0.9} \left(\frac{\rho_g}{\rho_f} \right)^{0.5} \left(\frac{\mu_f}{\mu_g} \right)^{0.1} \tag{7-5}$$
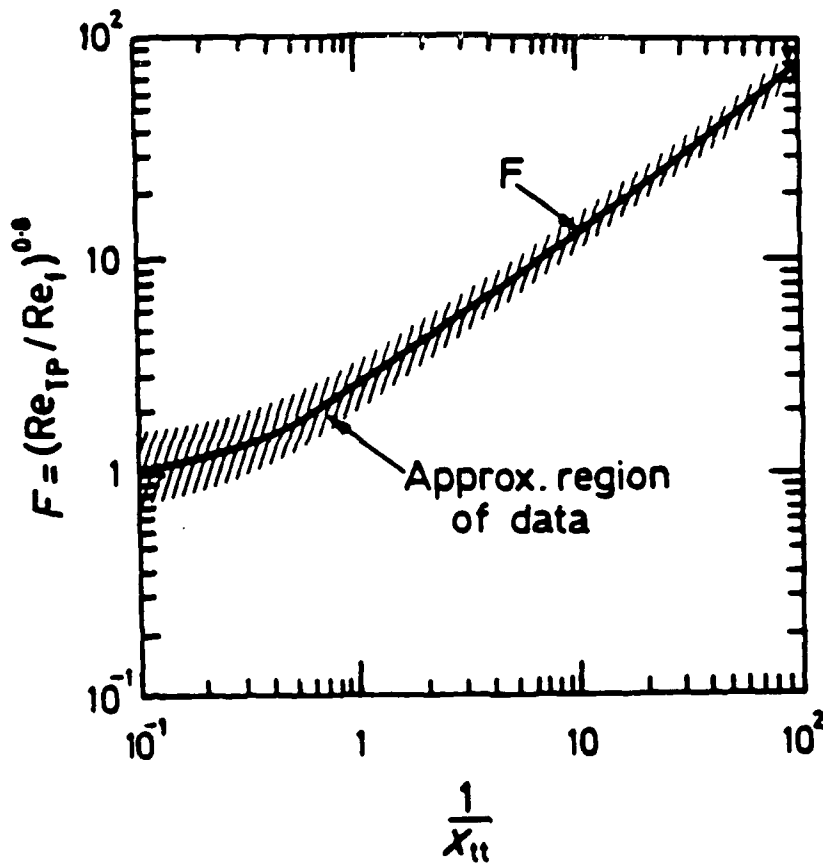
Figure 41.   The Enhancement Factor.

Twenty-three years later, Gungor and Winterton [1986] used the same concept as Chen and formulated the two-phase heat transfer coefficient as:

$$h_{TP} = E\, h_c + S'\, h_{pool} \qquad\qquad (7\text{-}6)$$

h_c is identical to Equation 7-4, but the heat transfer coefficient for pool boiling is formulated DIMENSIONALLY as:

$$h_{pool} = 55\; P_r^{0.12}\; (-\log P_r)^{-0.55}\; M^{-0.5} q''^{0.67} \qquad (7\text{-}7)$$

106

In Equation 7-7 above, h_{pool} has the units (W/m^2K), P_r is the dimensionless reduced pressure ratio, M is the molar mass, and q" is the heat flux (W/m^2).

The enhancement factor is formulated as follows:

$$E = 1 + 24000 \ Bo^{1.16} + \frac{1.37}{X_{tt}^{0.86}} \qquad (7-8)$$

where

$$Bo = \frac{q"}{(G \ h_{fg})} \qquad (7-9)$$

and X_{tt} is the Martinelli parameter according to Equation 7-5.

The suppression factor S' is

$$S' = \frac{1}{1 + (1.15 \cdot 10^{-6}) \ E^2 \ Re_f^{1.17}} \qquad (7-10)$$

This suppression factor is roughly inversely proportional to the Reynolds number. Again, the nucleate pool boiling heat transfer coefficient does not contain the gravity term and its validity for reduced gravity must be questioned.

The Gungor and Winterton correlation appears to predict saturated boiling data better than other correlations, based on much more data than Chen's correlation of many years earlier. Both correlations are similar in nature and are probably valid under microgravity conditions, despite the caveats noted, given sufficiently large Reynold's numbers.

The Chen correlation is well established and easier to calculate. The Gungor and Winterton correlation appears to be more accurate but requires re-iterative calculation to obtain the proper heat flux. In the absence of significant microgravity heat transfer data, either of these correlations is recommended to approximate microgravity forced convection heat transfer. Until improvements in predicting microgravity heat transfer are achieved, these will have to suffice for initial approximations.

7.3. Condensation Heat Transfer

Keshock et al. [1973] did one of the first experimental studies of heat transfer in microgravity and they compared their visual results with normal gravity condensation. Even though their paper does not include a wide range of flow rates in microgravity flow, it represents a first glimpse of two-phase condensing flow under such conditions.

From observations they concluded that the predominant flow patterns are annular, slug, and bubbly flow. In horizontal earth-bound condenser tubes, the flow behavior is often more complicated than in space because stratification effects can be of importance, especially at low mass fluxes. Whalley [1987] suggests that in the latter case essentially all the condensation will occur at the upper part of the tube, which is bare of liquid. In microgravity situations such stratification will not occur, thus simplifying the heat transfer evaluation. A uniform film thickness will be present around the circumference, but the condensation rate is impeded by thermal diffusivity through the liquid film.

Keshock et al. [1973] found from their preliminary experiments in normal gravity and microgravity no discernable difference in the tube length required for complete condensation. They concluded that in stratified flow, only part of the circumference is available for condensation. In microgravity the film allows less condensation per unit area, but allows condensation around the whole circumference. Thus, the average heat transfer rate in both cases is similar.

The above presumption allows the use of condensation heat transfer correlations presented by Collier [1972] and Whalley [1987].

For an annular film in a tube, the correlation from Soliman, Schuster, and Berenson [1968] should be applicable. For the local heat transfer coefficient they assumed:

$$h_f = \frac{0.036 \; c_{pf}^{0.65} k_f^{0.35} \; \rho_f^{0.5}}{\mu_f^{0.35}} \; \tau_w^{0.5} \tag{7-11}$$

The only disadvantage of this correlation is that is requires the knowledge of the shear stress at the outer edge of the laminar sublayer. This shear stress consists of two components, the interfacial shear stress and the momentum exchange in the vapor phase. More details can be found in the book by Collier.

Another approach was suggested by Whalley. The Reynolds number of the liquid in the film on the wall is:

$$Re = \frac{D\,(1-\alpha)\,\rho_f\,\tilde{v}_f}{\mu_f} = \frac{D\,j_f\,\rho_f}{\mu_f} = \frac{D\,G\,(1-x)}{\mu_f} \qquad (7\text{-}12)$$

If the same volumetric flow rate of liquid is occupying the whole pipe, the Reynolds number is identical. For both situations, the heat transfer should be of the form:

$$Nu = f(Re, Pr)$$

Because the Reynolds number and the Prandtl number are identical in the two cases, so should the Nusselt number. This Nusselt number is

$$Nu = \frac{h\,L}{k_f} \qquad (7\text{-}13)$$

where L is an appropriate length scale. In the case of the annular film this is the hydraulic diameter, $D(1-\alpha)$, which is for thin films approximately 4δ. For (single phase) liquid completely filling the tube, the length scale is simply D, the tube diameter. Thus, for the heat transfer coefficient in the film, h, and the heat transfer coefficient for the liquid only, h_f, the ratio

$$\frac{h}{h_f} = \frac{1}{1-\alpha} \doteq \frac{D}{4\delta} \qquad (7\text{-}14)$$

The single phase heat transfer coefficient h_f can be calculated from equation 7-4. Equation 7-14 just above shows that dividing this single phase coefficient by $(1-\alpha)$ yields the increased two-phase condensation heat transfer coefficient.

This very simple approach is probably preferable to other methods until more condensation heat transfer data are available at microgravity conditions.

7.4. Summary of Heat Transfer in Microgravity

Measurements of microgravity condensing or evaporative heat transfer were beyond the scope of this study. The study focused on adiabatic microgravity flow regimes. However, the observed flow regimes -- bubble, slug, and annular flow -- suggest that heat transfer correlations designed for the same flow regimes in earth-bound systems may be adequate for initial design of space-based designs. Nevertheless, the heat transfer correlations mentioned above can only be considered as recommendations for first order analyses of space-based two-phase systems. More data are needed before such calculations can be performed with confidence.

8. CONCLUSIONS AND RECOMMENDATIONS

Conclusions, covered in Section 8.1 below, summarize the analysis presented and attempt to put its results in perspective.

Recommendations, covered in Section 8.2 below, divide into two areas:

1) Tentative calculation methods suggested to predict microgravity flow regimes, pressure gradients, and heat transfer.

2) Unresolved issues needing further study -- summarized from recommendations within the report body.

8.1. Conclusions

The principle of minimized pressure gradient appears adequate to predict equi-density liquid-liquid flow regimes. For this purpose, its predictive successes seem reasonably well confirmed. The principle is also supported by liquid-liquid pressure drop data.

The same principle, minimization of pressure gradient, can be extended to help predict microgravity gas-liquid flow regimes. The principle can also be used to help solve a newly created analytical model of slug flow. This slug flow model can in turn be used in the prediction of the microgravity vapor-liquid slug-annular transition.

However, the gas-liquid flow regime transition analysis developed here is based on sparse gas-liquid microgravity data and on tenuous liquid-liquid simulation data. Therefore, the microgravity vapor-liquid flow regime map proposed here should be regarded as tentative.

Furthermore, the flow regime map recommended here is put forward with the understanding that a number of unresolved issues remain. Some of these unresolved issues are summarized in Section 8.2.2 below.

The model predicts three microgravity flow regimes: bubble, slug, and annular flow, with churn considered a subset of slug flow. The transitions between flow regimes are based on a hypothesized underlying principle: minimization of pressure gradient. The pressure gradient and flow regime data from the liquid-liquid simulations support the hypothesis. Unfortunately, there are essentially no known microgravity pressure drop data available to either support or refute the hypothesis of pressure gradient minimization. Nevertheless, this hypothesis can be used, in

111

conjunction with a newly proposed slug flow model and a void fraction limit, to predict flow regime transitions. The predictions do reasonably match the existing microgravity vapor-liquid _flow regime_ data.

The proposed flow regime map is influenced by diameter, viscosity, and flow rates. In its present implementation, it is uninfluenced by changes in surface tension. However, surface tension is not inherently excluded from the analysis. Recommendations below indicate several ways in which surface tension logically influences the analysis and should ultimately be introduced into the analysis.

The flow regime map suggested here agrees at least qualitatively with earth-gravity flow regime maps at high flow rates (see Figure 5). Specifically, the bubble-annular transition is, or basically parallels, lines of constant void fraction.

Maximum stable annular film thickness appears to be a more fundamental way to determine the slug-annular transition than using a single minimum stable annular void fraction for all diameters. Tube diameter seems to play a role secondary to absolute film thickness. From the data, first order calculations suggest that 2-3 mm is the maximum stable annular film thickness in 6 to 25.4 mm diameter tubes for air-water microgravity flows. A minimum annular void fraction for each pipe diameter can be calculated from this maximum thickness.

Several transition lines calculated by the minimized pressure gradient method also parallel or join with lines of constant void fraction (e.g., the bubble-slug line of Figure 38; the slug-annular pressure gradient line of Figure 37). Pressure gradient considerations may prove more fundamental than basing transition lines directly on lines of void fraction. To that end, the analytical framework developed here leaves much room for modification and improvement.

8.2. Recommendations

8.2.1. Best tentative methods to calculate microgravity flow regimes, heat transfer, and pressure gradient

Should it be necessary to predict microgravity flow regimes, the recommendation is to follow the methods of the analysis detailed in Section 5. They are summarized below:

The bubble-slug transition line is quite straightforward. It is based completely on the principle of a minimized pressure gradient.

112

For quick calculation of the slug-annular transition, a minimum annular void fraction line may be used. This line should be calculated, as detailed in Section 5, using the given rough interface shear correlation. This line should be a void fraction of 30 percent for small diameter tubes (approx 9 mm) and 60 percent for larger diameters (approx 25 mm). Engineering judgment must be used for geometries significantly outside this range.

Basing minimum annular void fraction on a maximum film thickness is probably the best approach. The maximum stable annular film thickness, suggested by data, appears to be 2-3 mm in 6-25 mm diameters with air-water flows.

The preferred alternative for the slug-annular transition is to use the detailed slug flow model, which incorporates the principle of a minimized pressure gradient. This method requires more calculation. It predicts a churn flow zone and a region of hysteresis on the slug-annular boundary. At high fluxes, the transition line is hypothesized as a line of minimum possible annular void fraction (20 percent when using the smooth interfacial shear assumption; 30 percent when using the rough interfacial shear assumption). Compared to the quick calculation method above, its predictions are less sensitive to choice of the interfacial shear expression. For these reasons, it is the preferred method for calculating the slug-annular transition.

The bubble-annular transition can be taken as a "transition zone" between the two previous transitions at high fluxes. Alternatively, it can be taken as the extension of the slug-annular transition. See Section 5 for details. Either choice agrees at least qualitatively with earth-gravity flow regime maps in the high flux region. That is, the bubble-annular transition is, or basically parallels, lines of constant void fraction.

Given a flow regime prediction, recommendations for calculating microgravity pressure drop are given in Section 6. The pressure drop equations are either purely analytical or strongly analytically-based. These are the same equations which should be used to predict flow regime transitions via the minimization of pressure drop principle.

Measurement of heat transfer was not within the scope of this work. However, from basic physical understanding, some tentative recommendations are made for the first order analysis of microgravity vapor-liquid boiling and condensing heat transfer. These heat transfer recommendations are made in Section 7. Extensive heat transfer measurements in microgravity conditions are needed before substantial confidence can be put in such predictions.

8.2.2. Areas needing further study

The study of microgravity flow regimes is in its early stages. More experiments and analysis are needed to confirm, improve, or refute the predictive methods proposed here.

Throughout this report, a number of areas have been noted where further study could be fruitful. These are summarized below:

Foremost, more microgravity flow regime data are needed. More fluids and more tube diameters need to be explored. Adiabatic experiments are recommended before introducing the added complexity of heat transfer. Pressure drop data appear to be especially important (see next point).

Microgravity gas-liquid or vapor-liquid pressure drop data, correlated with flow regime, are needed. These would either verify or refute the hypothesized principle that microgravity flow adjusts primarily to the regime which minimizes pressure gradient. These data are also needed simply to help develop (preferably analytical) expressions to accurately predict microgravity pressure drop. Data for slug and churn flow pressure gradients are especially important.

Detailed data regarding microgravity slug flow could support or oppose the detailed slug flow model proposed here. Mechanisms regarding lengthening of Taylor bubbles, hysteresis, and churn flow have been hypothesized. Experiments could determine whether or not the slug model is as useful as it appears.

Information on microgravity interfacial shear forces, interfacial waviness, and maximum annular film thickness is needed. The relationship of these factors to surface tension needs exploration. This information would either improve or supercede the present flow regime transition analysis.

The wave duct experiments of Appendices B and C might be continued and extended. They address some of the issues of the point above.

Earth gravity flow regimes should be better explored at high flow rates. At high flows, earth gravity and microgravity flow regimes should logically approach one another, since in earth flows gravity becomes a secondary force. It is also expected that better earth gravity flow regime maps, vertical and horizontal, should all approach each other at high flow rates.

The minimization of pressure gradient criterion may, combined with other criteria, help predict earth gravity flow regime transitions. The concept is worth pursuing. With gravity included, the analysis would be more complex than that offered here. However, the idea is intuitively appealing.

114

REFERENCES

Abdollahian, D.; Levy, S.; 1985
"A Two-Phase Flow and Heat Transfer Model for Zero Gravity"
Air Force Wright Aeronautical Laboratories (AFWAL) TR-85-3014,
May 1985

Andritos, N.; Hanratty, T. J.; 1987
"Interfacial Instabilities for Horizontal Gas-Liquid Flows in
 Pipelines"
International Journal of Multiphase Flow, 13, n5, 583-603 (1987)

Baker, O.; 1954
"Design of Pipe Lines for Simultaneous Flow of Oil and Gas"
Oil and Gas Journal 53, 12, 185-195

Bar-Cohen, A.; Ruder, Z.; Griffith, P.; 1986
"Development and Boundaries for Circumferential Isothermality in
 Horizontal Boiler Tubes"
International Journal of Multiphase Flow 12, 1, 63-77

Chen, J. C.; 1963
"A Correlation for Boiling Heat Transfer to Saturated Fluids in
 Convective Flow"
ASME-63-HT-34

Cochran, T. H. et al.; 1970
"Forced Convection Boiling Near Inception in Zero Gravity"
NASA TN D-5612, January 1970

Collier, J. G.; 1972
Convective Boiling and Condensation
McGraw-Hill, New York

Dukler, A. E.; Fabre, J. A.; Quillen, J. B.; Vernon, R.; 1987
"Gas-Liquid Flow at Microgravity Conditions: Flow Patterns and
 Their Transitions"
International Symposium on Thermal Problems in Space-Based
Systems, HTD-v.83 (1987)

Dzenitis, J.; 1988
"Modelling of Micro-Gravity Two-Phase Flow Regimes"
M.S. Thesis, Thayer School of Engineering, Dartmouth College,
Hanover, New Hampshire (1988)

Feldmanis, C. J.; 1966
"Pressure Drop and Temperature Changes in Closed Loop Convection
 Boiling and Condensing Processes Under Zero-Gravity Conditions"
Institute of Environmental Sciences, Annual Technical Meeting
Proceedings

Gungor, K. E.; Winterton, R. H. S.; 1986
"A General Correlation for Flow Boiling in Tubes and Annuli"
International Journal Heat Mass Transfer 29, 3, 351-358

Heppner, D. B.; King, C. D.; Littles, J. W.; 1975
"Zero-G Experiments in Two-Phase FLuid Flow Regimes"
ASME paper 75-ENAs-24 (1975)

Hewitt, G. F.; 1969
"Disturbance Waves in Annular Two-Phase Flow"
Proc. Inst. Mech Eng, 184, 142 (1969-1970)

Hill, D.; Downing, R. S.; Rogers, D.; Teske, D.; Niggerman,
R.; 1987
"A Study of Two-Phase Flow in a Reduced Gravity Environment"
Final Report Under Contract No. NAS9-17195 (1987)

Ishii, M.; 1982
"Wave Phenomena and Two-Phase Flow Instabilities"
Handbook of Multiphase Systems, G. Hestroni, ed., New York:
McGraw-Hill, 1982

Johnston, A. J.; 1984
"An Investigation into the Interfacial Shear Stress Contribution
 in Two-Phase Stratified Flow"
International Journal of Multiphase Flow, 10, n3, 371-383 (1984)

Karri, S. B. Reddy; 1988
"Experimental Study of Simulated Micro-Gravity Vapor-Liquid Flow
 Regimes"
Ph.D. Thesis, University of New Hampshire, Durham, NH (1988)

Keshock, E. G.; Spencer, G.; French, B. L.; 1973
"A Photographic Study of Flow Condensation in 1-G and Zero-
Gravity Environments"
Paper from the Fifth International Heat Transfer Conference in
Tokyo, Japan, September 3-7, 1973

Kordyban, E.; 1977
"Some Characteristics of High Waves in Closed Channels
 Approaching Kelvin-Helmholtz Instability"
ASME J. Fluids Eng., 99, 339-346 (1977)

Lee, Doojeong; 1987
"Flow Regime Analysis for Condensing Two-Phase Flow in a
 Microgravity Environment"
paper prior to Ph.D. Thesis, Nuclear Engineering Dept.,
Texas A&M University, College Station, Texas (1987)

Lin, P. Y.; Hanratty, T. J.; 1986
"Prediction of the Initiation of Slugs with Linear Stability Theory"
International Journal of Multiphase Flow, 12, n1, 79-98 (1986)

Lovell, T. W.; 1985
"Liquid-Vapor Flow Regime Transitions for Use in Design of Heat Transfer Loops in Spacecraft"
Air Force Wright Aeronautical Laboratories (AFWAL) TR-85-3021

Lyon, D. N. et al.; 1965
"Peak Nucleate Boiling FLuxes for Liquid Oxygen on a Flat Horizontal Platinum Surface at Buoyancies Corresponding to Accelerations Between -0.03 and 1g"
AIChE Journal 11, 5, 773-780, September 1965

Merte, H., Jr.; Clark, J. A.; 1964
"Boiling Heat Transfer with Cryogenic Fluids at Standard, Fractional, and Near-Zero Gravity"
Journal of Heat Transfer 86, 351

Milne-Thomson, L. M.; 1950
Theoretical Hydrodynamics, 2nd ed. New York: MacMillan Co., 1950

Quandt, E.; 1965
"Analysis of Gas-Liquid Flow Patterns"
Chemical Engineering Progress Symposium Series, 61, n57, 128-135

Sherley, E. J.; 1963
"Nucleate Boiling Heat Transfer Data at Standard and Zero Gravity"
Advances in Cryogenic Engineering 9, 8, 945, Plenum, New York

Siegel, R.; Keshock, E. G.; 1964
"Effects of Reduced Gravity on Nucleate Boiling Under Normal and Reduced Gravity Conditions"
AIChE Journal 10, 4, 509-516

Siegel, R.; 1967
"Effects of Reduced Gravity on Heat Transfer"
Advances in Heat Transfer, Academic Press, NY, London 4, 143-228

Soliman, M.; Schuster, J. R.; Berenson, P. J.; 1968
"A General Heat Transfer Correlation for Annular Flow Condensation"
Journal Heat Transfer, 5, 267-276

Taitel, Y.; Barnea, D.; Dukler, A. E.; 1980
"Modeling Flow Pattern Transitions for Steady Upward Gas-Liquid Flow in Vertical Tubes"
AIChE Journal, 26, 345-354 (1980)

Taitel, Y.; Dukler, A. E.; 1976
"A Model for Predicting Flow Regime Transitions in Horizontal and Near Horizontal Gas-Liquid Flow"
AIChE Journal, 22, 47-55 (1976)

Wallis, G. B.; 1969
One-Dimensional Two-Phase FLow
McGraw Hill, New York, 1969

Weisman, J.; Duncan, D.; Gibson, J.; Crawford, T.; 1979
"Effects of Fluid Properties and Pipe Diameter on Two-Phase FLow Patterns in Horizontal Lines"
International Journal of Multiphase Flow, 5, 437-462 (1979)

Weisman, J.; Kang, S. Y.; 1981
"Flow Pattern Transitions in Vertical and Upwardly Inclined Lines"
International Journal of Multiphase Flow, 7, 271-291 (1981)

Whalley, P. B.;; 1987
Boiling, Condensation, and Gas-Liquid Flow
Clarendon Press, Oxford, 1987

APPENDIX A

Data Report for Liquid-Liquid Simulation Experiments

V. K.   Mathur

S. B.   Reddy Karri

J.   O'Hearn

Department of Chemical Engineering
University of New Hampshire
Durham, New Hampshire 03824

TABLE OF CONTENTS

EXPERIMENTAL SET-UP AND PROCEDURE

The experimental set-up to study the simulated micro-g
liquid-vapor flow regime transitions is shown in Figures A-1-a and
A-1-b. It consists of 6.4 m (21 feet) of 0.0254 m (1 inch) ID pyrex
glass tube with two entrance ports for the introduction of two
immiscible liquids. For the reduced diameter work , diameters were
reduced to 0.0127 m and 0.008 m with the setup the same as in the one
inch I.D. case. Hot and cold water lines are run to a storage tank
(Feed 1) to allow for maintenance of a constant temperature water
supply. Water is pumped from the constant temperature storage tank
while the flow is controlled by hand valves and measured with various
rotameters of the appropriate range (total range covered: 0.241 to 210
gph).

Various oils are used as the second liquid. The second liquid
which is simulating the "liquid" phase in micro-g, is pumped from a 55
gallon drum (Feed 2) placed on its side on a weighing scale. Flow is
controlled by hand valves and measured with rotameters of appropriate
range. The temperature of the second liquid is kept constant at 25 $\pm$
$1^{\circ}C$ by a combination of two methods. The 55 gallon drum is wrapped
with a resistance tape heater which is turned on prior to conducting
experiments if the temperature is below $25^{\circ}C$. It is observed that the
viscous liquid heats up over a period of time, particularly at the low
flow rates, due to continuous recirculation through the pump (heat due
to viscous dissipation). For such cases, a countercurrent heat
exchanger is installed in the bypass line to cool the viscous liquid
and return it to the 55 gallon drum at the desired temperature of
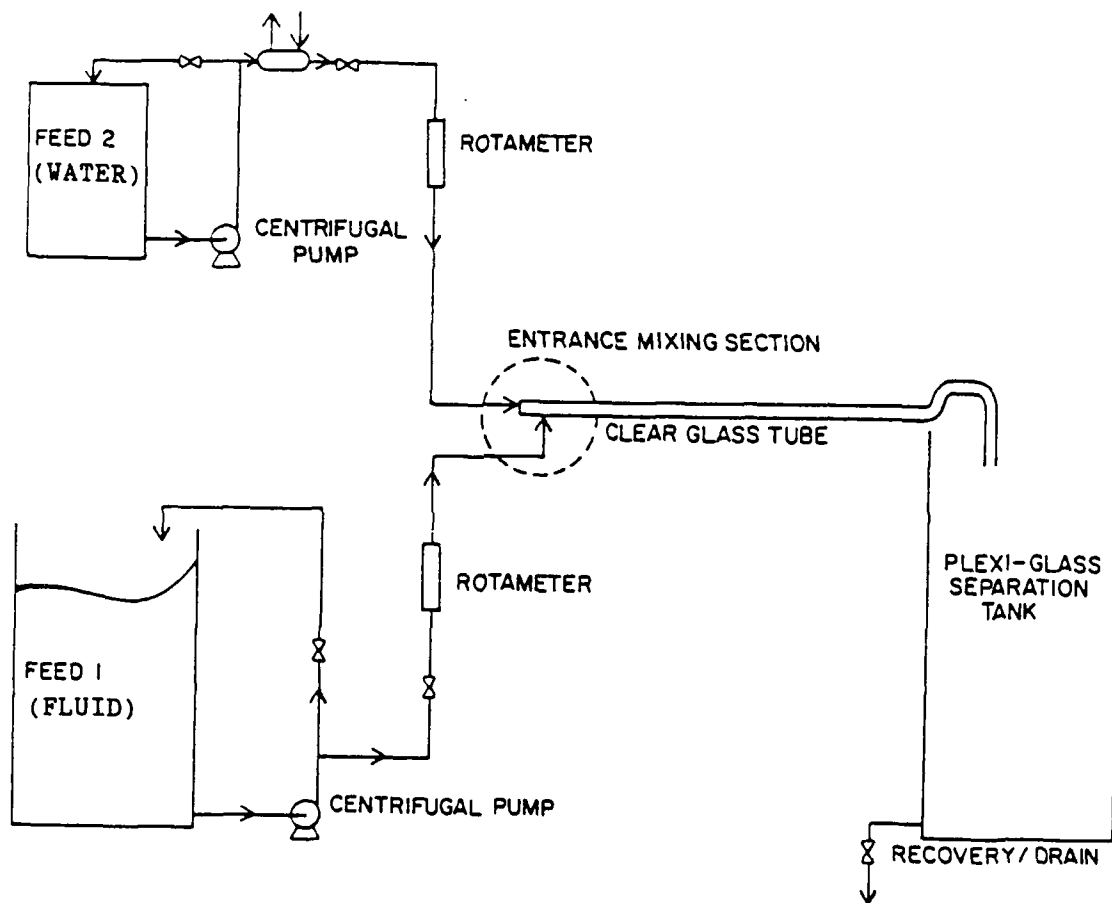
Figure A-1-a. Two Phase Flow Experimental Set-Up
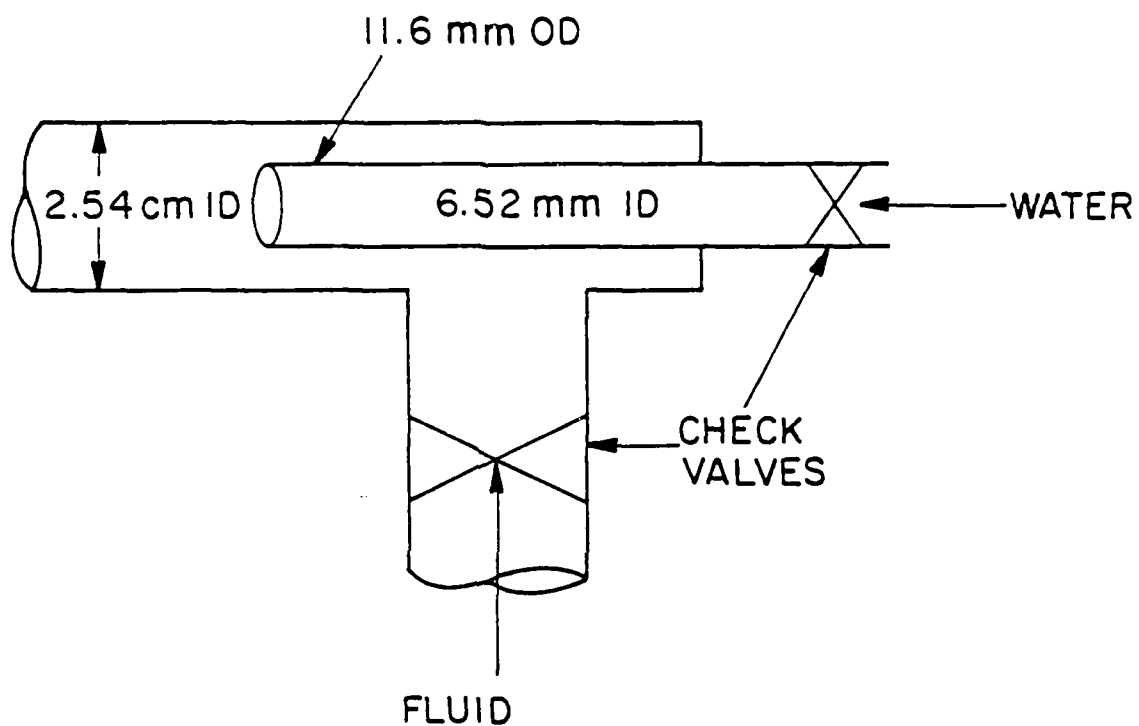
Figure A-1-b.   Annular-Type Nozzle Configuration

For Reduced Diameter Work:

    Pipe I.D.   = 12.7 mm
    Nozzle I.D. = 3.20 mm

    Pipe I.D.   = 8.0 mm
    Nozzle I.D. = 2.38 mm

$25^{\circ}C$. The temperature of the viscous liquid passing through the bypass line can be monitored at all times and the flow rate of the heat exchanger's cold side fluid (water) is adjusted continually to maintain "liquid" phase temperature at $25 \pm 1^{\circ}C$ throughout each experimental run. Two rotameters are installed in parallel for each liquid in order to cover the full range of flow rates. In addition, two manometers, one filled with carbon tetrachloride and the other filled with mercury, are placed in parallel to measure pressure drop across the two pressure taps located at each end of the glass tube. The connecting tubes are filled with water.

Visualization Section

The flow behavior/pattern is observed in a visualization section located approximately 75 diameters downstream of the entrance region to ensure a fully developed flow. Weisman et al. (1979) have found 60 diameters to be sufficient to attain fully developed flow over the full velocity range for a 0.0254 m I.D. horizontal system. In this study, it is found that the flow is fully developed at about 75 diameters downstream. This visualization section is fitted with a rectangular duct of plexi-glass filled with water. This arrangement reduces the optical distortions which are observed through the pyrex glass tube during the flow of the two immiscible liquids. The flow regimes/patterns are recorded on videotapes to allow for more in-depth off-line analysis (e.g., using slow motion and stop action) and to facilitate discussion with other researchers.

Separation Tank

The two immiscible liquids, after passing through the tube, discharge into a separation tank. Since the two liquids are of equal density, they form dispersions and therefore do not stratify. A small amount of sodium chloride (regular salt) is added to this tank and mixed thoroughly to increase the density of water slightly above its normal value. The solubility of sodium chloride in the more viscous oily liquids is found to be negligible. After allowing approximately 12 hours for maximum recovery, water separates into a distinct layer visible through the side of the collection tank. The water is then discharged into the drain and the top layer of viscous liquid is pumped off for recovery. The viscous liquid is heated to 120°C to evaporate off any water which may be present and to break the emulsion which sometimes forms at the higher flow rates. After cooling the liquid, the viscosity, specific gravi'y, and interfacial tension are measured prior to returning the recovered liquid to the 55 gallon drum for reuse. By this arrangement, approximately 90% of the viscous liquid is recovered. This is a time-consuming operation, requiring approximately twelve hours to recover 30 gallons of the liquid, enough to complete one experimental run.

Measurement of Physical Properties

In simulating micro-g vapor-liquid flow, the physical properties of the two liquids of equal density need to be considered carefully to have similitude between real and simulating systems. The physical properties important to the analysis are : density, viscosity, and

interfacial tension. These properties of the liquids used in the simulation experiments are listed in Table A-1. The measurement techniques for these properties are discussed as follows:

Density - The density of the liquids is measured using a specific gravity bottle in a temperature controlled environment.

Viscosity - A spindle-type viscometer supplied by Brookfield Laboratories, MA is used in conjunction with an eight gram sample adaptor. The adaptor is provided with a water jacket, connected to a hot bath to maintain the sample at a desired temperature.

Interfacial Tension - Typically, devices to measure interfacial tension use a force balance involving density difference. With equi-density liquids such techniques fail since the density difference is virtually zero. Therefore, a new method has been developed to measure the interfacial tension. The basic principle and the details of the apparatus and procedure are presented in the following section.

Table A-1. Physical Properties of Equi-Density Fluid Systems

System		Density kg/m3 (25°C)	Viscosity cP	Interfacial Tension (N/m)x10³
Fluid #1	PPG-2000	1003	300	~ 5
Fluid #2	Heavy Mineral Oil and Carbon Tetrachloride	998	~31	~32
Fluid #3	Dow Corning Fluid and Carbon Tetrachloride	998	~35	~47
Fluid #4	Same as Fluid #3 with Surfactant (Triton X-100)	998	~35	~ 5
Fluid #5	Kerosene and Carbon Tetrachloride	998	1.3	~38

Properties of Air-Water system : @ 25°C
μ_1/μ_g = 45
σ = 0.072 N/m

Properties of Freon-11 : @ 25°C
μ_1/μ_g = 41
σ = 0.018 N/m

Properties of Freon-12 : @25°C
μ_1/μ_g = 17
σ = 0.0085 N/m

MEASUREMENT OF INTERFACIAL TENSION OF
IMMISCIBLE LIQUIDS OF EQUAL DENSITY

The measurement of interfacial tension in equi-density liquid systems is complicated by the absence of a density difference. The equations used in the traditional interfacial tension measurement techniques such as capillary height method (Reynolds, 1921), ring method (Zuidema and Waters, 1941), and drop weight method (Harkins and Humphrey, 1916), contain a density difference term and, therefore, become invalid as the density difference approaches zero. In short, since two equally dense liquids forming an interface represent a relatively buoyancy free situation, these classical measurement techniques cannot be used, as they use the resultant gravity force at the interface giving rise to a density difference term in the final expression.

A new approach which was originally developed by Bartell and Miller (1928) to measure the interfacial tension between two liquids of equal density is used in our experiments. They used this method to measure the interfacial tension of dark liquids with water since they were unable to observe a falling drop in the dark liquid as required with the drop weight method, or to delineate the meniscus once the capillary was wetted with the dark liquid as in the capillary rise method. (Nomenclature is on page A-53.)

THEORY

A number of textbooks have discussed various methods which have been used for interfacial tension measurement. The most commonly used

techniques are capillary rise, drop weight, and ring method. However, these traditional interfacial tension measurement techniques cannot be used for systems of equal density liquids. Some of the interfacial tension measurement techniques and their analysis are briefly discussed below.

Capillary Rise Method: The capillary rise method has been used with several modifications by Reynolds (1921) and others. When the two liquids are in equilibrium inside a capillary, the interfacial and buoyancy forces can be equated to give an expression for interfacial tension, σ_{ab}:

$$\sigma_{ab} = 1/2 \; rhg(\rho_a - \rho_b) \tag{1}$$

where r = capillary radius, h = total height of liquid rise in the capillary, ρ = density of liquid, and subscripts a and b refer to liquid 'a' and liquid 'b', respectively.

Drop Weight Method: The drop weight method described by Harkins and Humphrey (1916), uses the size of a drop of liquid 'a' suspended in a liquid 'b' before falling (as opposed to height of liquid rise in the capillary rise method) as a measure of interfacial tension. A force balance on the drop leads to the correlation:

$$\sigma_{ab} = [V(\rho_a - \rho_b)g/r]F \tag{2}$$

where V = volume of the suspended drop at the point of breakaway, and F = correction factor, used since actual drop that falls is only a fraction of the drop that forms; this is a function of density for which standard tables are available.

Both the capillary rise and the drop weight methods require a $(\rho_a - \rho_b)$ term for calculation of σ_{ab} and, therefore, are not valid for determining interfacial tension between two liquids of equal

density. The same reasoning applies to ring-method (Zuidema and Waters, 1941) and it can not be used for measuring interfacial tension of equal density liquids. In short, since two equally dense liquids forming an interface represent a relatively gravity free situation, these classical measurement techniques cannot be used, as they use the resultant gravity force at the interface giving rise to a density difference term in the final expression.

Principle of the new method: The simple device shown in Figure A-2 is based on the capillary rise principle (Karri and Mathur, 1988). The apparatus consists of two cups, A and B, connected by a U-shaped tube, one leg of which is a capillary tube. Liquid 'b' is added to the cup B until it reaches the end of the U-tube at the bottom of cup A. Liquid 'a' is, then, added slowly from a burette to cup A, so that liquid 'b' is forced back until the liquid meniscus enters the lower end of the capillary and finally stabilizes at some reference point 'C'. The heights h_a and h_b of liquid 'a' and liquid 'b', respectively, above this reference point or meniscus, are measured using a cathetometer. The forces acting on the meniscus are:

gravity force :
$$F_g = \pi r^2 [\rho_a h_a - \rho_b h_b] g \qquad [3]$$
where r = capillary radius, and ρ the corresponding densities

(F_g is acting in the downward direction)

vertical force due to the interfacial tension :
$$F_{int} = 2\pi r \sigma_{ab} \qquad [4]$$
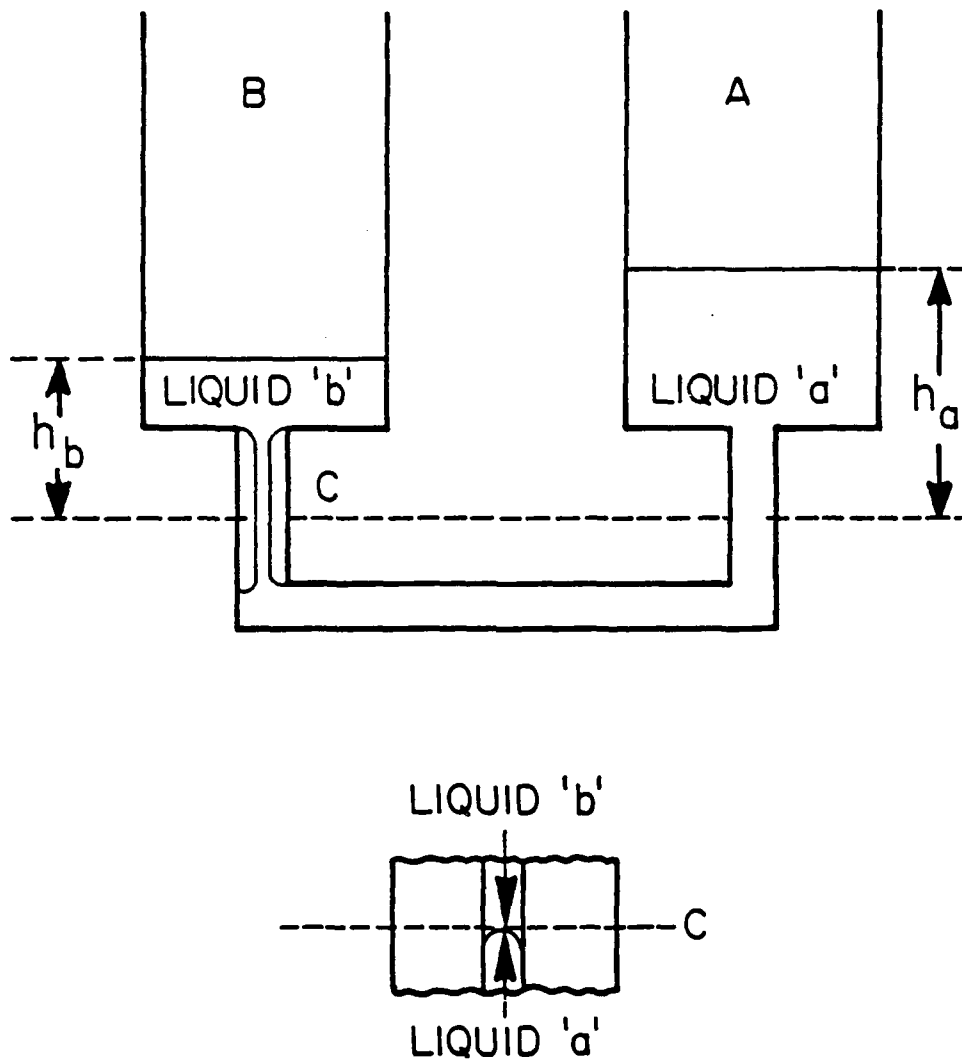
Figure A-2. Apparatus For Interfacial Tension Measurement
of Equal Density Fluids

Equating equations 3 and 4 for mechanical equilibrium-condition at the meniscus, one obtains:

$$\sigma_{ab} = 1/2 \ gr \ [\rho_a h_a - \rho_b h_b] \qquad [5]$$

It is noteworthy that the term $(\rho_a h_a - \rho_b h_b)$, which contains the difference between the products of corresponding density and height, does not approach zero even for equal density liquids. This method is general and therefore can be used to measure the interfacial tension of any combination of two immiscible liquids irrespective of their densities.

APPARATUS AND MEASUREMENT

The apparatus as shown in Figure A-2, is constructed with pyrex-glass. The two cups, A and B, are about 0.022 m ID and 0.12 m in height. These are connected by a U-type glass tubing, one arm of which is a capillary tube of approximately 0.75 mm, radius. The diameter of the capillary is determined from the weight difference between capillary tube when filled with mercury and when empty.

For constant temperature conditions, the apparatus is immersed in a constant temperature water bath with plane glass sides for visibility and recording. For the determination of interfacial tension, liquid 'b' (organic liquid or oil) is slowly added to cup B until it fills just below the top of the U-tube in the bottom of cup A. It is important to ascertain that there are no air-bubbles caught along the wall of the U-tube including capillary. Liquid 'a' (water) is then slowly added from a burette to cup A until the meniscus or interface is forced downward along the U-tube and stabilizes in the

capillary at some reference point 'C'. The height of each liquid above this reference point is then readily measured by means of a cathetometer.

The density of the liquid 'b' is measured using a specific gravity bottle. Knowing the densities and heights, the interfacial tension can readily be calculated using Equation [5].

Water is used as liquid 'a' throughout these experiments. Liquids 'b' used in these experiments are either pure organic liquids or oils. In the case of mineral oil or silicone oil, a small amount of carbon tetrachloride is added to adjust the density. All 'b' liquids have densities almost equal to that of water. The temperature of the apparatus is maintained at 25°C. The apparatus is cleaned with acetone followed by washing with NOCHROMIX solution. The washed apparatus is rinsed with distilled water and dried overnight at about 110°C.

VERIFICATION OF TECHNIQUE

Several liquid systems of unequal densities with known interfacial tension are used for calibration of this apparatus. The results are presented in Table A-2. The results are within acceptable accuracy. The chemicals used are of analytical grade purity. The use of high purity chemicals may have reduced the percent error. For ordinary accuracy requirements, no capillary corrections for meniscus height readings are necessary, as indicated by Bartell and Miller (1928).

TABLE A-2: Interfacial Tension of Various Systems of Unequal Densities at 25°C

System	Density of Organic Liquid (kg/m³)	Interfacial Tension (N/m)		%Error
		Measured	Literature	
Aniline : Water	1022	0.00541	0.00577	-6.3
Benzaldehyde : Water	1050	0.01478	0.01551	-4.7
Carbon Tetrachloride : Water	1583	0.0443	0.045	-1.6

This apparatus has also been used to measure the interfacial tension of eleven different systems of approximately equal densities. Table 2 presents the experimental results for these systems. Densities and interfacial tensions are also listed.

The liquid systems are so selected that the measured interfacial tension would cover a wide range of values. In the case of 3-phenyl-1-propanol and water system, the densities are almost equal and the measured heights are about the same, giving an interfacial tension of about 0 N/m. The highest interfacial tension of about 0.047 N/m (47 dynes/cm), is obtained for the liquid system of Dow Corning 200 silicone fluid (50 cSt at 25°C) (+CCl$_4$) and water. The apparatus is apparently sensitive enough to measure interfacial tension ranging from at least 0 to 0.05 N/m. From Table A-2, the accuracy of this method is within ±6% for liquids of unequal densities. Since the interfacial tension of liquid systems of equal density is unknown, it is anticipated that the accuracy of this

instrument would be within ±10%for equi-density liquids (such as in Table A-3).

CONCLUSION

This apparatus was used for measuring the interfacial tension of the various fluid systems used in this study. The development of this tensiometer is considered as one of the major contributions of this project.

This device can be used to measure the interfacial tension as a function of temperature for two liquids exhibiting equal or unequal density. This can be achieved by immersing the apparatus in a constant temperature water bath, maintaining the temperature at any desired value.

Besides its use in the present equi-density liquid-liquid flow regime study the technique can also be used to study micro-gravity fluid physics of interfacial tension driven flows (Marangoni effect) on earth (e.g., drop migration in a liquid matrix with temperature gradient).

TABLE A-3: Interfacial Tension of Various Systems of Equal Densities at 25°C

System	Density of Organic Liquid/Oil (kg/m^3)	Interfacial Tension (N/m)
Amyl Benzoate : Water	988	0.033
Anisole : Water	993	0.035
Benzonitrile : Water	1002	0.028
Butyl Benzoate : Water	1002	0.034
Diethyl Adipate : Water	1004	0.018
Diethyl Dimethyl-malonate : Water	1018	0.019
n,n-Diethyl-1-Naphthyl Amine : Water	1075	0.016
3-Phenyl-1-Propanol : Water	998	~0
Poly Propylene Glycol-2000 : Water	1003	0.005
Heavy Mineral Oil(+CCl_4) : Water	998	0.C31
Silicone Oil (+CCl_4) : Water	998	0.047

LIST OF REFERENCES

Bartell, F.E., and F.L. Miller,"A Method for the Measurement of Interfacial Tension of Liquid-Liquid Systems," *J. Amer. Chem. Soc.*, <u>58</u>, 1961 (1928).

Harkins, W.D., and E.C. Humphrey,"Surface Tension at Interface between 2 Liquids," *J. Amer. Chem. Soc.*, <u>38</u>, 228 (1916).

Karri, S.B.R., and V.K. Mathur, "Measurement of Interfacial Tension of Immiscible Liquids of Equal Density," *AIChE J.*, <u>34</u>, 155-157 (1988).

Karri, S.B.R., and V.K. Mathur,"Study of Simulated Micro-Gravity Vapor-Liquid Flow Regimes," *Annual AIChE Meeting*, New York, November 15-20, (1987).

Reynolds, W.C. "Interfacial Tension: Statical Measurement ofInterfacial Tension in Absolute Units." *Trans. Chem Soc.*,<u>119</u>, 460 (1921).

Zuidema, H.H., and G.W. Waters,"Determination of Interfacial Tension," *Ind. & Eng. Chem.*, <u>13</u>, 312 (1941).

Flow Regime Definitions of Two-Phase Flow in

Simulated Micro-G

--**Annular Flow (A)**. It is a form of separated flow. In this regime the liquid phase completely wets the circumference of the pipe and the vapor flow is confined to the central core of the pipe. Some liquid may flow as drops or mist in the vapor core.

--**Slug Flow (S)**. Under appropriate conditions, liquid waves created in the annular flow regime can bridge the pipe. This creates a flow regime characterized by long "bullet shaped" Taylor bubbles of vapor alternating with liquid slugs which completely fill the pipe cross-section.

--**Drop or Mist Flow (D,M)**. At higher vapor velocities, the waves on the liquid surface do not bridge but are destroyed becoming entrained as droplets which flow in the vapor core. At sufficiently high vapor qualities and vapor velocities the whole liquid phase flows almost entirely as a dispersion of droplets or mist within the continuous vapor phase.

--**Bubble or Dispersed Bubble Flow (B)**. At relatively large liquid flow velocities, with little vapor flow, the liquid phase is continuous and fills the pipe while the vapor is dispersed as scattered bubbles.

--**Inverse Annular Flow (I-A)**. Liquid travels predominantly in a continuous core while vapor travels predominantly in the annulus along the pipe wall. Observed in liquid-liquid flows (ie. when less viscous liquid travels in annulus along wall). Also possibly observed in vapor-liquid flows when a very high heat flux causes film boiling.

--**Inverse Slug Flow (I-S)**. The inverse of slug flow. This flow is sometimes seen in liquid-liquid systems, namely as, Taylor bubbles of the more viscous liquid flow in a continuous stream of the less viscous liquid.

DATA NOTATION

A-DROP	ANNULAR-DROP FLOW
A-D/S	ANNULAR-DROP/SLUG TRANSITION
A-MIST	ANNULAR-MIST FLOW
A-M/S	ANNULAR-MIST/SLUG TRANSITION
ANNULAR	ANNULAR FLOW
A/I-S	ANNULAR/INVERSE SLUG TRANSITION
A/S	ANNULAR/SLUG TRANSITION
BUBBLE	BUBBLE FLOW
DROP	DROP FLOW
D/I-A	DROP/INVERSE ANNULAR TRANSITION
D/M	DROP/MIST TRANSITION
I-ANN	INVERSE ANNULAR FLOW
I-SLUG	INVERSE SLUG FLOW
SLUG	SLUG FLOW
S/B	SLUG/BUBBLE TRANSITION
U-SLUG	UNSTABLE SLUG FLOW

( )   Indicate correlated video tape flow rates

$$Reg = d * \rho_g * Ugs / \mu_g$$

(Reynolds numbers based on superficial

$$Rel = d * \rho_l * Uls / \mu_l$$

velocities)

The following tables contain the data taken during the course of this experiment. The above notation definitions correspond to the flow regimes in the tables. A further point that must be stated is the numbers that appear in parentheses. These numbers refer to the flow-rates that are printed in the headings of each video run on the video tape. These are given, where necessary, so that the written data and video runs can be compared.

SIMULATED MICROGRAVITY FLOW REGIME DATA:
  FLUID SYSTEM #1 PPG-2000 : WATER
  DIAMETER = 25.4 mm
  ANNULAR NOZZLE CONFIGURATION
  T = 25°C

Ugs (m/s)	Uls (m/s)	Reg	Rel	ΔP/ΔL (ft H2O/ft)	Regime
0.0250	(10L) 0.0100	711.7363	0.8492	0.0026	I-ANN
	(20L) 0.0396		3.3629	0.0066	I-ANN
(12 GPH)	(30L) 0.0821		6.9720	0.0033	I-ANN
	(40L) 0.1342		11.3964	0.0053	I-ANN
	(45L) 0.1680		14.2667	0.0075	I-ANN
	(50L) 0.2087		17.7229	0.0097	I-ANN
	(60L) 0.2834		24.0665	0.0143	I-ANN
	(70L) 0.3579		30.3931	0.0209	I-ANN
	(80L) 0.4624		39.2673	-------	BUBBLE
0.0415	0.0100	1181.4823	0.8492	0.0022	I-ANN
	0.0396		3.3629	0.0051	I-ANN
(20 GPH)	0.0821		6.9720	0.0044	I-ANN
	0.1342		11.3964	0.0035	I-ANN
	0.1680		14.2667	-------	I-ANN
	0.2087		17.7229	0.0110	I-ANN
	0.2834		24.0665	0.0188	I-ANN
	0.3579		30.3931	0.0196	BUBBLE
	0.4624		39.2673	0.0202	BUBBLE
0.0747	0.0100	2126.6681	0.8492	0.0011	DROP
	0.0396		3.3629	0.0020	A/I-S
(36 GPH)	0.0821		6.9720	0.0027	A/I-S
	0.1342		11.3964	0.0036	I-ANN
	0.2087		17.7229	0.0042	I-ANN
	0.2834		24.0665	0.0073	I-ANN
	0.3579		30.3931	0.0109	I-ANN
	0.4624		39.2673	0.0142	BUBBLE
	(90L) 0.5220		44.3286	0.0191	BUBBLE
0.1200	0.0100	3416.3342	0.8492	0.0014	DROP
	0.0396		3.3629	0.0020	DROP
(60 GPH)	0.0821		6.9720	0.0025	I-SLUG
	0.1342		11.3964	0.0034	I-ANN
	0.2087		17.7229	0.0046	I-ANN
	0.2834		24.0665	0.0057	I-ANN
	0.3579		30.3931	0.0079	I-ANN

0.2075	0.0100	5907.4113	0.8492	0.0030	DROP
	0.0396		3.3629	0.0038	DROP
(100 GPH)	0.0821		6.9720	0.0049	DROP
	0.1342		11.3964	0.0058	DROP
	0.2087		17.7229	0.0068	D/I-A
	0.2834		24.0665	0.0085	D/I-A
	0.3579		30.3931	0.0109	I-ANN
	0.4624		39.2673	0.0130	I-ANN
	0.5220		44.3286	0.0160	I-ANN
0.4358	0.0100	12406.9872	0.8492	0.0109	D/M
	0.0396		3.3629	0.0128	D/M
(210 GPH)	0.0821		6.9720	0.0145	D/M
	0.1342		11.3964	0.0158	D/M
	0.2087		17.7229	0.0169	D/M
	0.2834		24.0665	0.0188	D/M
	0.3579		30.3931	0.0210	D/M
	0.4624		39.2673	0.0233	D/M
	0.5220		44.3286	0.0267	D/M

SIMULATED MICROGRAVITY FLOW REGIME DATA:
  FLUID SYSTEM #2   HEAVY MINERAL OIL+CCL4: WATER
  DIAMETER = 25.4 mm
  ANNULAR NOZZLE CONFIGURATION
  T = 25°C

Ugs (m/s)	Uls (m/s)		Reg	Rel	ΔP/ΔL (ft H2O/ft)	Regime
0.0062	(5s)	0.0067	176.5106	5.4787	0.0022	SLUG
	(10s)	0.0218		17.7853	0.0044	SLUG
	(15s)	0.0439		35.8977	0.0079	SLUG
	(20s)	0.0748		61.1652	0.0117	BUBBLE
	(25s)	0.1144		93.5467	0.0174	BUBBLE
	(10L)	0.1316		107.6114	0.0182	BUBBLE
	(20L)	0.3382		276.5516	0.0462	BUBBLE
	(30L)	0.4605		376.5583	0.0750	BUBBLE
0.0207		0.0067	590.4564	5.4787	0.0027	SLUG
		0.0218		17.7853	0.0065	SLUG
(10 GPH)		0.0439		35.8977	0.0111	SLUG
		0.0748		61.1652	0.0155	SLUG
		0.1144		93.5467	0.0215	SLUG
		0.1316		107.6114	0.0217	BUBBLE
		0.3382		276.5516	0.0475	BUBBLE
		0.4605		376.5583	0.0810	BUBBLE
0.0415		0.0067	1181.4823	5.4787	2.72E-05	SLUG
		0.0218		17.7853	0.0060	SLUG
(20 GPH)		0.0439		35.8977	0.0103	SLUG
		0.0748		61.1652	0.0139	SLUG
		0.1144		93.5467	0.0198	SLUG
		0.1316		107.6114	0.0245	SLUG
		0.3382		276.5516	0.0543	BUBBLE
		0.4605		376.5583	0.0863	BUBBLE
	(40L)	0.6930		566.6773	0.1210	BUBBLE
0.0750		0.0067	2135.2089	5.4787	--------	A-DROP
		0.0218		17.7853	0.0057	A-D/S
(36 GPH)		0.0439		35.8977	0.0092	SLUG
		0.0748		61.1652	0.0149	SLUG
		0.1144		93.5467	0.0190	SLUG
		0.1316		107.6114	0.0345	SLUG
		0.3382		276.5516	0.0630	SLUG
		0.4605		376.5583	0.0921	BUBBLE
		0.6930		566.6773	0.1270	BUBBLE
0.1244		0.0067	3541.5998	5.4787	0.0027	A-DROP
		0.0218		17.7853	0.0079	A-DROP
(60 GPH)		0.0439		35.8977	0.0065	A-DROP
		0.0748		61.1652	0.0133	A-DROP
		0.1144		93.5467	--------	A-DROP
		0.1316		107.6114	0.0304	A-DROP
		0.3382		276.5516	0.0690	A-DROP
		0.4605		376.5583	0.0860	BUBBLE

0.2074	0.0067	5904.5643	5.4787	0.0054	A-DROP
	0.0218		17.7853	0.0060	A-DROP
(100 GPH)	0.0439		35.8977	0.0071	A-DROP
	0.0748		61.1652	0.0073	A-DROP
	0.1144		93.5467	0.0082	A-DROP
	0.1316		107.6114	0.0101	A-DROP
	0.3382		276.5516	0.0230	A-DROP
	0.4605		376.5583	0.0630	A-DROP
	0.6930		566.6773	0.2070	BUBBLE
0.4356	0.0067	12401.2933	5.4787	0.0166	A-MIST
	0.0218		17.7853	0.0182	A-MIST
(210 GPH)	0.0439		35.8977	0.0198	A-MIST
	0.0748		61.1652	0.0198	A-MIST
	0.1144		93.5467	0.0209	A-MIST
	0.1316		107.6114	0.0260	A-MIST
	0.3382		276.5516	0.0345	A-MIST
	0.4605		376.5583	0.0490	A-MIST
	0.6930		566.6773	0.0580	A-MIST

SIMULATED MICROGRAVITY FLOW REGIME DATA:
  FLUID SYSTEM #3   DOW CORNING 200 FLUID+CCL4: WATER
  DIAMETER = 25.4 mm
  ANNULAR NOZZLE CONFIGURATION
  T = 25°C

Uqs (m/s)	Uls (m/s)		Reg	Rel	ΔP/ΔL (ft H2O/ft)	Regime
0.0062	(5s)	0.0055	176.5106	3.9834	0.0026	SLUG
	(10s)	0.0154		11.1536	0.0035	SLUG
(3 GPH)	(15s)	0.0336		24.3352	0.0074	S/B
	(20s)	0.0525		38.0238	0.0112	BUBBLE
	(25s)	0.0868		62.8660	0.0157	BUBBLE
	(10L)	0.0939		68.0083	0.0179	BUBBLE
	(20L)	0.2528		183.0937	0.0451	BUBBLE
	(30L)	0.4034		292.1676	0.0745	BUBBLE
0.0207		0.0055	590.4564	3.9834	0.0032	SLUG
		0.0154		11.1536	0.0086	SLUG
(10 GPH)		0.0336		24.3352	0.0118	SLUG
		0.0525		38.0238	0.0144	SLUG
		0.0868		62.8660	0.0208	SLUG
		0.0939		68.0083	0.0227	BUBBLE
		0.2528		183.0937	0.0500	BUBBLE
		0.4034		292.1676	0.0750	BUBBLE
	(40L)	0.5572		403.5593	0.1080	BUBBLE
	(50L)	0.7615		551.5262	0.1500	BUBBLE
0.0415		0.0055	1181.4823	3.9834	0.0035	SLUG
		0.0154		11.1536	0.0080	SLUG
(20 GPH)		0.0336		24.3352	0.0110	SLUG
		0.0525		38.0238	0.0120	SLUG
		0.0868		62.8660	0.0140	SLUG
		0.0939		68.0083	0.0260	SLUG
		0.2528		183.0937	0.0550	BUBBLE
		0.4034		292.1676	0.0881	BUBBLE
		0.5572		403.5593	0.1220	BUBBLE
		0.7615		551.5262	0.1560	BUBBLE
0.0750		0.0055	2135.2089	3.9834	0.0030	A-DROP
		0.0154		11.1536	0.0100	SLUG
(36 GPH)		0.0336		24.3352	0.0130	SLUG
		0.0525		38.0238	0.0200	SLUG
		0.0868		62.8660	0.0260	SLUG
		0.0939		68.0083	0.0280	SLUG
		0.2528		183.0937	0.0610	BUBBLE
		0.4034		292.1676	0.0950	BUBBLE
		0.5572		403.5593	0.1220	BUBBLE

0.1245	0.0055	3544.4468	3.9834	0.0064	A-DROP
	0.0154		11.1536	0.0064	A-DROP
(60 GFH)	0.0336		24.3352	0.0064	A-DROP
	0.0525		38.0238	0.0120	A-DROP
	0.0868		62.8660	0.0450	A-D/S
	0.0939		68.0083	0.0370	A-D/S
	0.2528		183.0937	0.0745	SLUG
	0.4034		292.1676	0.1020	SLUG
	0.5572		403.5593	0.1350	S/B
	0.7615		551.5262	0.1700	BUBBLE
0.2075	0.0055	5907.4113	3.9834	0.0064	A-DROP
	0.0154		11.1536	0.0070	A-DROP
(100 GFH)	0.0336		24.3352	0.0080	A-DROP
	0.0525		38.0238	0.0090	A-DROP
	0.0868		62.8660	0.0110	A-DROP
	0.0939		68.0083	0.0120	A-DROP
	0.2528		183.0937	0.0450	A-DROP
	0.4034		292.1676	0.1080	A-DROP
	0.5572		403.5593	0.1560	A-D/B
	0.7615		551.5262	0.1830	BUBBLE
0.4358	0.0055	12406.9872	3.9834	0.0016	A-MIST
	0.0154		11.1536	0.0200	A-MIST
(210 GFH)	0.0336		24.3352	0.0200	A-MIST
	0.0525		38.0238	0.0210	A-MIST
	0.0868		62.8660	0.0227	A-MIST
	0.0939		68.0083	0.0230	A-MIST
	0.2528		183.0937	0.0370	A-MIST
	0.4034		292.1676	0.0540	A-MIST
	0.5572		403.5593	0.0881	A-MIST
	0.7615		551.5262	0.1423	A-DROP

A-29

SIMULATED MICROGRAVITY FLOW REGIME DATA:
  FLUID SYSTEM #3   DOW CORNING 200 FLUID+CCL4: WATER
  DIAMETER = 12.7 mm
  ANNULAR NOZZLE CONFIGURATION
  T = 25°C

Ugs (m/s)	Uls (m/s)	Reg	Rel	ΔP/ΔL (ft H2O/ft)	Regime
0.0062	0.0053	88.2553	1.9193	0.0150	S/B
	0.0135		4.8888	0.0235	BUBBLE
(0.75 GPH)	0.0390		14.1231	0.0248	BUBBLE
	0.0570		20.6415	0.0325	BUBBLE
	0.0850		30.7812	0.0556	BUBBLE
	0.0990		35.8510	0.0599	BUBBLE
	0.2370		85.8251	0.1180	BUBBLE
	0.3760		136.1614	0.2450	BUBBLE
	0.6930		250.9571	0.4440	BUBBLE
0.0207	0.0053	295.2282	1.9193	0.0180	SLUG
	0.0135		4.8888	0.0210	SLUG
(2.5 GPH)	0.0390		14.1231	0.0325	SLUG
	0.0570		20.6415	0.0364	SLUG
	0.0850		30.7812	0.0621	S/B
	0.0990		35.8510	0.0635	S/B
	0.2370		85.8251	0.1540	BUBBLE
	0.3760		136.1614	0.2900	BUBBLE
	0.6930		250.9571	0.4710	BUBBLE
0.0415	0.0053	590.7411	1.9193	0.0321	SLUG
	0.0135		4.8888	0.0420	SLUG
(5 GPH)	0.0390		14.1231	0.0484	SLUG
	0.0570		20.6415	0.0552	SLUG
	0.0850		30.7812	0.0762	SLUG
	0.0990		35.8510	0.0725	S/B
	0.2370		85.8251	0.0163	S/B
	0.3760		136.1614	0.2540	BUBBLE
	0.6930		250.9571	0.4710	BUBBLE
0.0750	0.0053	1067.6044	1.9193	0.0026	A-MIST
	0.0135		4.8888	0.0081	A-MIST
(9 GPH)	0.0390		14.1231	0.0094	A-MIST
	0.0570		20.6415	0.0317	A-M/S
	0.0850		30.7812	0.0741	SLUG
	0.0990		35.8510	0.0816	SLUG
	0.2370		85.8251	0.1900	SLUG
	0.3760		136.1614	0.2630	S/B
	0.6930		250.9571	0.4620	BUBBLE

0.1245	0.0053	1772.2234	1.9193	0.0086	A-MIST
	0.0135		4.8888	0.0086	A-MIST
(15 GPH)	0.0390		14.1231	0.0099	A-MIST
	0.0570		20.6415	0.0154	A-MIST
	0.0850		30.7812	0.0154	A-MIST
	0.0990		35.8510	0.0154	A-M/S
	0.2370		85.8251	0.1810	SLUG
	0.3760		136.1614	0.3170	S/B
	0.6930		250.9571	0.4990	BUBBLE
0.2075	0.0053	2953.7056	1.9193	0.0077	A-MIST
	0.0135		4.8888	0.0090	A-MIST
(25 GPH)	0.0390		14.1231	0.0124	A-MIST
	0.0570		20.6415	0.0154	A-MIST
	0.0850		30.7812	0.0180	A-MIST
	0.0990		35.8510	0.0235	A-MIST
	0.2370		85.8251	0.0544	A-M/S
	0.3760		136.1614	0.3350	S/B
	0.6930		250.9571	0.5710	BUBBLE
0.4358	0.0053	6203.4936	1.9193	0.0272	A-MIST
	0.0135		4.8888	0.0272	A-MIST
(52.5 GPH)	0.0390		14.1231	0.0363	A-MIST
	0.0570		20.6415	0.0363	A-MIST
	0.0850		30.7812	0.0453	A-MIST
	0.0990		35.8510	0.0453	A-MIST
	0.2370		85.8251	0.0453	A-MIST
	0.3760		136.1614	0.0816	A-MIST
	0.6930		250.9571	0.1810	A-MIST

SIMULATED MICROGRAVITY FLOW REGIME DATA:
  FLUID SYSTEM #3   DOW CORNING 200 FLUID+CCL4: WATER
  DIAMETER =   8.0 mm
  ANNULAR NOZZLE CONFIGURATION
  T = 25°C

Ugs (m/s)	Uls (m/s)	Reg	Rel	$\Delta P/\Delta L$ (ft H2O/ft)	Regime
0.0050	0.0066	44.8338	1.5056	0.0320	SLUG
	0.0190		4.3342	0.0480	SLUG
(0.0152 LPM)	0.0320		7.2997	0.0800	SLUG
	0.0510		11.6338	0.1130	S/B
	0.0900		20.5303	0.1930	BUBBLE
	0.1020		23.2677	0.2410	BUBBLE
	0.2380		54.2912	0.4660	BUBBLE
	0.3710		84.6304	0.7720	BUBBLE
	0.5800		132.3063	1.1580	BUBBLE
	0.7740		176.5605	1.4480	BUBBLE
0.0219	0.0066	196.3720	1.5056	0.0190	SLUG
	0.0190		4.3342	0.0640	SLUG
(0.066 LPM)	0.0320		7.2997	0.0970	SLUG
	0.0510		11.6338	0.1290	SLUG
	0.0900		20.5303	0.2090	S/B
	0.1020		23.2677	0.2250	BUBBLE
	0.2380		54.2912	0.4660	BUBBLE
	0.3710		84.6304	0.7560	BUBBLE
	0.5800		132.3063	1.1580	BUBBLE
	0.7740		176.5605	------	BUBBLE
0.0450	0.0066	403.5040	1.5056	0.0210	A/S
	0.0190		4.3342	0.0800	SLUG
(0.137 LPM)	0.0320		7.2997	0.1130	SLUG
	0.0510		11.6338	0.1450	SLUG
	0.0900		20.5303	0.2410	SLUG
	0.1020		23.2677	0.2570	SLUG
	0.2380		54.2912	0.5150	SLUG
	0.3710		84.6304	0.8200	S/B
	0.5800		132.3063	1.5920	BUBBLE
0.0750	0.0066	672.5067	1.5056	0.0190	A-DROP
	0.0190		4.3342	0.0560	SLUG
(3.6 GPH)	0.0320		7.2997	0.1210	SLUG
	0.0510		11.6338	0.1850	SLUG
	0.0900		20.5303	0.2810	SLUG
	0.1020		23.2677	0.3220	SLUG
	0.2380		54.2912	0.5630	SLUG
	0.3710		84.6304	0.9010	S/B
	0.5800		132.3063	1.3190	BUBBLE
	0.7740		176.5605	1.6410	BUBBLE

0.1260	0.0066	1129.8113	1.5056	0.0290	ANNULAR
	0.0190		4.3342	0.0640	A/S
(6 GPH)	0.0320		7.2997	0.1130	SLUG
	0.0510		11.6338	0.1770	SLUG
	0.0900		20.5303	0.2900	SLUG
	0.1020		23.2677	0.3380	SLUG
	0.2380		54.2912	0.6920	SLUG
	0.3710		84.6304	0.9970	SLUG
	0.5800		132.3063	1.4200	S/B
	0.7740		176.5605	1.7500	BUBBLE
0.2050	0.0066	1838.1851	1.5056	0.0370	ANNULAR
	0.0190		4.3342	0.0640	ANNULAR
(10 GPH)	0.0320		7.2997	0.0640	ANNULAR
	0.0510		11.6338	0.1450	ANNULAR
	0.0900		20.5303	0.3380	A/S
	0.1020		23.2677	0.4020	A/S
	0.2380		54.2912	0.8520	SLUG
	0.3710		84.6304	1.2400	SLUG
	0.5800		132.3063	1.6300	S/B
	0.7740		176.5605	1.9900	BUBBLE
0.4100	0.0066	3676.3702	1.5056	0.0880	ANNULAR
	0.0190		4.3342	0.1130	ANNULAR
(20 GPH)	0.0320		7.2997	0.1210	ANNULAR
	0.0510		11.6338	0.1290	ANNULAR
	0.0900		20.5303	0.1290	ANNULAR
	0.1020		23.2677	0.1610	ANNULAR
	0.2380		54.2912	0.2730	ANNULAR
	0.3710		84.6304	0.4020	A-MIST
	0.5800		132.3063	0.6110	A-MIST
	0.7740		176.5605	1.1300	A-MIST

SIMULATED MICROGRAVITY FLOW REGIME DATA:
FLUID SYSTEM #4   DOW 200 FLUID+CCL4: 0.5 WT% TRITON X-100 SOLN.
    DIAMETER = 25.4 mm
    ANNULAR NOZZLE CONFIGURATION
    T = 25°C

Ugs (m/s)	Uls (m/s)		Req	Rel	ΔP/ΔL (ft H2O/ft)	Regime
0.0062	(5s)	0.0055	176.5106	3.9690	0.0003	U-SLUG
	(10s)	0.0154		11.1536	0.0010	U-SLUG
(3 GPH)	(15s)	0.0336		24.3352	0.0016	U-SLUG
	(20s)	0.0525		38.0238	0.0042	U-SLUG
	(25s)	0.0868		62.8660	0.0074	U-SLUG
	(10L)	0.0939		68.0083	0.0099	U-SLUG
	(20L)	0.2528		183.0937	0.0470	BUBBLE
	(30L)	0.4034		292.1676	0.0745	BUBBLE
	(40L)	0.5572		403.5593	0.0950	BUBBLE
	(50L)	0.7615		551.5262	0.1420	BUBBLE
0.0207		0.0055	590.4564	3.9690	0.0006	U-SLUG
		0.0154		11.1536	0.0010	U-SLUG
(10 GPH)		0.0336		24.3352	0.0010	U-SLUG
		0.0525		38.0238	0.0019	U-SLUG
		0.0868		62.8660	0.0029	U-SLUG
		0.0939		68.0083	0.0112	BUBBLE
		0.2528		183.0937	0.0420	BUBBLE
		0.4034		292.1676	0.0610	BUBBLE
		0.5572		403.5593	0.0880	BUBBLE
		0.7615		551.5262	0.1150	BUBBLE
0.0415		0.0055	1181.4823	3.9690	0.0006	A-DROP
		0.0154		11.1536	0.0006	A-DROP
(20 GPH)		0.0336		24.3352	0.0013	SLUG
		0.0525		38.0238	0.0035	SLUG
		0.0868		62.8660	0.0096	A-D/S
		0.0939		68.0083	0.0090	SLUG
		0.2528		183.0937	0.0473	A-D/B
		0.4034		292.1676	0.0677	BUBBLE
		0.5572		403.5593	0.0881	BUBBLE
0.0750		0.0055	2135.2089	3.9690	0.0010	A-DROP
		0.0154		11.1536	0.0016	A-DROP
(36 GPH)		0.0336		24.3352	0.0016	A-DROP
		0.0525		38.0238	0.0022	SLUG
		0.0868		62.8660	0.0029	SLUG
		0.0939		68.0083	0.0042	SLUG
		0.2528		183.0937	0.0610	A-DROP
		0.4034		292.1676	0.0813	A-DROP
		0.5572		403.5593	0.1290	A-D/B

0.1244	0.0055	3541.5998	3.9690	0.0045	A-DROP
	0.0154		11.1536	0.0019	A-DROP
(60 GPH)	0.0336		24.3352	0.0019	A-DROP
	0.0525		38.0238	0.0022	A-DROP
	0.0868		62.8660	0.0045	A-DROP
	0.0939		68.0083	0.0054	A-DROP
	0.2528		183.0937	0.0170	SLUG
	0.4034		292.1676	0.0474	BUBBLE
	0.5572		403.5593	0.1290	BUBBLE
0.2075	0.0055	5907.4113	3.9690	0.0029	A-MIST
	0.0154		11.1536	0.0029	A-MIST
(100 GPH)	0.0336		24.3352	0.0032	A-MIST
	0.0525		38.0238	0.0035	A-MIST
	0.0868		62.8660	0.0051	A-MIST
	0.0939		68.0083	0.0058	A-MIST
	0.2528		183.0937	0.0138	A-DROP
	0.4034		292.1676	0.0339	BUBBLE
	0.5572		403.5593	0.0474	BUBBLE

SIMULATED MICROGRAVITY FLOW REGIME DATA:
  FLUID SYSTEM #5   KEROSENE+CCL4: WATER
  DIAMETER = 25.4 mm
  ANNULAR NOZZLE CONFIGURATION
  T = 25°C

Uqs (m/s)	Uls (m/s)	Req	Rel	ΔP/ΔL (ft H2O/ft)	Regime
0.0062	0.0144	176.5106	294.3778	0.0010	SLUG
	0.0400		817.7161	0.0013	BUBBLE
(3 GPH)	0.0776		1586.3693	0.0013	BUBBLE
	0.1350		2759.7919	0.0019	BUBBLE
	0.2720		5560.4697	0.0080	BUBBLE
	0.4090		8361.1474	0.0118	BUBBLE
	0.5790		11836.4410	0.0202	BUBBLE
0.0207	0.0144	590.4564	294.3778	0.0010	SLUG
	0.0400		817.7161	0.0013	SLUG
(10 GPH)	0.0776		1586.3693	0.0016	S/B
	0.1350		2759.7919	0.0022	BUBBLE
	0.2720		5560.4697	0.0086	BUBBLE
	0.4090		8361.1474	0.0125	BUBBLE
	0.5790		11836.4410	0.0237	BUBBLE
0.0415	0.0144	1181.4823	294.3778	0.0010	A-D/S
	0.0400		817.7161	0.0013	SLUG
(20 GPH)	0.0776		1586.3693	0.0019	SLUG
	0.1350		2759.7919	0.0022	SLUG
	0.2720		5560.4697	0.0090	BUBBLE
	0.4090		8361.1474	0.0144	BUBBLE
	0.5790		11836.4410	0.0246	BUBBLE
0.0750	0.0144	2135.2089	294.3778	0.0010	A-DROP
	0.0400		817.7161	0.0019	SLUG
(36 GPH)	0.0776		1586.3693	0.0026	SLUG
	0.1350		2759.7919	0.0038	SLUG
	0.2720		5560.4697	0.0090	S/B
	0.4090		8361.1474	0.0138	BUBBLE
	0.5790		11836.4410	0.0272	BUBBLE
0.1245	0.0144	3544.4468	294.3778	0.0026	A-DROP
	0.0400		817.7161	0.0029	A-DROP
(60 GPH)	0.0776		1586.3693	0.0035	A-DROP
	0.1350		2759.7919	0.0086	A-D/S
	0.2720		5560.4697	0.0118	SLUG
	0.4090		8361.1474	0.0195	BUBBLE
	0.5790		11836.4410	0.0313	BUBBLE

0.2075	0.0144	5907.4113	294.3778	0.0032	A-DROP
	0.0400		817.7161	0.0038	A-DROP
(100 GPH)	0.0776		1586.3693	0.0051	A-DROP
	0.1350		2759.7919	0.0080	A-DROP
	0.2720		5560.4697	0.0163	BUBBLE
	0.4090		8361.1474	0.0240	BUBBLE
	0.5790		11836.4410	0.0342	BUBBLE
0.4358	0.0144	12406.9872	294.3778	0.0131	A-MIST
	0.0400		817.7161	0.0134	A-MIST
(210 GPH)	0.0776		1586.3693	0.0176	A-MIST
	0.1350		2759.7919	0.0218	A-MIST
	0.2720		5560.4697	0.0294	A-MIST
	0.4090		8361.1474	0.0339	A-MIST

ESTIMATION OF VOID FRACTION

For some selected experiments, void fractions are estimated.
This is accomplished by freezing the video tape at a desired frame
and then hand tracing the tube section picture. Next a planimeter
is used to determine the area of the bubbles that are traced.
From these areas an equivalent diameter is determined and the
volumes calculated. For the volume estimation these bubbles are
considered to be spherical, except Taylor bubbles, which are
considered elliptical. The void fraction is then calculated by
dividing the total volumes of the bubbles by the volume of the
traced section of tube. Two different video frames are used for
each flow rate and individual void fractions as well as the
average void fraction are reported (see following table). The
void fraction data for some selected experimental runs are
reported for 1.0 inch and 0.5 inch I.D. tubes. The void fraction
data for the 8.0 mm tube could not be estimated as it is difficult
to stop the video at a certain frame and still get a clear
traceable picture.

VOID FRACTION DATA FOR 1.0 " I.D.   Fluid System #3

Ugs	Uls	α_a	α_b	α_{avg}	REGIME	$\Delta P/\Delta L$
0.0062	0.00548	0.345	0.328	0.337	slug	0.00256
	0.0154	0.114	0.158	0.136	slug	0.00352
	0.0336	0.129	0.115	0.122	slug/bubble	0.00736
	0.0525	0.0908	0.102	0.0964	bubble	0.0112
	0.0868	0.059	0.073	0.066	bubble	0.0157
	0.0939	0.0419	0.0462	0.0441	bubble	0.0179
	0.2528	0.0158			bubble	0.0451
0.02074	0.0154	0.471	0.475	0.473	slug	0.00864

VOID FRACTION DATA FOR 0.5 " I.D.   Fluid System #3

Ugs	Uls	α_a	α_b	α_{avg}	REGIME	$\Delta P/\Delta L$
0.0062	0.0053	0.264	0.290	0.277	slug/bubble	0.0150
	0.0135	0.141	0.122	0.132	bubble	0.0235
	0.035	0.103	0.100	0.102	bubble	0.0248
	0.057	0.053	0.052	0.0525	bubble	0.0325
	0.085	0.025	0.030	0.0275	bubble	0.0556
	0.099	0.026	0.025	0.0255	bubble	0.0599

ROTAMETER CALIBRATION CURVE - FLUID #1

FOR BROOKS FLOW METER NO. 7305-49938
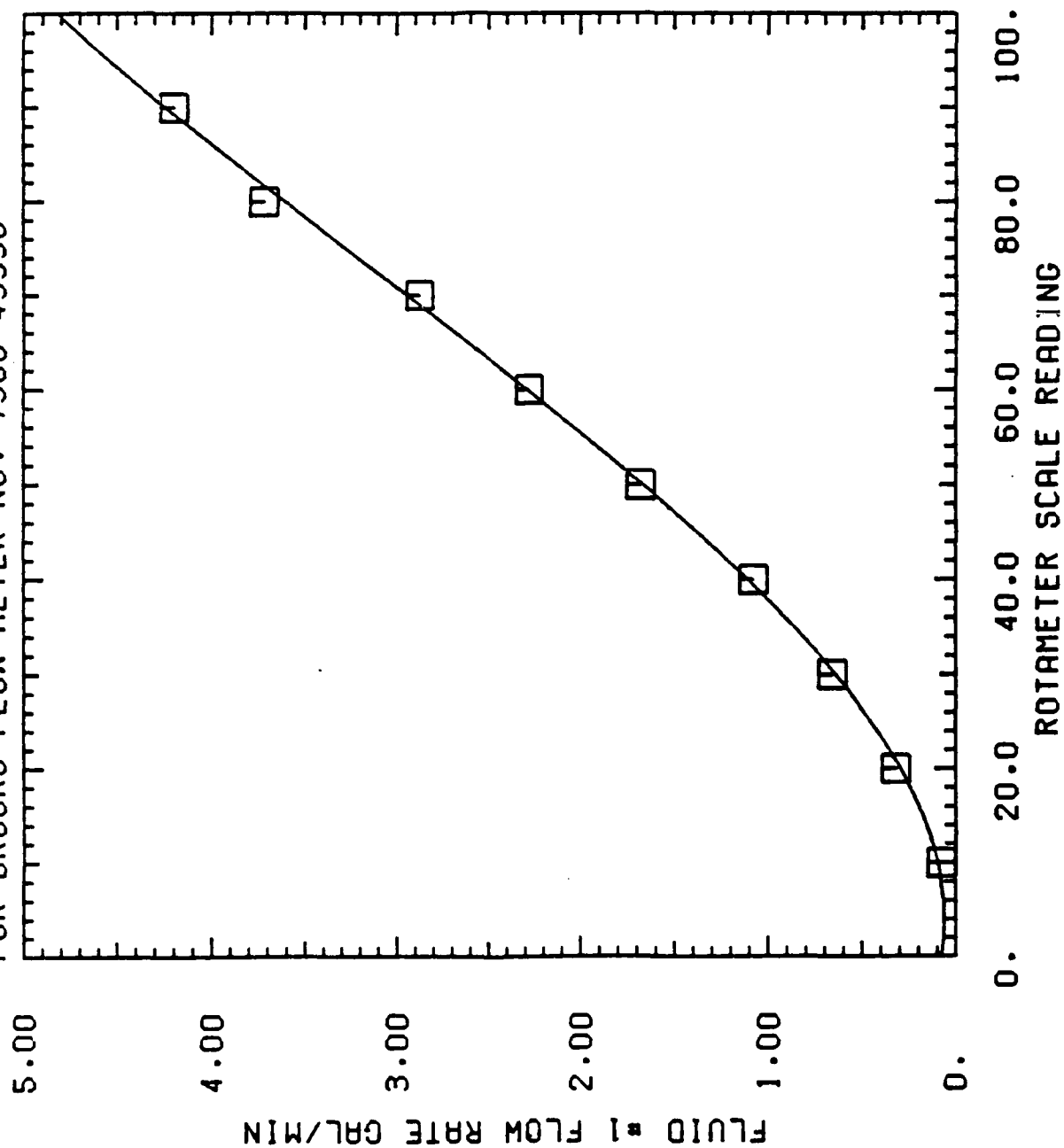
ROTAMETER CALIBRATION CURVE - FLUID # 2
FOR FISHER AND PORTER FLOW METER A-4578
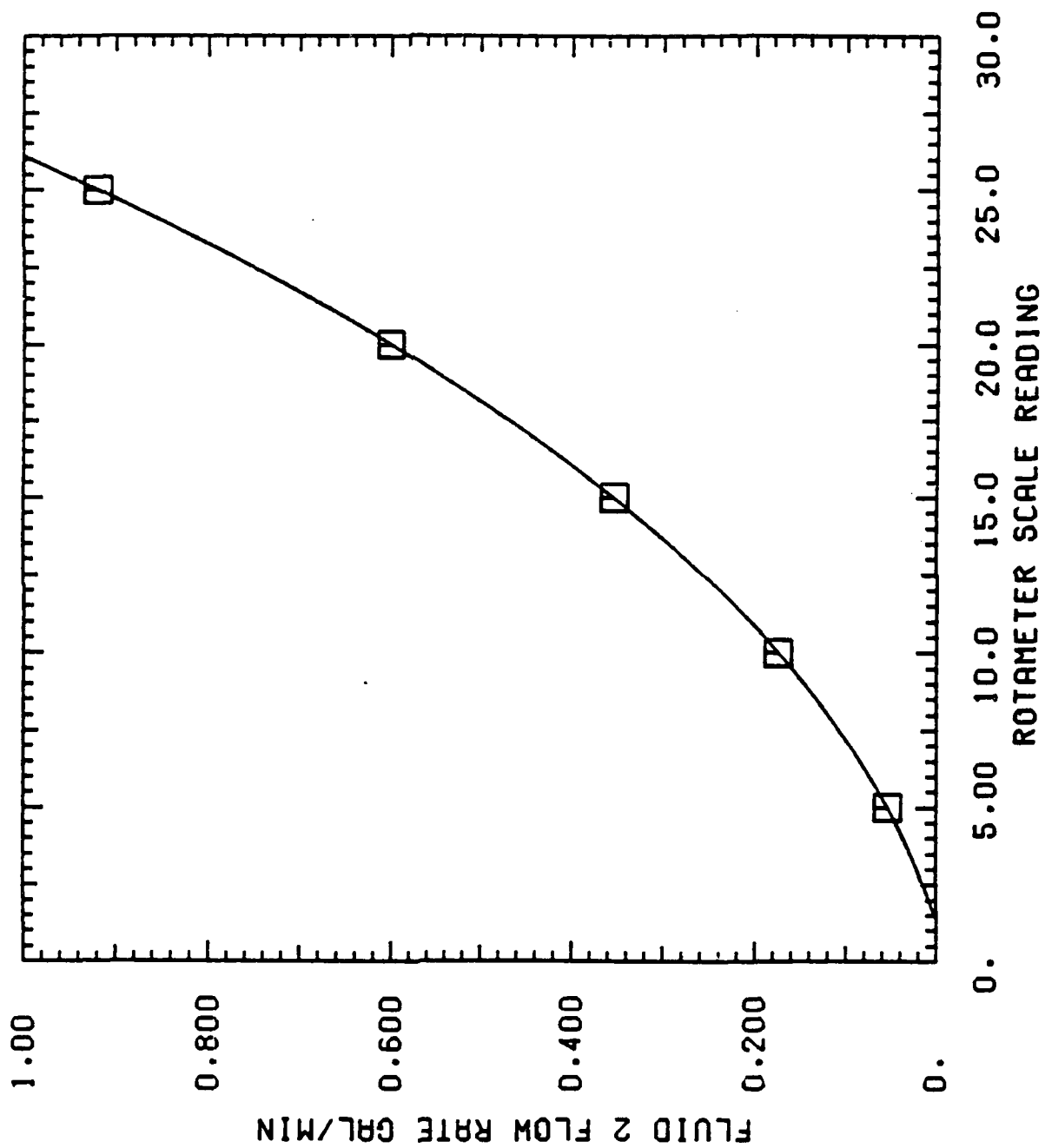
ROTAMETER CALIBRATION CURVE - FLUID # 2
FOR BROOKS FLOW METER NO. 7305-49938

FLUID 2 FLOW RATE GAL/MIN

ROTAMETER SCALE READING
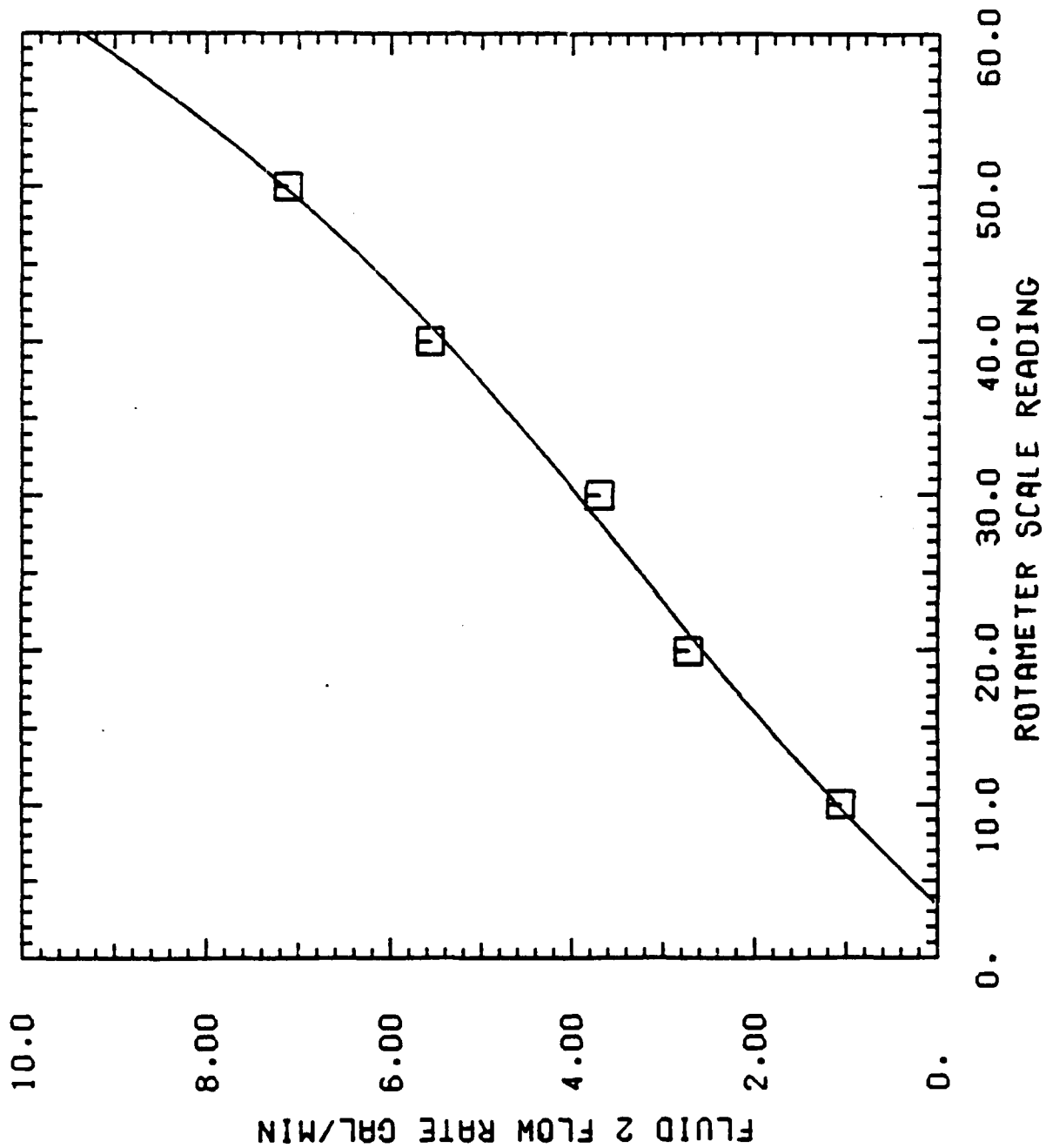
ROTAMETER CALIBRATION CURVE - FLUID # 3
FOR #4 GILMONT FLOW METER D4145   (used for 8.0 mm runs)
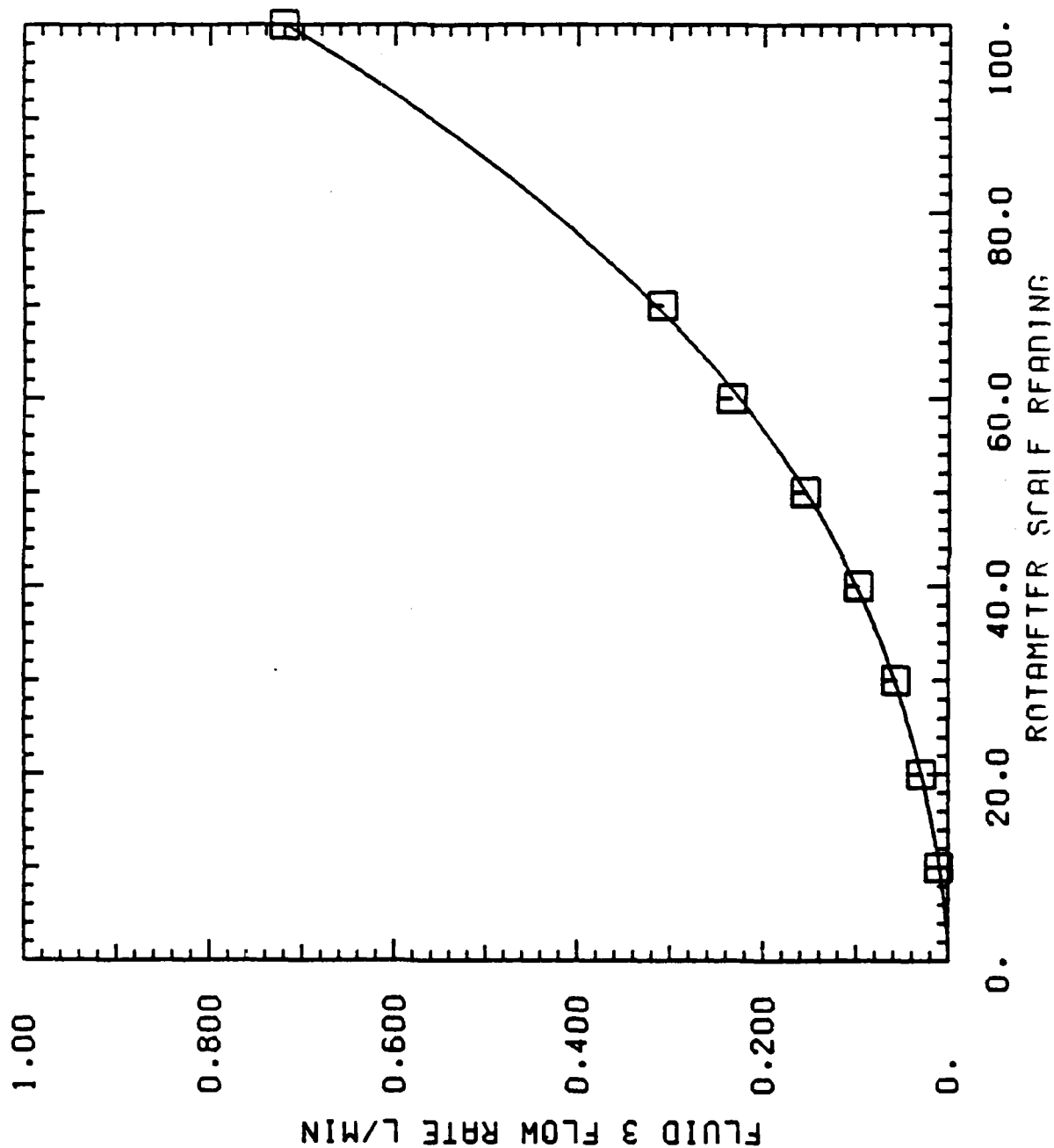
ROTAMETER CALIBRATION CURVE - FLUID # 3
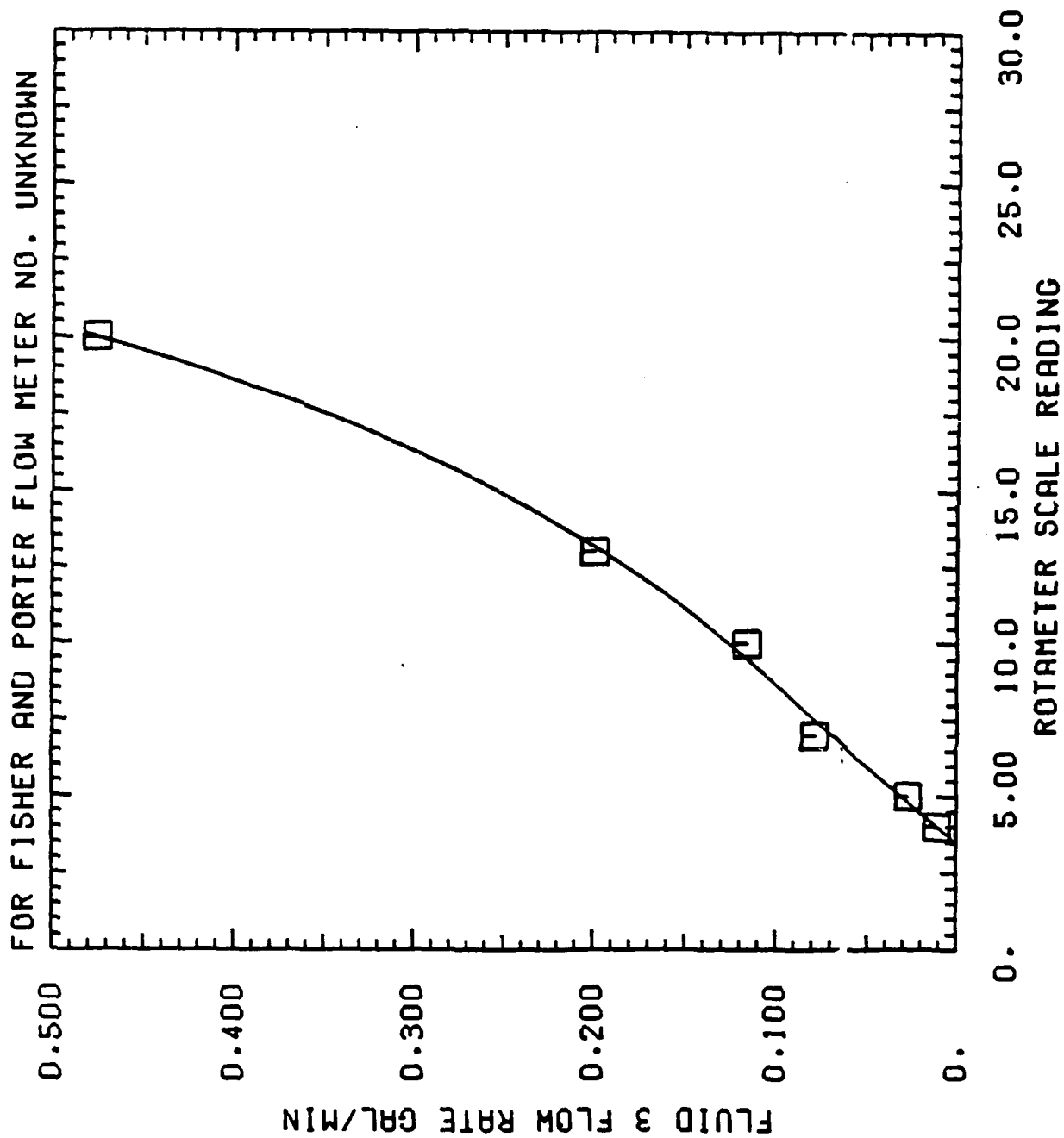
FOR FISHER AND PORTER FLOW METER NO. UNKNOWN

(12.7 and 8.0 mm runs)

FLUID 3 FLOW RATE GAL/MIN

ROTAMETER SCALE READING

A-44

ROTAMETER CALIBRATION CURVE - FLUID # 3
FOR FISHER AND PORTER FLOW METER A-4578

FLUID 3 FLOW RATE GAL/MIN

ROTAMETER SCALE READING
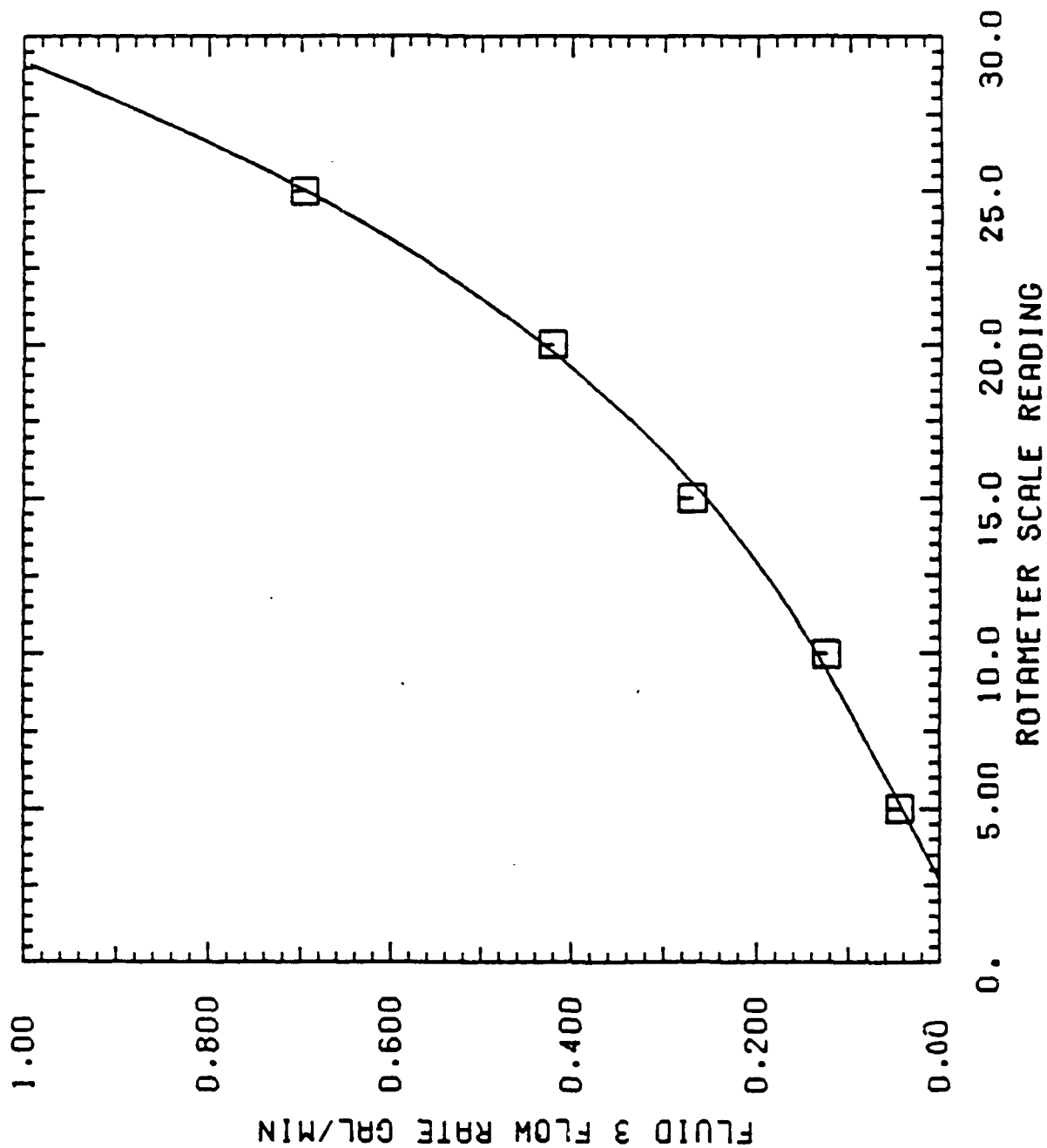
ROTAMETER CALIBRATION CURVE - FLUID # 3
FOR BROOKS FLOW METER NO. 7305-49938
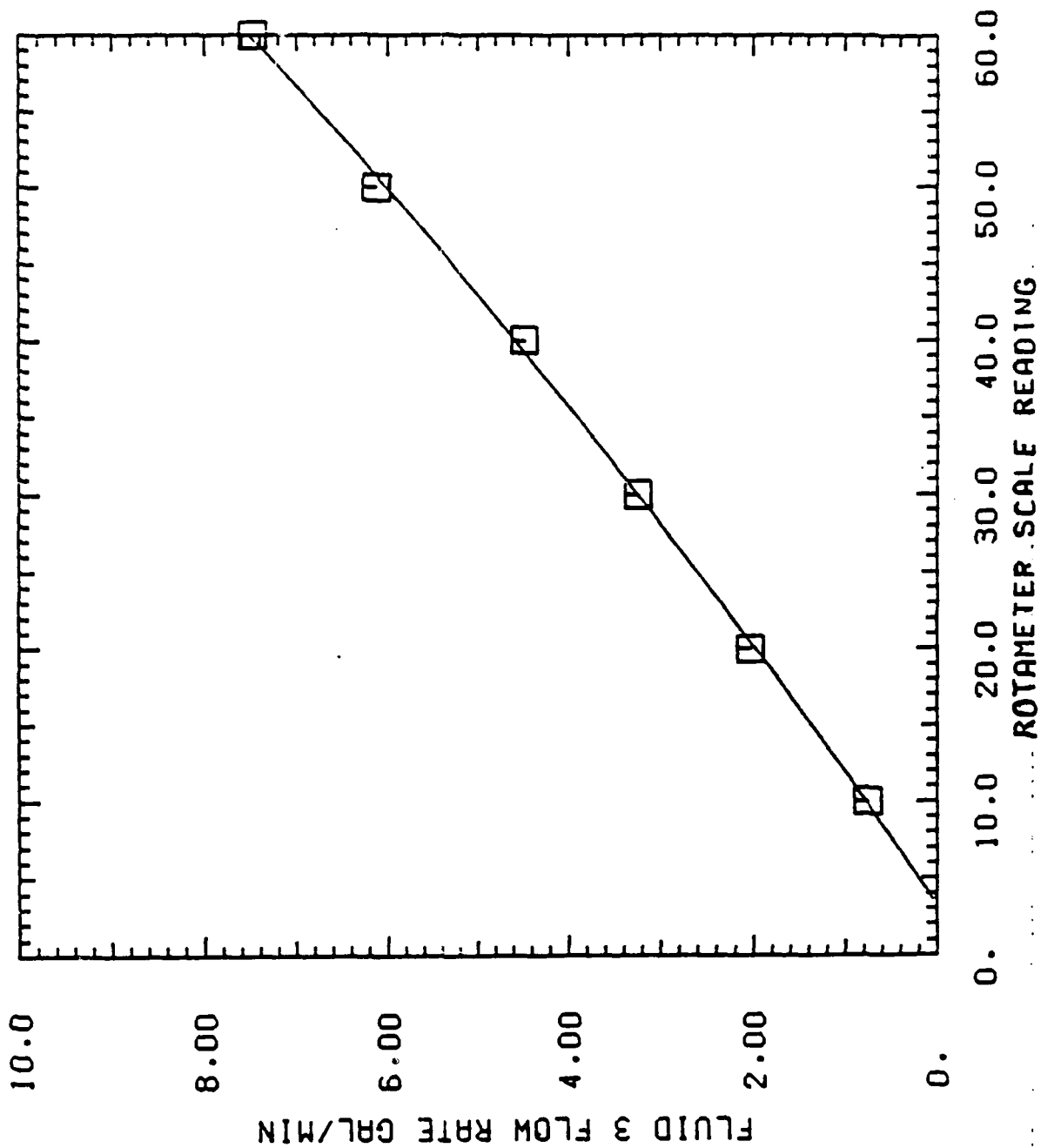
FLUID 3 FLOW RATE GAL/MIN

ROTAMETER SCALE READING

ROTAMETER CALIBRATION CURVE - FLUID # 5
FOR FISHER AND PORTER FLOW METER A-4578
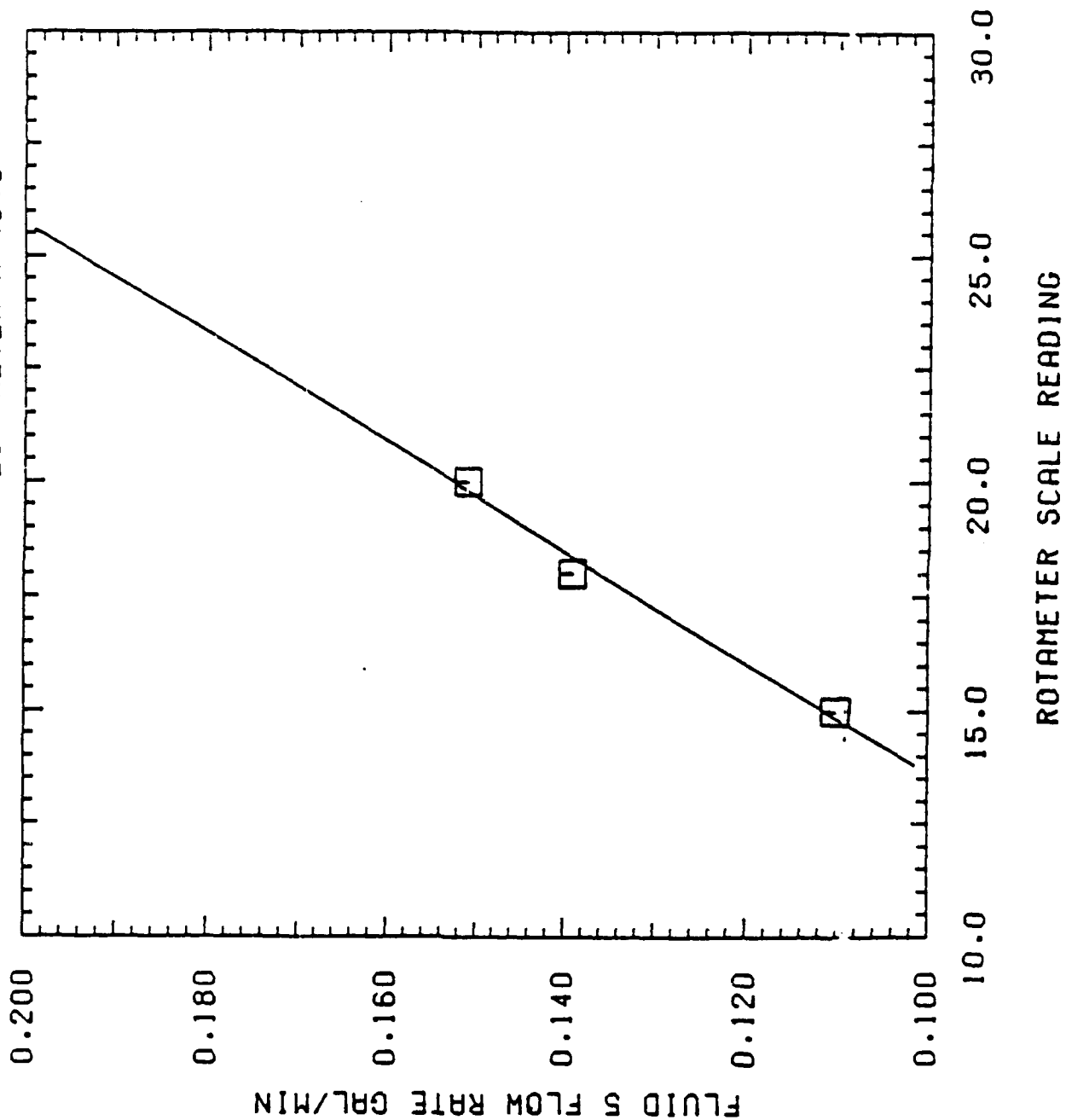
ROTAMETER CALIBRATION CURVE - FLUID # 5
FOR FISHER AND PORTER FLOW METER NO. UNKNOWN
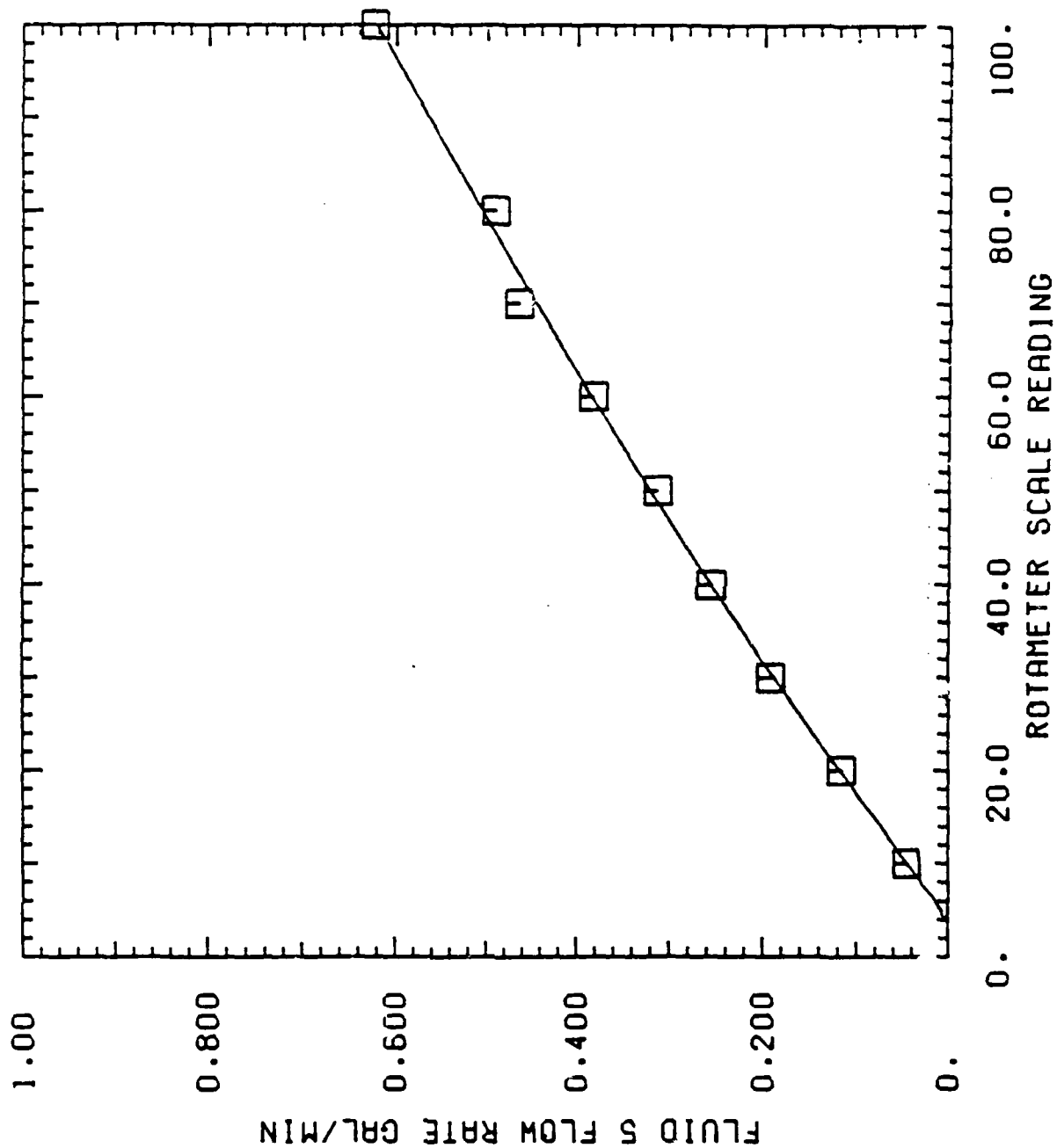
ROTAMETER CALIBRATION CURVE - FLUID # 5
FOR BROOKS FLOW METER NO. 7305-49938
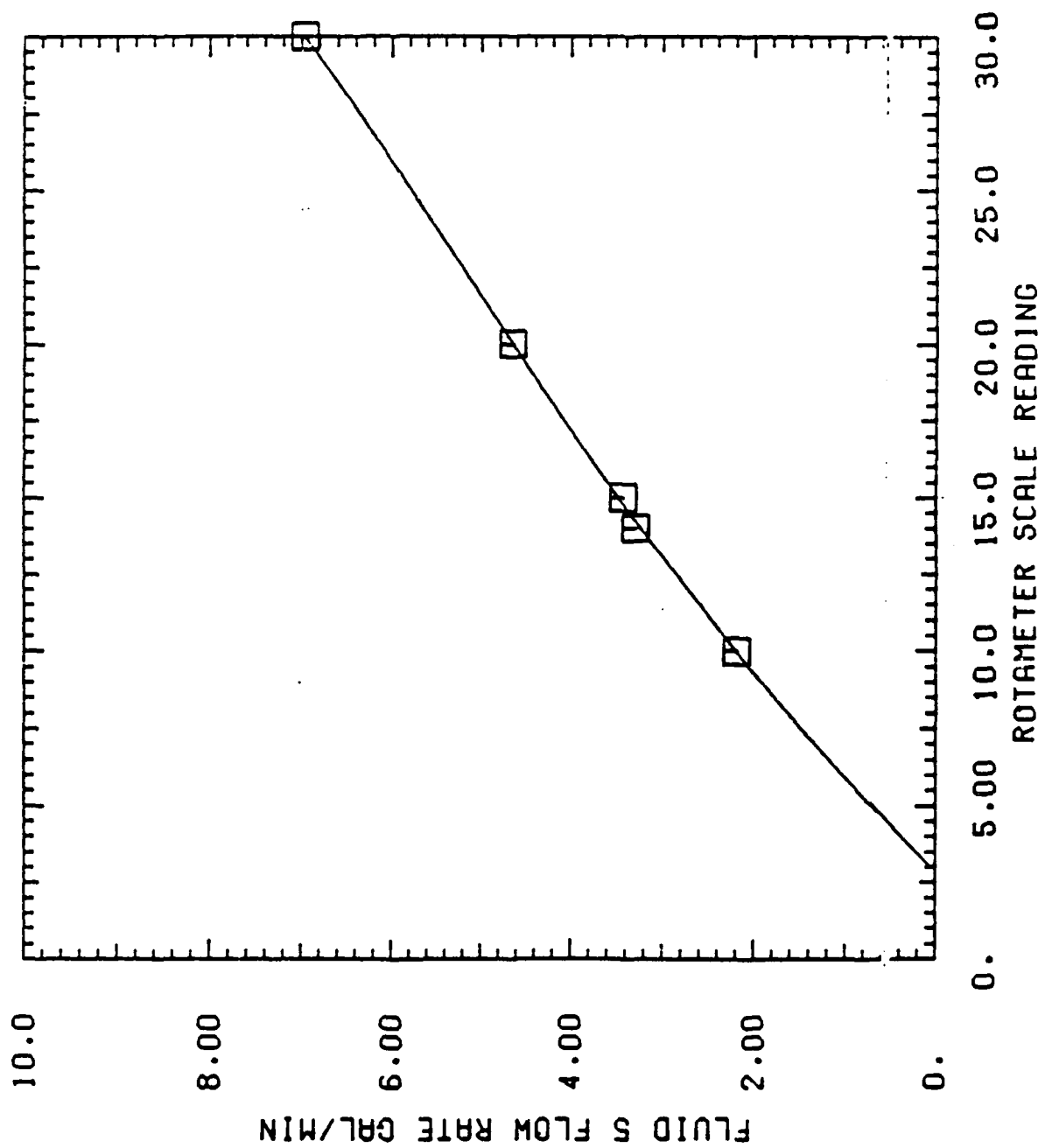
ROTAMETER CALIBRATION CURVE - WATER   (8.0 mm runs)
FOR # 13 GILMONT TYPE FLOW METER

ROTAMETER CALIBRATION CURVE - WATER
FOR DWYER TYPE FLOW METER (0.5-3.5 GPM)
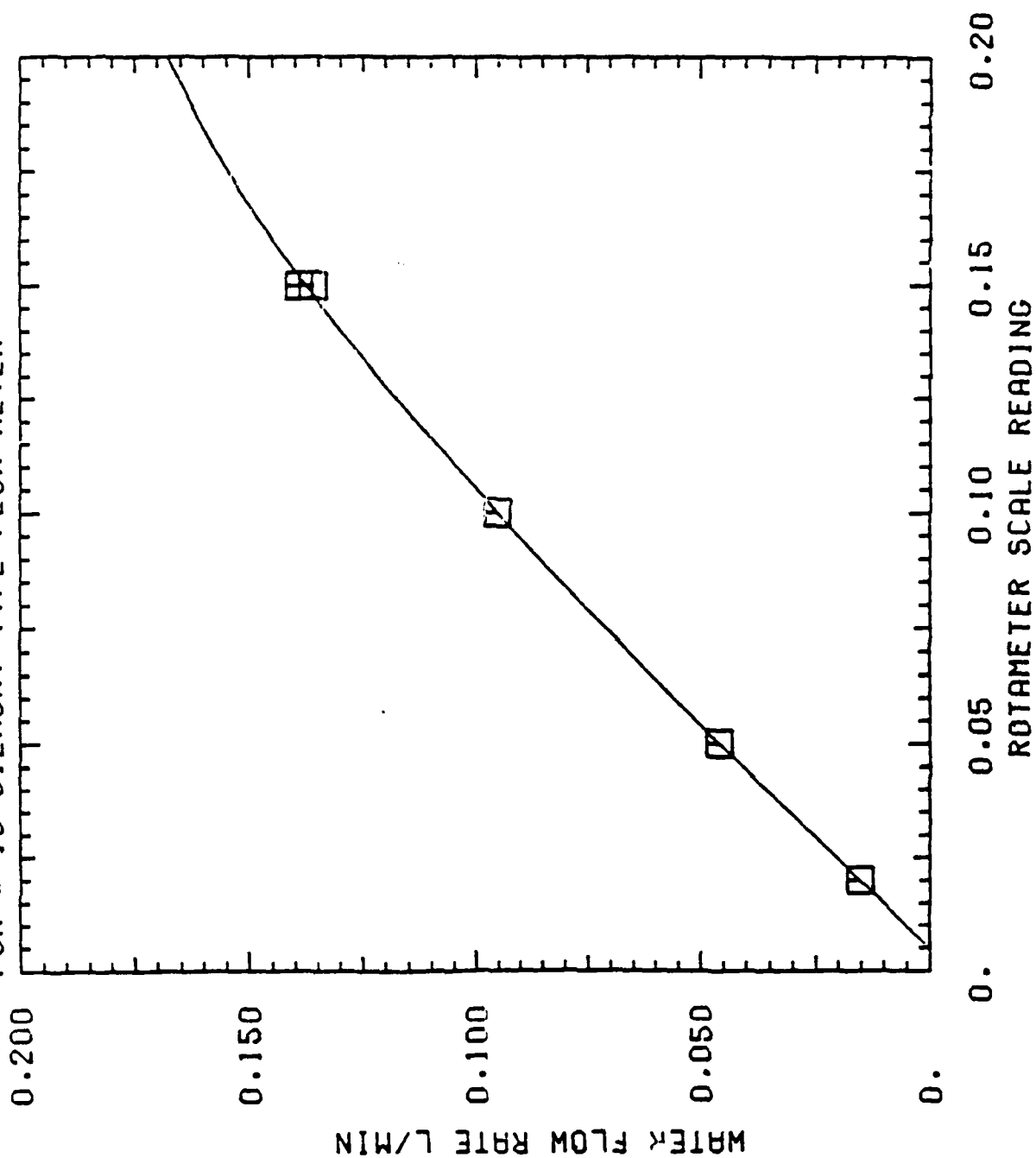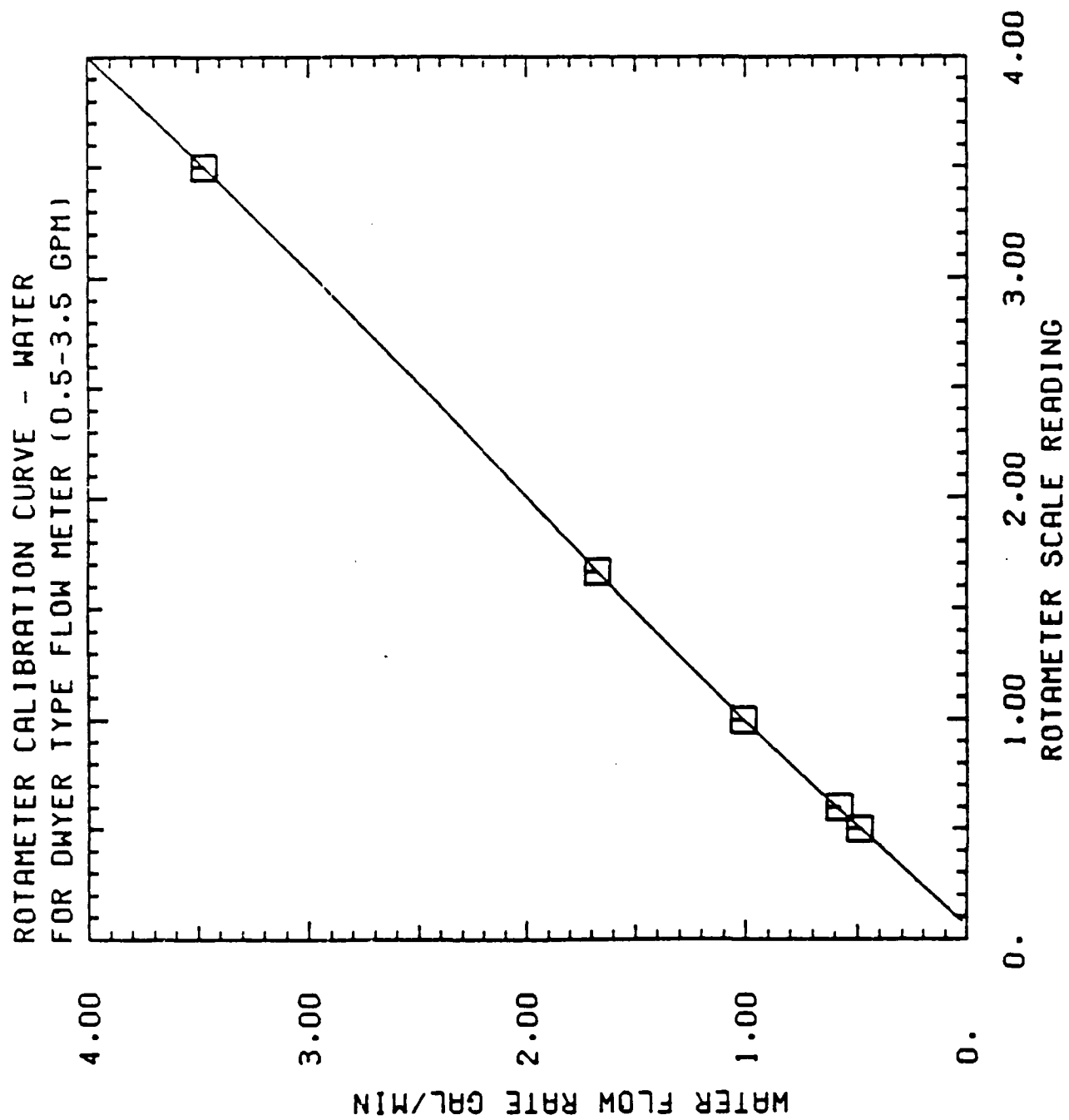
ROTAMETER CALIBRATION CURVE - WATER
FOR DWYER FLOWMETER RMC-134-SSV

WATER FLOW RATE GAL/HR

ROTAMETER SCALE READING
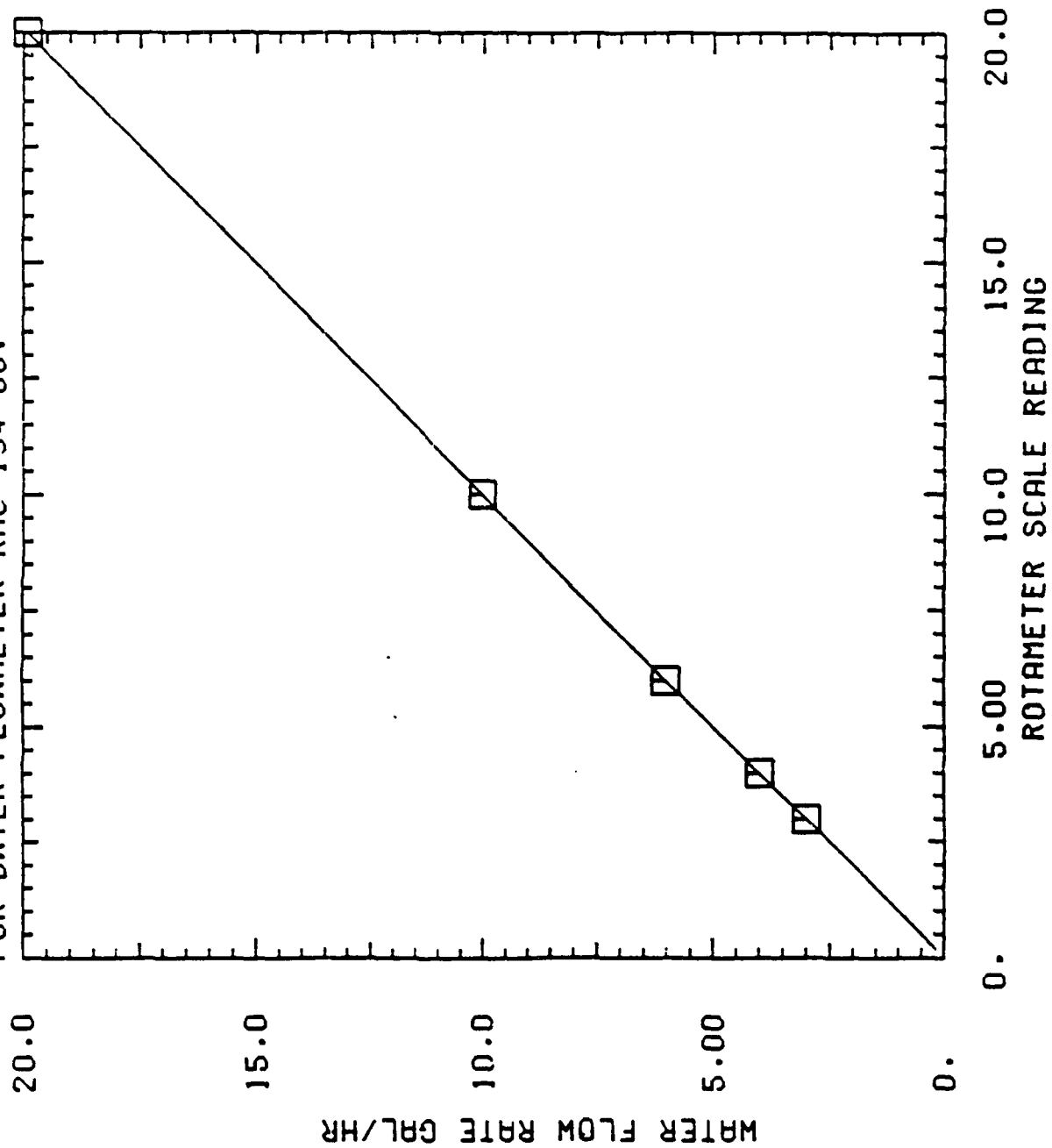
NOMENCLATURE

a,b	Subscripts referring to liquids a,b
d	Tube diameter
F_g	Gravity force, N
F_{int}	Interfacial force, N
g	Gravitational field, m/s^2
h	Height of liquid from a reference point, m
r	Capillary radius, m
Reg	Reynolds number based on superficial vapor velocity
Rel	Reynolds number based on superficial liquid velocity
Ugs	Superficial vapor velocity, m/s
Uls	Superficial liquid velocity, m/s

Greek Symbols

α	Void Fraction
ΔL	Distance between pressure taps, ft
ΔP	Pressure drop across pressure taps, ft H_2O
ρ	Liquid density, kg/m^3
σab	Interfacial tension between two liquids, N/m
μ	Liquid viscosity kg/m s

APPENDIX B

Supplemental Wave Duct Experiments

Extracted from:　　　J. Dzenitis
　　　　　　　　　　 M. S. Thesis, 1988
　　　　　　　　　　 Thayer School of Engineering
　　　　　　　　　　 Dartmouth College
　　　　　　　　　　 Hanover, New Hampshire　03755

Two-liquid Wave Duct Experiments

The general objective of the wave duct experiments performed at Dartmouth was to investigate interfacial shear and instability in a low-buoyancy situation. The results are examined on several fronts, determined by equipment limitations: Two standard normal-g gas-liquid predictions for onset of perturbation and limit of stable waves are shown to be inappropriate for this case, implying that they will not be generally applicable in reduced-g flows. Onset of perturbations are shown to occur at a threshold interfacial shear, which should be a pertinent consideration in future studies. Simple Kelvin-Helmholtz theory predicts transition to large-scale waves fairly well, and should be suitable for reduced-g situations when low flowrate instability is predicted. For low-g, long wavelength perturbations will be unstable.

B.1 Introduction
Background

It is known that interfacial shear and interfacial instability are key mechanisms in determining flow configurations. Interfacial shear is the tangential influence that one component has on another, and plays a role in any flow with relative velocities between the components. On the simplest level, interfacial shear determines the extent that one component is "dragged along" by the other, hence flow rates, void fractions, and pressure gradients. Furthermore, since the interface between fluids is often readily deformable, relative tangential motion in the presence of pressure, shear, and inertia perturbations can result in finite-scale motions normal to the interface. The stability of these deformations, in turn, can cause complete changes in flow configurations.

A great deal of work has been performed in this area, more recently in relation to flow regimes as the interest in predicting regimes has increased. Almost all of this work, however, has been based on experiments with air flow over water or some aqueous solution. This has allowed wide variations in viscosity ratio, but little changes in relative density [recently: Kordyban, 1977, Lin and Hanratty, 1986, Andritsos and Hanratty, 1987]. Johnston [1984] used density ratios of ~800 and ~4, but his work focused on expressing an interfacial friction factor without regard to stability conditions. (Because of this his attempts were largely unsuccessful.)

Objective

As theoretical micro-gravity flow regime predictions develop, questions about the validity of applying past stability work to environments with small buoyancy forces must be raised. To this end, a study of interfacial effects with reduced buoyancy was undertaken.

Originally, the investigation was to involve magnetically-induced motion of a ferro-fluid in another equi-density immiscible fluid. Initial analytical and experimental work, however, showed that this approach was not feasible within this contract. Large

magnetic field gradients are required for significant accelerations of the ferro-fluid, and the scale of the interfacial phenomena in relation to apparatus accuracy would have made measurements suspect at best. More generally, at this time the behavior of ferro-fluids even in simple flow situations is a research topic in itself.

The final approach settled upon was the flow of two immiscible liquids in a closed duct. The viscosity ratio of the liquids could be chosen such that a significant velocity difference resulted, while having a density ratio low enough would reduce the buoyancy effects much below that of air-aqueous experiments. This is not a simulation of reduced gravity stratified flow; it is an experiment directed at examining buoyancy and stability effects, as a step towards application of these theories to reduced gravity situations. Low flow ranges can explore the transition from an interface that is completely placid to slightly perturbed. Higher flow ranges can explore characteristics of existing waves, and stability as related to horizontal intermittent flows, entrainment, and annular bridging.

B.2 Description

The general setup of the wave duct is much like that of the UNH liquid-liquid simulations. In fact, the liquid pair selected was that referred to as "F3" in sections 4 and 5, except that there was no carbon-tetrachloride added to the Dow-Corning 200 silicone oil in this case. The less viscous liquid was water, and for 20°C the fluid properties were: $\rho_1/\rho_2 = 0.958$; $\mu_1/\mu_2 = 36.8$; $\sigma_{12} = {\sim}0.027$ N/m. Since the density ratio ρ_1/ρ_2 is less than one, the viscous DC200 fluid was the top layer, and the experiment resembled an inverted air-over-water wave experiment.

A schematic of the setup is shown in Fig. B.1. The DC200 was recovered and stored in its feed tank, and therefore was at room temperature (~22°C). The water used was not recovered, and temperature varied depending on the length of storage time and the lab cold water temperature. The temperature of both liquids was measured before each run so that variations in viscosity could be taken into account. (The viscosity of water varies by up to 30% in a range of temperatures from 10-22°C.) The fluid feeds are both diverted from recirculation loops, the water driven by a centrifugal pump and the oil by a gear pump. No cooling of the oil loop was necessary because the flow rates were at the upper end of the pump's capacity and there was little actual recirculation, and therefore minor heating effects. The water underwent more recirculation, but its relatively low viscosity also meant little heating occurred. A calibration curve was developed for each flow meter, and it was shown that the readings did not change measurably for the temperature ranges encountered.

The wave duct itself was constructed of 19.0 mm (0.75 in) thick plexiglass. The thickness was required for solid joining of the walls. The main duct section's inside measurements were 50.8 x 50.8 mm (2.0 x 2.0 in). The entrance section gradually expanded the flow area from the 3/4'NPT feed pipes to the 25.4 x 50.8 mm area prior to the fluids' meeting. After this

expansion, the liquids passed through a mesh designed to reduce
the cross-sectional and eddy variations of the velocity profiles.
The fluids met at the end of a sharpened steel plate, and from
there stabilized their interfacial height according to the flow
rates. The main duct section was ~1.83 m (72 in) long, and had
scales located at ~0.48, 0.89, and 1.40 m for measurement of the
interfacial height and its variations. The end section rose at
~11.° and prevented the channel from draining. There was no
observed back-reflection of waves due to the low grade of the
beach and the fact that both fluids exited the duct (as opposed to
most air-water experiments). The liquids were collected in a
runoff tank, and after settling for >9 hours most of the water
could be drained from the bottom of the tank. The remaining oil
and water were transferred to a 50 liter container that had a
sealing lid with a pipeline and a water inlet at the bottom.
After further settling, water was slowly added from the bottom
inlet, forcing the silicone oil out of the top pipeline and back
into its feed tank.
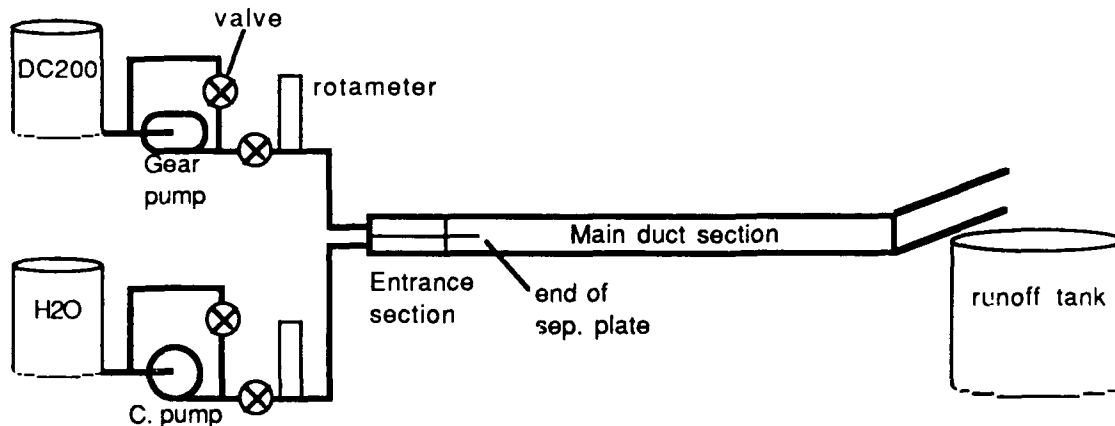
Fig. B.1: Two-liquid wave duct schematic

     Over-head lighting with a black background gave best
visualization of the interface. A video camera (running at 30
frames per second) was used to record the experiments,
specifically close-ups of the duct at the three height measurement
points. The videotapes were studied on a video editing machine
with frame-by-frame capability in order to divine mean interfacial
heights, perturbations, and wave speed and dominant wavelength
when possible.

B.3 Results
     Experiments were performed and taped for the range of flows
allowed by the pumps. The test matrix is shown in Fig. B.2 with
superficial velocity coordinates. As usual, j_1 refers to the more
viscous fluid (DC200 silicone oil), and j_2 the water. The square
symbols denote a smooth interface, the x's a wavy interface. x's
with a vertical line are points that showed waves large enough for
wavespeed and/or a dominant wavelength to be measured from the
videos. The points are labeled with the perturbation at location

B5

2 divided by the duct height (2h$_2$'). "Perturbation" here and throughout this chapter is defined as a dimensionless ratio of the peak-to-trough wave amplitude to the total duct height. In retrospect, more low-j$_2$/high-j$_1$ points would have been desirable.

Figure B.3 shows the void fraction a (average water height/duct height) measured at three locations versus j$_2$/j$_1$. For later use in models, the data can be fit well by

$$\alpha = K_\alpha \left(\frac{j_2}{j_1}\right)^m \qquad \text{where} \quad K_\alpha = 0.2576, \quad m = 0.3523 \text{(B.1)}$$

It was thought that relative velocity might be the key to perturbation degree, and the measured normalized perturbations are shown versus (j$_2$-j$_1$) in Figure B.4. There is a general trend, but obviously more than relative superficial velocity is involved in the degree of perturbation.
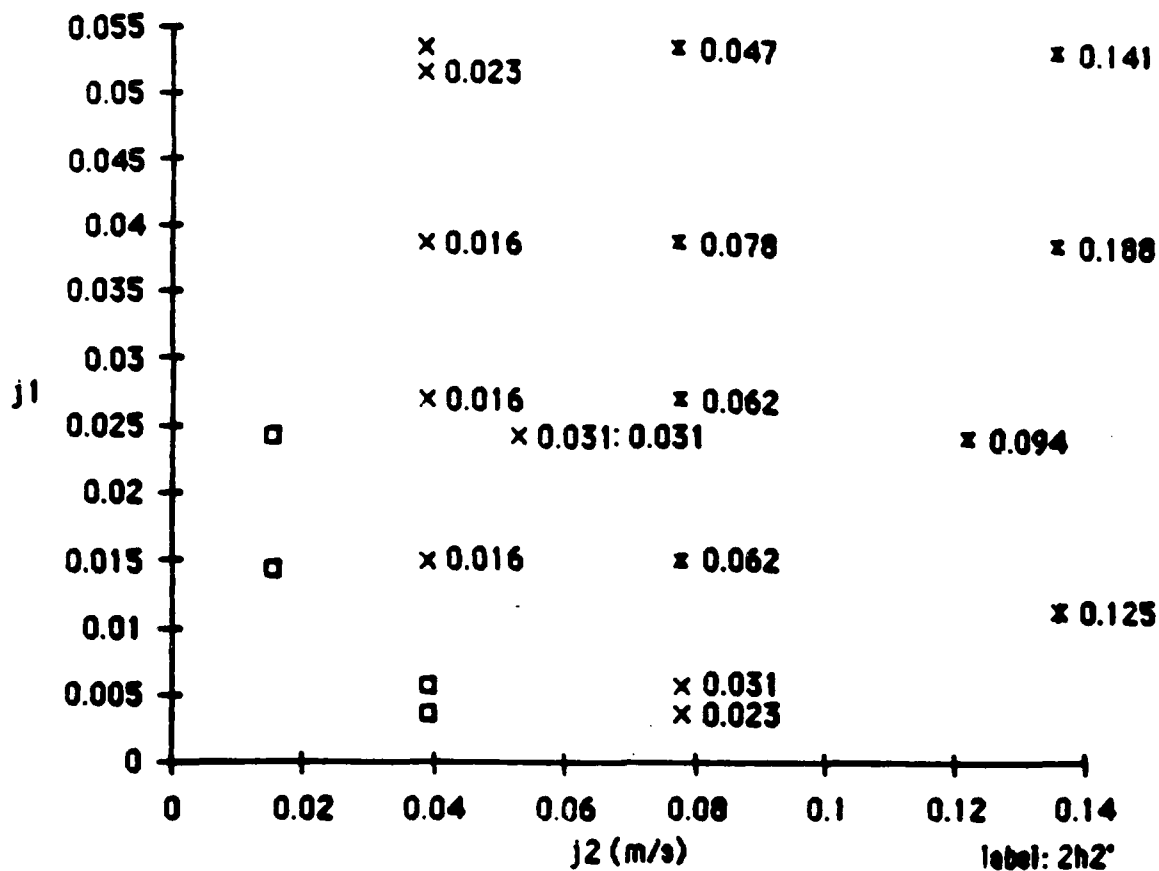
Fig. B.2: Wave duct test matrix
Superficial silicone oil velocity (j$_1$) vs. superficial water velocity (j$_2$). Squares denote placid interfaces, x's perturbed interfaces, and triple-crossed points large-scale roll waves. Attached numbers are dimensionless perturbations at the middle measuring point (location 2).

B6
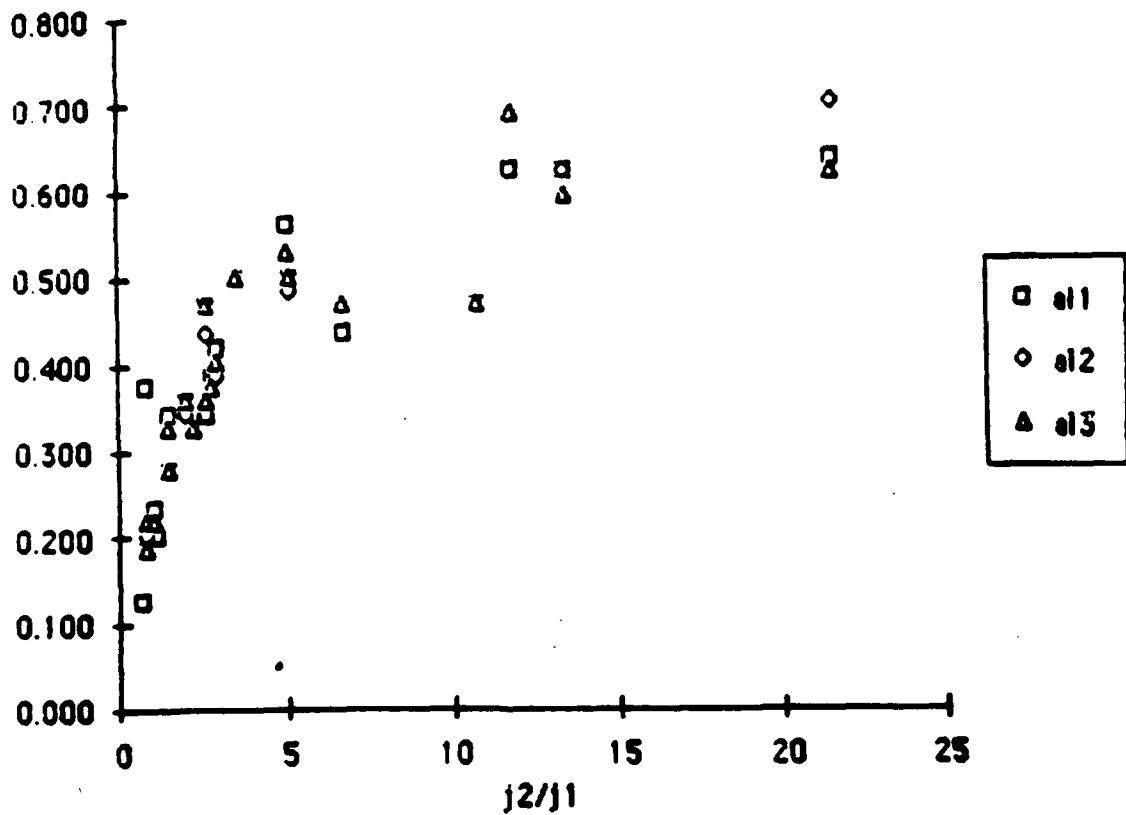
Fı . B.3: Measured void fractions
The void fraction a is the measured water depth divided by the
total duct height, and the values measured at the three locations
are shown. The data can be fit with an expression such as
Eq. (B.1).
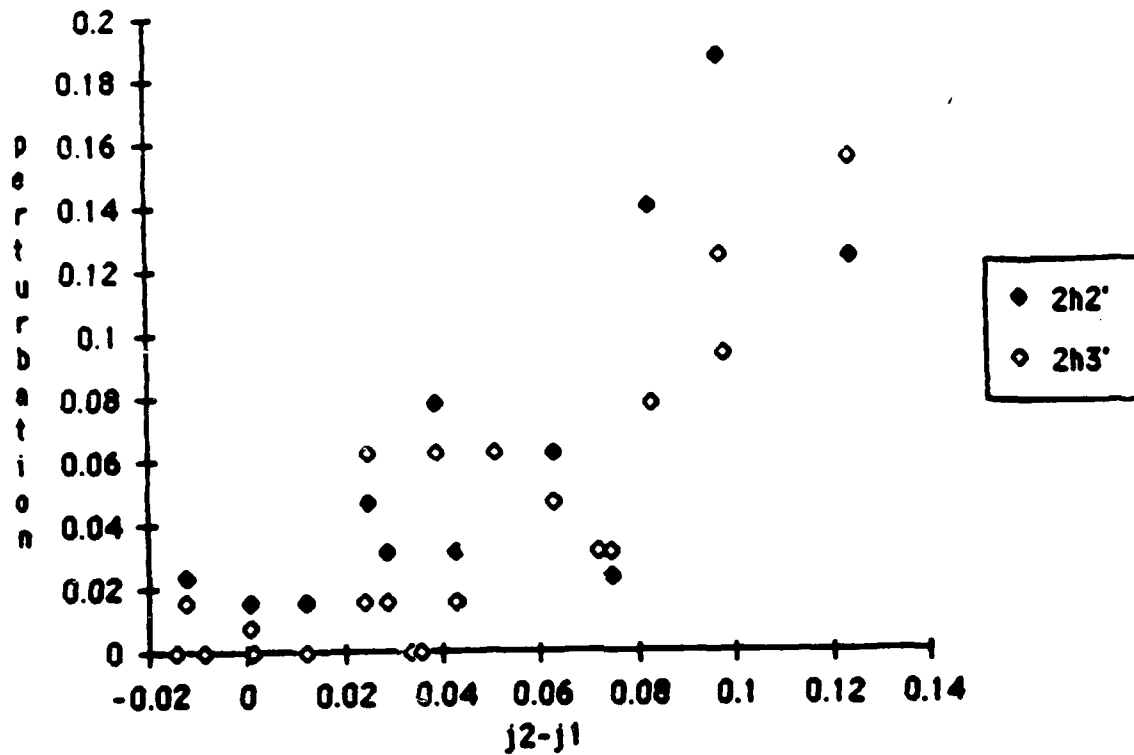
Fig. B.4: Measured perturbations
The dimensionless perturbations (peak-to-trough divided by duct
height) at the two downstream locations show only a general trend
with simple superficial velocity difference.

Unstable waves (showing bridging or entrainment) were not observed in the experiments, despite the low buoyancy forces. Two possibilities attributable to the apparatus are limited flow rates and the fairly short test section length. The instability of a wave should depend on the amount of energy fed to it, and it could be that the flow rates were too low to provide this energy. If an unstable wave is constructed of several lower level waves, then a duct longer than the 1.8 m might show unstable waves at the same flowrates. Another possibility based on the nature of the experiment is the inertial similarity of the two fluids, much like the point made in chapter 4. There inertial similarity meant little or no annular flow was seen, and supported an inertial view of annular flow. The wave stability in the wave duct suggests that in gas-liquid flow pressure and shear variations begin the motion normal to the interface, but that the inertia of the liquid relative to the gas is the key in continuing to the point of instability. The lack of unstable wave flow reduces the wide original scope to interfacial shear values and lower level waves.

There were four main limitations to the liquid-liquid wave duct experiments:

1) The meeting section introduced the fluids with equal cross-section for all flow rates. This caused initial disturbances and adjustments in the interfacial height that bring some of the wavy points into question. It is believed, however, that disturbances in the low flow points was minimal and quickly damped out.

2) Only fairly low flow rates where possible with the selected pumps. Higher rates may give opportunity for unstable wave conditions (see 4, however).

3) The test section was short. Steady-state may not have been reached for the placid flows, and more importantly there may not have been sufficient length for development of instability, either as perturbations to a smooth interface, or as unstable wave flow.

4) Making the density ratio low removes the inertial differences that contribute to gas-liquid instabilities. This may be the main reason for the absence of unstable waves.

B.4 Analysis and Discussion
Interfacial shear and onset of perturbations

One of the main areas of study was to be interfacial shear and its relation to waviness and instability. In order to accurately specify shear, it is necessary to have an accurate description of the velocity profiles (i.e. a differential instead of integral description of the flow). Analytical developments for differential approaches to 2-dimensional laminar-laminar, 2-dimensional laminar-turbulent, and 3-dimensional laminar-laminar flows were developed. Experimentally, several weeks were spent developing a data acquisition setup and calibration curves for hot-film anemometry to be used in finding the velocity profiles in the water layer. The sensors are extremely fragile, and experimenter clumsiness during calibration led to breaking the only two sensors available. It was discovered that the only

vendor of compatible probes (TSI Inc. of St. Paul, MN) had run out of the platinum film stock and was unable to provide any new probes or repairs for at least two months, well past the scope of the contract and availability of the lab space. The inability to measure the velocity profiles in turbulent water flow shot down the possibility of detailed investigation of wave-induced shear stress based on velocity profiles.

Given the setbacks above, some limited developments are still possible for low flow rates. When the Reynolds number of the water is low and the interfacial waviness is small, the 3-D laminar-laminar solution should describe the flow condition well. Figures B.5 and B.6 show the velocity profiles predicted by the 3-D solution for two of the data points. The point of Fig. B.5 showed a placid interface, and that of Fig. B.6 was perturbed. The upper frames are side views of the duct, with y-z plane slices every w/10 showing the profile. The lower frames are top views (down the y axis) with x-z plane slices at every h/16; curves are numbered from $y = 0$ to 1 (bottom to top), and those in the lower fluid2 (water) are indicated by broken lines. Once the velocity profiles are found, maximum and average interfacial shears (τ_i) are also known from the first y derivative of the velocity function in either fluid, multiplied by that fluid's viscosity.
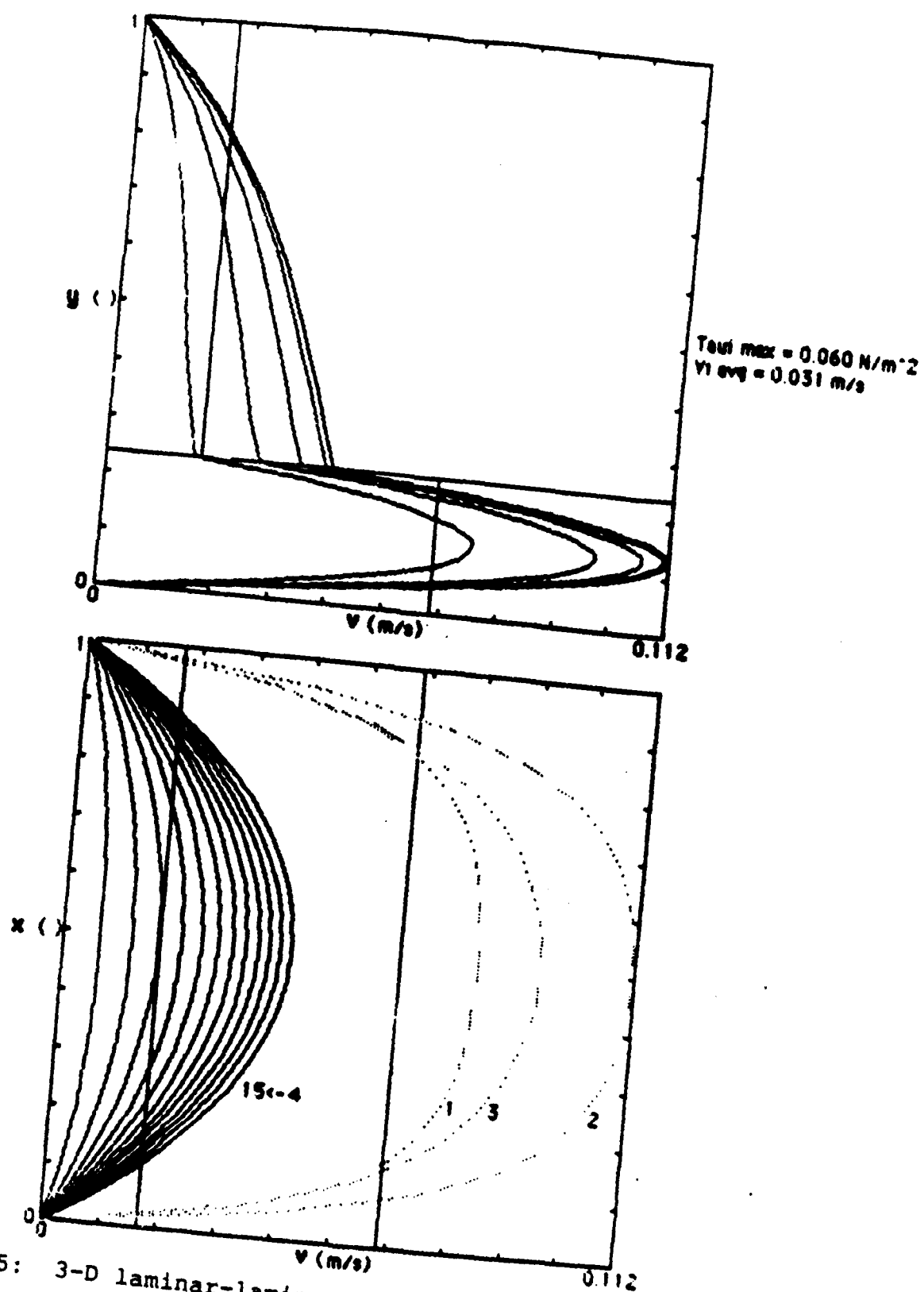
Fig. B.5: 3-D laminar-laminar velocity profiles for a placid point The top frame shows y-z plane slices at every w/10; the lower frame x-z plane slices at every h/16 (curves are numbered from bottom to top, and those in the lower fluid (water) are dotted).

B11
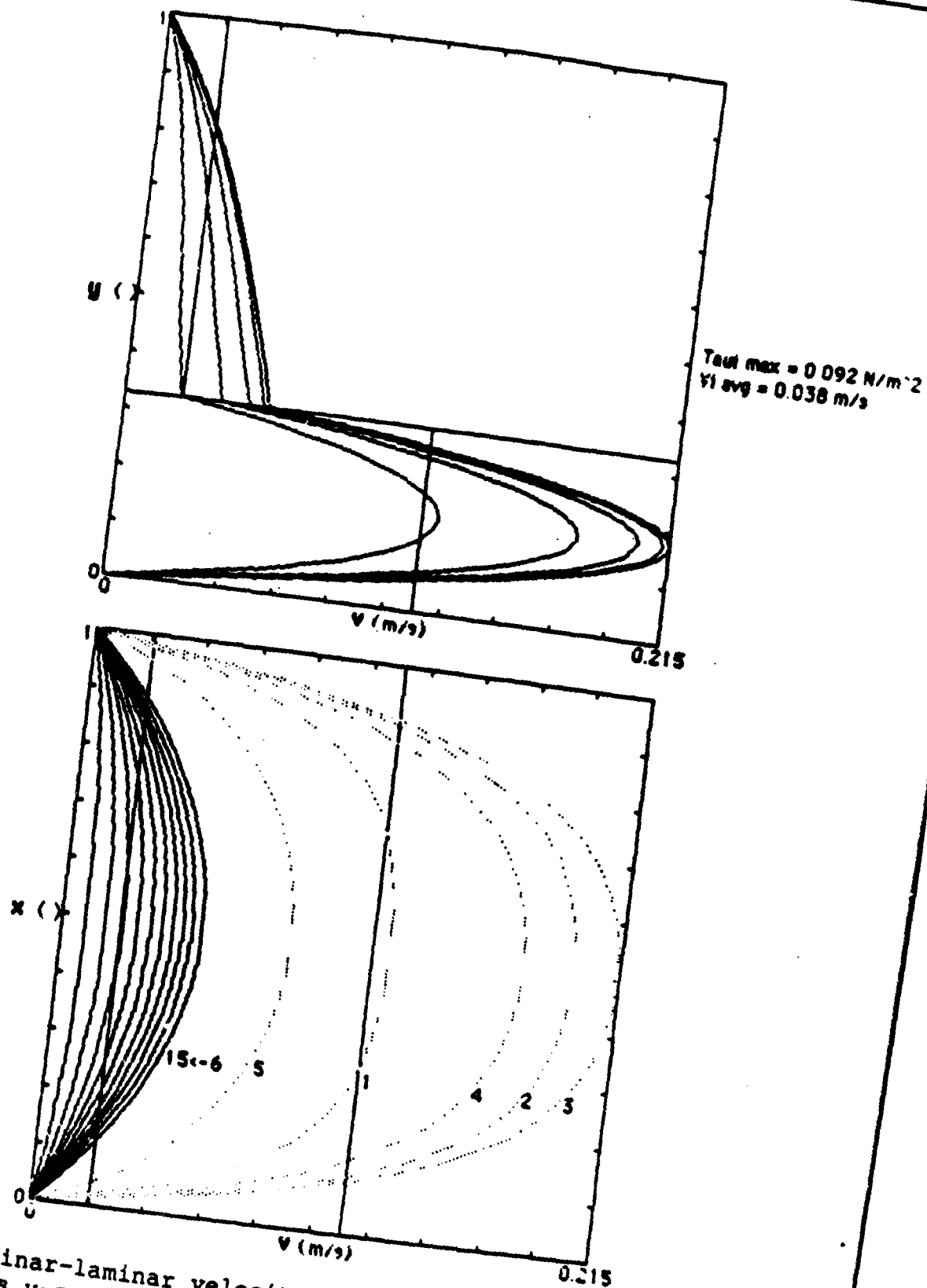
Fig. B.6: 3-D laminar-laminar velocity profiles for a perturbed point. The top frame shows y-z plane slices at every w/10; the lower frame x-z plane slices at every h/16 (curves are numbered from bottom to top, and those in the lower fluid (water) are dotted). This point shows a larger a and interfacial shear than that of Fig. B.5.

The validity of the analysis is tested by comparing predicted void fraction to that measured, as in Fig. B.7. The figure shows the difference between predicted and measured α divided by measured α, as a function of water Reynolds number Re_2. Figure B.7 also contains the results from a 2-D integral analysis for laminar-turbulent flow by Lin and Hanratty [1986], and from the differential 2-D laminar-laminar flow. Lin-Hanratty assumes turbulent viscosity, so over-predicts α until large Re_2 values. The 3-D laminar underpredicts α at high Re_2 because it neglects effective viscosity from turbulence. For Re_2 below 6,000, however, it predicts α within ~16% for 9 out of 10 points, and does not show a trend with Re_2 for these 9 points.

These low Re_2 points are selected for Figure B.8, where measured dimensionless perturbations are shown versus the maximum interfacial interfacial shear stress as predicted by the 3-D laminar model. The lower interfacial shear points show no disturbance, and there is some threshold τ_i (~0.08 N/m^3) beyond which the interface is always perturbed. This suggests that initial disturbance of the interface depends on an unstable slope of the velocity profile, most likely balanced in some way against buoyancy forces. This was a recent development and no further development has been achieved.
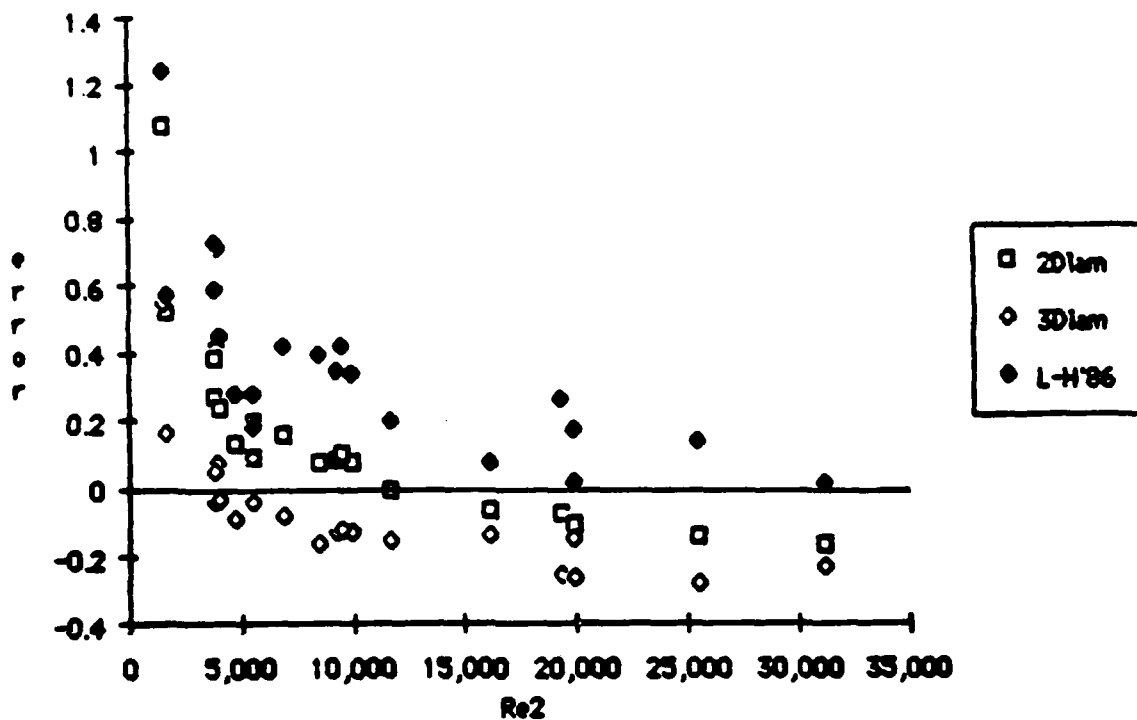
Fig. B 7:   Void fraction prediction error vs. water Reynolds

number

Errors defined as (predicted-measured)/measured are shown for 2-D
and 3-D laminar-laminar differential solutions, and a 2-D laminar-
turbulent integral solution by Lin-Hanratty [1986].   The 3-D
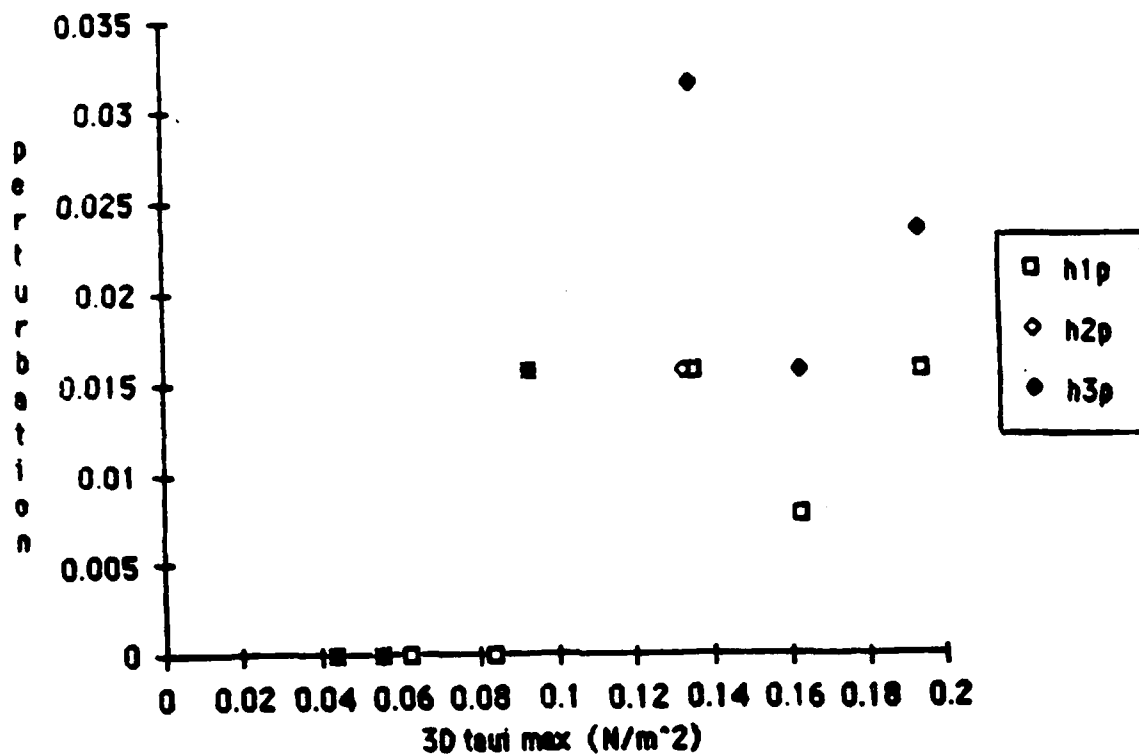laminar solution shows good results for points with $Re_2 < 6,000$.

Fig. B.8: Onset of measured perturbation vs. predicted

interfacial shear

Dimensionless perturbations at the three measurement points are shown with maximum interfacial shear from the 3-D laminar analysis. It is seen that there is a threshold τ_i for observed placid/perturbed points.

Existing wave stability

Kordyban [1977] applied a Kelvin-Helmholtz type analysis to existing (finite) waves by using a crest velocity for pressure variations (Kelvin-Helmholtz instability is explored in greater detail later). A modification of his model with surface tension included is used to plot the $2h_2'$ perturbations in Fig. B.9. Any point right of zero on the horizontal axis should be unstable. He makes use of a constant parameter equal to 1.35 for air-water flow; this is a factor that translates trough-to-crest velocity differences to pressure differences. Larger values could be used to shift the data to the left, but here it has just been set to 1.0. The large waves only occur past the critical j_{2c}, but small perturbations are also seen there, and, as discussed earlier, there were no truly unstable waves observed at all.
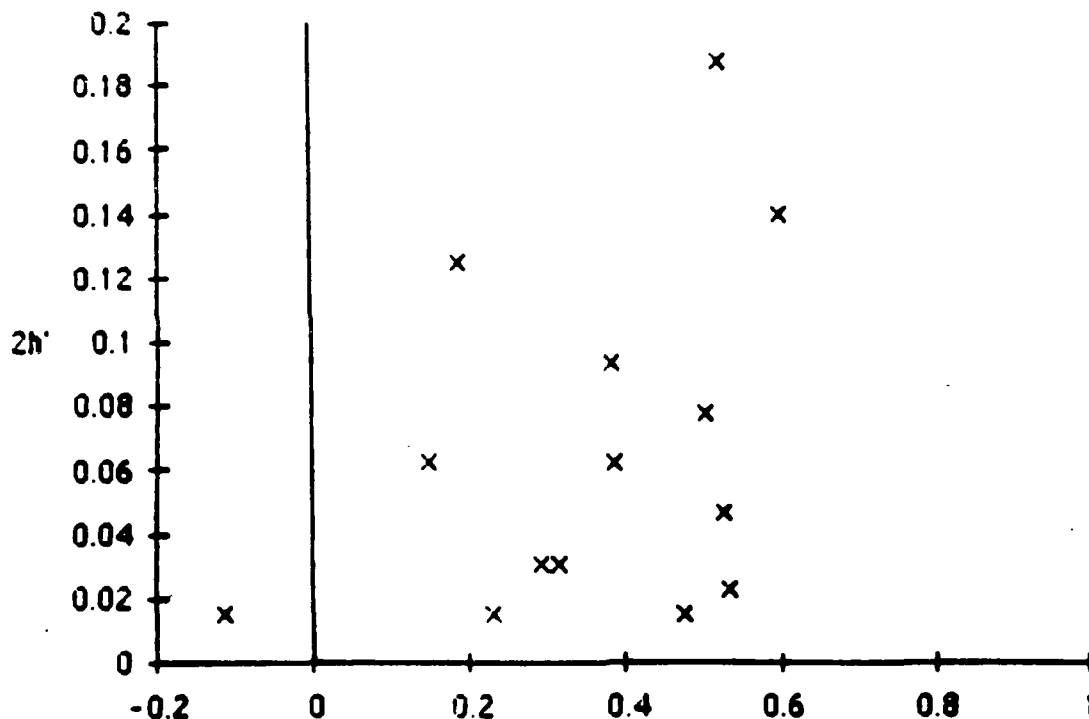
Fig. B.9: Perturbations vs. predicted critical velocity
Applying Kelvin-Helmholtz stability analysis to the crest of existing waves predicts that points to the right of zero will be unstable. In fact, no unstable waves were observed.

Jeffreys viscous sheltering

Taitel and Dukler [1976] present an expression due to Jeffreys in 1925 for generating waves by viscous force and use it in determining a transition from stratified-smooth to stratified-wavy flow. Andritsos and Hanratty [1987] use the equation for the transition to regular 2-D waves, which are only observed in low viscosity liquids for air-water flow. The necessary condition may be written

$$j_2 > \alpha \left(\frac{4 v_1 (\rho_2 - \rho_1) \ g(1-\alpha)}{S \ \rho_1 j_1} \right)^{1/2} \tag{B.2}$$

where S is some "sheltering coefficient." Jeffreys determined that the value should be around 0.3, Taitel-Dukler change this to 0.01 to fit their data, and Andritsos-Hanratty suggest 0.06 in their simplified "design criteria" section. The results for $S = 0.3$ and 0.06 are shown with the data in Fig. B.10. The correlation Eq. (B.1) is used to determine a given j_1 and j_2. It is clear that Jeffrey's original value of 0.3 is a better choice for the liquid-liquid wave duct. One point to be made is that the S value is fluid-specific, and the one-g air-water value should not be applied to other situations without some basis in experiments. More generally, Eq. (B.2) may only be a convenient correlation for gas-liquid design, whereas viscous energy transfer may actually be the mechanism of wave formation for the liquid-liquid wave duct. This is consistent with the threshold τ_i value seen in the Interfacial shear section above.
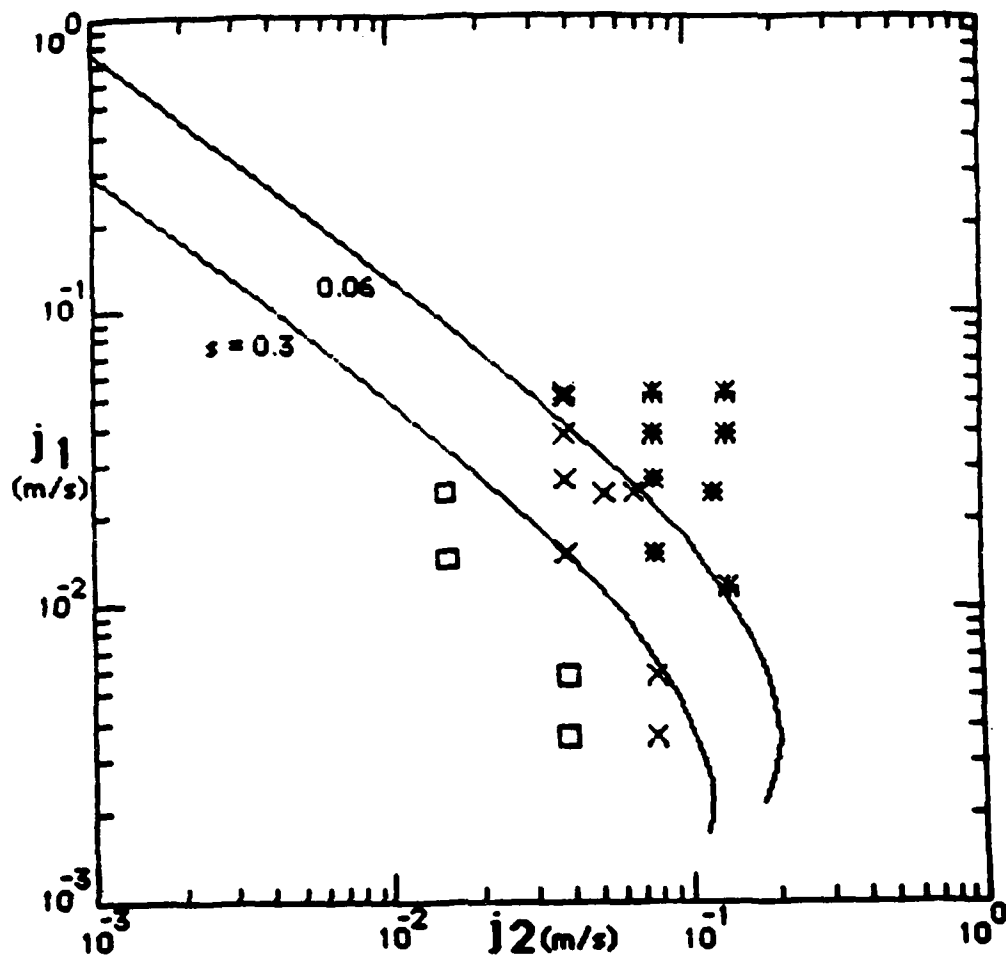
Fig. B.10: Onset of perturbations and Jeffreys viscous sheltering Flow rates to the right of the curves are predicted to show waviness. The sheltering coefficient S for air-water (0.06) and a good value for this experiment (0.3) are shown, demonstrating that the coefficient cannot be extrapolated to other fluid sets and situations such as reduced-g.

Kelvin-Helmholtz instability

A more intellectually pleasing analysis follows from the speed of small perturbations at the interface, and is known as Kelvin-Helmholtz instability [Milne-Thomson, 1950, Ishii, 1982]. For real values of the wavespeed, the waves can be propagated and the interface is stable. A quick summary based on Milne-Thomson and Ishii follows, where for the wave duct "2" is the lower fluid. For a small sinusoidal wave moving at velocity c in a closed duct, the pressure changes from fluid motion are equated to restoring effects from gravity and surface tension

$$k\rho_2(u_2-c)^2 \coth kh\alpha + k\rho_1(u_1-c)^2 \coth kh(1-\alpha) = \frac{g}{k}(\rho_2 - \rho_1) + \sigma k \quad (B.3)$$

Writing $\rho_a' = \rho_a \coth kh\alpha_a$ and $\Delta r = (\rho_2 - \rho_1)$ and solving for c gives

$$c = \frac{\rho_2'u_2 + \rho_1'u_1}{\rho_2' + \rho_1'} \pm \left(\frac{\frac{g}{k}\Delta\rho + \sigma k}{\rho_2' + \rho_1'} - \frac{\rho_1'\rho_2'(u_1 - u_2)^2}{(\rho_1' + \rho_2')^2}\right)^{1/2} \quad (B.4)$$

The interface is unstable if the term under the radical is less than zero. In terms of superficial velocity this corresponds to

$$\left(\frac{j_2}{\alpha} - \frac{j_1}{1-\alpha}\right)^2 > \left(\frac{g}{k}\Delta\rho + \sigma k\right)\left(\frac{\rho_1' + \rho_2'}{\rho_1'\rho_2'}\right) \quad (B.5)$$

If the void fraction can be expressed as in Eq. (B.1), then given an α the interface is unstable for

$$j_2 > \left(\frac{1}{\alpha} - \left(\frac{K\alpha}{\alpha}\right)^{1/m}\left(\frac{1}{1-a}\right)\right)^{-1} \sqrt{\left(\frac{g}{k}\Delta\rho + \sigma k\right)\left(\frac{\rho_1' + \rho_2'}{\rho_1'\rho_2'}\right)} \quad (B.6)$$

In order to find when the interface is stable for any value of k, the radical of Eq. (B.4) is differentiated with respect to k and set to zero. The resulting equation can be written as

$$k_c = \sqrt{\frac{g\Delta\rho}{\sigma + f(\Delta u, \alpha, k_c)}} \quad (B.7)$$

where

$$f(\Delta u, \alpha, k_c) = 2h\left(\frac{\rho_{1c}'\rho_{2c}'\Delta u}{\rho_{1c}' + \rho_{2c}'}\right)^2 \left(\frac{\alpha}{\rho_{2c}' \sinh 2k_c h\alpha} + \frac{1-\alpha}{\rho_{1c}' \sinh 2k_c h(1-\alpha)}\right) \quad (B.8)$$

and $\rho_{ac}' = \rho_a \coth k_c h\alpha_a$. The solution to Eq. (B.7) can then be substituted into Eq. (B.6) to give the condition for unconditional stability, or when the interface is stable to all wavelength perturbations. It turns out that in this case k_c varies by 16%

for the range of flows encountered, and results very close to
those of the full expressions can be found from the approximation

$$k_c = \sqrt{\frac{g\Delta\rho}{\sigma}}$$ (B.9)

and the resulting stability expression

$$\left(\frac{j_2}{\alpha} - \frac{j_1}{1-\alpha}\right)^2 < \frac{\rho_{1c}' + \rho_{2c}'}{\rho_{1c}'\rho_{2c}'} 2\sqrt{g\Delta\rho\sigma}$$ (B.10)

where   Eq. (B.10) can also be written in the form of Eq. (B.6).
     The solution to Eq. (B.10) is plotted with the data in
Fig. B.11, and is indistinguishable from the solution using the
full expression for k_c. The analysis becomes invalid for large
scale perturbations, but shows a remarkably good delineation of
the area of large waves. Again, the definition of large-scale
waves (those whose wavelength or wavespeed can be measured from
videotapes) is somewhat arbitrary. This onset of large "roll"
waves causes a marked departure from perturbed flow
characteristics, and is considered by several authors to denote
the onset of intermittent-type flows. The rightward curve of the
line is the result of considering the density of both fluids; when
gas density is neglected in comparison with the liquid density,
the line peels off to the left with increasing j_1.
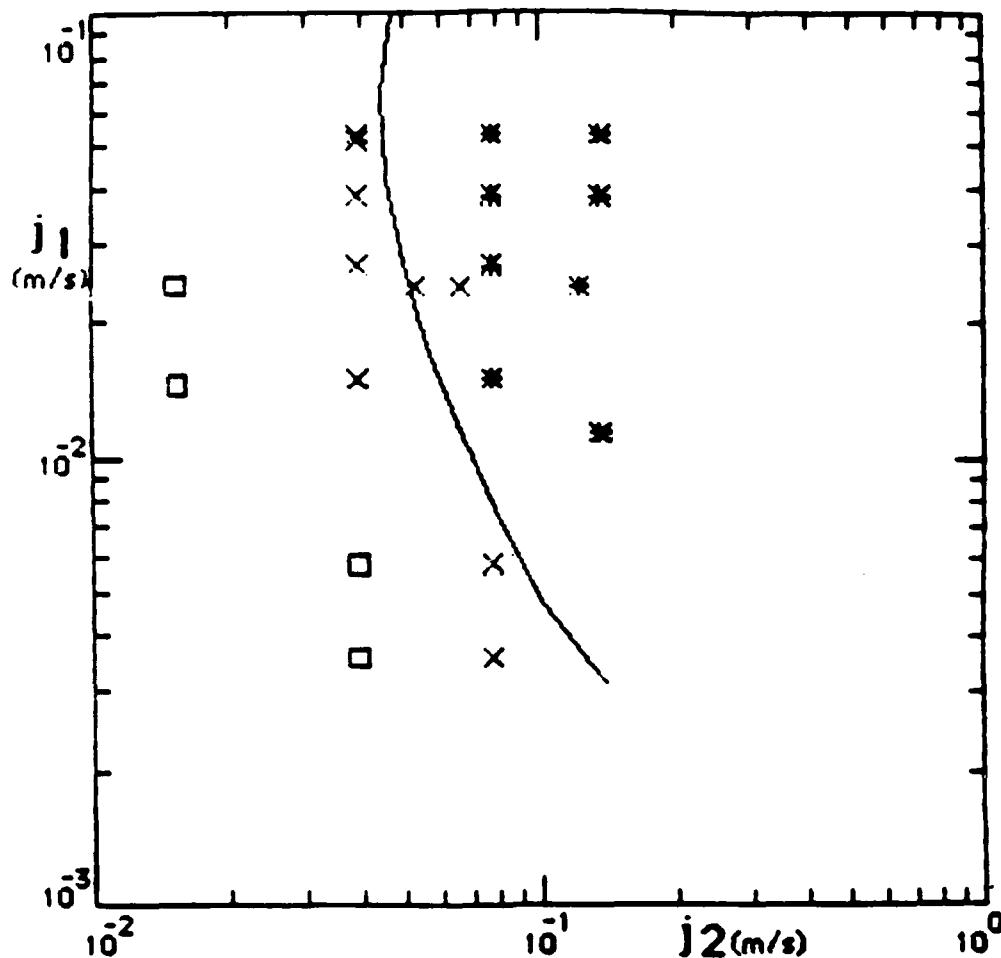
Fig. B.11:   Initiation of roll waves and Kelvin-Helmholtz
instability

Flow rates to the right of the curves are predicted to be unstable
to small perturbations, and therefore show larger roll waves.
Good results are seen for this simple theory.

   The wavelengths that could be measured ranged from 0.04 to
0.08 m and averaged 0.068 m; the average of critical wavelengths
predicted by Eq. (B.7) is 0.058 m. This is fairly close,
considering that the wavelengths are likely to change for the
large scale motions. Conditionally stable areas resulting from
Eq. (B.6) are shown in Fig. B.12, where neutral stability curves
are plotted as wavelength versus j_2 for a range of α's. The
contributions of the gravity and surface tension components are
displayed in Fig. B.13. Gravity stabilizes large wavelength
perturbations, and surface tension stabilizes small wavelength
disturbances. If either of these terms is zero, the flow is only
conditionally stable.

B21
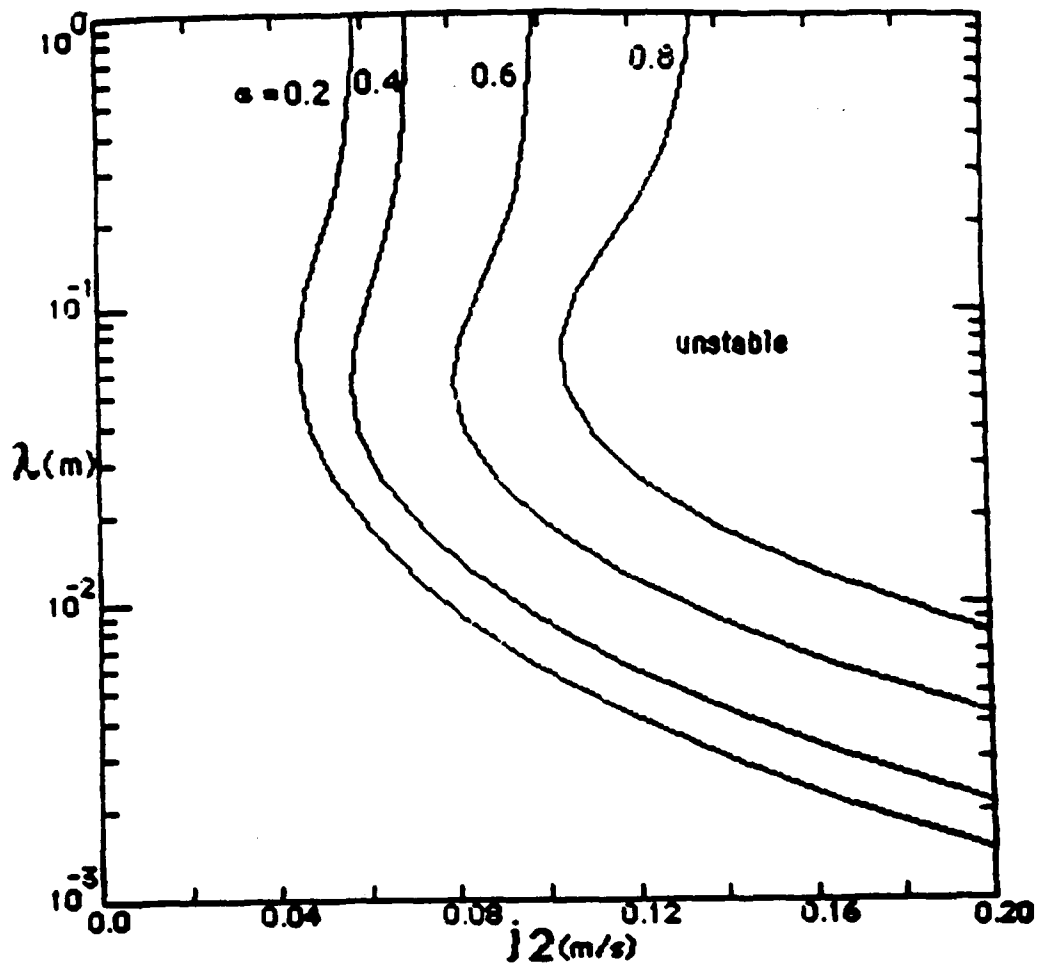
Fig. B.12: Conditional Kelvin-Helmholtz stability and wavelength
Four curves for different α values are shown, demonstrating which
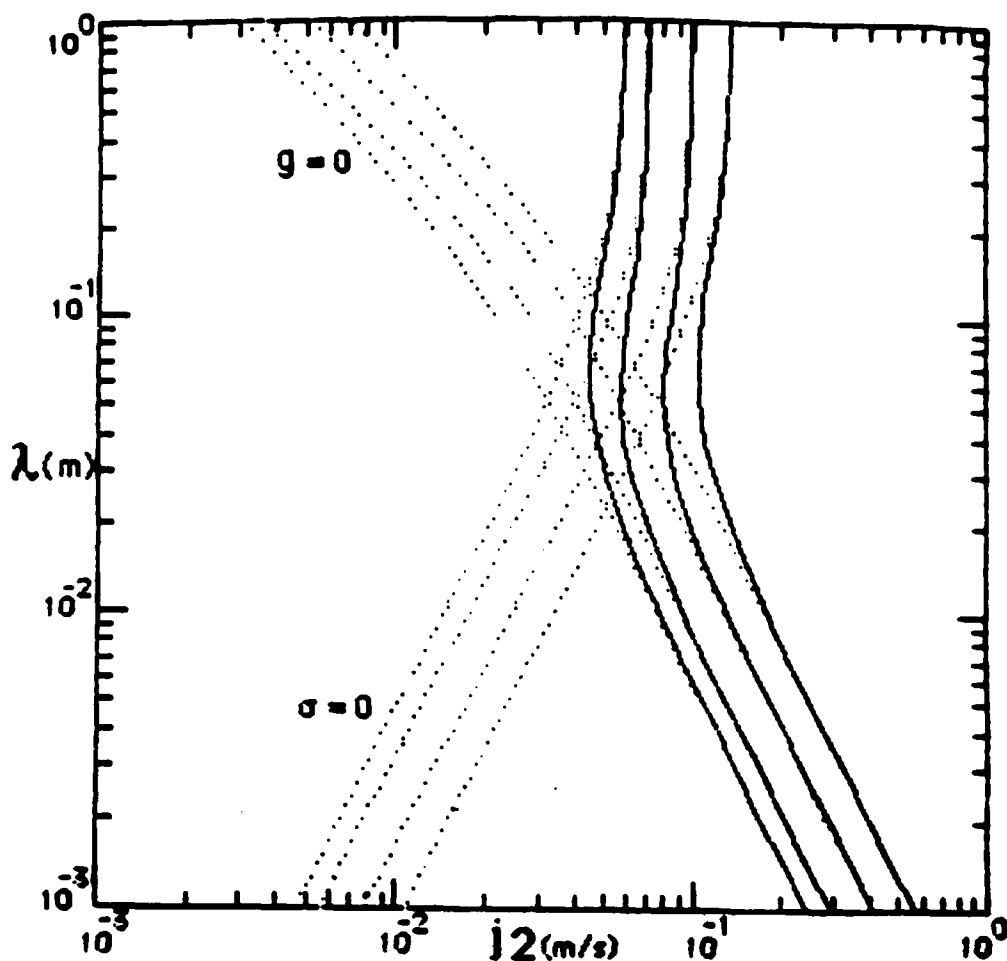wavelength perturbations are unstable for a given water flow.

Fig. B.13: Conditional stability, gravity and surface tension contributions

Figure B.12 is re-plotted with a different x-axis scale, and the contributions of gravity and surface tension are shown by setting either one to zero. In either case, any flow is only conditionally stable. For low-g conditions, long wavelength disturbances will be the cause of instability.

Lin-Hanratty [1986] and Andritsos-Hanratty [1987] extend the K-H analysis to include shear and inertia effects. These developments show good results for one-g gas-liquid, but are of a level beyond the scope of this study. These methods should apply to finite micro-g flow, but may be "overkill" if the instability occurs at low flow rates.

B.5 Conclusions

These experiments were initiated with a wide and rather amorphous objective of investigating interfacial shear and interfacial instabilities with low buoyancy. Equipment difficulties and limitations reduced this to smaller areas of investigation.

No unstable waves (showing bridging or entrainment) were observed, contrary to expectations for a situation with such small restoring forces from buoyancy. The possible reasons were low flow rates, short test section length, and lack of large inertial differences. It is suggested that the gas-liquid inertial difference is a key factor in wave instability, and must be addressed in attempts to analyze these instabilities.

The Jeffreys viscous sheltering criterion is often used to predict the onset of interfacial perturbations for one-g air-aqueous flows, using a sheltering coefficient $S = 0.01-0.06$. The suitable value for this fluid system was 0.3, and the conclusion is that the sheltering coefficient should not be extrapolated to other fluid sets or conditions without experimental tests.

On a differential level, a threshold interfacial shear was seen to separate placid and perturbed interfacial conditions. This is linked to velocity profiles by viscosity, and may be related to onset of perturbations of interfaces in other flow types (e.g. slug bubbles). Extensions into this area were not undertaken here.

Inviscid Kelvin-Helmholtz theory applied with given plug flow velocities and interfacial height showed good delineation of small perturbations and large-scale waves, despite neglecting the fluids' viscosity. K-H theory overpredicts the velocities required for perturbation instability in one-g gas-liquid flow because it does not involve liquid inertia and pressure and interfacial shear fluctuations. The predicted instability for reduced gravity levels will occur at lower flow rates, and hence the simple K-H theory may be applicable. Long wavelength perturbations are predicted to be unstable for reduced-g's.

Nomenclature

A	area of duct or pipe (m^2)
A_n	constant coefficient for harmonic terms (m/s)
B_n	constant coefficient for harmonic terms (m/s)
c	wavespeed (m/s)
C_1	slug flow duct/bubble area ratio ( )
C_f	friction factor ( )
D	diameter, hydraulic diameter (m)
h	duct height (m)
h'	vertical coordinate (m)
I_n	interfacial velocity integral term (m/s)
j	superficial velocity (velocity based on entire duct area) (m/s)
k	wavenumber, $= 2\pi/\lambda$ (m^{-1})
K_α	correlation factor for α ( )
l	dimensionless mixing length ( )
m	correlation exponent for α ( )
n	seperate-cylinders exponent ( ); summation variable ( )
N	duct summation factor, $= n\pi h/2w$ ( )
p	pressure; stress fluctuation (N/m^2)
Q	volumetric flow rate (m^3/s)
r_e	bubble-end radius of curvature (m)
r_e'	dimensionless bubble-end radius of curvature ( )
Re	Reynolds number ( )
Re_j	liquid slug Reynolds number ( )
S	viscous sheltering coefficient ( )
u	velocity (m/s)
v	velocity (m/s)
w	duct width (m)
w'	horizontal coordinate (m)
W	duct factor, $= w^2 \nabla p/\mu$
x	dimensionless horizontal coord ( ); quality (mass fraction of component 2) ( )
X	Martinelli parameter ( )
y	dimensionless vertical coord ( )

Y	dimensionless interface and viscosity term ( )
z, z'	flow direction coordintate (m)

Greek symbols

α	volume fraction (without subscript = void fraction, or volume fraction of component 2) ( )
ϕ	frictional pressure gradient ratio ( )
Φ	velocity function (m/s)
μ	viscosity (kg/ms)
ρ	density (kg/m^3)
ρ'	closed duct adjusted density, $= \rho_a \coth kh\alpha_a$
σ	surface tension (N/m)
τ	shear stress (N/m^2)

Subscripts

1	liquid; simulated liquid; more viscous component
2	gas; simulated gas; less viscous component
a,b	dummy subscripts representing 1 or 2
c	critical
H	homogeneous
i	at interface
l	laminar
s	from surface tension
SC	separate-cylinders
t	turbulent; from turbulence

APPENDIX C

Velocity of Surface Tension Waves

An equation has been derived to predict interfacial wave velocities between two fluids in a rectangular duct when buoyancy is almost negligible. The equation predicts the speed of a wave under the influence of surface tension alone. The equation is two-dimensional -- that is, effects from the sides of the duct are assumed insignificant. The equation assumes that an inviscid fluid with a finite depth and wave amplitude wets a flat solid surface. An infinite height is assumed for the second fluid, which does not wet the solid surface. Negligible buoyancy-- only enough to stratify the two fluids -- is assumed. The resulting equation for wave speed is:

$$c = \sqrt{\frac{2\sigma\left(A + \delta\right)}{\rho_f\left[\left(A + \delta\right)^2 - \delta\right]}} = \lambda f \qquad \text{(C-1)}$$

where: c is wave speed
           A is amplitude
           δ is average film thickness
           σ is interfacial tension
           ρ_f is density of liquid in the film
           λ is wave length
           f is frequency

Most of the wave speed equations in the literature are for$, stratified flow with significant buoyancy. The force of gravity is included in all such equations. Therefore, unlike equation C-1, they usually cannot be converted to calculate wave speed on$, microgravity annular films.

A diagram showing the derivation of equation C-1 is shown in Figure C-1. The equation expresses a balance between Bernoulli's equation and interfacial tension. Average velocities are used to solve the wave continuity equation.

In Figure C-2 the predicted wave speed is plotted versus the amplitude, with depth of the fluid as a parameter. Although the plotted depths are varied from 0.017 to 0.023 to 0.029 meters, the curves coincide. The three depths plotted are the maximum, average, and minimum film depths observed in the wave duct experiments of Appendix B. The fact that the three depths fall onto almost the same line shows that, in these experiments, predicted wave velocity is virtually uninfluenced by fluid depth. That is, in the experimental range of water depths, predicted wave speed is essentially a function of amplitude alone. Therefore, all further plots ignore water depth. Wave velocity is plotted as a function of amplitude alone, although the observed water depth is used at each individual point calculated.

A wave of amplitude A travels at velocity C along the interface between a stationary liquid of thickness δ_1 and density ρ_f and a stationary fluid of infinite depth. There is negligible buoyancy, just enough to maintain stratification. Wave speed is therefore a function of surface tension σ.
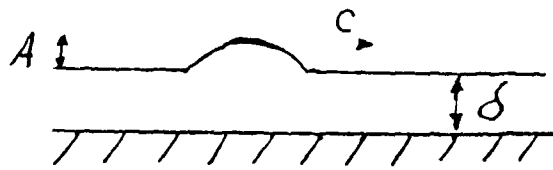
Select a control volume to travel at velocity C with the wave:
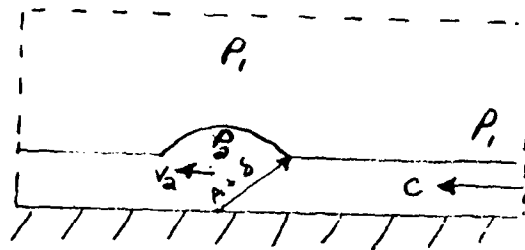
Calculate pressures P_1 and P_2 from Bernoulli's equation and surface tension relationships; calculate V_2 (velocity of liquid inside wave) from continuity:

$$P_1 + \frac{1}{2}\rho_f C^2 = P_2 + \frac{1}{2}\rho_f V_2^2$$

$$P_2 = P_1 + \frac{\sigma}{A + \delta}$$

$$V_2 = \frac{c\delta}{\delta + A}$$

Figure C-1.   Surface Tension Wave

These equations can be solved to show that:

$$C = \sqrt{\frac{2\sigma(A+\delta)}{\rho_f\left[(\delta+A)^2 - \delta^2\right]}}$$

As amplitude A approaches zero:

$$C \rightarrow \sqrt{\frac{2\sigma\delta}{\rho_f(\delta^2-\delta^2)}} = \infty$$

As film depth δ approaches zero:

$$C \rightarrow \sqrt{\frac{2\sigma}{\rho A}}$$

Figure C-1. (continued)
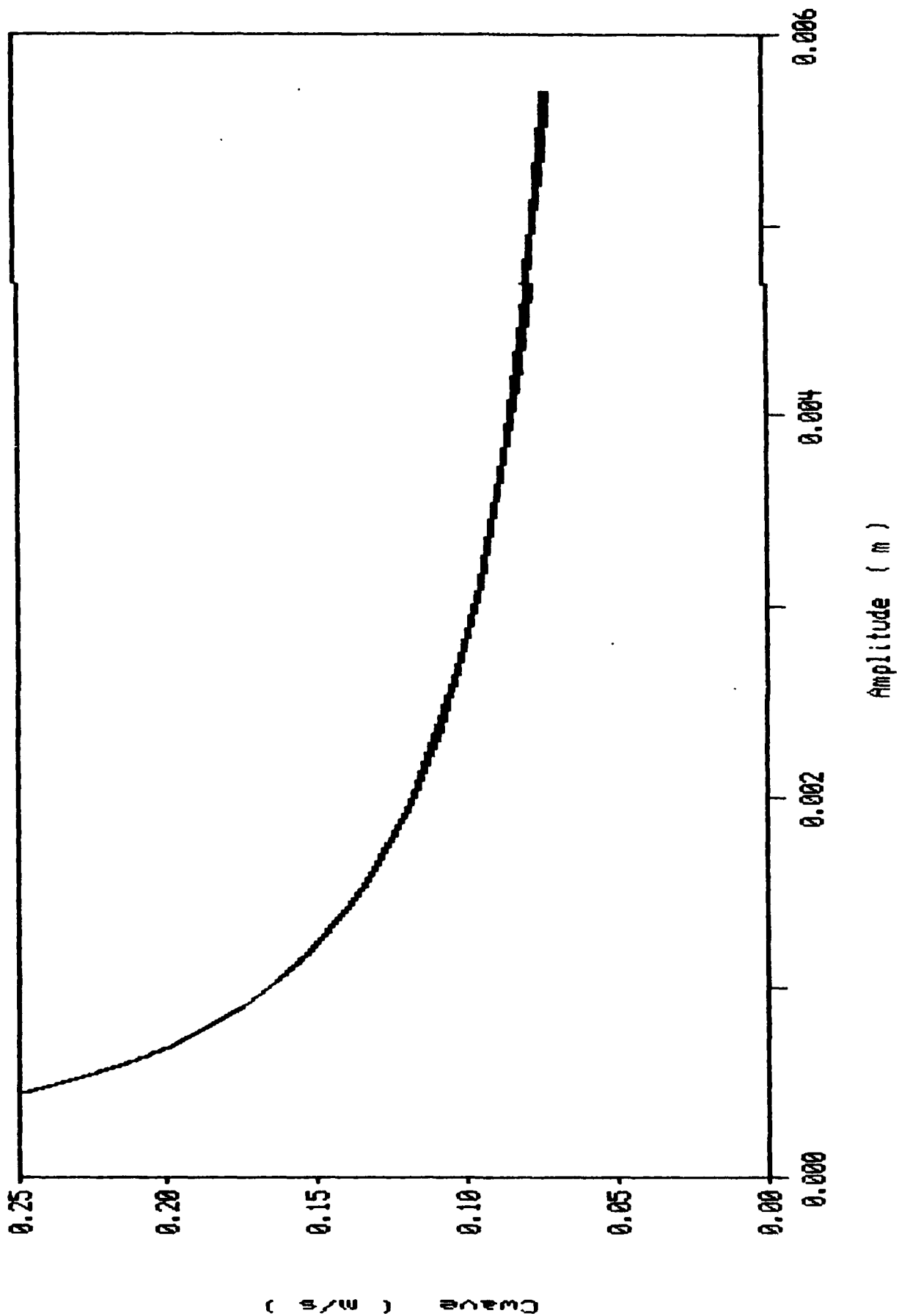
Figure C-2. Predicted Wave Speed as a Function of Amplitude.
Water Depth = 0.017 to 0.029 meters

Wave speed data from the wave duct experiments is compared with predictions in Figures C-3 through C-6. The plots should be relatively self-explanatory. The discussion below will clarify the details.

In all cases, waves were generated by proper choice of water and oil flow rates. Amplitudes and wave speed were recorded. Equation C-1 was used to predict a wave speed as a function of the observed amplitude.

Wave speed predictions from Equation C-1 are all with respect to the interface. Since the liquid interface was moving, the measured wave speed always includes an interface speed. To properly compare predictions with data, interface velocity must be accounted for. Unfortunately, interface velocities were difficult to measure. Therefore, predicted average interface velocities from a laminar, three-dimensional rectangular flow model[1] were subtracted from the wave speed data. This permitted direct comparison to predicted wave speed.

Appendix B gives full details of the wave duct experiments and geometry. Briefly, the fluids used were Dow-Corning 200 silicone oil and water. At 20° C the specific gravity of the silicone oil was 0.958 and interfacial tension with respect to water was 0.027 N/m. The water formed the inviscid film, the silicone was the fluid above the inviscid film.

The wave duct was square in cross section -- 50.8 x 50.8 mm (2.0 x 2.0 in). It was about 1.8 m (72 in) long. Wave measurements were made at three points along the wave duct. Location 1 was 0.48 m from the entrance. Location 2 was 0.89 m from the entrance. Location 3 was 1.4 m from the entrance and was thought to exhibit the most fully developed behavior.

Figure C-3 shows predicted and measured wave speed at Location 3.

Figure C-4 shows predicted and measured wave speed at Location 2.

Figure C-5 shows predicted and measured wave speed at Location 1.

Figure C-6 shows predicted versus measured wave speed from all the locations -- 1, 2, and 3.

---

[1] This model was created by J. Dzenitis [1988] who also performed the wave duct experiments. Verifiable predictions of this three dimensional model (such as void fraction) were generally in good agreement with wave duct measurements.
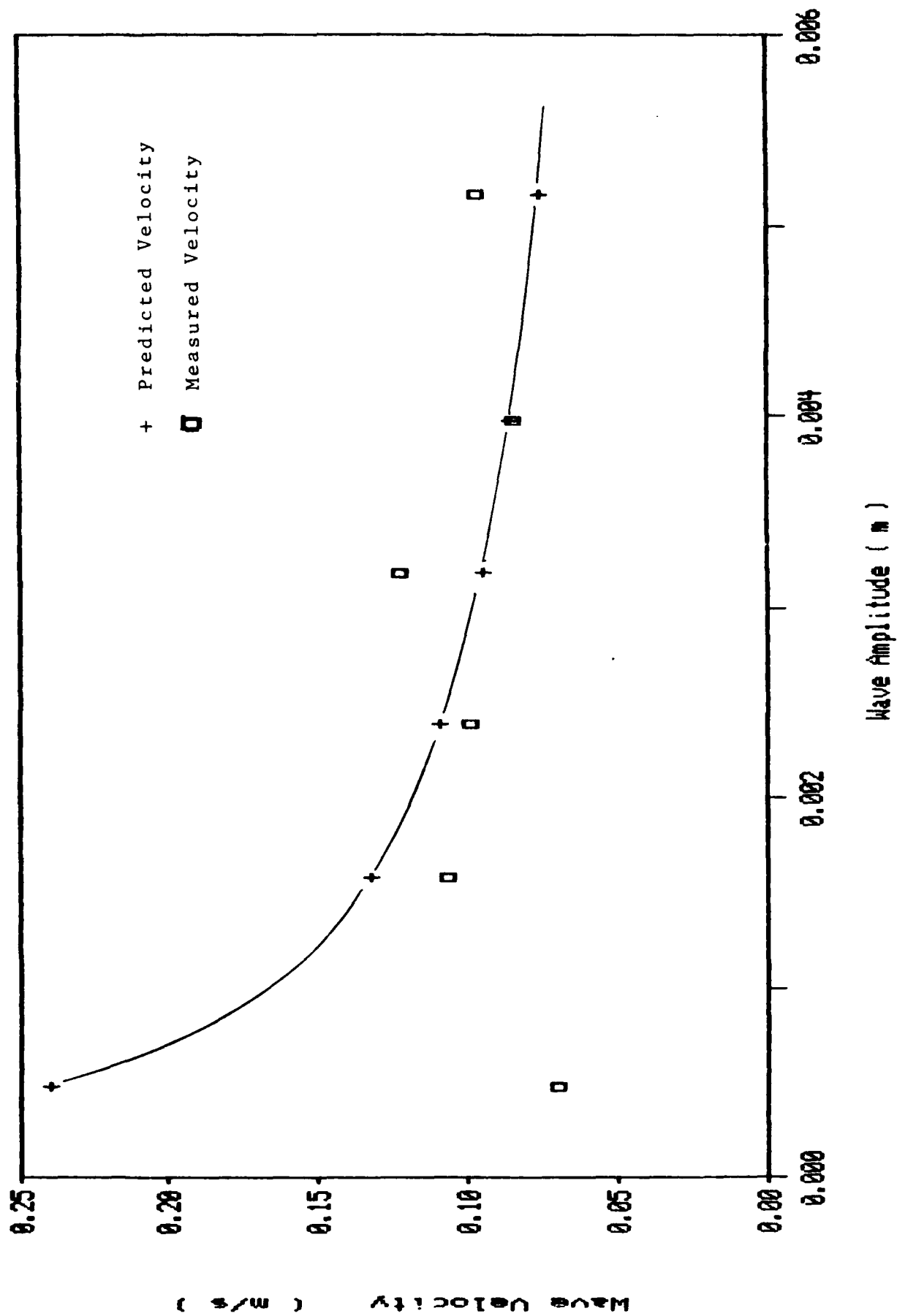
Figure C-3. Measured vs. Predicted Wave Velocity -- Location 3.
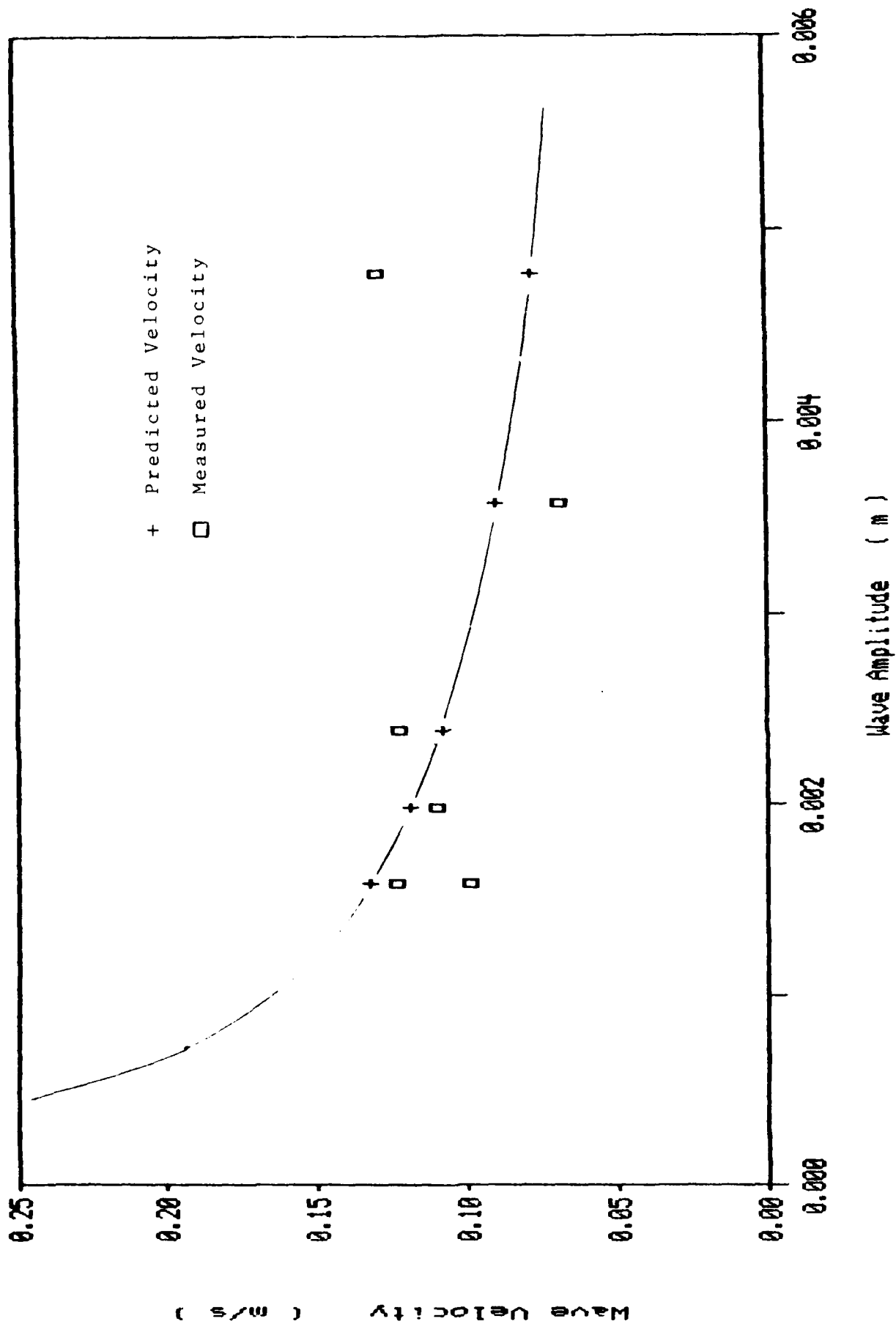RELATIVE to Interface Velocity.

Figure C-4. Measured vs. Predicted Wave Velocity -- Location 2.
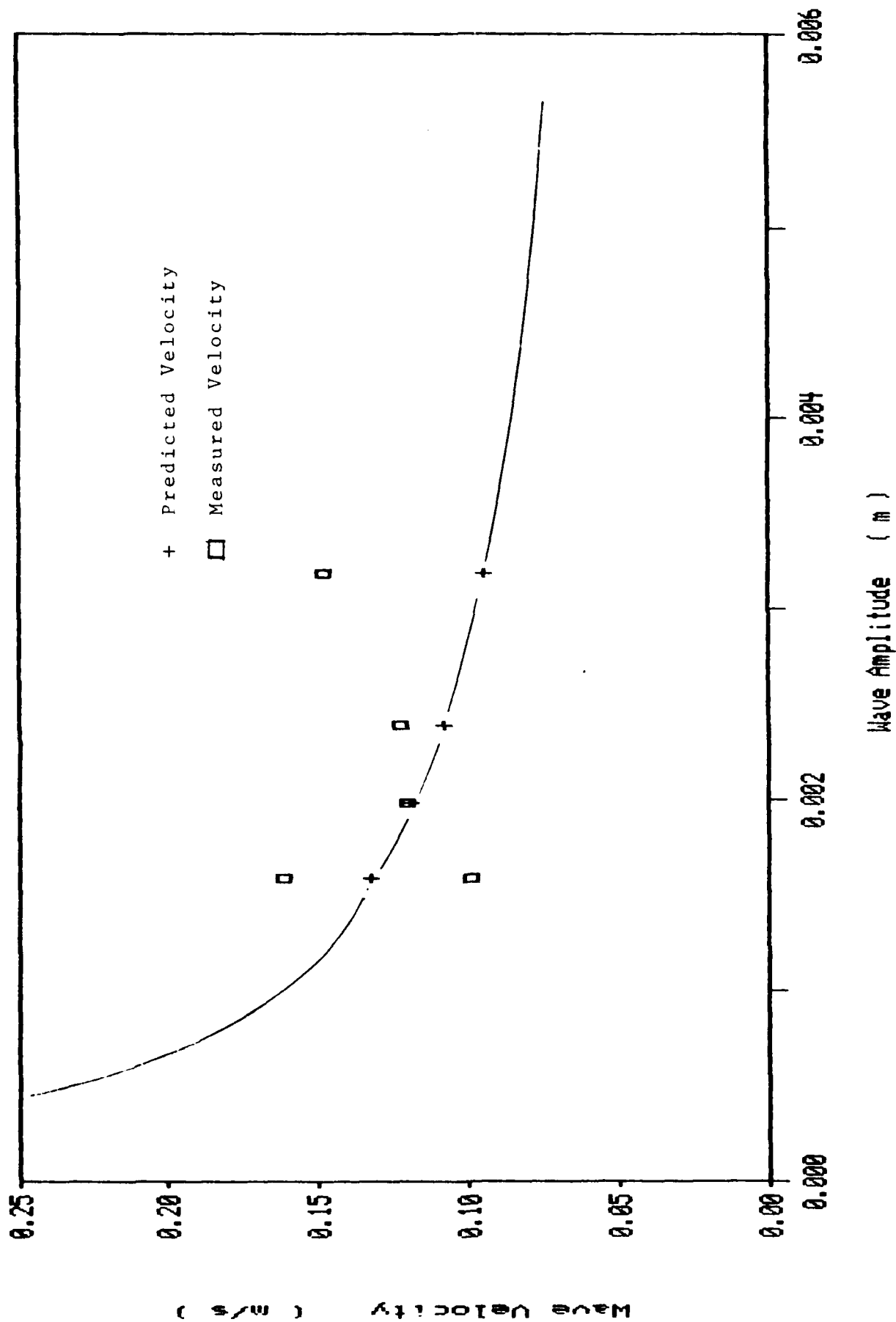RELATIVE to Interface Velocity.

Figure C-5. Measured vs. Predicted Wave Velocity -- Location 1.
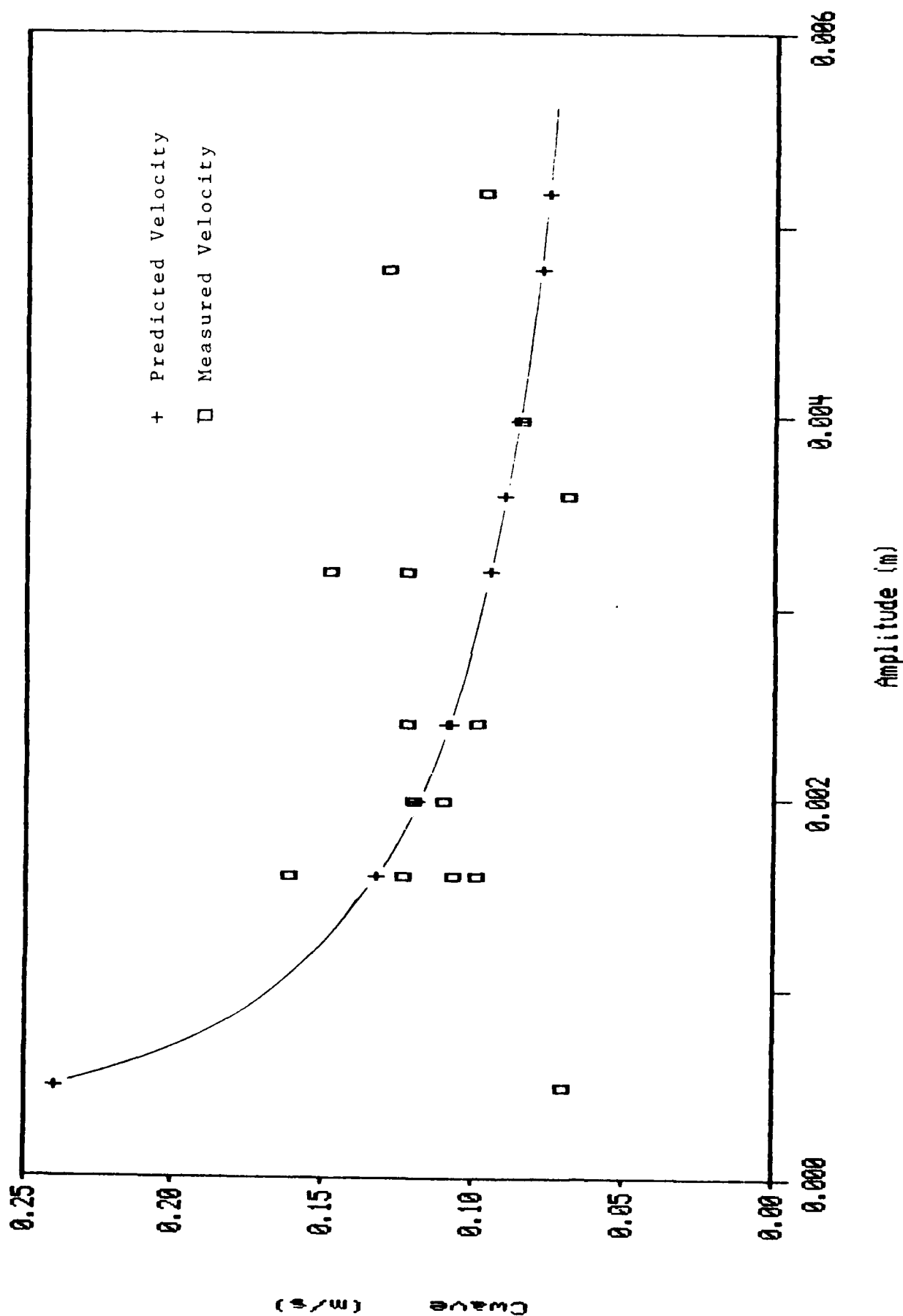RELATIVE to Interface Velocity.

Figure C-6.   Measured vs. Predicted Wave Velocity -- All Locations.
RELATIVE to Interface Velocity.

The following conclusions can be drawn from the figures:

- The agreement of this simple theory and the preliminary wave duct experiments, particularly at Location 3 where the flow is most fully developed, is quite good, except at very low amplitudes.

- Probably viscous forces not considered in this simple analysis are dominant at very low amplitudes. Such a viscous damping term would improve predictions at very low amplitudes, but would be of secondary effect at higher amplitudes. Nevertheless, even at higher amplitudes, such a term might improve predictions. If such a term is successfully discovered and added to the present equation, a wave equation with a maximum velocity may result. This would mean that some large waves will catch smaller waves, matching qualitative observations of films of microgravity annular flow.

The form and results of the surface tension wave speed equation are dependent on the wave geometry assumed. From Figure C-1 it should be clear that the wave radius is arbitrarily taken from the bottom of the duct. This approach seems to give a reasonable approximation to the top half of the sinusoidal waves observed. The analysis ignores wave troughs and deals only with wave peaks. An analysis of trough speed should produce the same results as this analysis of peak speed.

The derivation of the wave speed equation assumes that the fluid in the film is inviscid, in order to apply the Bernoulli equation. The only assumption made about the second fluid is that the same pressure exists just above the peak of a wave as exists behind the wave at the fluid interface. Because of the low wave amplitude, this seems a reasonable assumption, even in a closed duct.

As shown in Figures C-3 through C-6 and noted above, the wave duct experiments give a reasonably good confirmation of Equation C-1.

However, the wave duct data do not confirm the equation in all situations where negligible buoyancy exists (eg, microgravity annular flow). Specifically, the wave duct experiments have large "film" depths and small wave amplitudes. The situation is often reversed in microgravity annular flows, especially near transition to slug flow. Furthermore, the equation does not predict when waves form, it only attempts to predict the speed of a wave once it exists.

Nevertheless, it is encouraging that Equation C-1 is reasonably close to the data. It appears to give a good first order

C-12

approximation for wave speed in situations when wave amplitude is much smaller than the depth of either fluid.

Despite these unknowns, the wave speed equation was modified for annular geometry and the effect of wave "pinching" on core flow. It was then applied to microgravity annular flow. An attempt was made to predict the transition from annular to slug flow based on the bridging of annular waves. An annular wave was assumed to bridge when its volume was large enough to do so and its surface tension was not sufficient to prevent growth. Wave growth was hypothesized to be a balance between surface tension and Bernoulli effects. Bernoulli effects were calculated as a function of wave size and speed. Neglected effects were: inertial effects of the growing wave, shear and form drag on the wave from the vapor core, and drag on the wave from the tube wall.

However, the minimized pressure gradient principle, explained in the main report, proved a simpler and more successful approach to predicting flow regime transitions. Therefore, the work with wave speed was discontinued.

If the wave analysis were to be continued, it is believed that the neglected effects mentioned above would need to be included. Preliminary work balancing wave from drag against wall shear (and ignoring surface tension) indicates much lower predicted wave velocities than those of the surface tension waves. It is unclear how such shear effects will interact with surface tension effects in a final expression for wave speed on a microgravity annular film.

APPENDIX D

Integral Annular Flow Analysis

TABLE OF CONTENTS

NOMENCLATURE

Units are given in MKS system for clarity, although any consistent system of units will work with the equations in this Appendix.

Symbol		Description	Units
A	-	cross sectional area of pipe	[m^2]
A_f	-	cross sectional area of pipe occupied by liquid	[m^2]
A_g	-	cross sectional area of pipe occupied by vapor	[m^2]
c_i	-	interfacial friction factor	-
c_w	-	wall friction factor	-
D	-	diameter of pipe	[m]
d_o	-	diameter of vapor core in annular flow	[m]
j_f	-	liquid volumetric flux (or superficial velocity)	[m/s]
j_g	-	vapor volumetric flux (or superficial velocity)	[m/s]
j_i	-	component volumetric flux (i.e., liquid or vapor)	[m/s]
k_f	-	turbulent coefficient for liquid friction factor	-
k^g	-	turbulent coefficient for vapor friction factor	-
L	-	length of pipe	[m]
P	-	perimeter	[m]
ΔP	-	pressure drop	[N/m^2]
ΔP_f	-	pressure drop of liquid	[N/m^2]
ΔP_g	-	pressure drop of vapor	[N/m^2]
R	-	radius of pipe (= constant = D/2)	[m]
r	-	radius (variable)	[m]

Symbol		Description	Units
Re	-	Reynold's Number	-
Re_f	-	liquid Reynold's Number	-
Re_g	-	vapor Reynold's Number	-
V	-	velocity	[m/s]
V_f	-	velocity of liquid	[m/s]
V_g	-	velocity of gas or vapor	[m/s]
V_i	-	velocity of interface	[m/s]

Greek Letters

α	-	void fraction	-
ρ_f	-	density of liquid	[kg/m^3]
ρ_g	-	density of gas or vapor	[kg/m^3]
μ_f	-	viscosity of liquid	[$N\text{-}s/m^2$
μ_g	-	viscosity of gas or vapor	[$N\text{-}s/m^2$]
τ	-	shear stress	[N/m^2]
τ_i	-	shear stress at interface	[N/m^2]
τ_w	-	shear stress at pipe wall	[N/m^2]

Subscripts

f	-	refers to liquid
g	-	refers to gas or vapor (or the liquid simulating a vapor)
i	-	refers to interface, or rarely, to component
w	-	refers to pipe wall

Superscripts

     m   -   liquid turbulent velocity profile exponent

     n   -   vapor turbulent velocity profile exponent

     x   -   exponent for turbulent liquid friction factor

     y   -   exponent for turbulent vapor friction factor

     $\sim$ -   average value (e.g., $\tilde{v}_g$ - average vapor velocity)

ANNULAR FLOW RELATIONSHIPS

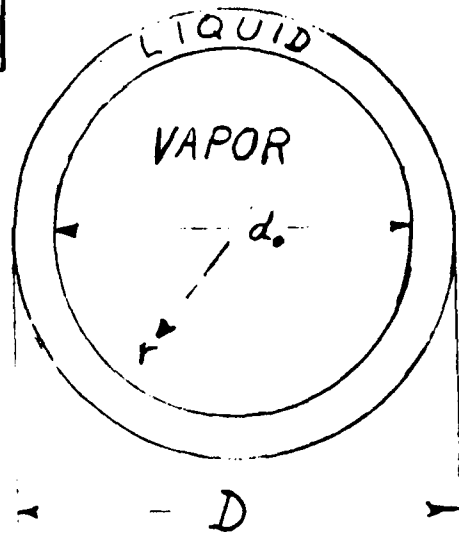$$\left[\text{For pure annular flow (eg. no entrained liquid)}\right]$$

flow areas:

$$A_g = \frac{\pi d_o^2}{4}$$

$$A_f = \frac{\pi}{4}(D^2 - d_o^2)$$

$$A = A_g + A_f = \frac{\pi D^2}{4}$$

void fraction:

$$\alpha = \frac{A_g}{A} = \frac{d_o^2}{D^2}$$

hydraulic diameter (liq.)

$$D_H = \frac{4A_f}{P_{wetted}} = \frac{4A_f}{\pi D} = D(1-$$

VAPOR MOMENTUM BALANCE
(frictional pressure drop only)

for VAPOR control volume of length L:
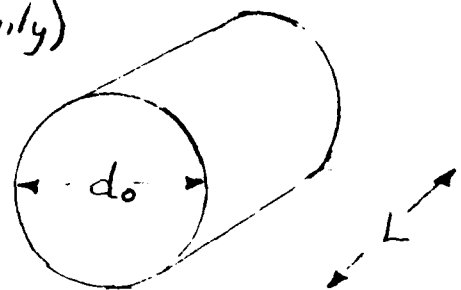
. shear force at perimeter:
(ie, at vapor-liquid interface)

$$\tau_i = C_i \frac{1}{2} \rho_g \left(\overline{V}_g - V_i\right)^2$$

frictional pressure drop:

$$\boxed{\Delta P_g = \frac{2 C_i \rho_g \left(\overline{V}_g - V_i\right)^2 L}{d_o}} \qquad (1)$$

eqn 1 is the standard single phase pressure drop derived by balancing frictional pressure loss against wall shear:

$$\Delta P_g \frac{\pi d_o^2}{4} = \tau_i \pi d_o L \qquad (1a$$

LIQUID MOMENTUM BALANCE:
(frictional press drop only)

note: $\Delta P = \Delta P_f = \Delta P_g$

$$\left(\begin{array}{c} \text{force on liquid} \\ \text{element due to } \Delta P \end{array} + \begin{array}{c} \text{force on liquid} \\ \text{element from} \\ \text{vapor shear} \end{array} \right) = \begin{array}{c} \text{shear force} \\ \text{of liquid} \\ \text{at wall} \end{array}$$

$$\Delta P \frac{\pi}{4}\left(D^2 - d_o^2\right) + \underbrace{\tau_i \, \pi \, d_o \, L} = \tau_w \, \pi \, D \, L$$

$$\updownarrow \text{ equivalent } \left[\text{Eqn } 1a\right]$$

$$\Delta P \frac{\pi}{4}\left(D^2 - d_o^2\right) + \overbrace{\Delta P \frac{\pi}{4} d_o^2} = \tau_w \, \pi \, D \, L$$

$$\therefore \quad \Delta P \frac{\pi}{4} D^2 = \tau_w \, \pi D L$$

where: $\quad \tau_w = C_w \frac{1}{2} \rho_f \tilde{V}_f^2$

$$\Delta P_f = \frac{2 C_w \rho_f \tilde{V}_f^2 L}{D} \qquad (2)$$

GENERAL EQUATION OF ANNULAR FLOW
since $\Delta P_f = \Delta P_g$; set EQN 1 = EQN 2

$$\boxed{\frac{C_i \rho_g \left(\tilde{V}_g - V_i\right)^2}{d_o} = \frac{C_w \rho_f \tilde{V}_f^2}{D}} \qquad (3)$$

(OVER-) SIMPLIFIED SOLUTION

start with eq^n 3:

$$\frac{C_i \, \rho_g \, (\tilde{V}_g - V_i)^2}{d_o} = \frac{C_w \, \rho_f \, \tilde{V}_f^2}{D} \qquad (3)$$

over-simplify by assuming:

$$C_i = C_w \quad (\approx 0.005)$$

$$\tilde{V}_g >> V_i$$

identities:
$$j_g = \tilde{V}_g \, \alpha$$
$$j_f = \tilde{V}_f \, (1-\alpha)$$

$$\frac{\rho_g \, \tilde{V}_g^2}{d_o} = \frac{\rho_f \, \tilde{V}_f^2}{D}$$

combining with Annular void fraction:

$$\sqrt{\alpha} = \frac{d_o}{D} = \frac{\rho_g \, \tilde{V}_g^2}{\rho_f \, \tilde{V}_f^2}$$

using volumetric fluxes (ie, superficial velocities):

$$\sqrt{\alpha} = \left(\frac{1-\alpha}{\alpha}\right)^2 \frac{\rho_g \, j_g^2}{\rho_f \, j_f^2}$$

$$\frac{\alpha^{2.5}}{(1-\alpha)^2} = \frac{\rho_g \, j_g^2}{\rho_f \, j_f^2} \qquad (4)$$

$$j_g = j_f \sqrt{\frac{\rho_f}{\rho_g}} \, \frac{\alpha^{1.25}}{1-\alpha} \qquad (5)$$

General Solution to
General Equation of Annular Flow

repeating eqn 3 from above:

$$\frac{c_i \rho_g (\hat{V}_g - V_i)}{d_o} = \frac{c_w \rho_f \hat{V}_f^2}{D}$$

Evaluate c_i, c_w V_i :

identities:
$$j_g = \tilde{V}_g \alpha$$
$$j_f = \tilde{V}_f (1-\alpha)$$

First evaluate Re_f, Re_g :

$$Re_f = \frac{D_H \rho_f \tilde{V}_f}{\mu_f} = \frac{(1-\alpha) D \rho_f \tilde{V}_f}{\mu_f} = \frac{j_f \rho_f D}{\mu_f}$$

$$Re_g = \frac{d_o \rho_g (\tilde{V}_g - V_i)}{\mu_g} = \frac{\sqrt{\alpha} D \rho_g (\tilde{V}_g - V_i)}{\mu_g}$$

If liquid film is laminar :

$$c_w = \frac{16}{Re_f}$$

$$V_i = 2\tilde{V}_f = 2j_f/(1-\alpha)$$

If liquid fim is turbulent

$$c_w = \frac{K_f}{Re_f^x}$$ where $\begin{pmatrix} K_f = 0.046 \\ \text{and} \\ x = 0.2 \end{pmatrix}$ OR $\begin{pmatrix} K_f = 0.079 \\ \text{and} \\ x = 0.25 \end{pmatrix}$

$$V_i = \frac{j_f (m+1)(m+2)}{2(1-\sqrt{\alpha})(1+(m+1)\sqrt{\alpha})}$$

where m is exponent of turbulent velocity profile. Typically $m = \frac{1}{7}$, but can be function of Re_f

---

V_i for laminar case is derived by integrating laminar shear stress over the radius in an annular film and solving for V_i

V_i for turbulent case is derived from the turbulent velocity distribution: $V(r) \propto (1 - \frac{r}{R})^m$ assumed for a turbulent annular film.

(CONTINUED →)

If vapor core is laminar:

$$C_i = \frac{16}{Re_g}$$

If vapor core is turbulent:

$$C_i = \frac{K_g}{Re_g^y} \quad ; \quad \left(\begin{matrix} K_g = 0.046 \\ \text{and} \\ y = 0.2 \end{matrix} \right) \quad \text{OR} \quad \left(\begin{matrix} K_g = 0.079 \\ \text{and} \\ y = 0.25 \end{matrix} \right)$$

(this last assumption is the "smooth tube"
friction factor; it is suspect if
liquid film is wavy)

For wavy liquid film and turbulent vapor:

$$C_i = 0.005 \left[1 + 150 \left(1 - \sqrt{\alpha} \right) \right]$$

(this form is good for small "surface
roughness" waves. It has not been
incorporated in present analysis,
but will be in future.)

L-L CASE (Laminar Vapor – Laminar Liquid)

analytical solution (by integration of laminar shear force over radius):

$$V_g = V_f \frac{\alpha}{1-\alpha} \left(\frac{\mu_f}{\mu_g} \frac{\alpha}{1-\alpha} + 2 \right)$$

other useful relationships:

$$\widetilde{V}_f = \frac{\Delta P D^2}{32 \mu_f L} (1-\alpha)$$

$$V_f(r) = \frac{\Delta P D^2}{16 \mu_f L} \left(1 - \frac{r^2}{R^2} \right) \quad ; \quad \frac{d_0}{2} \leq r \leq \frac{D}{2} = R$$

$$= \frac{2 \widetilde{V}_f}{(1-\alpha)} \left(1 - \frac{r^2}{R^2} \right) \qquad \frac{d_0}{2} = \frac{\sqrt{\alpha} D}{2}$$

$$= \frac{2 j_f}{(1-\alpha)^2} \left(1 - \frac{r^2}{R^2} \right)$$

$$V_i = V_{f,\,maximum} = V_f(r) \Big|_{r=\frac{d_0}{2}} = \frac{\Delta P D^2}{16 \mu_f L} (1-\alpha) = 2 \widetilde{V}_f = \frac{2 j_f}{(1-\alpha)}$$

$$\frac{\Delta P}{L} = \frac{32 \mu_f j_f}{(1-\alpha)^2 D^2}$$

$$\left(\text{L-L case continues} \longrightarrow \right)$$

L-L CASE (continued)

$$\tilde{V}_g = \frac{\Delta P \, D^2 \alpha}{32 \mu_g L} + V_i$$

$$V_g(r) = \frac{\Delta P \, D^2 \alpha}{16 \mu_g L}\left(1 - \frac{r^2}{R_o^2}\right) + V_i \qquad ; \qquad 0 \le r \le \frac{d_o}{2}$$

$$2(\hat{V}_g - V_i)\left(1 - \frac{r^2}{R_o^2}\right) + V_i \qquad ; \qquad \frac{r^2}{R_o^2} = \frac{4r^2}{\alpha \, D^2}$$

$$V_{g,\,maximum} = V_g(r)\Big|_{r=0} = 2\tilde{V}_g - V_i$$

$$\frac{V_{g,\,maximum}}{\hat{V}_g} = \frac{2\mu_f \alpha + 2\mu_g(1-\alpha)}{\mu_f \alpha + 2\mu_g(1-\alpha)}$$

$$\tilde{V}_g = V_f\left(\frac{\mu_f}{\mu_g} \, \frac{\alpha}{1-\alpha} + 2\right)$$

$$\frac{\Delta P}{L} = \frac{32 \mu_g \mu_f \, j_g}{(\alpha \mu_f + 2(1-\alpha)\mu_g)\,\alpha \, D^2}$$

$L-T$ CASE (LAMINAR VAPOR — TURBULENT LIQUID)

$L-T$ solution to general equation of annular flow:

$$j_g = \propto \left[\frac{K_f \, \mu_f^{\,x} \, \rho_f^{(1-x)}}{16 \, \mu_g} \frac{\propto D^{(1-x)}}{(1-\alpha)^2} \dot{j}_f^{\,(2-x)} + \underbrace{\frac{\dot{j}_f \,(m+1)(m+2)}{2(1-\sqrt{\alpha})(1+(m+1)\sqrt{\alpha})}}_{V_i} \right]$$

turbulent case (liquid fil..

Typically:

$$K_f = 0.046$$
$$x = 0.2$$

Typically $m = \frac{1}{7}$:

$$V_i = \frac{\dot{j}_f \; 60}{49 \,(1-\sqrt{\alpha})(1+\frac{8}{7}\sqrt{\alpha}}$$

if $\alpha = 0$, $\dot{j}_f = \widetilde{V}_f$ and:

$$V_i = \frac{60}{49} \, \widetilde{V}_f$$

or Typical single phase
flow turbulent relationsh

T-L CASE (TURBULENT VAPOR — LAMINAR LIQUID)

T-L solution to general equation of annular flow:

$$j_g = \alpha \left[\left(\frac{16 \mu_f \sqrt{\alpha}^{(1+y)}}{k_g \mu_g^y \rho_g^{(1-y)} \mathcal{D}^{(1-y)} (1-\alpha)^2} j_f \right)^{\frac{1}{2-y}} + \frac{2 j_f}{1-\alpha} \right]$$

$\underbrace{\qquad\qquad}$

V_i , laminar case of liquid film

Typically

$$k_g = 0.046$$
$$y = 0.2$$

$$V_i = 2 \widetilde{V}_f$$

T-T CASE (TURBULENT VAPOR — TURBULENT LIQUID)

T-T solution to general equation of annular flow

$$
\dot{J}_g = \alpha \int_f^{\frac{2-x}{2-y}} \left[\frac{K_f \mu_f^x \rho_f^{(1-x)} D^y \sqrt{\alpha}^{(1+y)}}{K_g \mu_g^y \rho_g^{(1-y)} D^x (1-\alpha)^2} \right]^{\frac{1}{2-y}} + \dot{J}_f \underbrace{\frac{(m+1)(m+2)}{2(1-\sqrt{\alpha})(1+(m+1)\sqrt{\alpha})}}_{V_i}
$$

V_i
for turbulent liquid fil.

Typically

$K_f = K_g = 0.046$ $m = \frac{1}{7}$

$x = y = 0.2$ (liquid turbulent velocity profile exponent)

and equation simplifies.

However, to permit the more general case, these co-efficients and exponents are kept separate, permitting them to vary separately (e.g., as a function of Reynold's number or film thickness).

T-T solution can be solved exactly. However an approximation is instructive:

Exact solution will show that for freon 11,
$\tilde{V}_g / \tilde{V}_f$ varies from 25 at $\alpha = 0.9$
to 9 at $\alpha = 0.1$

$\therefore V_i$ (approx $\frac{60}{49} \tilde{V}_g$) can be assumed negligible.

Using $K_f = K_g = 0.046$; $x = y = 0.2$:

$$\frac{\rho_g^{0.8} \, j_g^{1.8}}{\rho_f^{0.8} \, j_f^{1.8}} = \left(\frac{\mu_f}{\mu_g}\right)^{0.2} \frac{\alpha^{2.4}}{(1-\alpha)^2}$$

note that left side of equation is essentially the ratio of superficial momentum fluxes.

note also how close this form is to eqn (4) of the over-simplified solution.

note furthermore that the dependency on viscosity ratio is very small (ie, $1/5^{TH}$ power) and that μ_g could be removed entirely by using $C_i = 0.005 \left[1 + 150(1 - \sqrt{\alpha}) \right]$ instead of K_g / Re_g^y

T-T CASE (continued)

other useful relationships:

$$\frac{\Delta P}{L} = \frac{2 C_w \rho_f \tilde{V}_f^2}{D} \quad ; \quad C_w = \frac{K_f}{Re_f^x}$$

$$= \frac{2 C_i \rho_g (\hat{V}_g - V_i)^2}{\sqrt{\alpha} \, D} \quad ; \quad C_i = \frac{K_g}{Re_g^y}$$

$$V_i = \frac{j_f (m+1)(m+2)}{2 (1-\sqrt{\alpha})(1+\sqrt{\alpha}(m+1))}$$

$$\overset{r = \frac{\sqrt{\alpha} D}{2}}{}$$

$$V_f(r) = \frac{V_i}{(1-\sqrt{\alpha})^m} \left(1 - \frac{r}{R}\right)^m \quad ; \quad \frac{d_0}{2} \le r \le \frac{D}{2} = R$$

$$V_g(r) = \left(\hat{\tilde{V}}_g - V_i\right) \frac{(n+1)(n+2)}{2} \underbrace{\left(1 - \frac{r}{d_0/2}\right)^n}_{} + V_i \quad ; \quad \overset{0 \le r}{\frac{d_0}{2} = 1}$$

$$\longrightarrow \left(1 - \frac{2r}{\sqrt{\alpha} D}\right)^n$$

$$V_{g,maximum} = \left(\hat{V}_g - V_i\right) \frac{(n+1)(n+2)}{2} + V_i$$

m is turbulent liquid velocity profile exponent

n "   "   vapor "   "   "

Typically $m = \frac{1}{7}$; $n = \frac{1}{7}$

However each can be a function of Reynold's number. If so, will vary from $\frac{1}{6}$ at $Re = 4000$ To $\frac{1}{10}$ at $Re = 3,200,000$:

$Re \rightarrow$	4×10^3	2.3×10^4	1.1×10^5	1.1×10^6	3.2×10^6
m or n $\rightarrow$	1/6	1/6.6	1/7	1/8.8	1/10.0

APPENDIX E

Liquid-Liquid Pressure Drop Data and Correlations

Purpose and Introduction

This appendix presents the equations and correlations used in the report body to predict frictional pressure gradient, and the Figures show how well these predictions match data.

It must be emphasized that all data presented in this appendix is from <u>only liquid-liquid flow regime experiments</u>. These experiments are detailed in Appendix A. No data comes from true microgravity vapor-liquid experiments, since none is known available at this writing.

Most of the report body is concerned with prediction of flow regime. However, the proposed method to predict flow regime uses the minimization of pressure gradient principle. For this principle to work, reasonably accurate expressions for pressure gradient in each flow regime are clearly required. This appendix explains how the chosen expressions for pressure gradient were obtained.

Flow Regimes and Fluid Systems Considered

There are three flow regimes of interest in this study -- bubble, slug, and annular flow. As discussed in the report body, these are the three major flow regimes which have been observed in true microgravity vapor-liquid flows.

The initial experiments with Fluid #1 are now regarded as learning experiences and are not considered part of the simulations. Much inverse annular flow, little slug flow, and no annular flow was observed in this set of experiments. From these initial experiments, the importance of an annular flow entrance geometry and of waxing the tube wall to change its wetting properties (to prevent inverse annular flow) were learned. These two techniques helped better simulate true vapor-liquid microgravity flow in later fluid systems.

The experiments with Fluid #4 are also regarded as a special case. From these experiments, it was learned that when interfacial tension in equi-density liquid-liquid flows is too small, slug flow, by and large, does not form. Instead, the observed flow regime is a stratified flow of sorts. The stratification is caused by minuscule density differences which, in the presence of sufficient interfacial tension forces, do not usually dominate "micro-buoyant" flow behavior. Because slug flow did not, in general, occur with Fluid #4, the data from these simulations were not used.

Method Used to Develop Expressions for Pressure Gradient

The steps taken to develop equations for frictional pressure gradient for each of the three flow regimes follow:

- Analytical or semi-analytical equations were developed or found in the literature for each flow regime.

- Predictions from these equations were fit to each data set by choosing a single factor to correct the predictions to best match the data. A single data set was considered to be all the data points of a single flow regime for each fluid or diameter tested.

  Slug flow pressure drop predictions used an additional coefficient -- a slip velocity ratio C_1. This ratio was simultaneously varied with the overall correction factor to find the pair of values for each slug flow data set which best fit that data set.

- The correction factors (and the slip ratios for slug flow) were averaged. This single correction factor (plus a single average slip ratio for slug flow) were taken as valid for all fluids and diameters.

The reason for the final step is that each individual data set is quite small. Any given data set may not be fully accurate. For example, in some experiments a flow regime was still developing as the flow passed the upstream pressure tap. Thus, a uniform pressure gradient for a single flow regime was not always measured. Future experiments would place this pressure tap further downstream to avoid such errors. The averaging technique was an effort to increase overall accuracy by minimizing error introduced by experimental discrepancies.

A quick summary of the bubble pressure drop data illustrates the improvement in accuracy gained by using the above averaging technique. To best match data, the predicted bubble flow pressure drop was multiplied by the following correction factors:

Fluid System	Diameter	Correction Factor C_B
#2	25.4 mm	.97
#3	25.4 mm	1.03
#3	12.7 mm	.80
#3	8.0 mm	1.05
#5	25.4 mm	1.14
	Average:	0.998 = 1.00

Most data sets in the previous table showed excellent agreement with theory -- the correction factor was virtually unity. However, the prediction for the fluid #5 system needed a 14% increase to match data. In addition, the prediction for the fluid #3 system needed a 20% decrease to match data. Aside from unknown, inadvertent experimental inconsistencies, we can hypothesize no physical reasons for these variations from theory. For example, why should fluid #3 require a 20% adjustment only at 12.7 mm diameter? The simplest answer is that the small data sample and some form of experimental error or uncontrolled secondary effect have combined to introduce this error. The average correction factor of unity indicates that the bubble flow equations are valid without modification.

A similar approach was used to obtain average correction factors for the pressure gradient calculation of the slug and annular flow regimes. However, in these two cases, the correction factors were not unity.

Bubble Flow

Bubble flow frictional pressure gradient was predicted with a purely analytical expression. As will be seen, the match to data was in most cases excellent.

The homogeneous flow assumption was used. The homogeneous frictional pressure gradient can be calculated as:

$$- \frac{dP}{dz} = \frac{2 \ C_f \ \rho_m j^2}{D} \qquad\qquad (E\text{-}1)$$

with homogeneous density defined as:

$$\rho_m = \alpha \rho_2 + (1 - \alpha) \rho_1 \qquad\qquad (E\text{-}2)$$

Homogeneous ("virtual" viscosity is defined from theory (Wallis [1969], page 27) as:

$$\mu_m = \mu_1 \left[1 + 2.5\alpha \frac{\mu_2 + 2/5 \ \mu_1}{\mu_2 + \mu_1} \right] \qquad\qquad (E\text{-}3)$$

The coefficient of wall friction is defined as:

$$C_f = \frac{16}{Re} \quad \text{for laminar flow.} \qquad\qquad (E\text{-}4)$$

$$= \frac{0.046}{Re^{0.2}} \quad \text{for turbulent flow.} \qquad\qquad (E\text{-}5)$$

The viscosity equation assumes fluid spheres of substance 2 within continuous fluid 1. Theoretically, the equation is invalid above 5% void fraction. However, as will be seen, this formulation fit the data very well to at least 20% homogeneous void fraction. As will also be seen, this particular formulation of homogeneous viscosity fit the data much better than alternative formulations.

Figure E-1 shows predicted versus measured pressure gradient for bubble flow in fluid system #2. The theory matches data very well. Figures E-5 and E-6 for silicone and water, referred to later, show even better matches.

Three alternative (non-analytical) formulations for homogeneous viscosity from Wallis [1969], page 27, were also tried. They are:

$$\frac{1}{\mu} = \frac{x}{\mu_2} + \frac{1 - x}{\mu_1} \qquad\qquad \text{McAdams}$$

$$\mu = x\mu_2 + (1 - x)\mu_1 \qquad\qquad \text{Cicchitti}$$

$$\mu = (1 - \alpha)\mu_1 + \alpha\mu_2 \qquad\qquad \text{Dukler}$$
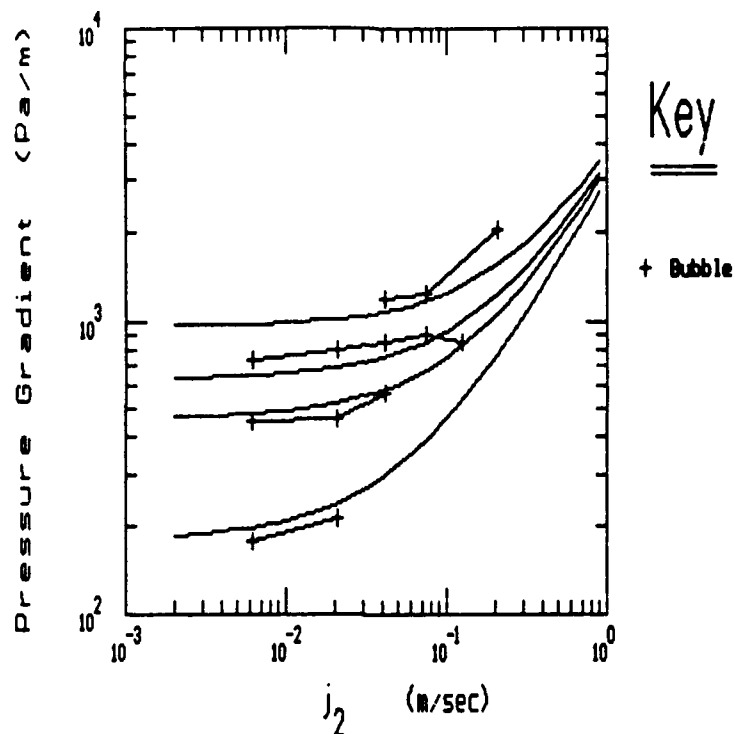
Figure E-1. Theoretical homogeneous viscosity. Mineral Oil (j1) and Water (j2). Predicted vs. Measured Bubble Flow Pressure Gradient at Constant j1. Diameter = 1 inch (25.4 mm)
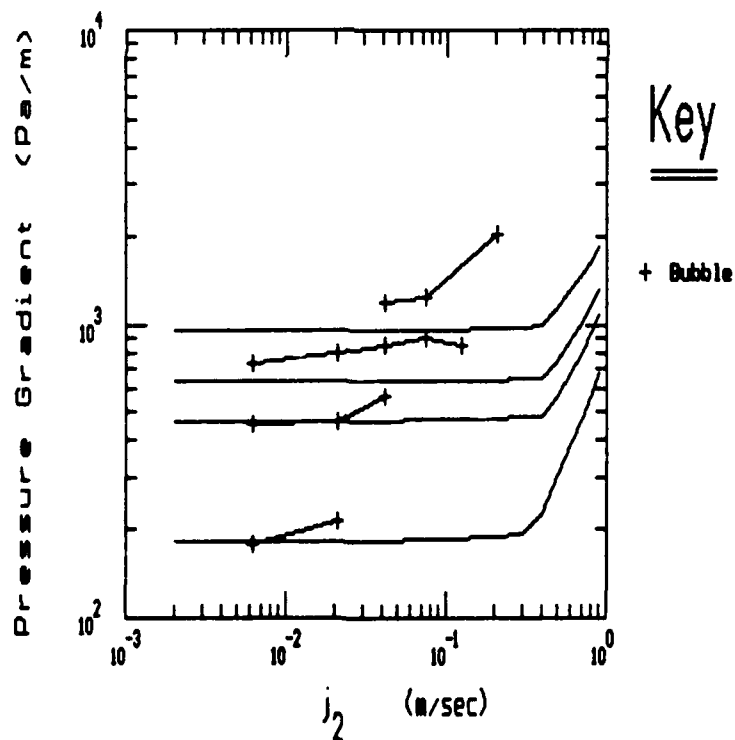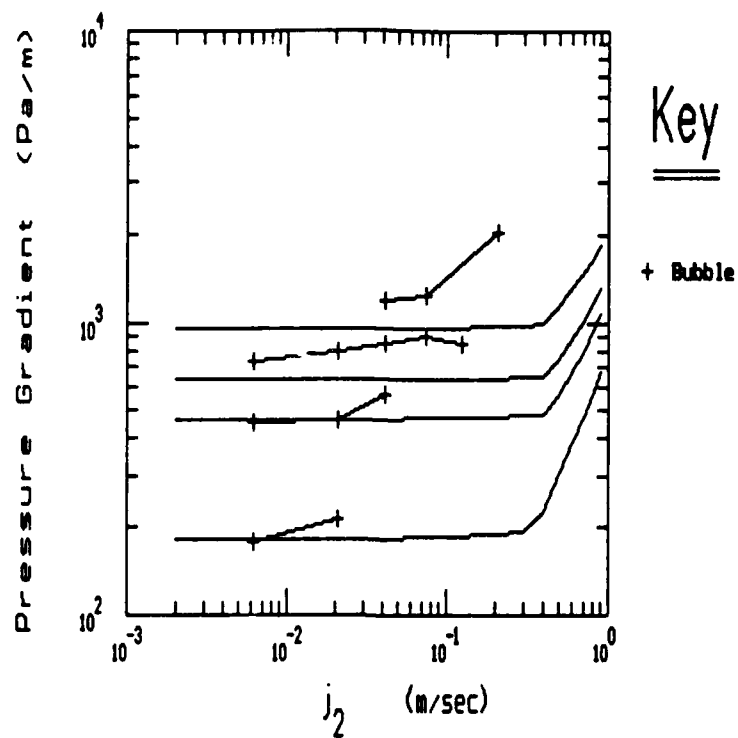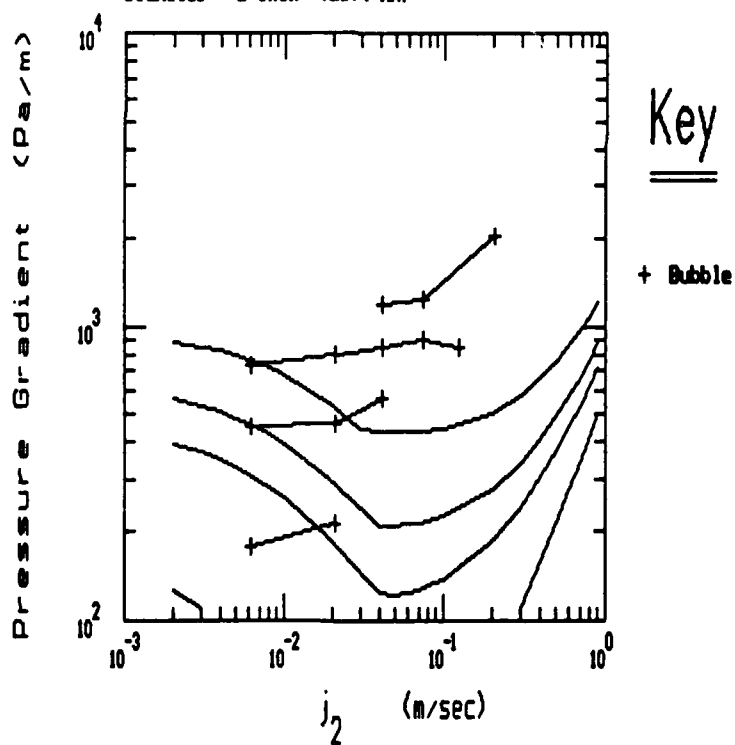

Figure E-2. Cicchitti's homogeneous viscosity. Mineral Oil (j1) and Water (j2). Predicted vs. Measured Bubble Flow Pressure Gradient at Constant j1. Diameter = 1 inch (25.4 mm)

Figure E-3. Dukler's Homogeneous Viscosity. Mineral Oil (j1) and Water (j2).
Predicted vs. Measured Bubble Flow Pressure Gradient at Constant j1.
Diameter = 1 inch (25.4 mm)

Figure E-4. McAdams' Homogeneous Viscosity. Mineral Oil (j1) and Water (j2).
Predicted vs. Measured Bubble Flow Pressure Gradient at Constant j1.
Diameter = 1 inch (25.4 mm)

E-8

None of the three previous expressions for homogeneous viscosity makes an allowance for which fluid contacts the tube wall. However, each yields the correct single phase viscosity at either limit and a continuous function in between. Such expressions are convenient for obtaining first-order approximations of two-phase pressure drop across the flow range, without regard to actual flow regime. However, the next three figures will show that these three viscosity formulations do not fit the present bubble flow data very well.

Figure E-2 shows that the Cicchitti viscosity equation does not match the bubble flow data very well for fluid system #2.

Figure E-3 shows that neither does the Dukler viscosity equation match the bubble flow data for fluid system #2.

Lastly, Figure E-4 shows that the McAdams viscosity equation does not match matches the bubble flow data for fluid system #2 either.

Clearly, of the choices above, the theoretical viscosity equation gives the best fit to the present data. Therefore it was chosen throughout the analysis. Similar comparisons of theory to data will yield similar results with data from any of the fluid systems used in this study.

Figures E-5 through E-8 show how well the bubble flow pressure drop predictions match data for the various liquid-liquid systems.

The agreement between prediction and measurement is generally very good. (Note especially Figures E-5 and E-6.) Therefore, the bubble flow pressure gradient equation is taken as theoretically pure homogeneous flow with the theoretically derived virtual viscosity given above. No adjustments to the theory are merited.
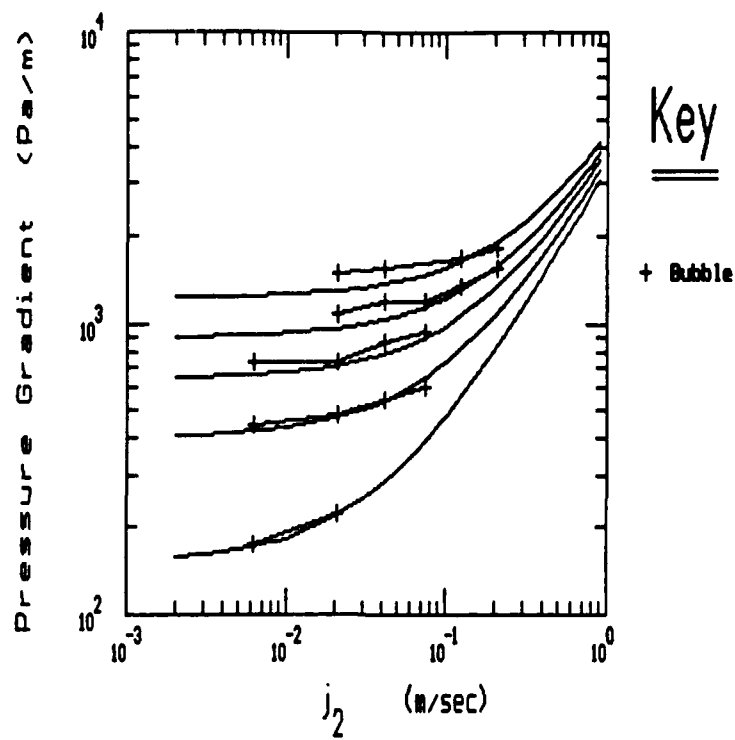
Figure E-5. Predicted vs. Measured Bubble Flow Pressure Gradient at Constant j1.
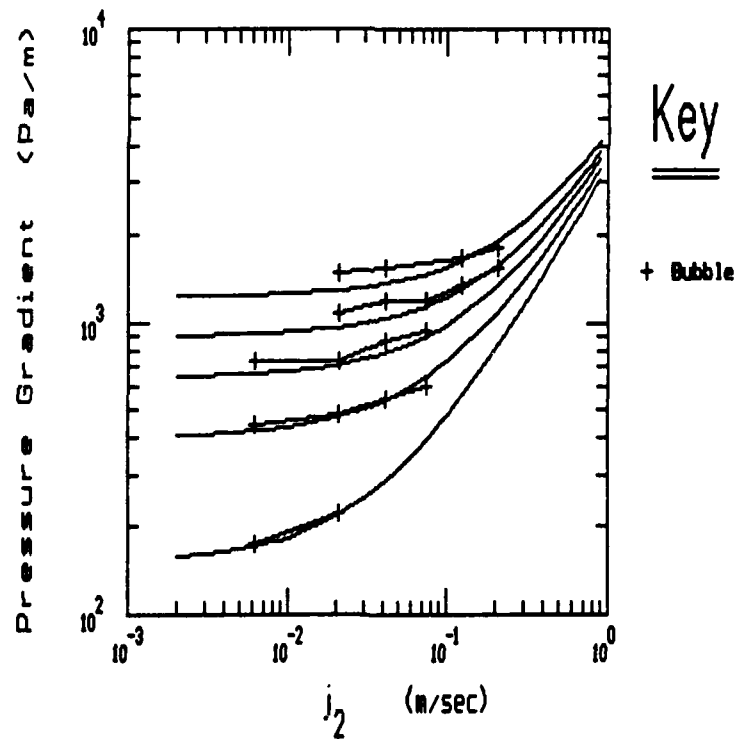Silicone (j1) and Water (j2).   Diameter = 1 inch   (25.4 mm)

Figure E-6. Predicted vs. Measured Bubble Flow Pressure Gradient at Constant j1.
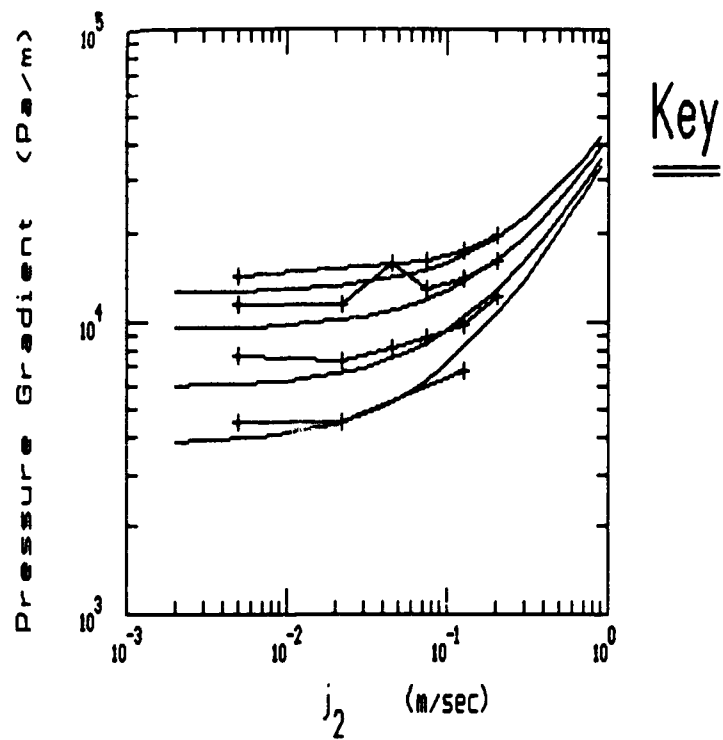Silicone (j1) and Water (j2).   Diameter = 1 inch   (12.7 mm)

Figure E-7. Predicted vs. Measured Bubble Flow Pressure Gradient at Constant j1.
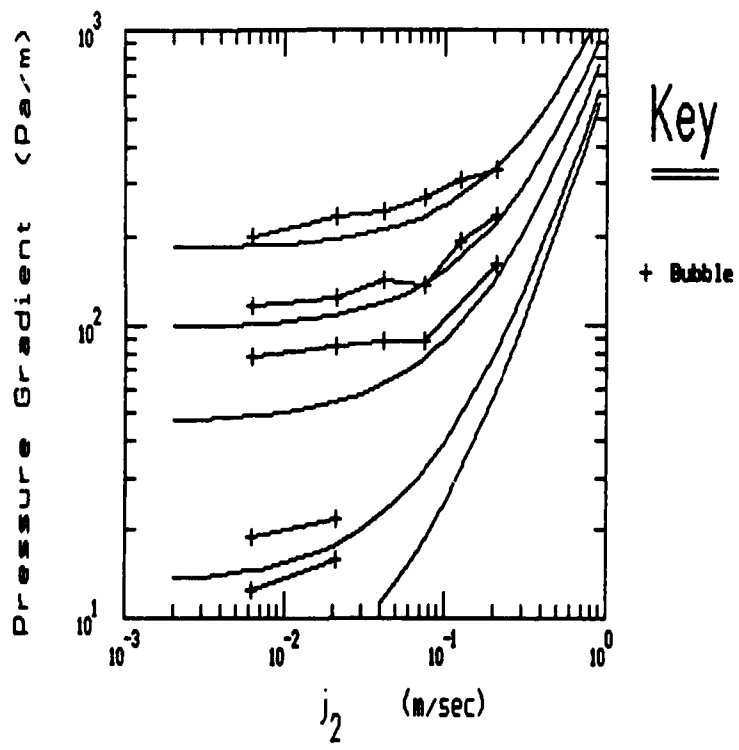Silicone (j1) and Water (j2).   Diameter = 5/16 (8mm)

Figure E-8. Predicted vs. Measured Bubble Flow Pressure Gradient at Constant j1.
Kerosene (j1) and Water (j2).   Diameter = 1 inch (25.4 mm)

Slug Flow

Slug flow frictional pressure gradient was predicted using a semi-analytical expression. A correction factor and a slip velocity ratio were used as part of this expression. The correction factor can be thought of as a multiplier to account for pressure drop due to end effects around Taylor bubbles. The slip ratio is the assumed ratio of Taylor bubble velocity to liquid slug velocity. Using these two parameters, measured slug flow pressure gradients could be correlated quite well.

The semi-analytical expression for slug pressure gradient follows:

$$- \frac{dP}{dz} = F_s \left[\frac{2 \, C_w \, \rho_1 j \left(1 - L_t^* \right)}{D} + \frac{2 \, C_i \, \rho_2 \tilde{v}_2 L_t^*}{d_o} \right] \tag{E-6}$$

$$\tilde{v}_2 = C_1 \, j \tag{E-7}$$

$$d_o = \sqrt{\frac{1}{C_1}} \, D \tag{E-8}$$

$$L_t^* = \frac{j_2}{j} \tag{E-9}$$

$$j = j_1 + j_2 \tag{E-10}$$

From the liquid-liquid experiments, the average slug pressure gradient correction factor F_s and slip velocity ratio C_1 that best matched the data were:

$$F_s = 1.21$$

$$C_1 = 1.86$$

These averages were derived from the best fits to the individual slug flow data sets below:

Fluid System	Diameter	F_s	C_1
#2	25.4 mm	1.27	1.49
#3	25.4 mm	1.30	2.54
#3	12.7 mm	1.12	1.90
#3	8.0 mm	1.50	1.81
#5	25.4 mm	0.88	1.56
	Averages:	1.21	1.86

E-12

Figures E-9 through E-13 show how well the slug flow pressure drop predictions agree with data for the various liquid-liquid systems. The agreements are reasonably good.
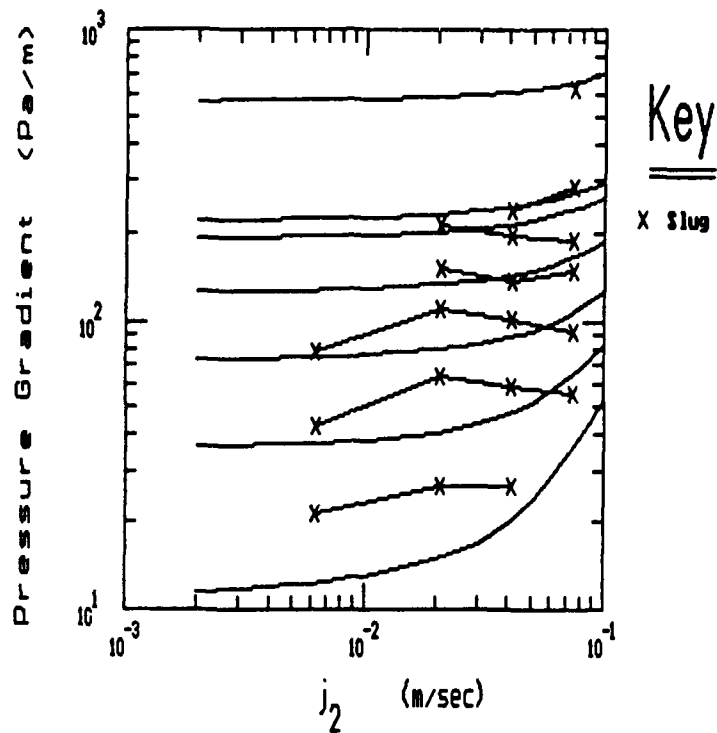
Figure E-9. Predicted vs. Measured Slug Flow Pressure Gradient at Constant j1.
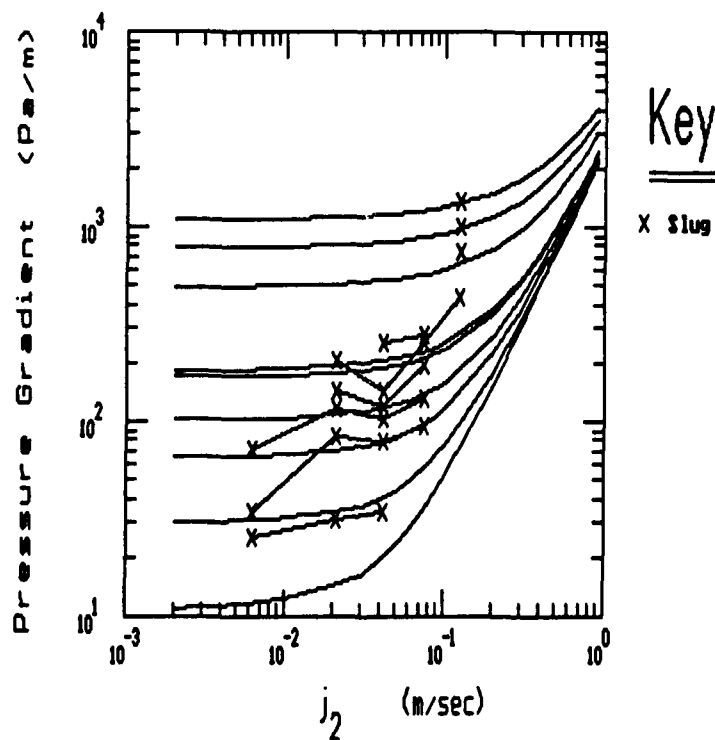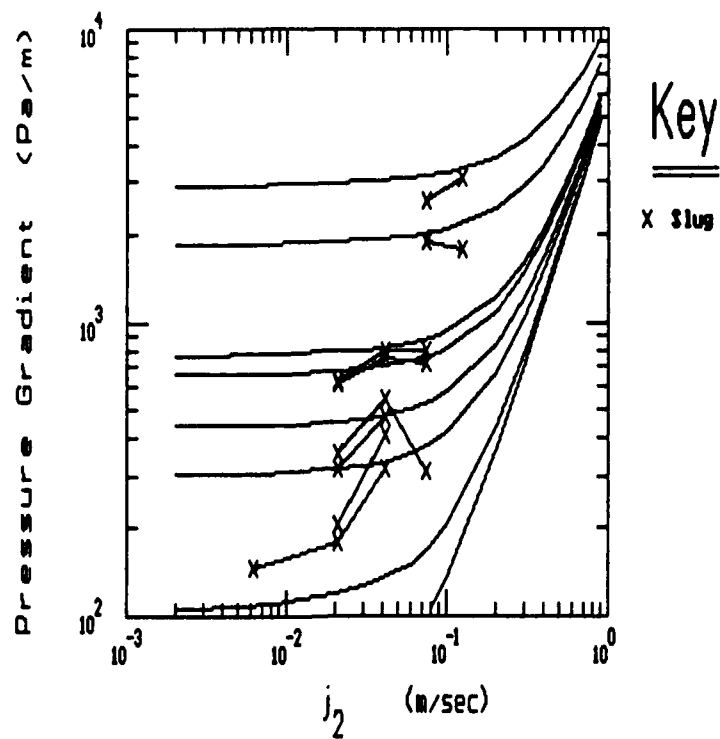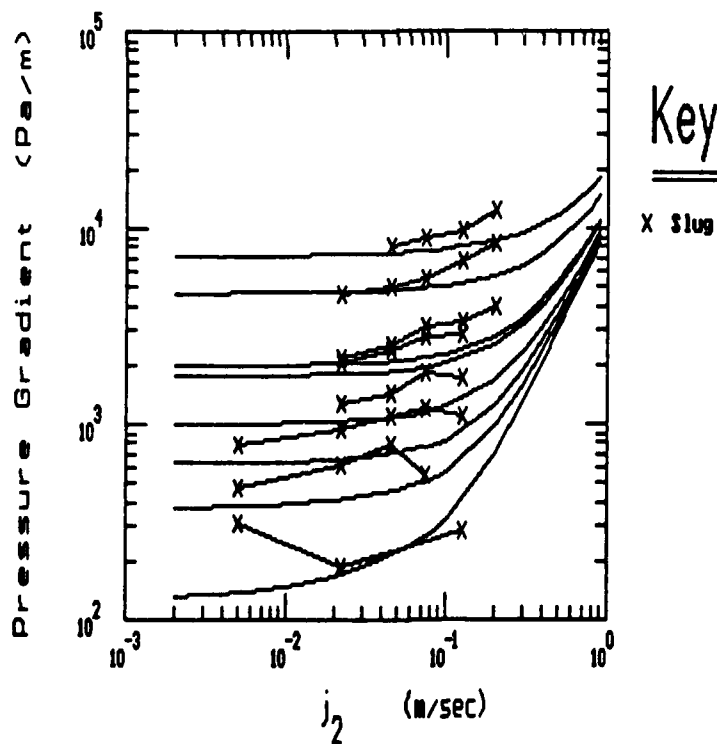Mineral Oil (j1) and Water (j2).   Diameter = 1 inch (25.4 mm)

Figure E-10. Predicted vs. Measured Slug Flow Pressure Gradient at Constant j1.
Silicone (j1) and Water (j2).   Diameter = 1 inch (25.4 mm)

Figure E-11. Predicted vs. Measured Slug Flow Pressure Gradient at Constant j1.
Silicone (j1) and Water (j2).   Diameter = 1/2 inch (12.7 mm)

Figure E-12. Predicted vs. Measured Slug Flow Pressure Gradient at Constant j1.
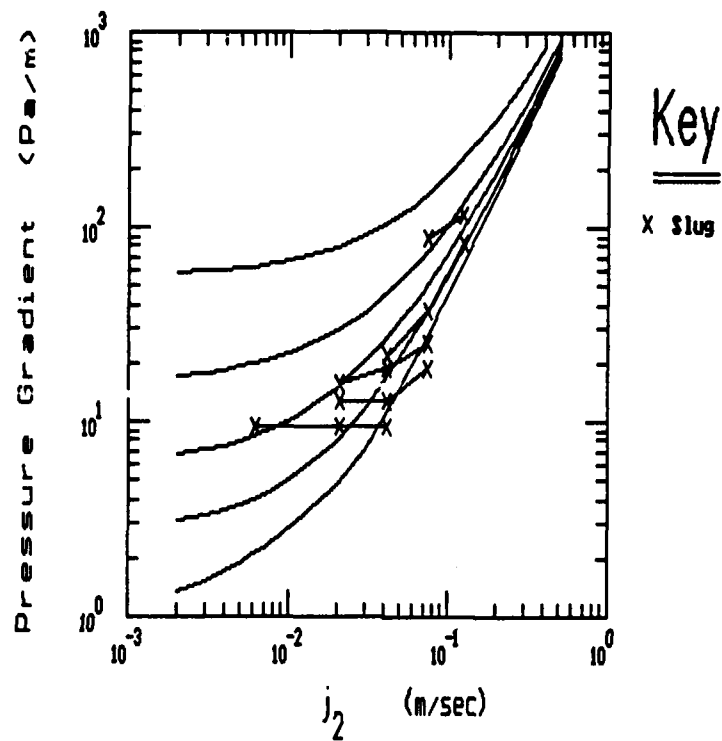Silicone (j1) and Water (j2).   Diameter = 5/16 inch (8mm)

Figure E-13. Predicted vs. Measured Slug Flow Pressure Gradient at Constant j1.
Kerosene (j1) and Water (j2).   Diameter = 1 inch (25.4 mm)

Annular Flow

Annular flow frictional pressure gradient was predicted with an analytical expression derived from an integral analysis -- see Appendix D. The expression is here multiplied by a correction factor C$%a. The correction factor can be thought of as a multiplier to account for such effects as interfacial roughness or droplet flow in the central core. Using this parameter, measured liquid-liquid annular flow pressure gradients can be correlated reasonably well. The equations then become:

$$- \frac{dP}{dz} = F_a \left[\frac{2C_i \, \rho_2 \left(\tilde{v}_2 - v_i \right)^2}{d_o} \right] = F_a \left[\frac{2C_w \, \rho_1 \tilde{v}_1^2}{D} \right] \quad \text{(E-11)}$$

$$F_a = 1.17 \qquad \text{(average annular correction factor from liquid-liquid experiments).}$$

$$\tilde{v}_1 = \frac{j_1}{(1 - \alpha)} \quad \text{(E-12)}$$

$$\tilde{v}_2 = \frac{j_2}{(1 - \alpha)} \quad \text{(E-13)}$$

$$\alpha = \frac{d_o^2}{D^2} \quad \text{(E-14)}$$

for laminar liquid: $C_w = 16/Re_1$ (E-15)

$$v_i = 2 \, \tilde{v}_1 \quad \text{(E-16)}$$

turbulent liquid: $C_w = \frac{0.046}{Re_1^{0.2}}$

$$v_i = \frac{\frac{60}{49} j_1}{\left(1 - \sqrt{\alpha} \right) \left(1 + \frac{8}{7}\sqrt{\alpha} \right)} \quad \text{(E-17)}$$

for laminar vapor: $C_i = \frac{16}{Re_2}$ (E-18)

turbulent vapor: $C_i = \frac{0.046}{Re_2^{0.2}}$ (E-19)

$$Re_1 = \frac{D \, (1 - \alpha) \, \rho_1 \tilde{v}_1}{\mu_1} = \frac{D \, \rho_1 \, j_1}{\mu_1} \quad \text{(E-20)}$$

$$Re_2 = \frac{d_o \, \rho_2 \left(\tilde{v}_2 - v_i \right)}{\mu_2} \quad \text{(E-21)}$$

The average annular correction factor F_a was obtained by averaging the following best fits from the each data set:

Fluid System	Diameter	Correction Factor C_a
#2	25.4 mm	1.17
#3	25.4 mm	0.83
#3	8.0 mm	0.69
#5	25.4 mm	1.98
	Average:	1.17

Note: There was no reasonably pure annular flow in the data for fluid system #3 at 12.7 mm diameter -- the flows were recorded as predominantly mist or drop flow. Therefore, these pressure gradient measurements were not used in the correlating scheme.

Figures E-14 through E-17 show how well the annular pressure drop predictions match data for the various liquid-liquid systems. The agreement between measurement and prediction is generally reasonable.

Figure E-16 deserves comment. The measured pressure gradient at constant j_1 actually decreases with increasing j_2. It is suggested that the decrease is almost certainly due to a regime change from annular to drop flow. This observed sudden reduction in pressure gradient is exactly what has led to the prediction of flow regimes by the minimized pressure gradient principle. Review of this data set on video may show that the regime here was actually not annular flow. However, until the review is made, the data is used as it stands.
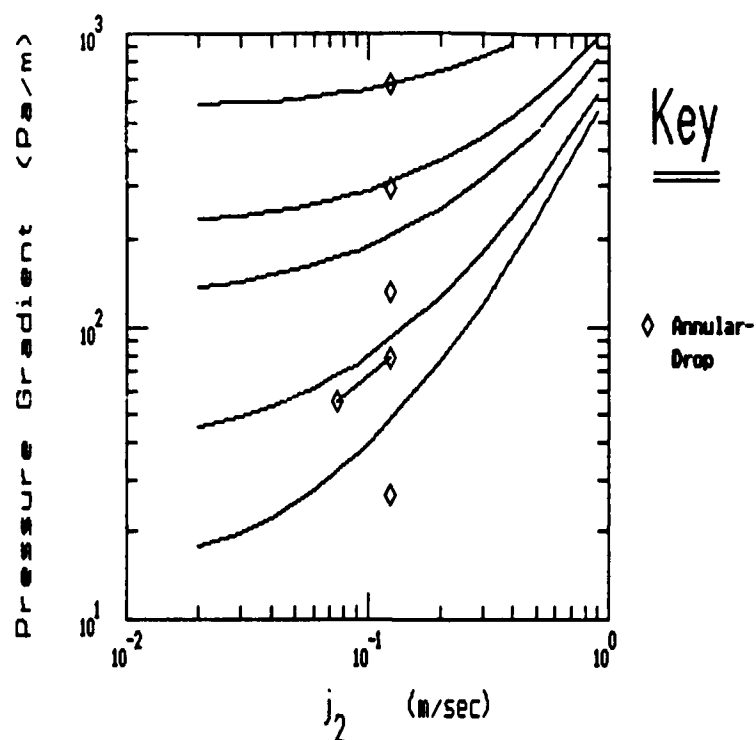
Figure E-14. Predicted vs. Measured Annular Flow Pressure Gradient at Constant j1
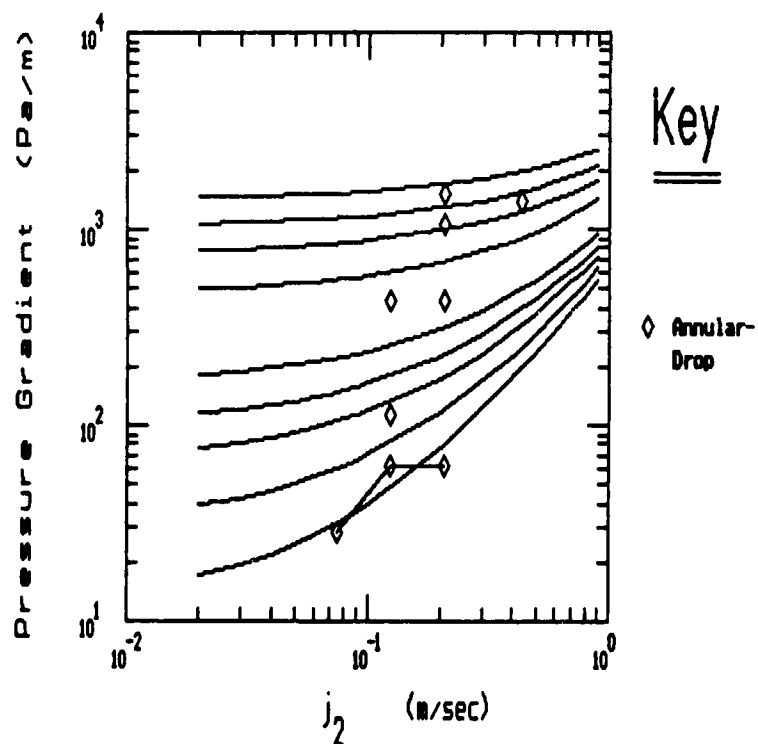Mineral Oil (j1) and Water (j2).   Diameter = 1 inch (25.4 mm)

Figure E-15. Predicted vs. Measured Annular Flow Pressure Gradient at Constant j1.
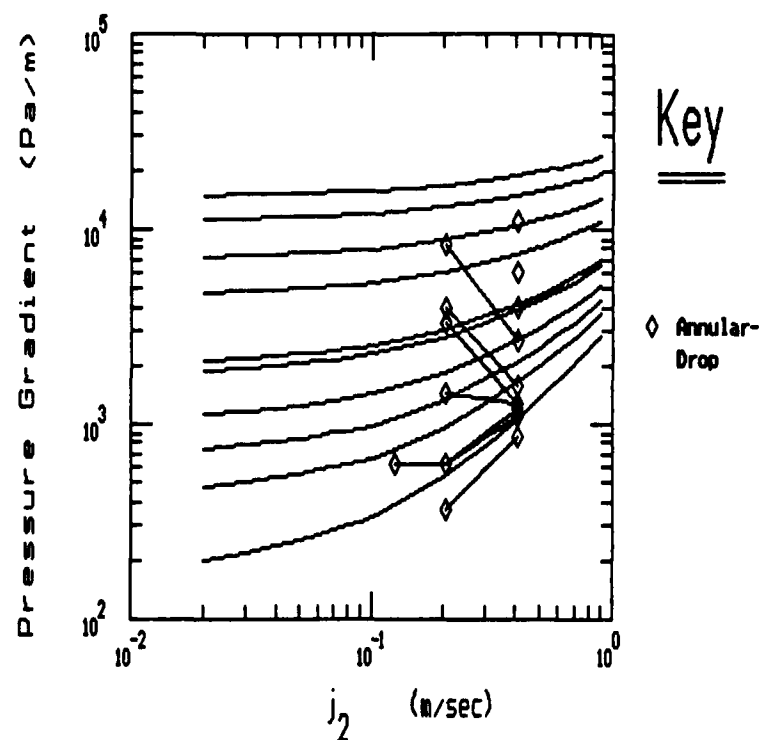Silicone (j1) and Water (j2).   Diameter = 1 inch (25.4mm)

Figure E16. Predicted vs. Measured Annular Flow Pressure Gradient at Constant j1.
Silicone (j1) and Water (j2).   Diameter = 5/16 inch (8 mm)
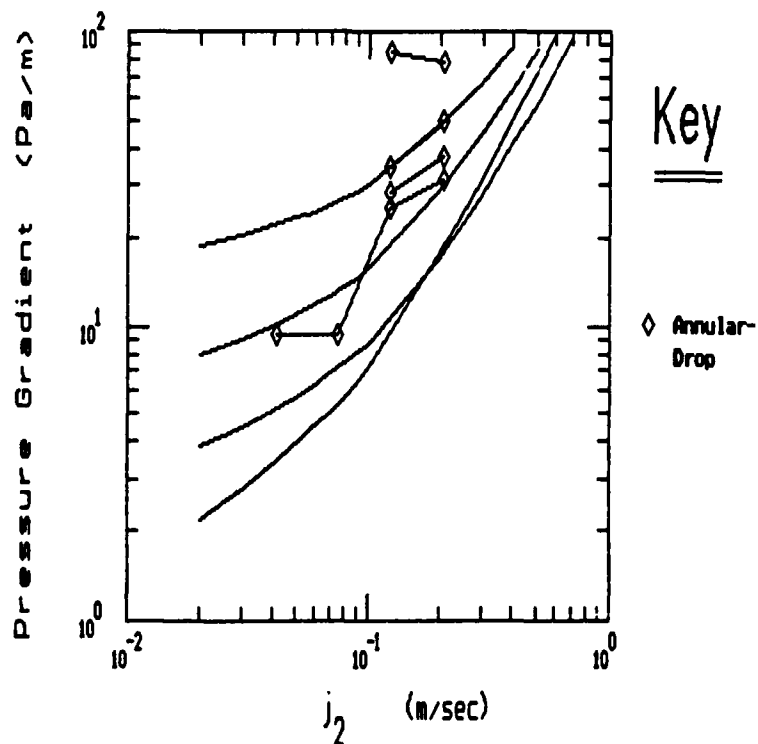

Figure E-17.   Predicted vs. Measured Annular Flow Pressure Gradient at Constant j1.
Kerosene (j1) and Water (j2).   Diameter = 1 inch (25.4 mm)

Conclusion

Simple modifications of analytically-based expressions for frictional pressure gradient have been developed for bubble, slug and annular flow. Good fits to the data have, in general, been obtained.

An averaging method was used to calculate, from the pressure gradient data, a uniform correction for each of the slug and annular flow regimes. Within each flow regime, the correction is the same for every fluid pair. The resulting pressure gradient predictions are quite successful. This method attempts to reduce the errors inherent in small data samples.

As the report body shows, these pressure gradient equations have been used quite successfully to predict observed <u>liquid-liquid</u> flow regimes boundaries and trends.